

Function Follows Form

Geometric Effects in Colloidal Self-Assembly

Cover: the front cover shows four densest packings of rounded tetrahedra, from left to right the dimer crystal, a quasicrystal approximant, a crystal similar to β -tin, and a deformed face-centered cubic crystal. The back cover shows rounded tetrahedral particles self-assembled within a slowly shrinking spherical shell. During this process, particles pack together to fill space as efficiently as possible, which leads to a complicated structure with hexagonal cells that is revealed by coloring particles according to their orientation. The background image of both the front and back is a snapshot of a simulation of self-propelled rods.

PhD Thesis, Utrecht University, The Netherlands, December 2021

ISBN: 978-90-393-7411-5

DOI: <https://doi.org/10.33540/624>

Digital version of this thesis available at: <https://colloid.nl/publications/theses/>

Function Follows Form

Geometric Effects in Colloidal Self-Assembly

Functie Volgt Vorm

Geometrische Effecten in Colloïdale Zelforganisatie

(met een samenvatting in het Nederlands)

Proefschrift

ter verkrijging van de graad van doctor aan de Universiteit Utrecht op gezag van de rector magnificus, prof. dr. H.R.B.M. Kummeling, ingevolge het besluit van het college voor promoties in het openbaar te verdedigen op

woensdag 15 december 2021 des middags te 2.15 uur

door

Robin van Damme

geboren op 11 september 1992
te Utrecht

Promotoren:

Prof. dr. ir. M. Dijkstra

Prof. dr. R.H.H.G. van Roij

Contents

1	Introduction	9
1.1	Scope of this thesis	9
1.2	Nano- and colloidal scale particles	10
1.3	Equilibrium versus non-equilibrium	11
1.4	Entropic crystals and the shape explosion	11
1.5	Statistical mechanics in a nutshell	13
1.6	Computer simulations of statistical mechanics	14
1.7	The anisotropic hard-particle model	16
1.8	Phase transitions and coexistence	18
1.9	Outline of this thesis	19
2	Suppression of Motility-Induced Phase Separation	21
2.1	Introduction	22
2.2	Computational methods	23
2.2.1	Active Brownian Particles	23
2.2.2	Choice of model parameters and additional assumptions	25
2.2.3	Identifying motility-induced phase separation by clustering regions of similar density	26
2.3	An analytical criterion for the onset of MIPS	28
2.3.1	Effective Smoluchowski equation	28
2.3.2	Stability analysis of the homogeneous isotropic phase	29
2.3.3	Finite-size effects when measuring effective swim speed and rotational diffusion	31
2.4	Results & Discussion	32
2.4.1	Phase diagrams of self-propelled disks, spheres and rods	34
2.4.2	Torque-induced suppression of motility-induced phase separation	39
2.5	Conclusions & Outlook	42
2.6	Addendum	43
3	Capillary-driven self-assembly of hourglass-shaped particles at a fluid-fluid interface	45
3.1	Introduction & experimental motivation	46
3.2	Theory & Methods	49
3.2.1	Effective pair interactions and shape parametrization	49
3.2.2	Thermodynamics and simulation of the adsorption of particles at a fluid-fluid interface	51

3.2.3	Multipole expansion of the interfacial deformation	52
3.3	Results & Discussion	55
3.3.1	Adsorption modes	55
3.3.2	Capillary pair interactions	58
3.3.3	Elongation of the quadrupolar mode	60
3.4	Conclusions	68
3.5	Acknowledgements	69
4	Densest packings and bulk phase behaviour of rounded tetrahedra	71
4.1	Introduction	72
4.2	Model & Methods	73
4.2.1	The spherotetrahedron shape	73
4.2.2	Predicting the densest packings	74
4.2.3	Crystallography and bond-orientational order parameters	75
4.2.4	Self-assembly and equation of state simulations	78
4.3	Dense packings	79
4.3.1	Classification of dense packings	79
4.3.2	Crystal structures	87
4.3.3	The maximum packing fraction of the quasicrystal approximant	89
4.4	Phase behaviour at intermediate density	91
4.4.1	Quasicrystal self-assembly near $s = 0$	93
4.4.2	Plastic crystal pFCC for $s > 0.5$	93
4.4.3	Absence of crystallization for $s \in (0.16, 0.5)$	94
4.4.4	Transitions between crystals V, VI and VII	98
4.5	Conclusions & Outlook	100
5	Determining order parameters for crystals of rounded tetrahedra using dimensionality reduction	103
5.1	Introduction	104
5.2	Data set construction	106
5.3	Principal component analysis with \bar{q}_l for $2 \leq l \leq 12$	107
5.4	A larger set of possible bond order parameters with \bar{q}_l and w_l for $2 \leq l \leq 24$	112
5.4.1	Excluding w_2	114
5.5	Conclusions	117
6	Egg-shaped supraparticles of rounded tetrahedra	119
6.1	Introduction	120
6.2	Mapping the experimental particle shape to the model	120
6.3	Determining the supraparticle crystal structure from its structure metric fingerprint	123
6.4	Free-energy calculations	126
6.4.1	Free energy of the fluid	126
6.4.2	Free energy of the plastic crystal pFCC	127
6.4.3	Free energy of crystal VII	131
6.5	Hard spherotetrahedra in spherical confinement	136

6.5.1	Mackay/anti-Mackay structural order	136
6.5.2	Orientational order at the spherical boundary	140
6.6	Conclusions	143
6.7	Outlook	144
A	An algorithm for calculating the volume of arbitrary convex spheropolyhedra	145
B	Free energies of three-dimensional ideal rotator systems	147
B.1	Rotational free energy of an ideal gas of classical uniaxial rotators	147
B.2	Rotational free energy of an ideal Einstein crystal of classical uniaxial rotators	147
B.3	Rotational free energy of an ideal gas of classical rigid body rotators using quaternion orientations	148
B.4	Rotational free energy of an ideal Einstein crystal of arbitrarily symmetric objects	149
	Summary	165
	Samenvatting	168
	Acknowledgements	171
	Publications	174
	Oral and poster presentations	175
	About the author	176

1

Introduction

1.1 Scope of this thesis

Form follows function. A famous design rule in architecture, this phrase states that the shape of a building should be determined by its intended function. In materials science, however, one could state the opposite: function follows form. The properties of materials, and thus their possible functions, are determined by the form of the interactions between the microscopic building blocks that make up the material.

Of course, there are many more differences between architecture and materials science. Building a material is not like building a house. One cannot lay it brick-by-brick, atom-by-atom. Atoms and molecules are too small, too light, too fast, and one needs far too many to form a chunk of material of any reasonable size. While one can build a house with only a few thousand bricks, to build even a cube of sugar one already needs some 10^{21} atoms. You would have to place them either very fast or spend a very long time building. Of course, nature provides a much more elegant way. When it snows, there is no tiny machine in the clouds that prints snowflakes — they simply form from the water itself. The diamonds we find in the earth are not constructed, they are formed naturally at the high pressures and temperatures found deep in the earth's crust. These materials are not manually assembled, but rather they assemble themselves. This process of *self-assembly* is a cornerstone of modern material design: rather than performing the assembly ourselves, we make clever use of chemistry and thermodynamics to instead design a process that will cause our material to assemble itself for us. This requires two things: the right building blocks, and an appropriate environment. These building blocks can be many things: atoms, molecules, polymers, proteins, nanocrystals, generally anything smaller than a few hundred micrometers can be made to self-assemble. The appropriate environment is generally described in terms of thermodynamics and chemistry: a certain temperature, pressure, pH or salt concentration, occasionally supplemented by reservoirs of specific chemicals, polymers or an applied electric or magnetic field. The astute reader will at this point exclaim “that description is so broad it covers pretty much everything!”, and they would be right. The design space of materials is absolutely, staggeringly huge. As a result, much of modern material science is devoted to investigating what does what: how do the properties of some material change with the temperature, or with the concentration

of some added chemical? And, importantly: why? With this knowledge, we can make *design rules* that provide us with general recipes that we can follow in order to obtain materials with specific properties: compress or cool a fluid quickly, and it will likely become a glass. Do so slowly, and it will instead form a crystal. Want this crystal to form at low densities? Make particles interact over a long range. Good design rules are useful heuristic tools that allow us to quickly and effectively design materials without going through the lengthy process of checking the influence of all variables every time.

In this thesis, we do a similar what-does-what investigation with a focus on the effects of *geometry*. Specifically, we study how the *shape* of particles and the shape of the environment they assemble in influences their self-assembly. We investigate geometric effects on self-assembly in four settings: in bulk, within a droplet of fluid, at the interface between two fluids, and far from thermodynamic equilibrium. Before we can get started, however, there are a few concepts and methods to introduce and review.

1.2 Nano- and colloidal scale particles

What is it that drives small enough objects ($\lesssim 100\ \mu\text{m}$) to self-assemble? Though not his intention, this answer to this question was already discovered back in 1827 by the botanist Robert Brown [1]. Using a microscope, Brown closely studied the behaviour of plant pollen suspended in water and made the following observation:

While examining the form of these particles immersed in water, I observed many of them very evidently in motion; [...] These motions were such as to satisfy me, after frequently repeated observation, that they arose neither from currents in the fluid, nor from its gradual evaporation, but belonged to the particle itself.

To Brown, it appeared that these particles (the pollen) possessed some motion inherent to themselves. The smallest of such particles that he observed he called “molecules”, speculating that he was seeing the elementary particles of which all organic matter was composed. In truth, the smallest particles that Brown observed were approximately $1\ \mu\text{m}$ in size — far larger than our current definition of molecules, which are a thousand times smaller ($\sim 0.1 - 1\ \text{nm}$). Instead, what Brown had observed was the random motion that results from the countless collisions between the plant pollen particles and the many (to him invisible) water molecules in which they were suspended. The underlying cause of this phenomenon that we now call *Brownian motion* was later explained by William Sutherland [2] and Albert Einstein [3]. Combined with further experiments by Jean-Baptiste Perrin [4], their results cemented the idea of the existence of atoms in the scientific community. Brownian motion occurs for any small enough particle suspended in a fluid, and it is this motion that allows small enough objects to self-assemble. But how small is “small enough”? By its definition, the size of particles undergoing Brownian motion must be large enough to have their behaviour dominated by collisions with multiple, smaller particles such as atoms or smaller molecules. This places a lower bound of around $1\ \text{nm}$. On the other end, if particles become too large, a molecule bumping into them will barely change their momentum, and collisions will become so numerous that they average out to zero.

In practice, this then results in an upper bound of about $1\text{ }\mu\text{m}$. We call this regime in which particles are larger than a few molecules, yet small enough to self-assemble the *colloidal* regime. The name “*colloid*” comes from the Greek word $\kappa\omicron\lambda\lambda\alpha$, meaning “glue”, as coined by Thomas Graham in 1860 [5]. It is a bit of a misnomer for its more modern use. Colloids are found in a much wider range of products than just glue: from care products such as gels, shampoo, and sunscreen to foods like milk, mayonnaise and salad dressing, to the solar panels that increasingly adorn our roofs, and even to the ink or the display that you are using to read this thesis. Not only are colloids interesting in their own right, they also serve as a convenient window into the behaviour of atoms and molecules at the even smaller scales. Like colloids, atoms and molecules undergo a random *thermal motion* due to collisions with each other. This similarity in random motion allows us to use colloids, which are large and slow enough to study under a microscope, to study the self-assembly of the much smaller and harder to follow atoms and molecules.

1.3 Equilibrium versus non-equilibrium

In this thesis we encounter in a number of ways the concepts of *equilibrium* and *non-equilibrium*. While many who study thermodynamics or materials science will have a learned understanding of these concepts, it is worthwhile to consider them in more detail. The laws of thermodynamics state that two otherwise isolated systems brought into contact with one another may exchange e.g. energy or volume, but that there are certain quantities such as temperature or pressure that will eventually become equal between them. The exchange of energy or volume between the two systems does not stop, but instead reaches a balance — an *equilibrium*, in which no *net* energy or volume flows from one to the other, at least on average. However, most things we see in our daily lives are not actually in equilibrium. Glasses, gels and many plastics exist in a state of *kinetic arrest*: they are perpetually in a state of inching ever so slowly towards thermodynamic equilibrium, yet this rate is so slow that it may as well be zero. Correspondingly, these materials have properties that are quite different from what they would have were they in equilibrium. Furthermore, their non-equilibrium nature makes it challenging to predict their properties using statistical thermodynamics theories, which are generally built around the assumption of thermodynamic equilibrium.

The most dramatic example of non-equilibrium matter, however, has to be life. Biological processes have evolved in such a way that they consume available energy around them to actively avoid moving towards a state of thermodynamic equilibrium. In recent times there has been an increased interest in extending the concepts of equilibrium thermodynamics to these *far-from-equilibrium* or *active matter* systems, both in theoretical settings and in experimental ones.

1.4 Entropic crystals and the shape explosion

It is no secret that physicists love spheres. Many complicated problems in physics have been solved by first considering how it works for spheres. A famous example relevant to this thesis is the crystallization of hard spheres. Owing to their simplicity, hard spheres

were one of the first systems to be studied by using computer simulations. “Hard” here refers to the fact that interactions between particles simply follow one rule: they cannot overlap. Defined in physical terms, we say that the interaction energy u of two overlapping hard spheres is infinite, and that it is zero when they do not. Correspondingly, the Boltzmann weight $e^{-u/k_B T}$ (with T denoting the temperature and k_B Boltzmann’s constant), which describes the statistical probability of such a configuration occurring, is respectively either zero ($e^{-\infty} = 0$) or one ($e^0 = 1$). Introducing some more thermodynamics, a system in equilibrium is one that minimizes the (Helmholtz) *free energy**:

$$F = U - TS \quad (1.1)$$

where S is the *entropy* of the system and U is the total potential energy, which is the sum of all interaction energies u . Since the interaction energy of non-overlapping hard spheres is just $u = 0$, and the probability of finding an overlapping system is $e^{-\infty} = 0$, the total potential energy of the system is always zero and the free energy is determined solely by the entropy S . Thus, hard spheres are an example of an *entropic* system: one for which its thermodynamics is determined exclusively by entropy and not by energy. Back in 1957, Wood and Jacobson [6] as well as Alder and Wainwright [7] performed computer simulations on a system of hard spheres, and demonstrated that this system can undergo a phase transition from a fluid to a crystal. At the time, their results were somewhat controversial. In fact, when the results of Wood, Jacobson, Alder and Wainwright were discussed at a meeting between physicists in New Jersey in 1957, half of the audience stated they did not believe that the presented results could indicate a fluid-to-solid phase transition [8–10]. It was and still is counterintuitive that entropy, being associated with disorder, could stabilize a highly ordered crystalline phase. The resolution of this conundrum is to go back to Boltzmann’s famous statement $S = k_B \ln W$ and to realize that entropy is *not* a measure of disorder, but a measure of *the amount of possibilities* or, slightly more accurately, the number of possible configurations (the W in that equation). A crystal of hard spheres (which is a face-centered cubic lattice) is stabilized by the fact that particles have more space to move in a crystal lattice than in a disordered fluid of equal density. Correspondingly, having more space to move gives them more possible places to be, and thus more entropy. Nowadays, we call these crystals that are stabilized by entropy *entropic crystals*.

Sixty years after Wood, Jacobson, Alder and Wainwright we are still discovering new things about hard-sphere crystallization. However, most things in life are not spheres, and to look beyond spheres is a fruitful endeavor. For instance, particles elongated along one direction can form liquid crystal phases [11], and their study eventually led to the development of liquid crystal displays (LCDs) which you and I likely spend much of our time looking at. On the colloidal scale, the shape of particles determines for a large part the phases they can form, particularly at high densities. Advances in chemistry over the last few decades have made it possible to synthesize nano- and colloidal scale particles with a

*Technically we should also consider the kinetic energy K here and write $F = E - TS$ with $E = K + U$ the total energy of the system, but for the calculations of many systems (including hard spheres) the kinetic energy K can be computed analytically and its free energy subtracted as a constant. It is really the potential energy part that is interesting, and so we omit the kinetic energy throughout most of this text.

zoo of different shapes, such as ellipsoids [12], tetrahedra [13], cubes [14], octahedra [15, 16], dodecahedra [17], and many more. This rich variety in particle shapes is accompanied by an equally rich variety in crystal phases, and much recent work has been devoted to documenting these phases and finding design rules for these anisotropic particles [18, 19], either for use in designing colloidal entropic crystals or simply to better understand the entropic contributions in nanoparticle crystals. Currently, the most widely considered applications of these materials are based on their optical properties. Just like the aforementioned liquid crystals are now widely in use for displays, nanoparticle and colloidal crystals are considered promising candidates for photonic crystals: crystals with highly specific optical properties that can be used in e.g. fibre optics [20] or sensing [21]. Nature also uses such photonic crystals quite a bit: the vivid colors of butterfly wings [22, 23] or beetle shells [24] are often the result of photonic crystal Bragg refraction, rather than from pigments. In addition to the geometry of the particle shape, there are also geometric effects arising from the environment in which self-assembly takes place. The process of crystallization is heavily influenced by the presence of walls, with wall-assisted *heterogeneous nucleation* generally being many orders of magnitude faster than bulk *homogeneous nucleation* [25]. Self-assembling particles inside of an evaporating droplet can lead to significantly different behaviour from what is found in bulk, due to the interactions between the particle shape and the geometric confinement induced by the spherical droplet [26, 27]. Confining particles between two walls enforces a (quasi-)2D self-assembly, which can introduce completely different phases than in 3D [28, 29]. Likewise, some methods of colloidal self-assembly take place at the interface between two fluids: here not only the shape of the particles is of influence [30–32], but also that of the interface, and there are even interactions between these two effects [33]. The next few sections describe the theoretical and computational methods required to study such systems.

1.5 Statistical mechanics in a nutshell

In the field of statistical physics, we are interested in the collective or large-scale behaviour of a system of many particles. We can describe such a system *microscopically* by considering the evolution of the relevant properties of the individual particles: their position \mathbf{r} , orientation $\mathbf{\Omega}$, momentum \mathbf{p} and angular momentum \mathbf{L} . These properties all vary over time t as they interact and collide with one another. The state of the system at one particular point in time, which we call the *microstate*, is then given by the set of properties of all individual particles $\Gamma(t) = \{\mathbf{r}(t)^N, \mathbf{p}(t)^N, \mathbf{\Omega}(t)^N, \mathbf{L}(t)^N\}$ where

$$\begin{aligned}\mathbf{r}(t)^N &= \{\mathbf{r}_1(t), \mathbf{r}_2(t), \dots, \mathbf{r}_N(t)\} \\ \mathbf{\Omega}(t)^N &= \{\mathbf{\Omega}_1(t), \mathbf{\Omega}_2(t), \dots, \mathbf{\Omega}_N(t)\} \\ \mathbf{p}(t)^N &= \{\mathbf{p}_1(t), \mathbf{p}_2(t), \dots, \mathbf{p}_N(t)\} \\ \mathbf{L}(t)^N &= \{\mathbf{L}_1(t), \mathbf{L}_2(t), \dots, \mathbf{L}_N(t)\}\end{aligned}\tag{1.2}$$

are the sets of all particle positions, orientations, momenta and angular momenta at a given moment in time. The set of all possible microstates forms a *phase space* [34]. However, we are rarely interested in individual microstates. When we drink a glass of

water, we do not care about the momenta of all the individual water molecules, but rather whether the water is hot or cold. These large-scale, *macroscopic* properties such as temperature and pressure are *macrostates*. Macrostates describe collective properties of a system, while microstates describe the complete state of all of its components. For a typical system, its microstate changes extremely rapidly. However, we know that our glass of water is not likely to quickly and spontaneously cool down or heat up. Somehow, the way its macrostate (its temperature T) depends on its microstate $\Gamma(t)$ must be such that for all the configurations Γ the system visits, the temperature T must be almost the same. This independence leads to a concept known as *ergodicity*. Let us assume we have some function $T(\Gamma(t))$ that can extract the temperature from a given microstate Γ . If we measure this temperature times over some time period τ , we can define the time averaged temperature \bar{T} as:

$$\bar{T} = \frac{1}{\tau} \int_0^\tau T(\Gamma(t)) dt \quad (1.3)$$

A system that is ergodic (i.e. that possesses ergodicity) then has the following property:

$$\bar{T} = \lim_{\tau \rightarrow \infty} \frac{1}{\tau} \int_0^\tau T(\Gamma(t)) dt = \int f(\Gamma) T(\Gamma) d\Gamma = \langle T \rangle. \quad (1.4)$$

This states that for an ergodic system the time average \bar{T} of our macroscopic quantity (here the temperature T) is equivalent to the *ensemble average* $\langle T \rangle$ of that quantity, where the latter is the average over some normalized probability distribution $P(\Gamma)$. This probability distribution $P(\Gamma)$ assigns a probability to every possible microstate Γ of the system, and importantly, it is static — it does not change with time. This static property should seem familiar, and indeed: systems in thermodynamic equilibrium are (generally) ergodic.

The appropriate form of this probability distribution $P(\Gamma)$ depends on the *thermodynamic ensemble*, which describes the properties that a system is allowed to exchange with its environment. For a *canonical ensemble* i.e. for a system that can exchange only energy with its surroundings but for which the number of particles N , the volume V and the temperature T are fixed, this probability distribution is the Boltzmann distribution normalized by the *partition function* $Z = 1 / \int e^{-E(\Gamma)/k_B T} d\Gamma$:

$$P(\Gamma) = \frac{e^{-E(\Gamma)/k_B T}}{\int e^{-E(\Gamma)/k_B T} d\Gamma} \quad (1.5)$$

1.6 Computer simulations of statistical mechanics

We have just seen from Eq. 1.4 that there are two ways to obtain the macroscopic properties of ergodic systems from their microscopic ones: either by time averaging, or by ensemble averaging. Mirroring this duality in an entirely non-coincidental way, there are two main methods of doing computer simulations of statistical mechanics: one can either simulate the system by evolving its microstate $\Gamma(t)$ in time according to its equations of motion, which describes Molecular Dynamics simulations (MD), or one can sample Γ from the probability distribution $P(\Gamma)$, which describes Monte Carlo simulations (MC). For an excellent in-depth introduction into MD and MC methods, see Ref. [9]. We use

a variation of an MD method in Chapter 2, while in the rest of this thesis we primarily use MC simulations. For the sake of being concise, we describe the MD-based method in Chapter 2 itself, and describe the MC method that we use throughout the rest of the thesis here.

The typical goal of Monte Carlo simulations is the evaluation of the statistical average, which is the integral equation

$$\langle A \rangle = \int P(\Gamma) A(\Gamma) d\Gamma, \quad (1.6)$$

where $A(\Gamma)$ measures some macroscopic observable property of our system and $P(\Gamma)$ is the equilibrium probability distribution of the system. For a system of any appreciable complexity, this integral cannot be computed analytically. Instead, one has to sample it numerically, which in this case means finding an approximation to $\langle A \rangle$ by computing the value of the integrand $P(\Gamma)A(\Gamma)$ at a finite number of points. The simplest way of doing so is by simply looking at what values the integrand takes at different random values of Γ . This, however, turns out to be extremely inefficient. In many cases, the majority of possible values of Γ have a probability $P(\Gamma)$ that is extremely low, if not zero. As a result, they barely contribute to the integral. A much more efficient way to obtain a good estimate is to do *importance sampling*, in which we sample the important parts of the integral where $P(\Gamma)$ is large more than the unimportant parts where $P(\Gamma)$ is small. However, to do so we would need to know which points Γ are more probable, *before* generating them and calculating $P(\Gamma)$. In practice, for this to be possible we would need to know the partition function Z analytically, which is a similar integral as the one we are trying to compute in the first place. However, courtesy of Metropolis et al. [35] and Hastings [36], there is a clever trick we can do to calculate the statistical average without computing the partition function Z , which has the additional benefit of evaluating Eq. 1.6 in such a way that it mimics the time evolution of a real system. This trick is to use *Markov chains*. Markov chains are a method to construct a series of steps through a phase space for which one only needs to compute the *transition probabilities* $P(\Gamma_1 \rightarrow \Gamma_2)$ of going from an old state Γ_1 to a new state Γ_2 , rather than the absolute probability $P(\Gamma)$. An example of a possible step in a Markov chain would be one that moves a single particle from a position \mathbf{r}_1 to a new nearby position $\mathbf{r}_2 = \mathbf{r}_1 + \Delta\mathbf{r}$, where $\Delta\mathbf{r}$ is a small displacement. When used to evaluate ergodic systems, these transition probabilities inherit some of the properties of the absolute probability $P(\Gamma)$. Like $P(\Gamma)$, $P(\Gamma_1 \rightarrow \Gamma_2)$ must be constant in time. For this probability to remain constant, there must be a balance between the probability to go *from* any point Γ_1 and the probability to go *to* that point:

$$\int P(\Gamma_1 \rightarrow \Gamma_2) d\Gamma_2 = \int P(\Gamma_2 \rightarrow \Gamma_1) d\Gamma_2 \quad \forall \Gamma_1. \quad (1.7)$$

This is known as the *balance* condition. It can also be more formally expressed in matrix notation [9, 36, 37]. One can understand this condition by making the analogy with a fluid: if more probability “flows into” a point than out of it, the probability in that point will increase, and the underlying absolute probability distribution $P(\Gamma)$ would no longer be constant. Typically, a stronger condition is used, known as *detailed balance*, in which

the transition probabilities between *any* two points are balanced:

$$P(\Gamma_1 \rightarrow \Gamma_2) = P(\Gamma_2 \rightarrow \Gamma_1) \quad \forall \Gamma_1, \forall \Gamma_2. \quad (1.8)$$

So how do we construct a Markov chain in practice, and how does it help us avoid needing to calculate the partition function? To start, we rewrite the total transition probability into a product of three parts:

$$P(\Gamma_1 \rightarrow \Gamma_2) = P(\Gamma_1)p(\Gamma_1 \rightarrow \Gamma_2)a(\Gamma_1 \rightarrow \Gamma_2), \quad (1.9)$$

which are the absolute probability $P(\Gamma_1)$ of starting at Γ_1 , the probability $p(\Gamma_1 \rightarrow \Gamma_2)$ of generating a step from Γ_1 to Γ_2 , and the probability $a(\Gamma_1 \rightarrow \Gamma_2)$ of accepting this generated step. We can use this to rewrite Eq. 1.8 into:

$$P(\Gamma_1)p(\Gamma_1 \rightarrow \Gamma_2)a(\Gamma_1 \rightarrow \Gamma_2) = P(\Gamma_2)p(\Gamma_2 \rightarrow \Gamma_1)a(\Gamma_2 \rightarrow \Gamma_1). \quad (1.10)$$

The absolute probabilities are known up to their normalization, e.g. Eq. 1.5. Generally, the generation probability is chosen to be symmetric i.e. $p(\Gamma_1 \rightarrow \Gamma_2) = p(\Gamma_2 \rightarrow \Gamma_1)$ [9, 35]. Doing the same for simplicity, we can rewrite Eq. 1.10 to obtain the acceptance ratio $a(\Gamma_1 \rightarrow \Gamma_2)/a(\Gamma_2 \rightarrow \Gamma_1)$:

$$\frac{a(\Gamma_1 \rightarrow \Gamma_2)}{a(\Gamma_2 \rightarrow \Gamma_1)} = \frac{P(\Gamma_2)}{P(\Gamma_1)} = \frac{e^{-E(\Gamma_2)/k_B T}/Z}{e^{-E(\Gamma_1)/k_B T}/Z} = e^{-(E(\Gamma_2)-E(\Gamma_1))/k_B T}, \quad (1.11)$$

where we can see that the partition functions Z fortuitously cancel out. Following Metropolis' original choice, this ratio holds if we choose the acceptance probability of just one move to be:

$$a(\Gamma_1 \rightarrow \Gamma_2) = \begin{cases} e^{-(E(\Gamma_2)-E(\Gamma_1))/k_B T} & \text{if } E(\Gamma_2) > E(\Gamma_1); \\ 1 & \text{if } E(\Gamma_2) \leq E(\Gamma_1). \end{cases} \quad (1.12)$$

We can now generate new trial points Γ_2 in a wide variety of ways, and as long as we accept transitions $\Gamma_1 \rightarrow \Gamma_2$ only according to the Metropolis criterion 1.12 these points will efficiently sample the underlying, normalized distribution $P(\Gamma)$. This is the power of the Metropolis-Hastings or Markov chain Monte Carlo method: that we can evaluate the statistical integral (Eq. 1.6) without computing the partition function by using a series of steps that additionally have importance sampling built in.

1.7 The anisotropic hard-particle model

Real particle interactions are complicated. In general, interactions between colloidal particles are a combination of electrostatics, Pauli exclusion, van der Waals forces and ligand interactions between their constituent atoms/molecules. For all of these forces individually there exist models that describe their behaviour, and for simple geometries such as between two flat walls or two spheres there are often even analytical expressions available. However, as we have remarked earlier, most things in life are not spheres. Thus, we usually have to approximate. Experimentally, colloidal particles are generally stabilized

against rapid aggregation to allow for self-assembly. This stabilization tends to remove significant long-range interactions such as the electrostatic ones, leaving only the short-range interactions: van der Waals, Pauli exclusion and ligand interactions. Under some conditions it is possible to model such systems as *hard particles*. Extending the idea of hard spheres discussed in Section 1.4, this amounts to simplifying their interactions to the following pair potential energy u :

$$u = \begin{cases} \infty & \text{if the two particles overlap;} \\ 0 & \text{if the two particles do not overlap.} \end{cases} \quad (1.13)$$

This model has a number of significant benefits. In terms of thermodynamics, the hard-particle model simplifies matters considerably by always having zero potential energy. As a consequence, these systems are governed purely by entropy. Furthermore, in this model thermodynamic problems often reduce to *packing* problems: because the Boltzmann weight of any overlapping configuration is $e^{-\infty} = 0$, hard-particle behaviour is determined by how to most efficiently fill the available space. As an example: the thermodynamic equilibrium solid phase of hard spheres can be found in a grocery shop: a face-centered cubic lattice — the most space-efficient way to stack oranges — is also the one that thermodynamics favors for a crystal of hard spheres. Similarly, the crystal phase of hard cubes is a simple cubic crystal. The importance of packing in these systems allows us to borrow from our spatial intuition to hypothesize, verify and interpret phenomena in hard-particle systems. Finally, the hard-particle model lends itself very well to MC simulations, since the corresponding acceptance probabilities for MC moves reduce to

$$a(\Gamma_1 \rightarrow \Gamma_2) = \min \left[1, e^{-\beta(U(\Gamma_2) - U(\Gamma_1))} \right] = \begin{cases} 1 & \text{if } i \rightarrow j \text{ causes no overlap;} \\ 0 & \text{if } i \rightarrow j \text{ causes overlap.} \end{cases} \quad (1.14)$$

Thus, computing the transition probabilities reduces to finding out whether a change in microstate $\Gamma_1 \rightarrow \Gamma_2$ makes any particles overlap or not. For some shapes, determining whether two particles of this shape overlap with one another is simple. For hard spheres, it is almost trivial: if the distance between two particles, r , is less than the sum of their radii R , they overlap. Otherwise, they do not:

$$a(r_1 \rightarrow r_2) = \begin{cases} 0 & \text{if } r_2 < R; \\ 1 & \text{if } r_2 \geq R. \end{cases} \quad (1.15)$$

Such analytical overlap expressions can be derived for a few other shapes as well, such as spherocylinders [38], ellipsoids [39] or superballs [40, 41]. For other, more general particle shapes this gets a little more complicated, and we must venture into the computer science field of *collision detection*. This field of research provides us with several algorithms to detect collisions and overlaps between objects of general shapes. These algorithms are typically devised to work for *convex* objects: objects for which a line between any two points on their surface stays entirely within that object. The simplest of such algorithms is the Separating Axis Theorem (SAT) algorithm [42]. In simple terms, it reduces the complicated problem from three to one dimension by stating that two shapes are non-overlapping as long as at least one axis can be found for which the projections of the two

shapes onto this axis are non-overlapping. A more advanced algorithm is the Gilbert-Johnson-Keerthi (GJK) algorithm [43], which is the one we will be using throughout this thesis. We will not describe the GJK algorithm in detail here. Due to its popularity, many excellent resources exist beyond the original article both in the form of scientific articles [44] as well as tutorials [45]. Due to GJK's somewhat complex nature, some significant effort has been made to find simpler algorithms of equivalent (or superior) performance. One such algorithm is the Minkowski Portal Refinement (MPR) algorithm [46]. For non-convex objects, one has two options. For simple non-convex objects, one can decompose them into multiple convex objects and use the SAT/GJK/MPR algorithms. For more complex ones, it is possible to decompose their surfaces into triangular facets and check whether any facets of two particles intersect. We apply the former approach for the non-convex hourglass-shaped particles we consider in Chapter 3.

1.8 Phase transitions and coexistence

Thermodynamic phases, roughly speaking, are macrostates with specific properties. Most people are familiar with the basic three: gas, liquid and solid. Each phase has some set of properties that is different from the rest: a gas is dilute and flows, a liquid is dense and flows, and a solid is dense and does not flow. Thermodynamic systems can undergo a *phase transition* from one phase to another. A solid can melt into a liquid, a liquid can freeze into a solid, a solid sublimates into a gas, etc. In truth, there are many, many more phases than the basic three. Thermodynamics allows us to calculate properties of phases and phase transitions by considering the free energy. Which free energy to use depends on the thermodynamic ensemble i.e. which properties the system is allowed to exchange: working primarily in the canonical ensemble, we will use the *Helmholtz free energy* F . Calculating free energies can be quite challenging. We will describe the methods we use to do so later on in this thesis when they are required, but for the moment let us consider how we can extract information about phase transitions once the free energy is known. While these concepts are general, let us as an example consider the free energy per unit volume $\mathcal{F} = F/V$ of a system that has a fluid-solid phase transition that depends on its density $\rho = N/V$. Fig. 1.1 shows the free energy per unit volume \mathcal{F} of the two phases as a function of the density ρ . The equilibrium state of the system is the one in which it minimizes its total free energy F . In between the two densities ρ_f and ρ_x , this occurs through a *coexistence* of the two phases: part of the system is a fluid, and part of it a solid. Though the total number of particles N , volume V and temperature T of the system as a whole are fixed, the two phases can exchange volume and particles freely. Phase coexistence between two phases is given by the following equilibrium conditions of equal temperature, pressure p and chemical potential μ :

$$T_f = T_x; \tag{1.16}$$

$$p_f = p_x; \tag{1.17}$$

$$\mu_f = \mu_x. \tag{1.18}$$

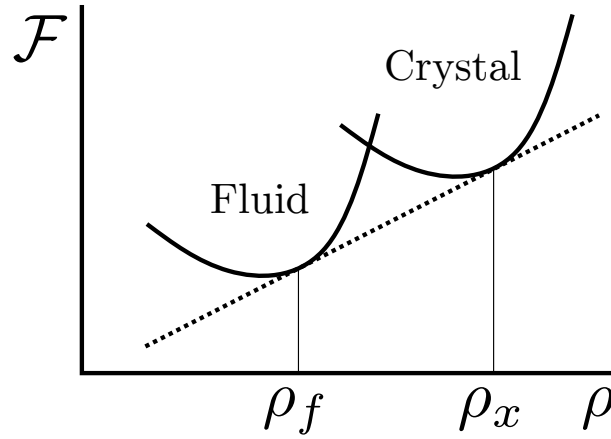


Figure 1.1: Phase coexistence between a low-density fluid and a high-density crystal. The free energy of the system as a whole is minimized when part of the system occupies the fluid phase, while another part occupies the crystal phase. The properties of this phase coexistence can be extracted from the common tangent indicated by the dotted line.

Fig. 1.1 shows a very useful geometric way to extract the coexistence properties. Let us write the chemical potential as:

$$\mu = \left. \frac{\partial F}{\partial N} \right|_{V,T} = \left. \frac{\partial \mathcal{F}}{\partial \rho} \right|_T, \quad (1.19)$$

and the pressure as:

$$p = - \left. \frac{\partial F}{\partial V} \right|_{N,T} = -\mathcal{F} + \rho \left(\left. \frac{\partial \mathcal{F}}{\partial \rho} \right) \right|_T. \quad (1.20)$$

Combining Eqs. 1.19, 1.20 and 1.17 then yields:

$$\mu_f = \mu_x = \frac{\mathcal{F}_f - \mathcal{F}_x}{\rho_f - \rho_x}. \quad (1.21)$$

The combination of Eq. 1.21 and the condition that the $\mathcal{F}(\rho)$ must have the same slope (Eq. 1.19) dictates that the minimum total free energy is achieved by a coexistence with densities ρ_f and ρ_x , which geometrically forms a straight line tangent to the free-energy curves of the two phases. It is this *common tangent construction* that we use to obtain phase coexistence properties.

1.9 Outline of this thesis

In this thesis we study the geometric effect of particle and environment shape on self-assembly in four different settings, spread over five chapters.

In Chapter 2 we study the effect of particle shape on a far-from-equilibrium system of self-propelled rods, and demonstrate that changing their shape from disks/spheres to rods suppresses the seemingly-universal Motility-Induced Phase Separation (MIPS) that is widely exhibited by self-propelled particles.

In Chapter 3 we model how a system of experimentally realized hourglass-shaped NaYF_4 nanoparticles self-assembles at a fluid-fluid interface. The assembly of these particles at the interface is dominated by the extremely strong capillary interactions between particles, which in turn depend sensitively on their shape. We determine numerically the form of the capillary deformation induced by the anisotropic particle shape, and combine this information with MC simulations to explain qualitatively a number of self-assembly phenomena observed in the experimental system.

In Chapter 4 we consider the bulk self-assembly of a system of particles with a rounded tetrahedral shape. Following up on recent literature that suggests these particles can form a densely packed quasicrystal approximant [47] and on recent experimental work in which nanoparticles with this shape form elongated supraparticles, we determine the densest packings and bulk phase behaviour, which turns out to feature a veritable wealth of solid phases.

The complexity of the phase behaviour exhibited by the rounded tetrahedra motivated us to search for ways to automate the detection and classification of solid phases. For this reason, we perform in Chapter 5 a dimensionality reduction technique known as Principal Component Analysis (PCA) to identify features that can be used to identify and distinguish between crystal structures without knowing their structure or good order parameters *a priori*.

Finally, in Chapter 6 we further investigate the self-assembly of the rounded tetrahedra that has them forming elongated supraparticles in the experimental setting. Leveraging our knowledge of the bulk crystal phases determined in Chapter 4, we determine the crystal structure of the experimental supraparticles, finding it to indeed be one of our suggested candidates, though there are also some subtle differences. We subsequently use free-energy calculations to characterize the coexistence properties phases relevant to the range of experimental particle shapes, and spherical confinement simulations to investigate the effect of the spherical boundary on the self-assembly in further detail.

2

Suppression of Motility-Induced Phase Separation

To study the role of torque in motility-induced phase separation (MIPS), we simulate a system of self-propelled particles whose shape varies smoothly from isotropic (disks/spheres) to weakly elongated (rods). We construct the phase diagrams of 2D active disks, 3D active spheres and 2D/3D active rods of aspect ratio $l/\sigma = 2$. A stability analysis of the homogeneous isotropic phase allows us to predict the onset of MIPS based on the effective swimming speed and rotational diffusion of the particles. Both methods find suppression of MIPS as the particle shape is elongated. We propose a suppression mechanism based on the duration of collisions, and argue that this mechanism can explain both the suppression of MIPS found here for rodlike particles and the enhancement of MIPS found for particles with Vicsek interactions.

Based on:

R. van Damme, J. Rodenburg, R. van Roij and M. Dijkstra, “*Interparticle torques suppress motility-induced phase separation for rodlike particles*”, J. Chem. Phys. 150, 164501 (2019)

2.1 Introduction

Recently, there has been an increased interest in the thermodynamics of what has been coined active matter: systems formed by agents that can convert ambient or external energy into kinetic energy. These systems are diverse. Many are biological in nature: birds, fish, cells and bacteria all convert some form of ambient chemical energy into kinetic energy. Synthetic systems also exist in the form of colloidal particles that self-propel, typically by diffusiophoresis [48–51]. All these active-matter systems are driven so far out of thermodynamic equilibrium that current theories of statistical thermodynamics fail to describe many of their properties. The problem lies not in constructing models for their dynamics – computational active matter models are quite simple and have been around for a while, one of the most famous of which being the seminal work of Vicsek from 1995 [52]. However, it has unfortunately proven to be very difficult to relate the dynamics to their steady states or to any kind of probability distribution. If we could apply the concepts of equilibrium statistical thermodynamics to active systems, it would greatly improve our ability to describe and predict the structure and behaviour of these systems. Some progress has been made in this regard. For instance, for self-propelled disks, studies have investigated the non-equilibrium pressure [53, 54], the glass [55, 56] and hexatic [57–59] transitions, equations of state [60], and effective free energies [61].

For active 2D disks or 3D spheres, two well-studied model systems, there is often a parameter regime in which the system demixes into a dense and a dilute region. This phase separation closely resembles the well-known gas-liquid coexistence found in, for instance, water or Lennard-Jones systems. Unlike the gas-liquid phase separation, however, the clustering in active matter occurs because of the motility rather than the particle-particle attractions. Hence, the phenomenon has been coined *motility-induced phase separation* (MIPS). Fig. 2.1 shows an example of this phenomenon. MIPS has been studied extensively in recent years: it has been identified for both active Brownian [62–65] and run-and-tumble particles [66], its nucleation has been studied [67], its interface has been shown to allow for a negative surface tension [68], and it has been derived from equations of state [54, 60], and from nonequilibrium thermodynamics theories [61].

All of the above studies logically constrained themselves to the simplest possible model systems, in which particles interact either through isotropic hard-particle excluded-volume or short-range repulsive interactions. Importantly, such models contain no torques. Studies that do include torques typically fall into two categories. The first uses particles with Vicsek-like alignment interactions [69, 70], which mimic a visual alignment mechanism, such as for birds or fish. The second uses particles with an anisotropic, typically rod-like shape [71–75]. This most closely mimics bacteria, whose alignment arises not from a visual interaction, but rather simply from bumping into one another. While studies of active rods reveal a zoo of nonequilibrium phases, they most curiously do not exhibit MIPS; there seems to be no parameter regime for which there is a separation into dense and dilute regions without strong alignment. Naturally, this raises questions such as: why does MIPS occur for 2D disks and 3D spheres, but not for 2D and 3D rods? How anisotropic or rod-like must a particle be for MIPS to disappear? In this chapter, we will address these questions by both simulations and theory.

To address these questions numerically, we need a model system which exhibits MIPS,

and a means to identify MIPS when it occurs. Section 4.2 describes both the Active Brownian Particle model we use, and the modified cluster algorithm we apply to identify MIPS. To study the disappearance of MIPS, we require a theoretical model that includes the effect of torques between particles. In Section 2.3 we derive an analytical criterion for the onset of MIPS based on a stability analysis of density fluctuations in the homogeneous and isotropic fluid phase. In Section 2.4.1 we discuss the phase diagrams for the 2D disks, 3D spheres and 2D and 3D rods, showing unambiguously that MIPS indeed disappears for increasing aspect ratio. Subsequently, we discuss the mechanism behind this suppression in Section 2.4.2. Section 2.5 then concludes this chapter by discussing the influence of torque on MIPS in a more general context.

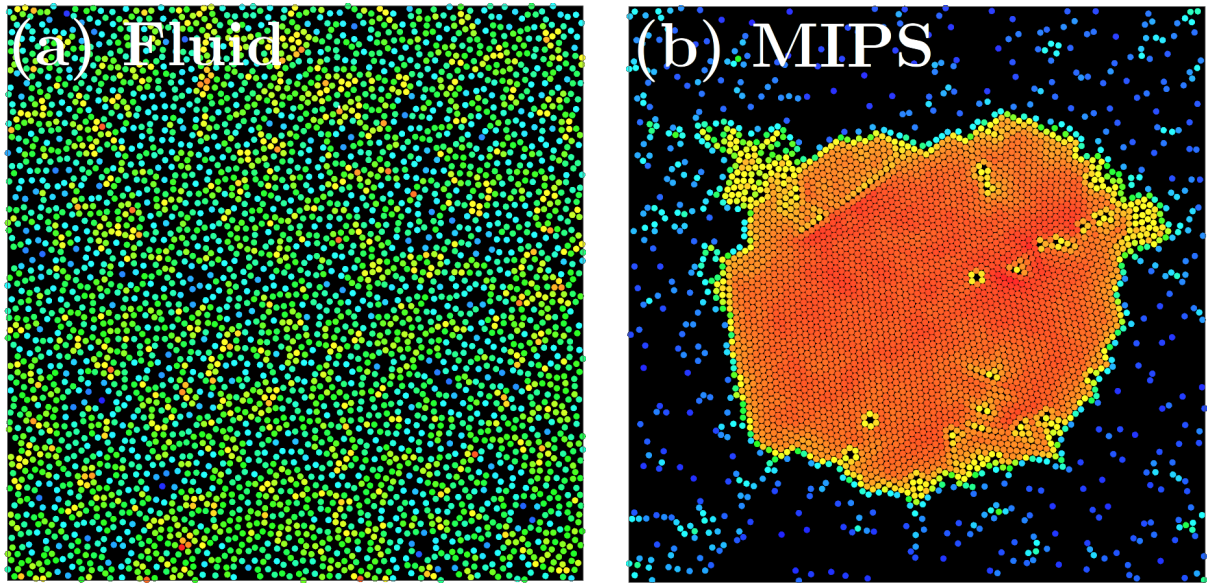


Figure 2.1: Motility-induced phase separation for a 2D system of hard disks with diameter σ at a packing fraction of $\phi = (\pi/4)\sigma^2/A = 0.36$, where A is the total system area. The color-coding helps visualize the local density. (a) In the absence of self-propulsion, the system is in a homogeneous and isotropic fluid state. (b) With strong self-propulsion the system phase-separates into a dilute gas and a dense, dynamic hexatic phase.

2.2 Computational methods

2.2.1 Active Brownian Particles

Using Brownian Dynamics (BD) simulations, we study a 2D system of N spherocylinder-shaped active Brownian particles (ABP) of end-to-end length l and diameter $\sigma \leq l$ in a periodic area A , self-propelling with a velocity v_0 along their long axis \hat{e} . The particles are subject to rotational and translational noise, with rotational diffusion constant D_r and translational diffusion tensor $\mathbf{D}_t = D_{\parallel}\hat{e}\hat{e} + D_{\perp}(\mathbf{I} - \hat{e}\hat{e})$, with parallel and perpendicular components D_{\parallel} and D_{\perp} , respectively. For such a 2D system, shown schematically in Fig.

2.2, the overdamped Langevin equations are given by

$$\partial_t \mathbf{r}_i = v_0 \hat{\mathbf{e}}_i + \beta \mathbf{D}_{t,i} \cdot \sum_{i \neq j} \mathcal{F}_{ij} + \sqrt{2\mathbf{D}_{t,i}} \cdot \boldsymbol{\Lambda}_i^t, \quad (2.1)$$

$$\partial_t \theta_i = \beta D_r \sum_{i \neq j} \mathcal{T}_{ij} + \sqrt{2D_r} \Lambda_i^r, \quad (2.2)$$

where $i = 1, \dots, N$ is the particle label, \mathbf{r}_i is the position of particle i , $\hat{\mathbf{e}}_i = (\cos \theta_i, \sin \theta_i)$ the particle orientation, and $\beta = 1/k_B T$. The force \mathcal{F}_{ij} and torque \mathcal{T}_{ij} are due to particle-particle interactions. We assume fluctuation-dissipation to hold on the scale of individual particles*, such that the translational and rotational noise terms $\Lambda_i^{t,\alpha}$ and Λ_i^r , respectively, are Gaussian distributed random numbers with zero mean and unit variance, i.e.:

$$\langle \Lambda_i \rangle = 0; \quad (2.3)$$

$$\langle \Lambda_i^\alpha(t) \Lambda_j^\beta(t') \rangle = \delta_{ij} \delta_{\alpha\beta} \delta(t - t'). \quad (2.4)$$

To describe excluded-volume interaction between particles i and j , we let the forces $\mathcal{F}_{ij} = (\partial u_{WCA}(r_{s,ij}) / \partial r_{s,ij}) \hat{\mathbf{r}}_{s,ij}$ be the result of a pairwise short-range repulsive Weeks-Chandler-Andersen potential (WCA) [76] $u_{WCA}(r_{s,ij})$ acting on the shortest distance $r_{s,ij}$ between particle cores:

$$u_{WCA}(r_{s,ij}) = \begin{cases} 4\epsilon \left[\left(\frac{\sigma}{r_{s,ij}} \right)^{12} - \left(\frac{\sigma}{r_{s,ij}} \right)^6 \right] + \epsilon & \text{if } r_{s,ij} < 2^{1/6} \sigma; \\ 0 & \text{if } r_{s,ij} \geq 2^{1/6} \sigma. \end{cases} \quad (2.5)$$

For disks ($l/\sigma = 1$), the distance $r_{s,ij}$ is simply the distance between their centers. For rods ($l/\sigma > 1$) the cores of the particles are no longer points, but lines. The distance $r_{s,ij}$ then corresponds to the shortest distance between these two line segments. The torques \mathcal{T} are calculated from the forces by $\mathcal{T}_{ij} = \mathbf{a}_{ij} \times \mathcal{F}_{ij}$, where \mathbf{a}_{ij} is the lever arm for the applied force \mathcal{F}_{ij} on rod i by rod j . For each pair of particles, both the shortest distance $r_{s,ij}$ and the lever arms \mathbf{a}_{ij} are calculated using the algorithm described in Ref. [38]. In 2D this torque always points out of plane, so we only need to consider its scalar magnitude \mathcal{T} in the equations of motion.

This 2D model easily generalizes to 3D: aside from vectorial quantities now being three- rather than two-dimensional, we must now also consider the direction of the torque. For convenience, we also switch to vector notation in the orientational equation of motion. The equations of motion in 3D are thus:

$$\partial_t \mathbf{r}_i = v_0 \hat{\mathbf{e}}_i + \beta \mathbf{D}_{t,i} \cdot \sum_{i \neq j} \mathcal{F}_{ij} + \sqrt{2\mathbf{D}_{t,i}} \cdot \boldsymbol{\Lambda}_i^t, \quad (2.6)$$

$$\partial_t \hat{\mathbf{e}}_i = \beta D_r \sum_{i \neq j} \mathcal{T}_{ij} \times \hat{\mathbf{e}}_i + \sqrt{2D_r} (\hat{\mathbf{e}}_i \times \boldsymbol{\Lambda}_i^r). \quad (2.7)$$

*As fluctuation-dissipation is an equilibrium phenomenon, there is reason to believe that it may not hold for active matter systems. If it does not, the force/torque and noise terms in Eqs. 2.1 and 2.2 will not be related by a common diffusion constant D .

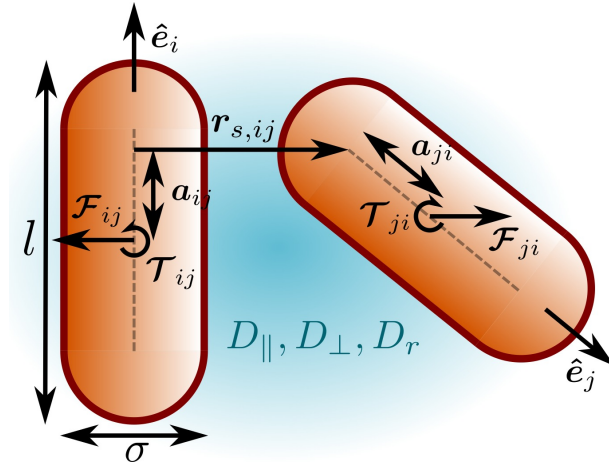


Figure 2.2: Schematic representation of the model. Particles are 2D or 3D spherocylinders of diameter σ and end-to-end length l , self-propelled with a velocity v_0 in their forward direction \hat{e} . They interact based on their core-to-core distance $r_{s,ij}$, causing repulsive forces \mathcal{F}_{ij} and torques \mathcal{T}_{ij} . Additionally, they diffuse rotationally with diffusion constant D_r , and translationally along their long and short axis with diffusion constants D_{\parallel} and D_{\perp} , respectively.

We nondimensionalize the 2D and 3D system by expressing all distances in units of the particle diameter σ , all energies in terms of the thermal energy $k_B T$, and all units of time in terms of $\tau = 1/D_r$.

2.2.2 Choice of model parameters and additional assumptions

For our investigation, we will study the influence of four parameters: the dimensionality $d = 2$ and $d = 3$, the aspect ratio l/σ , the packing fraction $\phi = N((\pi/4)\sigma^2 + (l - \sigma)\sigma)/A$ ($\phi = N((\pi/6)\sigma^3 + (\pi/4)(l - \sigma)\sigma^2)/V$ in 3D) and the Péclet number $\text{Pe} = v_0/\sigma D_r$. Note that literature sometimes defines the Péclet number in terms of the translational diffusion instead.

The diffusion constants D_{\parallel} , D_{\perp} and D_r for 3D cylindrical particles (or rather, their hydrodynamic friction coefficients) were determined by Tirado et al. [77]. As their expressions are valid for $l/\sigma \gtrsim 4.6$, the very short spherocylinders we use in the present work are not very well described by this method. To determine the effect of shape anisotropy on the diffusion of 3D spherocylinders, the hydrodynamic friction coefficients were determined by Bram Bet using the bead-shell model from Ref. [78] and compared them to the exact expressions for ellipsoids derived by Perrin [79, 80]. Fig. 2.3 shows the dimensionless friction coefficients ξ_{\parallel} , ξ_{\perp} and ξ_r (as defined in Ref. [78]) of short spherocylinders and ellipsoids for aspect ratios $1 \leq l/\sigma \leq 2.5$. It is evident from the similarity between the two that for these aspect ratios one can safely use the exact ellipsoid expressions as a good approximation. After further research, however, we found that the influence of the diffusion constant change with aspect ratio is negligible for the aspect ratio range we look at in both 2D and 3D, so for simplicity we will set $D_{\parallel} = D_{\perp} = D_t = \sigma^2 D_r / d$ from now on, with d being the dimensionality i.e. $d = 2$ in 2D and $d = 3$ in 3D. This choice corresponds

to the correct ratio between translational and rotational diffusion for spheres.

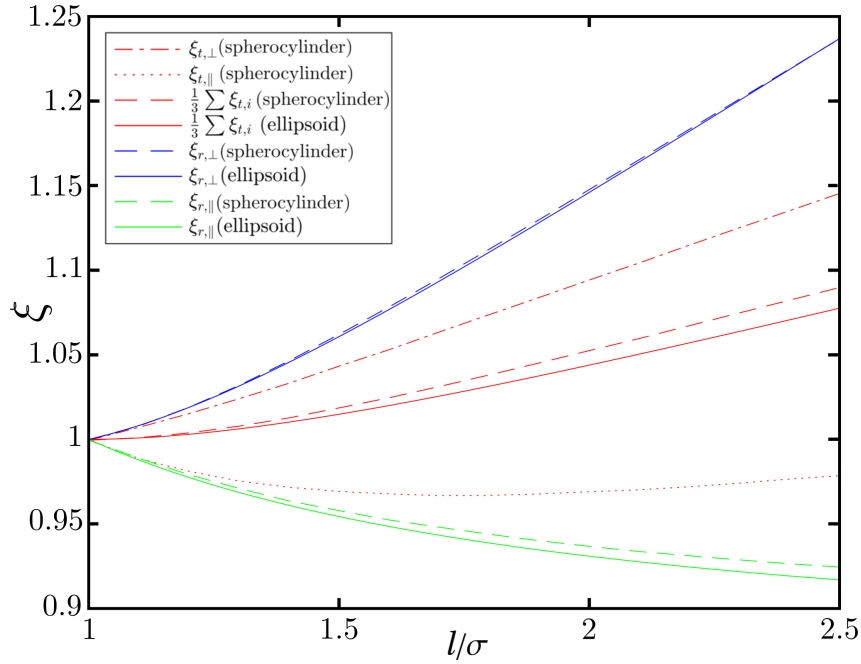


Figure 2.3: Dimensionless hydrodynamic friction coefficients ξ for 3D ellipsoids and spherocylinders for small aspect ratios $1 < l/\sigma < 2.5$, defined with respect to a sphere of the same volume [78]. The red long-short dashed and dotted lines indicate the translational friction coefficients of spherocylinders $\xi_{t,\parallel}$ and $\xi_{t,\perp}$, while the red solid and dashed lines indicate the total friction coefficient $\xi_t = (\xi_{\parallel} + 2\xi_{\perp})/3$ of ellipsoids and spherocylinders, respectively. The green and blue lines indicate the rotational friction coefficients around and perpendicular to the long axis $\xi_{r,\parallel}$ and $\xi_{r,\perp}$, respectively.

Some care is required in the way we vary the Péclet number. The most straightforward way is to simply vary it by changing the self-propulsion velocity v_0 . However, if we do this and keep the pair interaction strength fixed, the ratio between active and interaction forces will depend on the Péclet number. The result of changing this ratio is that the particle interaction effectively becomes softer as the Péclet number increases. In the extreme case, MIPS may even disappear for high enough Péclet numbers. Earlier work has remarked on this subtlety of varying the Péclet number [81, 82]. As our aim is not to provide quantitative but only qualitative data on the phase behaviour, we nevertheless use the straightforward approach by fixing $\epsilon = 24k_B T$ and changing the Péclet number by varying v_0 .

2.2.3 Identifying motility-induced phase separation by clustering regions of similar density

MIPS is a separation of a system of self-propelled particles into a dense and a dilute region. While it can be identified quite readily from visual inspection of particle configurations, it is also useful to have a more quantitative method. Two of these methods are common. The first is to measure the distribution of the local density: for a homogeneous system,

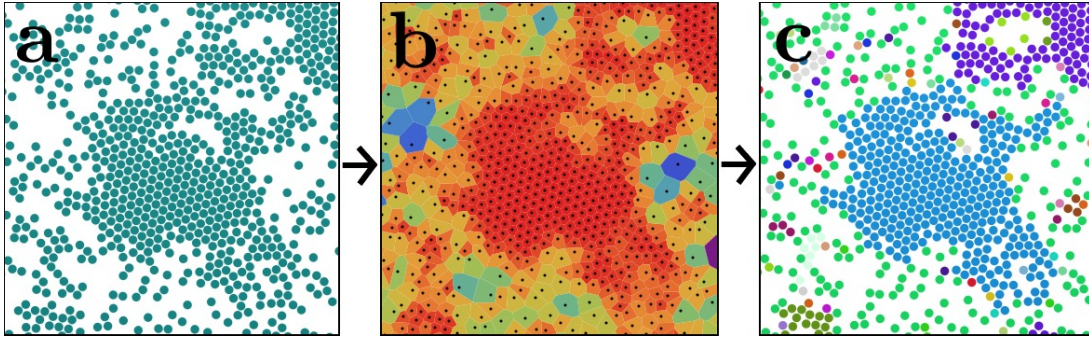


Figure 2.4: Representation of our clustering algorithm. From unlabeled coordinates (a), construct a Voronoi tessellation and obtain local densities (b), then use these to create clusters of particles with similar density (c).

such a distribution is unimodal, while for a phase-separated system it is bimodal [83–85]. However, such a distribution can not tell us whether the system has separated into one or into multiple domains, which means it cannot distinguish between micro- and macrophase separation. This distinction becomes important for rods.

The other method is to group particles together into clusters based on a distance cutoff and to determine the fraction f_{cl} of particles in the largest cluster [50, 62, 86]. Since MIPS eventually forms one large, dense cluster in a very dilute background gas, $f_{cl} \rightarrow 1$ for MIPS for large enough systems, while for a homogeneous fluid $f_{cl} \rightarrow 0$. This latter method requires a cutoff distance that specifies whether particles are close enough to belong to the same cluster. In practice, we found that there is no single cutoff distance that yielded reasonable results for the resulting cluster fraction across all shapes and densities we wish to study.

To solve this problem, we developed a slightly different clustering method, shown schematically in Fig. 2.4. From the particle positions (Fig. 2.4a), we make a Voronoi construction. This provides us not only with a parameter-free way to define neighbouring particles, but also with a means of measuring the local packing fraction: $\phi_l = ((\pi/4)\sigma^2 + (l - \sigma)\sigma)/A_v$ (in 2D) or $\phi_l = ((\pi/6)\sigma^3 + (\pi/4)(l - \sigma)\sigma^2)/V_v$ (in 3D), with A_v and V_v the area and volume of the Voronoi cell (colors in Fig. 2.4b), respectively. Our requirements for two particles to belong to the same cluster are then that (a) their Voronoi cells are connected and (b) they both have a local packing fraction that is either lower or higher than the mean packing fraction ϕ by a certain cutoff $\Delta\phi$. Using this method, we create clusters of similar local density (Fig. 2.4c). We choose $\Delta\phi = 0.025$, as we found through trial and error that this cutoff allows us to meaningfully distinguish between homogeneous states with $f_{cl} < 0.5$ and phase-separated states with $f_{cl} \geq 0.5$ for all aspect ratios and Péclet numbers of interest and for nearly all densities, both in $d = 2$ and $d = 3$. Note that f_{cl} is not guaranteed to go to zero in the homogeneous phase when using this definition of clusters due to density fluctuations, but $f_{cl} = 0.5$ still offers a reasonable threshold.

2.3 An analytical criterion for the onset of MIPS

Having described the means to obtain and identify MIPS numerically, we now describe an analytical criterion for the onset of MIPS. We are aware of three ways to obtain such a criterion: by constructing an effective free energy and proceeding as in equilibrium [61, 87], by looking at the particle flux balance between a dense cluster and a dilute gas phase [63, 88], and by a stability analysis of density fluctuations of the homogeneous isotropic phase [82, 89]. The first method cannot be applied directly to our system, as one of its underlying assumptions is that no torques act between the particles. The second method is also likely to fail, as it relies on the assumption that the orientations of particles in the boundary of the dense cluster evolve diffusively, which is not the case for rods. Thus, we opt for the third method: deriving a criterion for the (in)stability of the homogeneous isotropic phase to density fluctuations, by extending the mean-field-like method from Ref. [89] to 3D systems with torques. In short, we map our system to an active ideal gas, where the effect of the many-body forces and torques is subsumed into a modified, *effective* swim speed v_0^{eff} , rotational diffusion D_r^{eff} , and translation diffusion D_t^{eff} . These effective constants then depend on the mean density $\bar{\rho}$ and input swimming speed v_0 . By doing this mapping, we effectively make two approximations: that the only effect of the interparticle forces \mathcal{F} is to slow particles down, and that the only effect of the torques \mathcal{T} is to change the rate at which particles change their orientation. The former is a good approximation in the absence of structural order, the latter in the absence of orientational order. Both approximations become poorer at higher densities, where structure and alignment become important.

2.3.1 Effective Smoluchowski equation

To render the problem analytically tractable, our first goal is to simplify the effect of the pairwise forces and torques. We will do this using a mean-field-like approximation. Following the same procedure as Refs. [82, 89], we start from the Smoluchowski equation for the one-particle probability density function (PDF) $\psi(\mathbf{r}, \hat{\mathbf{e}}, t)$, given by

$$\partial_t \psi = -\nabla \cdot (v_0 \hat{\mathbf{e}} \psi + \beta D_t \mathcal{F} - D_t \nabla \psi) - \mathcal{R} \cdot (\beta D_r \mathcal{T} - D_r \mathcal{R} \psi), \quad (2.8)$$

where ∇ are the 2D and 3D gradient operators and \mathcal{R} is the rotation operator, defined as $\mathcal{R} = \partial_\theta$ in 2D and $\mathcal{R} = \hat{\mathbf{e}} \times \nabla_{\hat{\mathbf{e}}}$ in 3D. Note that similar to our numerical model we neglect the influence of particle shape anisotropy on the translational diffusion and simply set $D_t = D_t \mathcal{I}$. The pairwise force density \mathcal{F} and torque density \mathcal{T} , which arise due to the particle-particle interactions of a pair potential $V_{\hat{\mathbf{e}}_1, \hat{\mathbf{e}}_2}(\mathbf{r}_1, \mathbf{r}_2)$, can then be written in terms of the two-body probability density $\psi_{\hat{\mathbf{e}}_1, \hat{\mathbf{e}}_2}^{(2)}(\mathbf{r}_1, \mathbf{r}_2, t)$ as

$$\mathcal{F}(\mathbf{r}_1, \hat{\mathbf{e}}_1, t) \equiv \int d\mathbf{r}_2 d\hat{\mathbf{e}}_2 (-\nabla_1 V_{\hat{\mathbf{e}}_1, \hat{\mathbf{e}}_2}(\mathbf{r}_1, \mathbf{r}_2)) \psi_{\hat{\mathbf{e}}_1, \hat{\mathbf{e}}_2}^{(2)}(\mathbf{r}_1, \mathbf{r}_2, t); \quad (2.9)$$

$$\mathcal{T}(\mathbf{r}_1, \hat{\mathbf{e}}_1, t) \equiv \int d\mathbf{r}_2 d\hat{\mathbf{e}}_2 (-\mathcal{R}_1 V_{\hat{\mathbf{e}}_1, \hat{\mathbf{e}}_2}(\mathbf{r}_1, \mathbf{r}_2)) \psi_{\hat{\mathbf{e}}_1, \hat{\mathbf{e}}_2}^{(2)}(\mathbf{r}_1, \mathbf{r}_2, t). \quad (2.10)$$

In order to close this hierarchy, the force and torque densities \mathcal{F} and \mathcal{T} need to be expressed in terms of the one-body PDF. To do so, we first use the identity

$$\psi_{\hat{\mathbf{e}}_1, \hat{\mathbf{e}}_2}^{(2)}(\mathbf{r}_1, \mathbf{r}_2, t) = \psi(\mathbf{r}_1, \hat{\mathbf{e}}_1, t) \psi(\mathbf{r}_2, \hat{\mathbf{e}}_2, t) g_{\hat{\mathbf{e}}_1, \hat{\mathbf{e}}_2}(\mathbf{r}_1, \mathbf{r}_2, t) \quad (2.11)$$

to rewrite Eq. (2.9) as $\mathcal{F} = \tilde{\mathcal{F}}\psi$, where

$$\tilde{\mathcal{F}}(\mathbf{r}_1, \hat{\mathbf{e}}_1, t) \equiv \int d\mathbf{r}_2 d\hat{\mathbf{e}}_2 (-\nabla_1 V_{\hat{\mathbf{e}}_1, \hat{\mathbf{e}}_2}(\mathbf{r}_1, \mathbf{r}_2)) \psi(\mathbf{r}_2, \hat{\mathbf{e}}_2, t) g_{\hat{\mathbf{e}}_1, \hat{\mathbf{e}}_2}(\mathbf{r}_1, \mathbf{r}_2, t). \quad (2.12)$$

To obtain a closure, we make the following assumptions. First, we assume that the force \mathcal{F} acts along the direction of self-propulsion, i.e. $\mathcal{F} = (\mathcal{F} \cdot \hat{\mathbf{e}})\hat{\mathbf{e}}$, making Eq. 2.8:

$$\partial_t \psi = -\nabla \cdot ((v_0 + \tilde{\mathcal{F}} \cdot \hat{\mathbf{e}})\hat{\mathbf{e}}\psi - D_t \nabla \psi) - \mathcal{R} \cdot (\beta D_r \mathcal{T} - D_r \mathcal{R}\psi). \quad (2.13)$$

Whereas this is exact in a homogeneous, isotropic bulk as dictated by symmetry, in general we neglect a possible second component that is perpendicular to $\hat{\mathbf{e}}$. In Ref. [89], Speck et al. consider this second component to act along the gradient of the one-particle PDF i.e. $\mathcal{F} = (\mathcal{F} \cdot \hat{\mathbf{e}})\hat{\mathbf{e}} + a \nabla \psi$. This additional assumption leads to a modified translational diffusion $D_t^{\text{eff}} = (1 - \beta a)D_t$. We measured the magnitude of this modification for 3D spheres and rods, and found that the modification provided by βa is of negligible influence on the location of the phase boundaries except near $\text{Pe} = 0$. For simplicity, we thus neglect this effect by setting $a = 0$, i.e. $D_t^{\text{eff}} = D_t$ from now on. We did not explicitly check the validity of this assumption in the 2D case, but see no reason to assume a difference.

To continue our derivation, we make the second assumption that $\tilde{\mathcal{F}} \cdot \hat{\mathbf{e}}$ is linear in the local density $\rho(\mathbf{r}, t) = \int d\hat{\mathbf{e}} \psi(\mathbf{r}, \hat{\mathbf{e}}, t)$ and has no further dependence on $(\mathbf{r}, \hat{\mathbf{e}}, t)$:

$$\tilde{\mathcal{F}}(\mathbf{r}, \hat{\mathbf{e}}, t) \cdot \hat{\mathbf{e}} = -\rho(\mathbf{r}, t)\zeta(\bar{\rho}, v_0). \quad (2.14)$$

Here the constant ζ is independent of $(\mathbf{r}, \hat{\mathbf{e}}, t)$, but can still depend on the mean density $\bar{\rho} = N/A$ (or N/V in 3D) and the self-propulsion strength v_0 . In this way, using Eq. (2.8), the effect of the interaction forces can be absorbed into a modified self-propulsion velocity v^{eff} , which is given by

$$v^{\text{eff}}[\rho(\mathbf{r}, t)] = v_0 - \beta D_t \rho(\mathbf{r}, t)\zeta(\bar{\rho}, v_0), \quad (2.15)$$

Applying a similar approach for the torque, we make the approximation that its only influence is to modify the rotational diffusion i.e.

$$\mathcal{T}(\mathbf{r}, \hat{\mathbf{e}}, t) \approx b \mathcal{R}_1 \psi(\mathbf{r}, \hat{\mathbf{e}}, t), \quad (2.16)$$

We assume the corresponding constant b to be homogeneous and isotropic, depending only on the mean density and self-propulsion i.e. $b = b(\bar{\rho}, v_0)$. With these approximations we can further simplify Eq. (2.13) to the Smoluchowski equation for an active ideal gas:

$$\partial_t \psi = -\nabla \cdot (v^{\text{eff}} \hat{\mathbf{e}}\psi - D_t \nabla \psi) + D_r^{\text{eff}} \mathcal{R} \cdot \mathcal{R}\psi, \quad (2.17)$$

where the influence of forces and torques is now captured by the *effective* self-propulsion v^{eff} and rotational diffusion constant and D_r^{eff} , respectively.

2.3.2 Stability analysis of the homogeneous isotropic phase

Now that we have reduced the full Smoluchowski Eq. (2.8) into the ideal-gas form of Eq. (2.17), we can perform a linear stability analysis on the homogeneous isotropic phase. We

start by defining the relevant moments of the one-particle PDF $\psi(\mathbf{r}, \hat{\mathbf{e}}, t)$,

$$\rho(\mathbf{r}, t) = \int d\hat{\mathbf{e}} \psi(\mathbf{r}, \hat{\mathbf{e}}, t) \quad (\text{density}); \quad (2.18)$$

$$m_\alpha(\mathbf{r}, t) = \int d\hat{\mathbf{e}} e_\alpha \psi(\mathbf{r}, \hat{\mathbf{e}}, t) \quad (\text{polarization}); \quad (2.19)$$

$$S_{\alpha\beta}(\mathbf{r}, t) = \int d\hat{\mathbf{e}} (e_\alpha e_\beta - \frac{1}{d} \delta_{\alpha\beta}) \psi(\mathbf{r}, \hat{\mathbf{e}}, t) \quad (\text{nematic}). \quad (2.20)$$

Here, the Greek indices label the Cartesian vector- or tensor components, and in the following we shall employ the Einstein summation convention. Considering the same moments of the ideal gas Smoluchowski equation (2.17) yields the following evolution equations:

$$\partial_t \rho = - \nabla \cdot (v^{\text{eff}} \mathbf{m} - D_t \nabla \rho); \quad (2.21)$$

$$\partial_t m_\alpha = - \partial_\beta [v^{\text{eff}} (S_{\alpha\beta} + \frac{1}{d} \rho \delta_{\alpha\beta}) - D_t \partial_\beta m_\alpha] - (d-1) D_r^{\text{eff}} m_\alpha; \quad (2.22)$$

$$\partial_t S_{\alpha\beta} = - \partial_\gamma [v^{\text{eff}} (B_{\alpha\beta\gamma} - \frac{1}{d} m_\gamma \delta_{\alpha\beta\gamma}) - D_t \partial_\gamma S_{\alpha\beta}] - d(d-1) D_r^{\text{eff}} S_{\alpha\beta}. \quad (2.23)$$

Here B is the next (third) order moment. The structure of this hierarchy of time-evolution equations (2.21)-(2.23) is such that the time-derivative of each moment depends linearly on itself and on the moment one order lower and higher. However, as we shall see, moments beyond m are irrelevant for the instability we wish to consider.

A steady-state solution to Eq. (2.17) is the homogeneous isotropic phase: $\psi(\mathbf{r}, \hat{\mathbf{e}}, t) \propto \bar{\rho}$. Expressed in terms of the moment equations (2.21)-(2.23), this gives $\rho(\mathbf{r}, t) = \bar{\rho}$ (homogeneity) and $\mathbf{m}(\mathbf{r}, t) = \mathbf{S}(\mathbf{r}, t) = 0$ (isotropy). To obtain a criterion for the stability of this solution, we investigate the behaviour of small perturbations to the homogeneous state:

$$\rho(\mathbf{r}, t) = \bar{\rho} + \delta\rho(\mathbf{r}, t); \quad (2.24)$$

$$\mathbf{m}(\mathbf{r}, t) = \delta\mathbf{m}(\mathbf{r}, t); \quad (2.25)$$

$$\mathbf{S}(\mathbf{r}, t) = \delta\mathbf{S}(\mathbf{r}, t). \quad (2.26)$$

Since MIPS is a macroscopic phase separation, we should study the instability with respect to long-range perturbations i.e. perturbations with small spatial gradients. In this limit, the dynamics are dominated by the terms in Eqs. (2.21)-(2.23) with the fewest gradients. Of the three moments, it is ρ whose time evolution is slowest. Its timescale is of order ∇^{-1} , while \mathbf{m} and \mathbf{S} evolve as $(D_r^{\text{eff}})^{-1} \sim \nabla^0$. As we are interested in the evolution of the density perturbations, i.e. of the slow variable, we can assume that at any given time, the higher moments \mathbf{m} and \mathbf{S} are given by their steady-state solutions that correspond to the density profile $\rho(\mathbf{r}, t)$ at that instant. Solving Eq. (2.23) for its steady-state solution $\delta S_{\alpha\beta}$ reveals that it scales as $\mathcal{O}(\nabla^1)$. Therefore, its contribution to the evolution of polarization perturbations (Eq. (2.22)) is of higher order. To leading order, the evolution of polarization perturbations is then given by

$$\delta\mathbf{m}(\mathbf{r}, t) = - \frac{1}{d(d-1)D_r^{\text{eff}}} \nabla (v^{\text{eff}}(\mathbf{r}, t) \rho(\mathbf{r}, t)). \quad (2.27)$$

Recalling that $v^{\text{eff}} = v_0 - \beta D_t \rho(\mathbf{r}, t) \zeta(\bar{\rho}, v_0)$, we can take this gradient explicitly and obtain

$$\delta \mathbf{m}(\mathbf{r}, t) = -\frac{1}{d(d-1)D_r^{\text{eff}}} (v_0 - 2\beta D_t \rho(\mathbf{r}, t) \zeta) \nabla \rho(\mathbf{r}, t). \quad (2.28)$$

Using this result, the equation for the time evolution of density perturbations becomes

$$\partial_t \delta \rho(\mathbf{r}, t) = \mathcal{D}_{\delta \rho}(\bar{\rho}, v_0) \nabla^2 \delta \rho(\mathbf{r}, t), \quad (2.29)$$

which is a diffusion equation with diffusion constant

$$\begin{aligned} \mathcal{D}_{\delta \rho}(\bar{\rho}, v_0) &= D_t + \frac{(v_0 - \beta D_t \bar{\rho} \zeta)(v_0 - 2\beta D_t \bar{\rho} \zeta)}{d(d-1)D_r^{\text{eff}}} \\ &= D_t + \frac{v^{\text{eff}}(2v^{\text{eff}} - v_0)}{d(d-1)D_r^{\text{eff}}}. \end{aligned} \quad (2.30)$$

Whenever the diffusion constant $\mathcal{D}_{\delta \rho}$ is negative, density perturbations $\delta \rho(\mathbf{r}, t)$ will grow. Therefore, the region in $(\bar{\rho}, v_0)$ -space where the homogeneous isotropic phase becomes unstable is given by the condition $\mathcal{D}_{\delta \rho}(\bar{\rho}, v_0) < 0$. This can only occur for self-propulsion velocities v_0 above the critical threshold $v^* = 2\sqrt{2}\sqrt{d(d-1)}\sqrt{D_t D_r^{\text{eff}}}$.

The effective constants v^{eff} and D_r^{eff} can now be found in two ways: we can either formulate closed-form equations for these effective constants, or we could measure them in some way. We choose the latter method, and determine their value from the following correlation functions:

$$\langle \dot{\mathbf{r}}_i(t) \cdot \hat{\mathbf{e}}_i(t) \rangle = v^{\text{eff}}; \quad (2.31)$$

$$\langle \hat{\mathbf{e}}_i(t) \cdot \hat{\mathbf{e}}_i(0) \rangle = \exp(-(d-1)D_r^{\text{eff}}t), \quad (2.32)$$

which measure the effective velocity in the direction of self-propulsion and how quickly a particle loses its orientation, respectively. In this way, we can measure v^{eff} and D_r^{eff} by simulating a system in the homogeneous isotropic phase at different values of the mean density $\bar{\rho}$ and self-propulsion v_0 , calculate the diffusion constant $\mathcal{D}_{\delta \rho}$ and use that to predict the stability of the state. In the next section we show how finite size effects suppress the formation of a MIPS phase, and how we use this effect to measure the v^{eff} and D_r^{eff} of the fluid phase even for mean densities $\bar{\rho}$ and self-propulsions v_0 for which a larger system would undergo MIPS.

2.3.3 Finite-size effects when measuring effective swim speed and rotational diffusion

Measuring the effective swim speed v^{eff} and rotational diffusion D_r^{eff} from simulations with only a few particles ($N \sim 100$) means these constants will suffer from finite-size effects. Figure 2.5 shows the scaling of (a) the effective swim speed v^{eff} and (b) the fraction of particles in the largest cluster f_{cl} with the inverse of the number of particles N for 3D active spheres, at a packing fraction $\phi = 0.44$ and a Péclet number of $\text{Pe} = 100$. A clear kink can be seen in both graphs at roughly the same system size ($N \sim 4000$), which

after visual inspection of the corresponding snapshots (Fig. 2.6) can be associated with MIPS. As our small- N simulations take place well below this threshold and v^{eff} does not scale strongly with the number of particles in this regime, we assume that they provide a reasonable estimate of the effective swim speed even when a larger system would phase-separate.

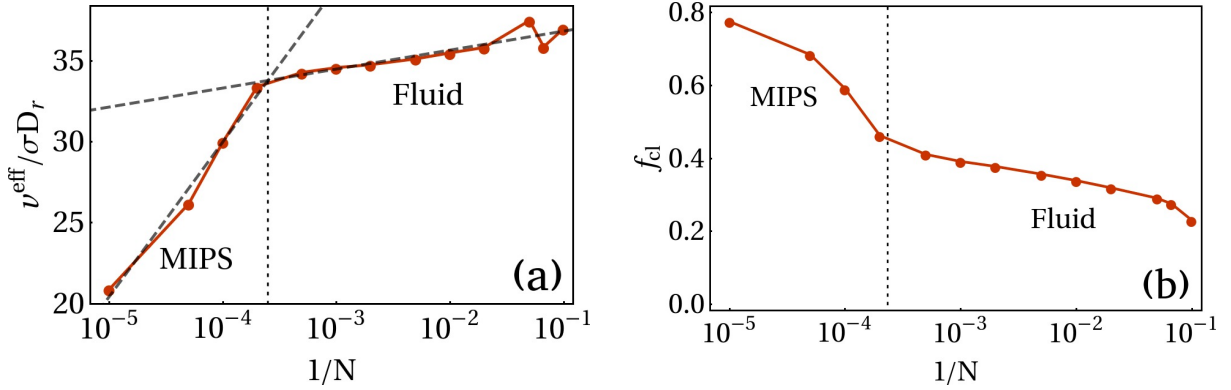


Figure 2.5: Effective swim speed v^{eff} (a) and fraction of particles in the largest cluster f_{cl} (b) for 3D active spheres as a function of the inverse of the number of particles N , at a packing fraction $\phi = 0.44$ and a Péclet number of $\text{Pe} = 100$. Both v^{eff} and f_{cl} display a clear kink around $N \sim 4000$ that denotes MIPS. The dashed lines are drawn to show the transition in scaling from the fluid to the MIPS regime, and the dotted line denotes the intercept at $N \approx 4000$.

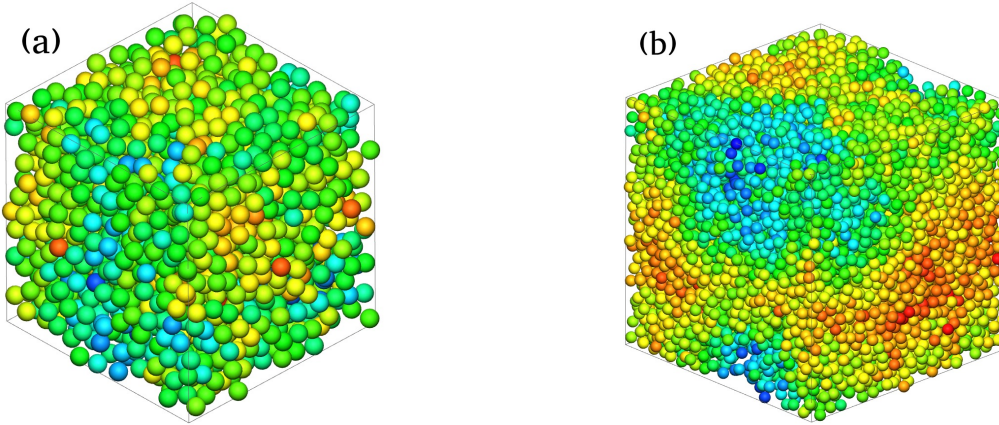


Figure 2.6: Two representative snapshots of the simulated system of Fig. 2.5 for (a) $N = 2000$ in the fluid regime, and (b) $N = 10000$ in the MIPS regime. Particles are coloured according to their local density. While no large-scale phase separation can be seen for (a), (b) has clearly separated into a dense and a dilute region.

2.4 Results & Discussion

Before we start looking at the influence of particle elongation on MIPS, it is worthwhile to consider the established behaviour of 2D active disks. While the phase boundaries of MIPS

for disks have been studied by a number of authors [53, 60, 63, 89, 90], comprehensive studies that also include the high-density hexatic and solid phases have only appeared more recently [57–59], spurred on by developments in the understanding of the melting of 2D disks in equilibrium [91–95]. Digregorio et al. [57] report not only the commonly-reported U-shaped MIPS region (in the density-activity plane), but also that there is a narrow density regime in which a hexatic phase can be found. This regime spans from the passive system ($Pe = 0$) to the MIPS region ($Pe \sim 100$). Klamser et al. [58] and Paliwal and Dijkstra [59] focus on this hexatic phase in greater detail and compare its behaviour to equilibrium 2D disks.

In the present work we focus on the MIPS phase specifically, and will not consider the hexatic/solid phase boundaries in detail. Instead, we will restrict ourselves to a density regime that largely excludes these phases, and merely identify any solid-like phases by looking at where the effective velocity v^{eff} becomes sufficiently small: $v^{\text{eff}} < 0.1\sigma D_r$. Although this is not a very accurate measure, it serves to crudely distinguish the solid or hexatic phases from the fluid and MIPS phases, at least at low self-propulsion. We use this criterion for all phase diagrams throughout this chapter.

To explore the MIPS-related phase behaviour, we performed Brownian Dynamics simulations with $N = 10^4$ particles in the packing-fraction range $0.1 \leq \phi \leq 0.7$, and the Péclet-number range $1 \leq Pe \leq 100$ (2D) and $1 \leq Pe \leq 150$ (3D). This spans the entire density range from the fluid regime to just below the hexatic/solid regimes [57, 96]. The Péclet range spans from below the MIPS critical point to high enough Péclet that the MIPS region attains a near-constant width in density [81, 90]. We also performed simulations with a smaller number of particles $N = 100$ to measure the effective constants v^{eff} and D_r^{eff} . The initial state for all simulations was one with random positions and orientations. As previously discussed, using only a limited number of particles ($N = 100$) ensures that the system remains in the homogeneous isotropic phase regardless of density or activity.

A few more remarks considering the differences between the present work, Refs. [57–59] and others: Ref. [57] defines the Péclet number in terms of the active force, while we express it in terms of v_0 and D_r – this shifts the scale by a constant factor of $D_r\sigma^2/D_t = 3$. Qualitatively, we can expect to find similar features. Quantitatively, the phase boundaries will be shifted somewhat because of differences in the repulsive pair potential: Ref. [57] uses the repulsive part of $U \propto (\sigma/r)^{64} - (\sigma/r)^{32}$, while we use the repulsive part of $U \propto (\sigma/r)^{12} - (\sigma/r)^6$. Our softer potential decreases the size of the liquid-hexatic coexistence region [94]. Given the similar temperatures ($k_B T/\epsilon = 1/24$, versus $k_B T/\epsilon = 1/20$ in Ref. [57]), the slightly longer range of the WCA potential (cutoff radius $r/\sigma = 2^{1/6} \sim 1.12$, as opposed to $r/\sigma = 2^{1/32} \sim 1.02$ in Ref. [57]) will shift the solid phases to slightly lower packing fractions. A similar comparison can be made to Paliwal and Dijkstra [59], who use a similar WCA potential, but with an interaction strength of $\epsilon/k_B T = 1$ compared to our $\epsilon/k_B T = 24$, which likewise slightly shifts the position and width of the hexatic and solid phase boundaries. We ourselves have not done so, but in principle the phase boundaries of all these systems should be comparable using the definitions of dimensionless density and interaction strength used by Klamser, Kapfer and Krauth [58].

Let us now leave the hexatic phase behind, shift our focus back to MIPS, and try to answer the questions posed in the introduction: How elongated do particles have to be to

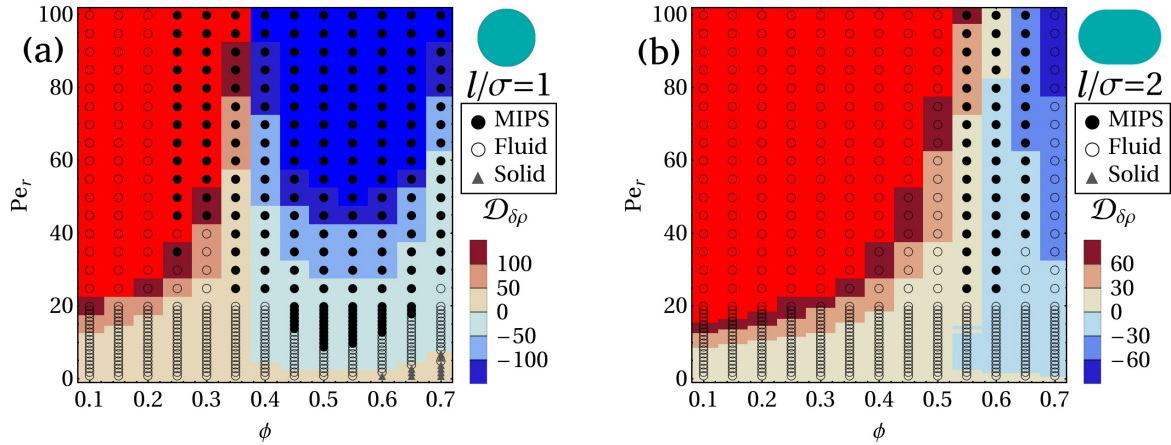


Figure 2.7: Phase diagram of 2D self-propelled disks (a) and rods of aspect ratio $l/\sigma = 2.0$ (b), for different Péclet numbers Pe and packing fractions ϕ . Data points indicate the resulting phase of $N = 10^4$ particles as obtained from Brownian dynamics simulations, in which we distinguished MIPS, fluid and solid phases. The colors indicate the diffusion constant of density fluctuations $\mathcal{D}_{\delta\rho}$. Spinodal decomposition to a MIPS state is then predicted where $\mathcal{D}_{\delta\rho} < 0$.

not display MIPS? And what is the mechanism that suppresses MIPS for rods?

2.4.1 Phase diagrams of self-propelled disks, spheres and rods

Figure 2.7 shows phase diagrams in the Péclet number Pe - packing fraction ϕ representation for 2D disks (a) and rods (b). Both show the MIPS region predicted on the basis of the stability analysis (blue-tinted region, $\mathcal{D} < 0$), and the MIPS region found from simulations with $N = 10^4$ using the cluster method (black points). Let us focus on the disks first (Fig. 2.7a). Both methods seem to indicate MIPS in roughly the same region, but there are a few notable differences.

On the low density side, we find a discrepancy: MIPS is found outside of the predicted spinodal region. In analogy with the gas/liquid phase separation, this might be because MIPS in this region occurs through nucleation and growth rather than through spinodal decomposition. Is this also the case? A simple way to see whether MIPS forms through a nucleation process or not is to look at domain growth, which we can track using a time series of cluster fraction f_{cl} defined in Section 2.2.3. If the system immediately decays from an isotropic to a MIPS state in a manner similar to spinodal decomposition, this fraction will likewise increase immediately. If, on the other hand, the system stays in the fluid state for a prolonged period of time, only to later transition into MIPS through a nucleation process, f_{cl} will retain the value corresponding to the fluid for a nonzero amount of time. Figure 2.8 compares the time evolution of the fraction f_{cl} of particles in the largest cluster for a number of Péclet numbers at two different densities: one on the low density side of the MIPS regime at $\phi = 0.25$ and one on the high density side at $\phi = 0.7$. On the low density side and outside of the predicted spinodal region, the cluster fraction can stay constant for a significant amount of time ($t > 30\tau$) before transitioning to a MIPS state. On the high density side of the MIPS region, such a delay is absent. The stability analysis predicts spinodal decomposition in this regime, and the cluster

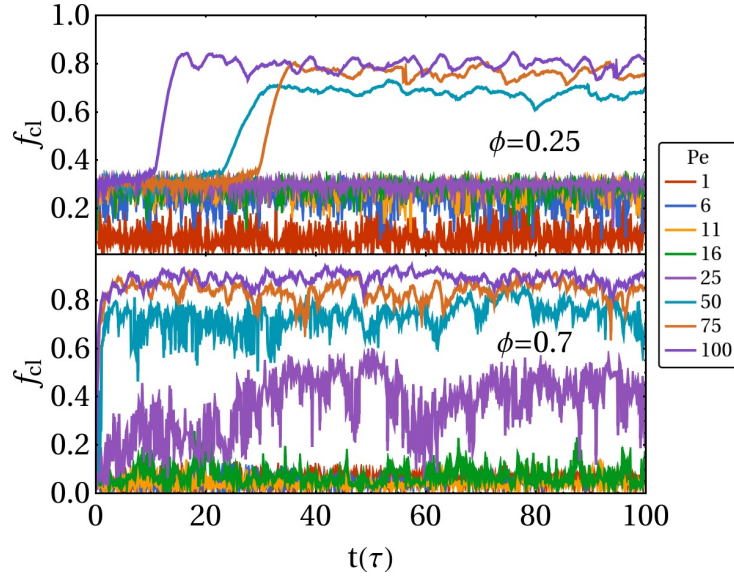


Figure 2.8: Time series of the largest cluster fraction f_{cl} for active disks ($l/\sigma = 1$). At low density $\phi = 0.25$, the system occasionally only clusters after a significant amount of time ($t > 10\tau$), suggesting that the transition is triggered by a rare nucleation event. At high density $\phi = 0.7$, this is never the case—only spinodal decomposition is observed.

growth agrees. This asymmetry is consistent with the findings of Speck et al. [89], who report that the MIPS transition is discontinuous at low densities, but continuous at high densities.

There is also a discrepancy between the stability analysis and the large-scale simulation at low Péclet numbers. This is to be expected: in this region the fluid-MIPS transition is continuous, and the difference in density between the coexisting phases is small when we are close to a critical point. Consequently, distinguishing between clusters of particles is difficult, and the exact choice of cluster fraction threshold f_{cl} can shift the boundary quite a bit in this region.

Having identified the most important features of the phase diagram for active disks, let us now turn to rods and see how these features change. Figure 2.7b shows the phase diagram in the density-activity representation for rods with an aspect ratio of $l/\sigma = 2$, using the same density and activity ranges as for the disks. The most obvious difference with the rods is that the MIPS region is now both shifted to higher densities and much narrower. The predictions of the stability analysis are worse for the rods: the predicted spinodal now lies in the middle of the simulated MIPS region. We find that the transition from fluid to MIPS now appears to be completely continuous—the system always starts clustering immediately, without any nucleation-like transient period. As can be seen from Figure 2.9a, the suppression is continuous with increasing aspect ratio, and it eventually pushes the fluid-MIPS transition into the regime where solid phases typically emerge.

Let us now see whether the 3D case is similar. Figure 2.10 displays phase diagrams in the (ϕ, Pe) representation, in Fig. 2.10a for 3D spheres and in Fig. 2.10b for 3D rods with $l/\sigma = 2$. Somewhat unsurprisingly, they are similar to their 2D counterparts. The most important feature is retained: MIPS disappears when the aspect ratio is increased. The

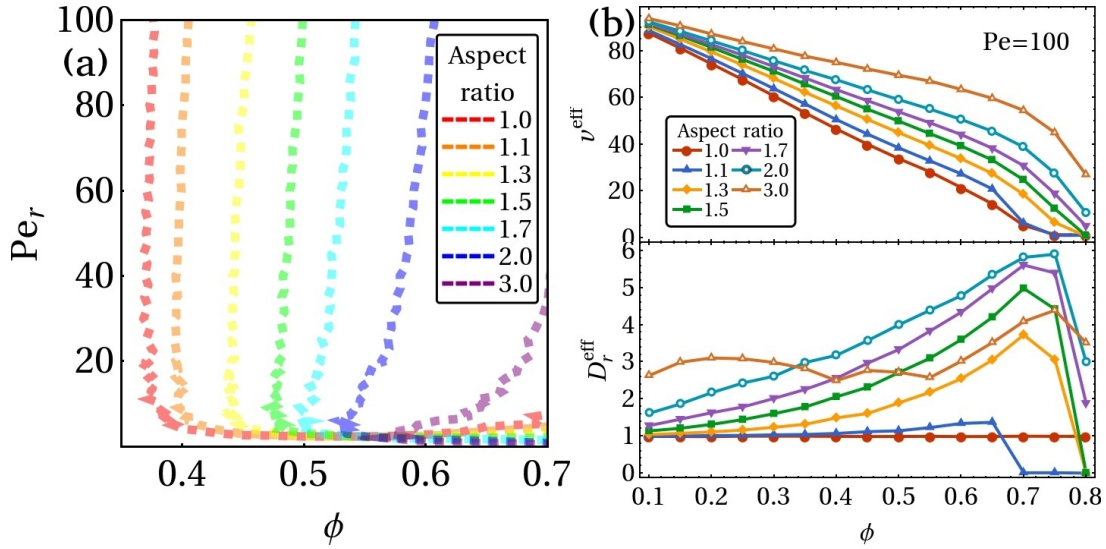


Figure 2.9: (a) Spinodal lines for 2D active rods as predicted from Eq. 2.30, as a function of the packing fraction ϕ for varying aspect ratios, and (b) the corresponding effective self-propulsion velocity v^{eff} and rotational diffusion D_r^{eff} at Péclet number $Pe = 100$ as a function of the packing fraction ϕ for varying aspect ratios. At high activity, the effective self-propulsion decreases more slowly with density, while the rotational diffusion is enhanced.

fluid gap we found in between the solid and MIPS phases is also present for the active spheres. However, there are also notable differences between the 2D and 3D cases.

In contrast to the 2D case, we observe no region for the active spheres where the MIPS transition is discontinuous. All simulations that form MIPS appear to undergo immediate spinodal decomposition. This does not necessarily mean that there is no binodal region: it may simply be quite small or have low nucleation barriers. The density regime of the metastable region for 3D active spheres is not well understood. We are only aware of one comparable simulation study by Stenhammar et al. [81], who looked at 2D and 3D active disks/spheres to study the influence of dimensionality. However, their binodal lines were defined as the density at which a high-Péclet system phase separated, which is not directly comparable to the metastable region we define here. Hence, further studies are needed to explain the difference in the width of the metastable region between $d = 2$ and $d = 3$.

Another difference occurs at high Péclet number, where the predicted MIPS region for the spheres continues to shift towards higher density, instead of moving towards a constant one. We believe this to be the behaviour that we discussed in Section 2.2.2: for higher Péclet numbers the particles can approach each other closer due to the active forces, causing the effective diameter of the particles to decrease. This effect appears to be stronger in 3D than in 2D, presumably due to the increased coordination of each particle.

The final difference between the 2D and 3D cases is perhaps the most notable one: for the rods, no MIPS is detected at all in the simulations by using the cluster method. Whatever mechanism suppresses MIPS appears to be stronger in 3D than in 2D. Curiously enough, the stability analysis still predicts MIPS in a significant portion of the phase diagram. This discrepancy, combined with its 2D counterpart, suggests that our

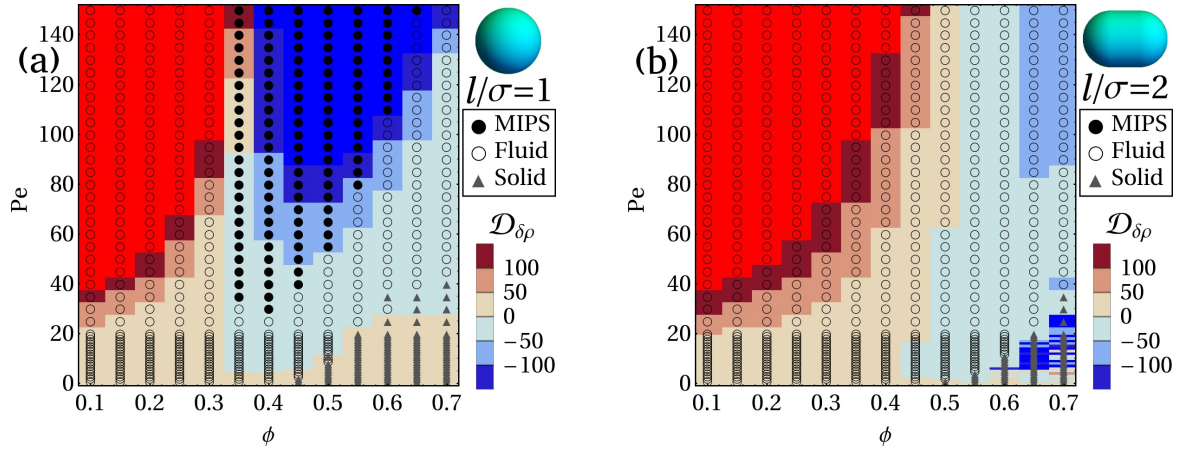


Figure 2.10: Phase diagram of 3D self-propelled spheres (a) and rods of aspect ratio $l/\sigma = 2.0$ (b), in the Péclet number Pe -packing fraction ϕ representation. Data points indicate the resulting phase of $N = 10^4$ particles as obtained from Brownian dynamics simulations, in which we distinguished MIPS, fluid and solid phases. The colors indicate the diffusion constant of density fluctuations $\mathcal{D}_{\delta\rho}$. Spinodal decomposition to a MIPS state is then predicted to occur in the blue region where $\mathcal{D}_{\delta\rho} < 0$. The small region of predicted instability in (b) under the points indicated as solid is an artefact of the fluid-solid transition there, where $D_{\delta\rho}$ fluctuates strongly as both v_r^{eff} and D_r^{eff} go to zero.

theoretical approach breaks down for higher aspect ratios. We will see why this is the case in the next section, where we discuss the suppression mechanism.

Armed with the knowledge of these phase diagrams, can we now answer the first question posed in our introduction: “How rodlike must a particle be for MIPS to disappear?” Only partially, unfortunately. Determining the exact aspect ratio where MIPS disappears turns out to be quite difficult. We now know that the nature of the suppression stems from the fluid-MIPS transition shifting to higher densities, but unfortunately our methods to identify MIPS are less reliable at higher densities. More importantly, however, when the particle interactions are not isotropic, MIPS is no longer defined unambiguously and multiple types of clustered phases are possible which all fit the present criteria. When we identify MIPS according to a) the system phase-separating into a single dense cluster in a background gas and b) this cluster having no net orientational order, there are still multiple realizations of such a system (Fig. 2.11), such as a dense cluster with large domains of oppositely oriented particles ($l/\sigma = 1.1$) or a percolating cluster with low orientational order and many voids ($l/\sigma = 1.3, 2.0$). Therefore, establishing the boundaries of MIPS at these higher densities requires a more careful consideration of both hexatic [57] and orientational order [97]. We leave this investigation to future work and instead, having established *that* MIPS is suppressed when particles become elongated, we now turn to finding out *why*.

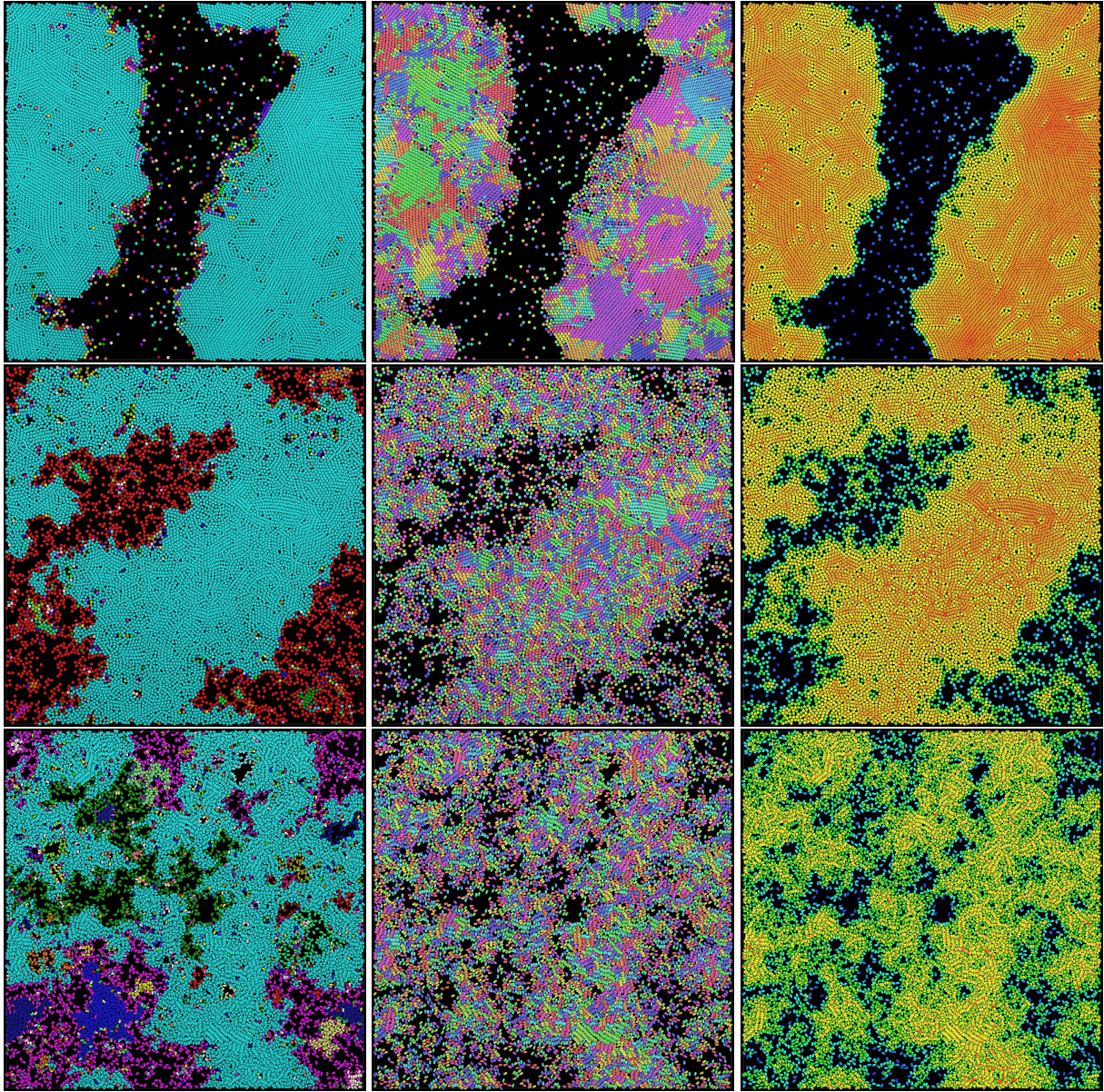


Figure 2.11: 2D Simulation snapshots for $N = 10000$ rods with aspect ratios $l/\sigma = 1.1$ (top), $l/\sigma = 1.3$ (middle) and $l/\sigma = 2.0$ (bottom), at $\phi = 0.6$, $Pe = 100$, deep within the MIPS region. The columns depict the same snapshot three times with various color maps. The left column shows the distribution of clusters, where each cluster is assigned a unique color. In the middle column the color is indicative of the particle orientation, with nematic symmetry. Zooming in also shows black stripes that indicate the polar orientations. In the right column the color represents the local density. Even though all three snapshots show a separation into dense and dilute regions, form a single connected cluster and have no global orientational order (and are thus classified as MIPS), the three cases are clearly different.

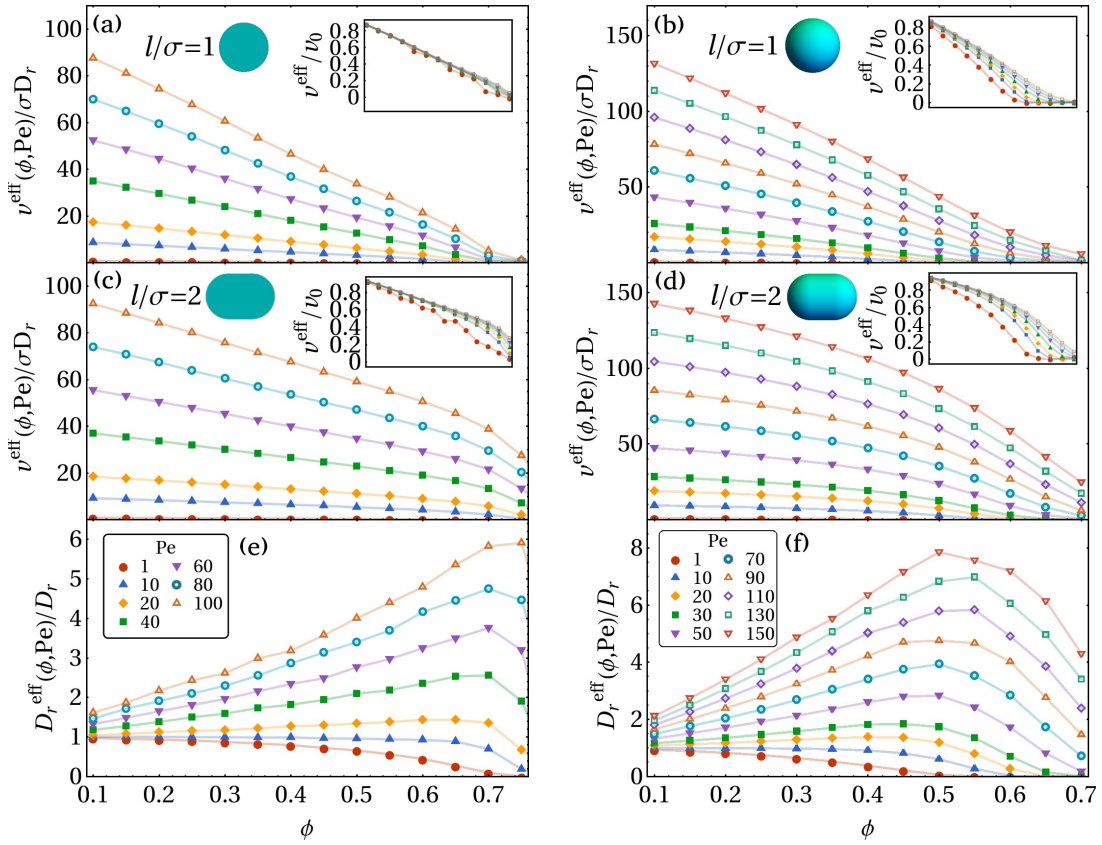


Figure 2.12: Simulation results for the effective self-propulsion speed v^{eff} of 2D active disks and 3D active spheres (a,b), effective self-propulsion speed v^{eff} for 2D and 3D active rods (c,d), and effective rotational diffusion D_r^{eff} for 2D and 3D rods with an aspect ratio $l/\sigma = 2.0$ (e,f). All insets show effective velocity divided by input velocity, for comparison with $v^{\text{eff}} = v_0(1 - \phi/\phi_{cp})$ with ϕ_{cp} the close packing density.

2.4.2 Torque-induced suppression of motility-induced phase separation

Since the main difference between the disk and rod systems is the presence of torque, it is likely that the suppression of MIPS must arise there. In our stability analysis, the only effect of torques seems to be to modify the rotational diffusion. Looking at Eq. (2.30), it might be possible to suppress MIPS if D_r^{eff} is increased enough to make the second term smaller than D_t^{eff} . Is this the case? Is the rotational diffusion perhaps enhanced so much that we effectively end up with a thermal system again?

Not so. Looking at Figs. 2.12e and 2.12f, we can see that D_r^{eff} is indeed increased significantly where MIPS vanishes. However, when we insert the actual values of v^{eff} and D_r^{eff} , we see that this is not the case: the typical values of v^{eff} are simply too large. So if it is not D_r^{eff} , it must be v^{eff} that contains the key information that allows us to predict MIPS or its suppression. After all, the stability analysis does correctly predict that MIPS is suppressed for high aspect ratios. Comparing the effective swimming speeds of different aspect ratios (Figs. 2.12a and 2.12c, or 2.12b and 2.12d), we see that the rods slow down less with increasing density than the disks. In other words, the rods hinder each other's

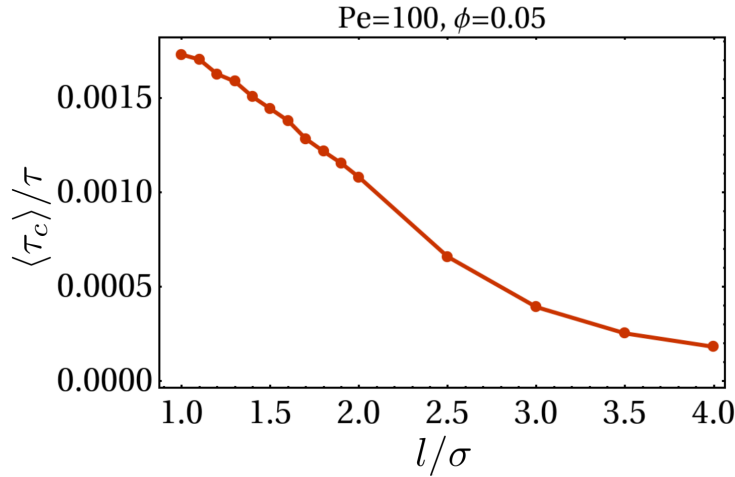


Figure 2.13: Mean duration of collisions $\langle \tau_c \rangle$ normalized by the timescale of rotations $\tau = 1/D_r$ for 2D self-propelled rods at a packing fraction $\phi = 0.05$ and a Péclet number of $Pe = 100$. As the aspect ratio increases, collisions between particles become shorter.

movement less than the disks do. Why is this? Again we must look to the main difference between the two systems: torque.

For disks, one can derive a linear decrease of the velocity with increasing density $v^{\text{eff}} = v_0(1 - \rho/\rho^*)$ from mean-field theory and kinetic arguments [55, 85, 98]. This is done by assuming that particles slow down at low density due to time spent in binary collisions, which leads to $v^{\text{eff}}(\rho) \simeq v_0(1 - \tau_c/\tau_f)$, where τ_c is the time spent in a collision and $\tau_f = 1/(\sigma v_0 \rho)$ the mean free time between collisions. At low density, we expect the mean free time τ_f to be mostly unaffected by the presence of torques as long as there are no significant short-range orientational correlations. The duration of collisions τ_c , however, can change significantly when torques are involved. For disks, the duration of their collision—of their hindrance—is determined by how long it takes for them to slide around each other. Rods, however, will rotate to reorient their swimming directions away from the combined center of mass of the collision. This will decrease the collision duration. Since collisions are now shorter, the rods spend more time moving freely: less hindered. Furthermore, this reorientation leads to an enhanced rotational diffusion—exactly what we find.

To verify this hypothesis, we measured the duration of particle collisions for 2D rods in a homogeneous and isotropic fluid by timing how long pairs of particles are within a certain distance r_c of each other. We choose this to be $r_c = 2^{1/6}\sigma$ i.e. the interaction range of the WCA potential Eq. 2.5. In Fig. 2.13 we show the mean duration of collisions between 2D rods measured at a Péclet number of $Pe = 100$ and a packing fraction of $\phi = 0.05$ as a function of their aspect ratio l/σ . As can be seen from the decrease in $\langle \tau_c \rangle / \tau$, collisions between particles indeed become shorter as the aspect ratio is increased. It would be interesting to see whether it is possible to derive the suppression of MIPS from a kinetic theory based on the duration of collisions. Perhaps future work could explore this avenue.

Interestingly, the existence of this suppression mechanism suggests that an inverse mechanism might also exist. If the torques between two colliding particles cause the

particles to rotate towards their center of mass, collisions would be prolonged and MIPS would be enhanced. Precisely this inverse effect was reported earlier in Refs. [69, 70]: MIPS is enhanced for self-propelled particles that align through Vicsek interactions. In binary collisions, the Vicsek torques always rotate particles towards the combined center of mass, increasing the duration of collisions, increasing hindrance and thus enhancing MIPS.

Is the changing density dependence of v^{eff} with increasing anisotropy enough to completely describe the suppression of MIPS? If we would have a system of self-propelled particles with some arbitrary shape and we would know how the effective swim speed depends on density, could we then predict whether and where it will undergo MIPS? Unfortunately, no. As we can see from the rod phase diagrams in Figs. 2.7b and 2.10b, our stability analysis predicts the right qualitative trend, but its quantitative prediction is poor. This is probably due to neglecting alignment effects in the stability analysis. As the rod length increases, nematic and polar alignment of the particles start playing a more significant role in their phase behaviour, which is not captured by our theory. For instance consider Fig. 2.14, where we show a snapshot of rods at $\phi = 0.5$, $\text{Pe} = 100$, just outside the MIPS region, and colour particles according to nematic orientation. The clusters formed by the rods have significant short-range nematic order. Incorporating the dynamics of the polarization and nematic fields using theory developed for active nematics [99, 100] might allow for more accurate predictions for the onset of MIPS for longer rods.

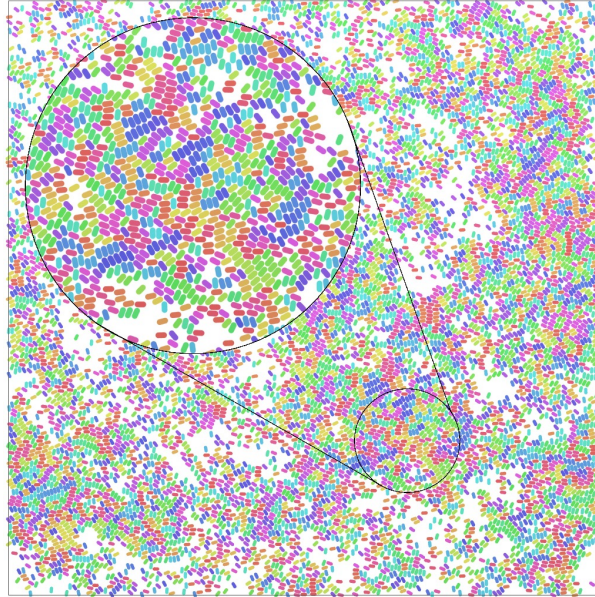


Figure 2.14: Simulation snapshot of 2D rods with aspect ratio $l/\sigma = 2$ at a packing fraction of $\phi = 0.5$ and a Péclet number of $\text{Pe} = 100$. Particles are coloured according to their orientation. Dense clusters display significant short-range orientational order, and no large-scale phase separation can be seen.

2.5 Conclusions & Outlook

In this chapter, we showed that motility-induced phase separation does not occur for rod-like particles when they become sufficiently anisotropic. This disappearance is observed both from many-particle simulations and from a stability analysis of the homogeneous isotropic fluid phase. The latter provides a simple criterion for the onset of MIPS by considering the effective swimming speed of the particles and their effective rotational diffusion. Both methods agree qualitatively in that MIPS is pushed to higher densities for increasing rod aspect ratio, and they agree quantitatively for short rods that deviate only slightly from disks or spheres. For longer aspect ratios the quantitative agreement is lost, presumably due to alignment interactions that are present, but not taken into account in the stability analysis.

We also propose a more intuitive explanation for the suppression mechanism. MIPS relies on particles slowing down sufficiently with increasing density [61]. This hindrance is closely linked to the duration of collisions between particles [55, 85, 98]. Excluding torques, the duration of collisions is determined by how long it takes for them to slide along one another. Including torques can dramatically decrease the duration of collisions by rotating the forward axes of the self-propelled particles away from each other. Formulated in this way, we can also explain the results of Refs. [69, 70], where MIPS is enhanced for particles with Vicsek interactions. Simply put, Vicsek torques prolong particle collisions, while rodlike excluded volume torques shorten them. Intriguingly, this provides us with a particle design tool to enhance or suppress MIPS. MIPS is enhanced for Vicsek-like interactions [69, 70], for faceted, concave and/or rough particles [86, 101, 102], while it is suppressed for smooth particles and rodlike shapes [97]. In addition to steric interactions, hydrodynamic interactions between active particles also play an important role in whether or not MIPS can form. While hydrodynamics seems to usually suppress MIPS [103–105], the details depend on whether particles are “pushers” or “pullers” and on the dimensionality [106, 107].

Despite recent advancements, the role of torque in active systems is still not well understood. Much of the developed theory has been restricted to the torque-free regime, but recent numerical studies suggest that torque, either from boundaries [108] or from particle interactions [69, 70], can have a significant effect on the structure and dynamics of active matter systems. In order to understand active matter beyond torque-free model systems, more theoretical work is needed to elucidate the influence of torques in active systems.

2.6 Addendum

Active matter is a fast-moving field. Since the original publication on which this chapter is based, a number of works have been published on similar questions, yielding additional insights. While we cannot discuss all of them, we would be remiss if we did not at least mention two works that are particularly relevant to the contents of this chapter.

Most directly related is the work of Großmann, Aranson and Peruani [109], who developed an analytical model for self-propelled rodlike particles (“vectorial active matter”) for which the polar and nematic fields could be fully taken into account in the derivation of the phase boundaries. They show that for their model, elongation of particles from disks ($l_{\parallel}/l_{\perp} = 1$) to even slightly elongated particles ($l_{\parallel}/l_{\perp} = 1.04$) immediately destabilizes the MIPS phase into a phase of global positional and orientational disorder, but with large density fluctuations. Elongation to $l_{\parallel}/l_{\perp} = 1.21$ causes local nematic order to arise in the globally disordered phase, and further elongation has the nematic alignment overtaken by a polar one, wherein particles form increasingly larger dense polar domains.

One of the assumptions we have made early on in this work in Section 2.2.1 to construct the Langevin equations Eq. 2.1 and 2.2 is that the fluctuation-dissipation theorem (FDT) holds. An interesting recent work exploring the validity of this assumption is provided by Burkholder and Brady [110]. Their findings suggest that in general the FDT does *not* hold for self-propelled swimmers, but that one can still construct a modified Stokes-Einstein-Sutherland expression (relating the diffusivity to the drag) that includes the effects of activity.

Acknowledgements

It is a pleasure to thank Jeroen Rodenburg for the fruitful collaboration this chapter is based on and specifically for deriving the stability analysis presented in Sections 2.3.1 and 2.3.2. I would also like to thank Bram Bet for providing the information on the hydrodynamic friction coefficients shown in Fig. 2.3, which proved very useful especially in the early stages of this research.

Capillary-driven self-assembly of hourglass-shaped particles at a fluid-fluid interface

In this chapter we study the self-assembly of hourglass-shaped NaYF_4 nanoparticles at an air-hexane interface. We use capillary deformation calculations to show that particles adsorb onto the interface in three ways: with their long axes horizontal, vertical or tilted with respect to the interface. The vertical and tilted configurations also deform the surrounding fluid-fluid interface, causing capillary interactions between adsorbed nanoparticles. We capture the deformation of the interface with a multipole expansion, and describe the resulting capillary interactions between particles as pairwise multipole-multipole interactions. We subsequently perform many-particle Monte Carlo simulations in which particles interact through a combination of a non-convex hard-particle interaction and the aforementioned capillary multipole-multipole interactions. We find that this effectively reproduces experimental observations on the self-assembly, namely i) that particles are found in both the vertical and horizontal adsorption configurations, ii) that these two configurations demix, but only partially, iii) that horizontally adsorbed particles do not form large dense-packed domains and iv) that horizontal particles form end-to-end attached strings at low density.

Based on:

S. Najmr, R. van Damme, M. Zhang, G. Soligno, M. Zanini, M.A. Fernandez-Rodriguez, J.D. Lee, L. Isa, M. Dijkstra, C.B. Murray, *“Synthesis of Nanocrystalline $\beta\text{-NaYF}_4$ Heterostructures with Tunable Negative Curvature and their Self-Assembly Patterns at Interfaces”*, to be submitted.

3.1 Introduction & experimental motivation

When two immiscible fluids such as oil and water are put together, they do not mix. Instead, an interface forms between the two. The formation of this interface has a free-energy cost, but this cost is smaller than having the two fluids mix. Interestingly, because of this free-energy cost, it can be favorable for particles to attach to the interface between the two fluids if the cost for them to be in contact with both fluids is lower than that to form the interface. This phenomenon of *interfacial adsorption* is used to great effect in multiple methods for 2D nanoparticle self-assembly [111–114]. In most cases these methods were applied for spherical nanoparticles, for which the adsorption at a fluid-fluid interface is fairly well understood (e.g. Refs. [115–117]). For spherical particles small enough to neglect the influence of gravity, the fluid-fluid interface is pinned to roughness on the surface of the particles, which causes the interface to be deformed locally in the shape of a quadrupole [116]. Recent advances in synthesis, meanwhile, have made it possible to synthesize monodisperse nanoparticles with a variety of shapes beyond spheres. In applying the aforementioned self-assembly methods to these nonspherical particles, one naturally has to wonder: how do these nonspherical particles adsorb at a fluid-fluid interface, and what effect does this have on the self-assembly? This is not an easy question to answer. As a first step beyond spheres, studies of the last twenty years or so have investigated the adsorption of rodlike particles such as ellipsoids [30, 118–121], cylinders [33, 122], dumbbells [123, 124], cuboids [125], and even mosquito eggs [126]. The quadrupolar deformation of the interface found for spheres is also found for rods, but the elongated particle shape introduces additional anisotropy that significantly influences the self-assembly. More recent studies have also investigated faceted polyhedral particle shapes: cubes [32, 119, 127–129], octahedra [130] and rhombicuboctahedra [131], to name a few. These cubelike particles display both a quadrupolar or a hexapolar deformation depending on specific system parameters. The adsorption behaviour of all these particle shapes turns out to be significantly richer than that of spheres and depends sensitively on the particle shape and chemical composition of the system. In this chapter we will consider a next step up in complexity and study the adsorption and self-assembly of faceted, non-convex particles shaped like hourglasses.

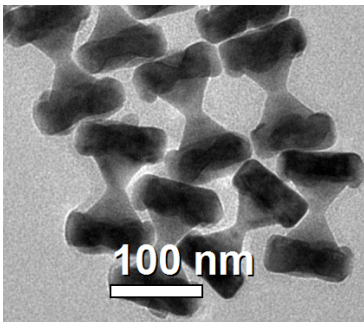


Figure 3.1: Transmission Electron Microscopy (TEM) image of hourglass-shaped particles.

The particles we consider in this chapter were synthesized and characterized by Stan Najmr and Mingyue Zhang in the group of Christopher Murray from the University of Pennsylvania. We here briefly describe the synthesis and self-assembly procedure they employed, which is based on those of Refs. [132–134]. In short, the particles are made from hexagonal prism NaYF_4 cores [135, 136] that are etched in a way whereby NaYF_4 is removed from the middle of the prism while another material (NaNdF_4) nucleates and grows onto the ends. The endcaps obtain a roughly hexagonal shape, while the middle is rounded slightly from the initial hexagonal prism shape to become more like two cones. The result is an hourglass-shaped particle of roughly $L = 200$ nm in size, as can be seen in Fig. 3.1.

Following the procedure of Ref. [113], the particles are dispersed in hexane and left to self-assemble by dropcasting them onto a surface of diethylene glycol (DEG) and letting the hexane slowly evaporate. Once the hexane has evaporated, the self-assembled structures are left adsorbed onto the air/DEG interface. They can then be deposited onto a substrate from the bottom-up, leaving the self-assembled structure intact for imaging techniques such as Transmission Electron Microscopy (TEM). Representative TEM images of the resulting dried systems are shown in Figs. 3.1, 3.2 and 3.3. In Fig. 3.2 we see that particles can be found in two orientations: either vertical or horizontal with respect to the substrate. Vertically aligned hourglasses are typically found in nearly close-packed hexagonal domains, while horizontally aligned hourglasses are typically found in large domains with low long-range structural order. The two orientations often appear demixed i.e. domains are composed of *either* horizontally *or* vertically oriented particles. We do occasionally observe interlocking arrangements of horizontally and vertically aligned particles, such as on the bottom right of Fig. 3.3, but these hardly ever form extended domains. Our goal in this chapter will be to explain this behaviour by modeling the adsorption and capillary self-assembly of these non-convex, anisotropic particles using simulations, and to use the resulting knowledge to improve our control over the self-assembly.

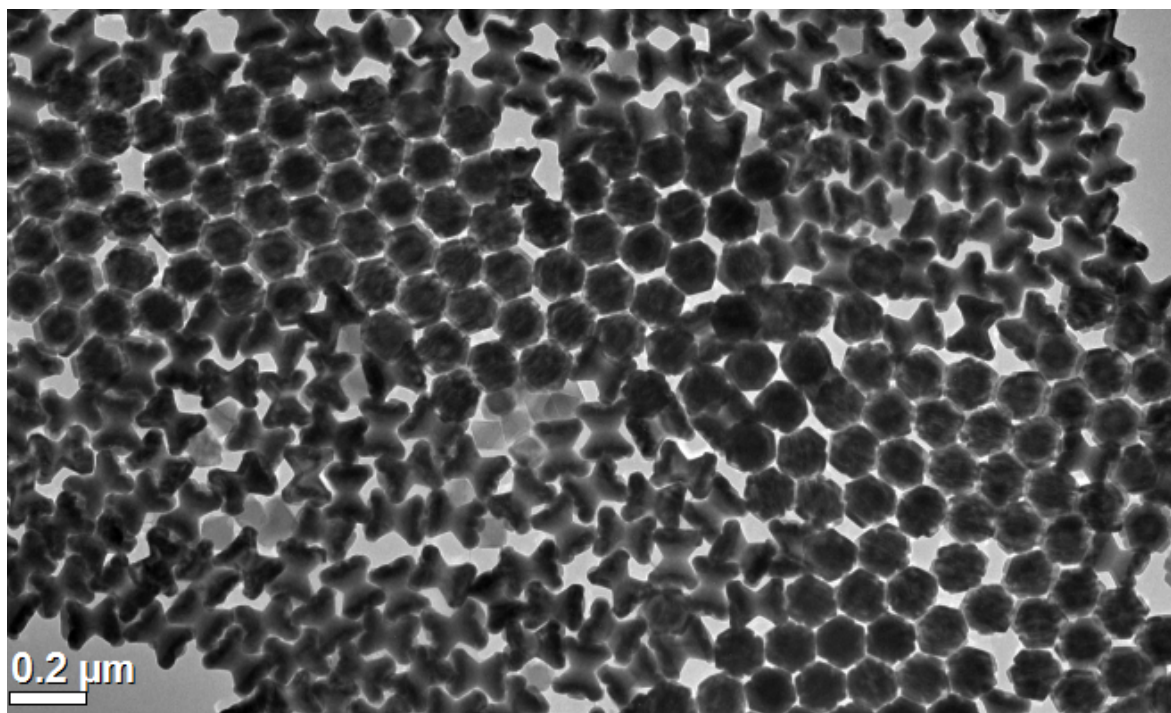


Figure 3.2: Transmission Electron Microscopy (TEM) image of hourglass-shaped particles lying on a TEM grid. Particles are oriented either vertically or horizontally with respect to the substrate, and the two orientations are typically found to be demixed.

Before we turn to the more involved numerical analysis of the adsorption and self-assembly of these particles, it is instructive to first consider the importance of capillary adsorption and gravity in the self-assembly process with a few order-of-magnitude estimates. The air/hexane interface has a surface tension of approximately $\gamma \approx 0.018$ N/m at

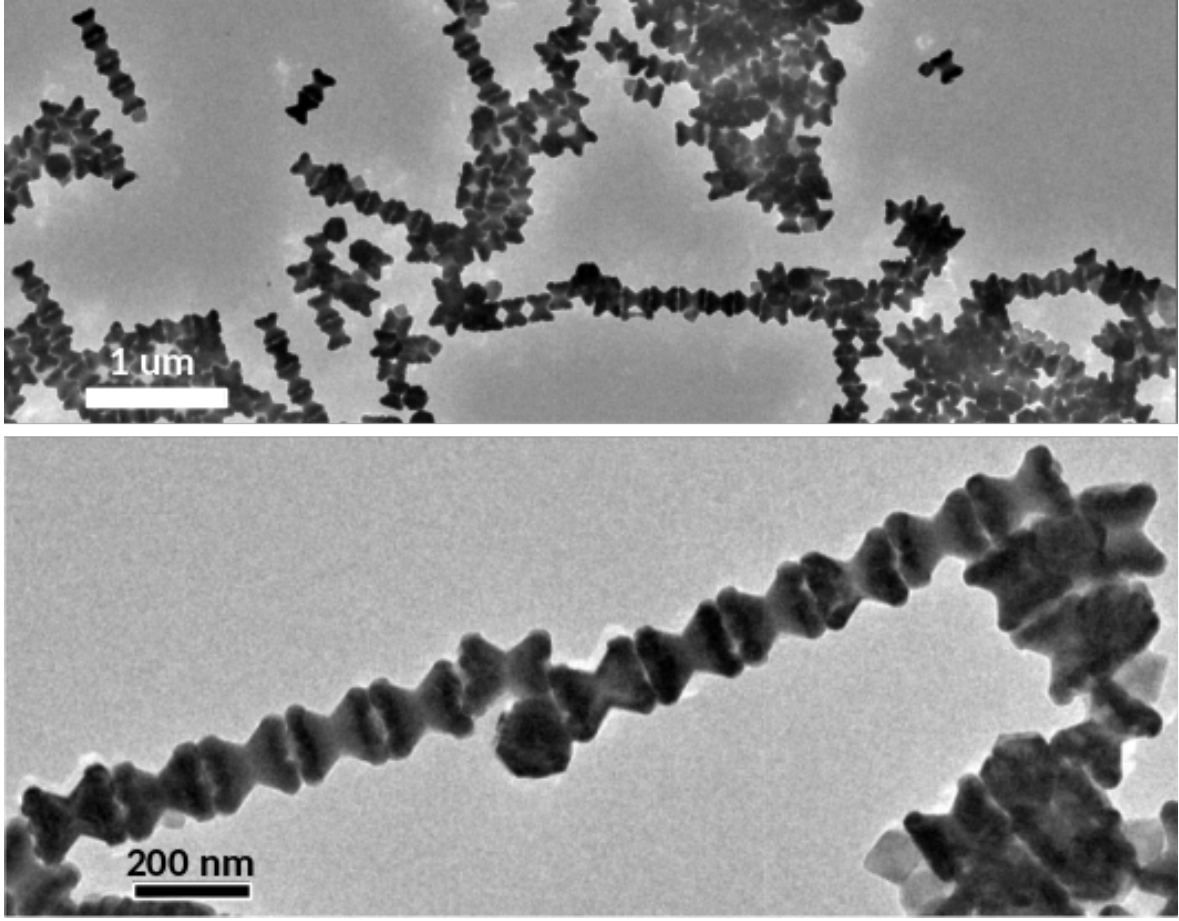


Figure 3.3: Transmission Electron Microscopy (TEM) image of hourglass-shaped particles lying on a TEM grid. Horizontally aligned particles are often found arranged end-to-end in string-like assemblies. Some interlocking arrangements of horizontally and vertically oriented particles can also be seen.

room temperature (e.g. Ref. [137]). As an order-of-magnitude estimate, we assume each particle to exclude an area $A = L^2 \approx 4 \cdot 10^{-14} \text{ m}^2$ when it adsorbs onto the air-hexane interface. This adsorption provides an energy gain of roughly $\gamma A \approx 7 \cdot 10^{-16} \text{ J}$. Expressed in terms of the thermal energy at room temperature (293 K), $k_B T_r \approx 4 \cdot 10^{-21} \text{ J}$, this yields $\gamma A \approx 2 \cdot 10^5 k_B T_r$. In other words, particles will strongly and irreversibly adsorb onto the air/hexane interface. The influence of gravity in capillary systems is typically captured by two numbers. First, the *capillary length* $\ell = \sqrt{\gamma/(g\Delta\rho)}$, which characterizes the length over which gravity-induced deformations of the fluid-fluid interface decay, with γ the relevant interfacial tension, $g \approx 9.81 \text{ m/s}^2$ and $\Delta\rho$ the difference in mass density between the two fluids. Second, the *Bond number* $\text{Bo} = L^2/\ell^2$ with L a characteristic length scale of the system, a dimensionless number that captures the relative importance of gravitational forces relative to capillary ones. For our system of $L \approx 200 \text{ nm}$ -sized hourglass particles adsorbed at an air/hexane interface with $\gamma = 0.018 \text{ N/m}$ and $\Delta\rho \approx 655 \text{ kg/m}^3$, we have $\ell \approx 2 \text{ mm}$ and $\text{Bo} \sim 10^{-8} \ll 1$, which means we can safely neglect the effects of gravity in our calculations.

3.2 Theory & Methods

To model the self-assembly of the hourglass particles we will need to consider both effective pair interactions between the hourglasses and their capillary interactions. We discuss the particle interactions and the parametrization of the model particle shape in Section 3.2.1. In Section 3.2.2 we introduce the thermodynamics associated with the adsorption of the hourglasses at a fluid-fluid interface and describe the numerical method we use to simulate how anisotropic particles adsorb at and deform the fluid-fluid interface. Finally, Section 3.2.3 describes how to express the deformation of the interface in terms of a multipole expansion, and how this can be used to obtain an effective capillary pair interaction between adsorbed particles.

3.2.1 Effective pair interactions and shape parametrization

The effective pair interactions of nanoparticles can be complicated, as they are the combined result of Pauli exclusion, van der Waals dispersion, electrostatic forces and ligand interactions. The fact that these particles are stable (i.e. do not aggregate) in the hexane solution suggests that there are no significant long-range attractions between the particles. In contrast, it is clear from Figs. 3.2 and 3.3 that particles approach each other close enough during self-assembly that we will need to take into account their anisotropic shape. To make the problem analytically tractable, we assume that we can model the effective pair interactions with an anisotropic hard-particle model.

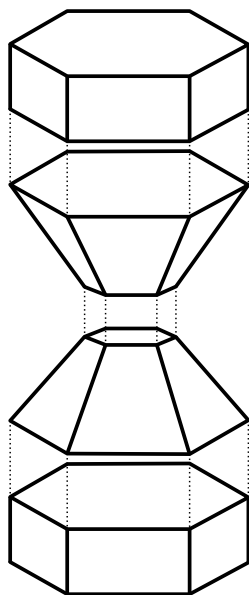


Figure 3.4: Decomposition of the non-convex hourglass shape into four convex components.

To model the hard-particle interactions between these hourglass-shaped particles we need to be able to calculate when two particles are overlapping. Because the hourglass shape is not convex, we cannot directly calculate overlaps using the Gilbert-Johnson-Keerthi algorithm as described in Section 1.7. However, this is relatively easy to solve: we simply decompose the non-convex hourglass shape into four convex components: two regular hexagonal prisms and two hexagonal frustums (Fig. 3.4). We then check for overlaps between all pairs of components belonging to different particles. If any two components overlap, the composite hourglasses overlap, and if no components overlap then neither do the hourglass particles. This decomposition does come at a performance cost: we now need to perform up to 16 overlap checks per particle pair. However, this cost can be reduced by i) stopping the overlap check if any pair of components is found to overlap, since overlap is then already established and ii) checking for overlap between the circumscribed spheres of each component first, which is considerably cheaper and allows one to discard pairs of components that are far away from each other. Note also that one could form the hourglass shape with only two components, which may be more computationally efficient. Although the overlap check could probably be further optimized, we found the described method sufficient for our purposes.

The synthesis procedure by which the hourglass-shaped particles are created allows for a fair degree of control over the exact particle shape simply by varying the duration of the etching step. Figure 3.6 shows a selection of particle shapes obtained in this way with a table of their associate shape parameters. In this chapter we will focus specifically on the hourglass shape shown in Fig. 3.5, which has shape parameters $L_1 = 157$ nm, $L_2 = 81$ nm, $W_1 = 136$ nm, $W_2 = 65$ nm and $\phi = 116^\circ$. Note that this set of shape parameters is from a different synthesis batch than those of Fig. 3.6, but its shape is very similar. We also investigated the adsorption of the particle shapes obtained after $t = 60$ min. and $t = 75$ min. of etching, but we found the adsorption not significantly different from that of the shape in Fig. 3.5.

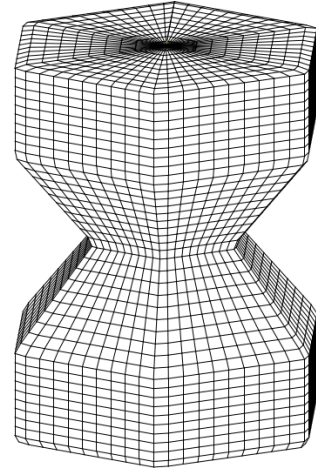


Figure 3.5: The exact hourglass shape investigated in this chapter, with $L_1 = 157$ nm, $L_2 = 81$ nm, $W_1 = 136$ nm, $W_2 = 65$ nm and $\phi = 116^\circ$.

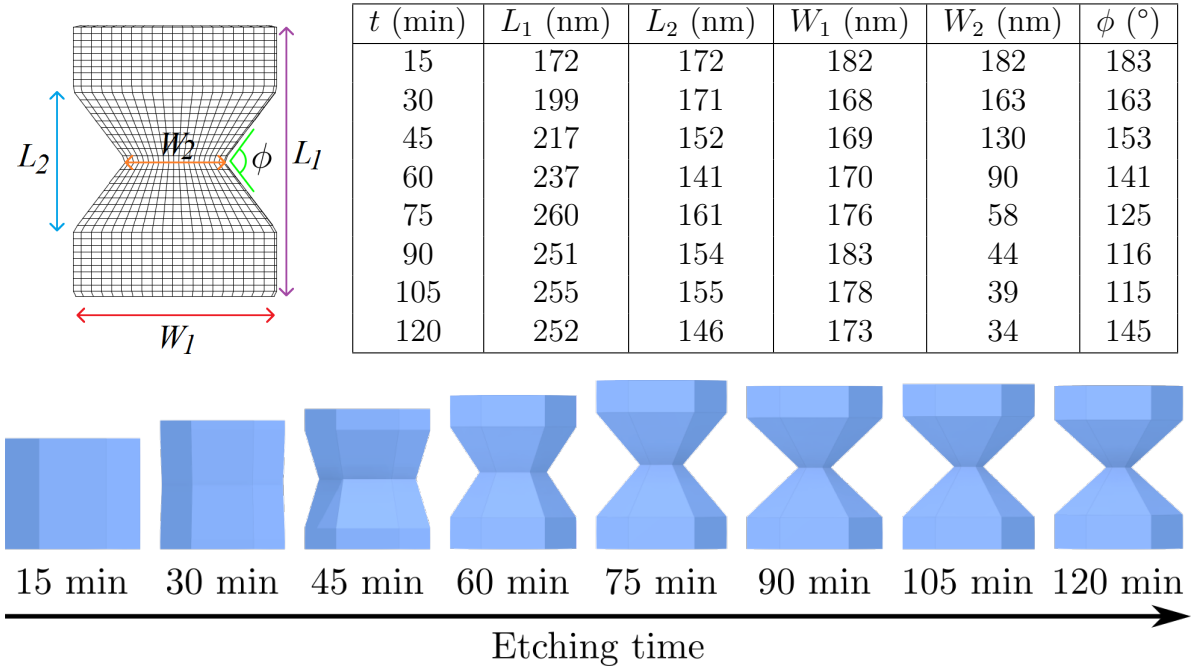


Figure 3.6: Experimentally obtainable particle shapes by stopping the etching process at various times t .

3.2.2 Thermodynamics and simulation of the adsorption of particles at a fluid-fluid interface

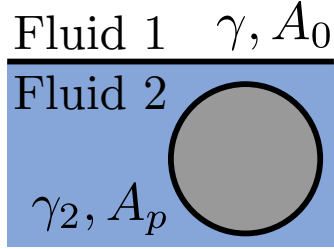


Figure 3.7: A particle with surface area A_p desorbed from a fluid-fluid interface with surface area A_0 .

Consider the system shown in Fig. 3.7: two immiscible fluids and a particle suspended in one of the fluids. The immiscibility of the two fluids implies an energy cost γA_0 for the interface between them, with $\gamma > 0$ the interfacial tension between the two fluids and A_0 the area of the interface. A similar cost is given for the particle with $\gamma_2 A_p$, though if fluid 2 is a good solvent for the particle we will likely have that $\gamma_2 \ll \gamma$. The total thermodynamic potential Ω_{des} for this desorbed case is then given by:

$$\Omega_{des} = \gamma A_0 + \gamma_2 A_p. \quad (3.1)$$

Now consider what happens if the particle adsorbs onto the interface, as shown in Fig. 3.8. It will expose some part A_1 of its area A_p to fluid 1, and the rest of its area i.e. $A_2 = A_p - A_1$ to fluid 2 such that the thermodynamic potential Ω_{ads} is given by

$$\Omega_{ads} = \gamma A + \gamma_1 A_1 + \gamma_2 A_2, \quad (3.2)$$

where A is the area of the fluid-fluid interface excluding the area now occupied by the particle, and γ_1 is the surface tension between the particle and fluid 1. Note that we are neglecting the influence of gravity in this description, which is justified given the small size of the particles.

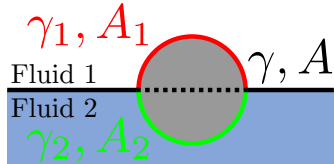


Figure 3.8: A particle adsorbed onto a fluid-fluid interface. Due to the adsorption of the particle, the area of the interface between the two fluids is now $A < A_0$, and the particle has two areas A_1 and A_2 in contact with fluids 1 and 2, respectively.

One can now answer the question “where does the particle go?” with “wherever the total energy is minimized”. At this point, it is convenient to consider the energy difference E between the adsorbed and non-adsorbed case i.e.

$$E = \Omega_{ads} - \Omega_{des} = \gamma A - \gamma A_0 + A_1(\gamma_1 - \gamma_2). \quad (3.3)$$

Since the potential of the desorbed case Ω_{des} does not depend on the particle coordinates as long as it remains away from the interface, this difference E has the same energy minimum as Eq. 3.2. Eq. 3.3 can be rewritten in terms of the contact angle θ :

$$\cos \theta = \frac{\gamma_1 - \gamma_2}{\gamma}; \quad (3.4)$$

$$E = \gamma(A - A_0 + A_1 \cos \theta). \quad (3.5)$$

The interfacial tension γ now sets the energy *scale* of adsorption, while the contact angle θ describes the *preference* of the particle for either fluid. We can now find the equilibrium adsorption configuration by minimizing Eq. 3.5 with respect to the particle’s position and orientation. A particle of arbitrary shape at a fluid-fluid interface has three degrees of freedom: its height z_c with respect to the flat interface, the polar angle φ of its long

axis with respect to the surface normal, and the angle ψ of its orientation around its own long axis. Thus, we have that

$$E(z_c, \psi, \varphi) = \gamma (A(z_c, \psi, \varphi) - A_0 + A_1(z_c, \psi, \varphi) \cos \theta) \quad (3.6)$$

and we obtain the equilibrium configuration by minimizing with respect to z_c , ψ , and φ . While earlier work on the adsorption of colloidal particles at fluid-fluid interfaces followed this route [118, 119, 138–142], later work [128, 143, 144] revealed that an important effect was missing: when a particle adsorbs onto the interface, the interface will *deform* to further minimize the energy. To include this effect, we must not only minimize Eq. 3.6 with respect to the particle coordinates, but also with respect to the shape of the interface. This can be done by describing the shape of the interface surrounding the particle by a height profile h , which leads to the adsorption energy

$$E[h_{z_c, \psi, \varphi}] = \gamma (A[h_{z_c, \psi, \varphi}] - A_0 + A_1[h_{z_c, \psi, \varphi}] \cos \theta), \quad (3.7)$$

where E , A and A_1 are now functionals of the height profile $h_{z_c, \psi, \varphi}$ and we use the subscript to indicate that each set of particle coordinates z_c , ψ , and φ has its own equilibrium height profile.

We minimize Eq. 3.7 using the numerical method developed in Refs. [143, 144]. In short, we apply a simulated annealing Monte Carlo scheme to find the equilibrium height profile $h(r, \phi)$ (in our method given in polar coordinates) for a fixed input particle orientation (ψ, φ) and contact angle θ . The height of the particle z_c is automatically solved for by allowing the volume of the two fluids in the simulation to vary.

3.2.3 Multipole expansion of the interfacial deformation

While the numerical method described in the previous section allows us to find the adsorption energy, the associated capillary deformation and even the capillary interactions *between* particles, we still need some way to incorporate their results into a many-particle simulation. Ideally, we would like to capture the capillary interactions in the form of some pair potential $u(\mathbf{r}, \phi_i, \phi_j)$ that depends only on the relative position \mathbf{r} and planar orientations $\phi_{i,j}$ of the two particles i and j . To what extent it is possible to reduce the many-body capillary interactions to an effective capillary pair potential is a matter of current research (e.g. [145]) which will be discussed later in this chapter. For now, we will simply introduce the framework by which it can be done by describing the height profile, or rather the *deformation field* h in terms of a polar multipole expansion. This derivation follows those of Refs. [143, 144, 146, 147]. Consider a 2D fluid-fluid interface whose normal at a point (x, y, z) is given by $\hat{\mathbf{n}}(x, y, z)$, and where we have chosen the $\hat{\mathbf{z}}$ -direction to be antiparallel to gravity. For completeness we include the gravitational terms in the derivation and only neglect them later. The Young-Laplace equation then states that:

$$\nabla \cdot \hat{\mathbf{n}}(x, y, z) = \frac{\Delta p}{\gamma} - \frac{\hat{\mathbf{z}} \cdot (x, y, z)}{\ell^2}, \quad (3.8)$$

where $\nabla = (\frac{\partial}{\partial x}, \frac{\partial}{\partial y}, \frac{\partial}{\partial z})$, Δp is the Laplace pressure, γ the surface tension between the two fluids, and $\ell = \sqrt{\gamma/(g\Delta\rho)}$ is the capillary length as defined earlier. If the surface is

sufficiently flat, we can describe its shape by the height profile $h(x, y)$ similar to Section 3.2.2. One can then express the divergence of the surface normal in terms of the mean curvature $2H(x, y) = \nabla \cdot \hat{\mathbf{n}}(x, y)$ to obtain [148]:

$$2H(x, y) = \frac{\Delta p}{\gamma} - \frac{h(x, y)}{\ell^2}. \quad (3.9)$$

If the interface is only weakly curved, one can apply the linear approximation

$$\left(\frac{\partial h}{\partial x}\right)^2 \approx \left(\frac{\partial h}{\partial y}\right)^2 \approx \frac{\partial h}{\partial x} \frac{\partial h}{\partial y} \ll 1 \quad (3.10)$$

to obtain the linearized Young-Laplace equation

$$\nabla^2 h = \frac{h}{\ell^2} - \frac{\Delta p}{\gamma}. \quad (3.11)$$

In our experimental system of evaporating hexane the interface is flat in the absence of any adsorbed particles, which means that the Laplace pressure $\Delta p = 0$. This leaves us with only the simple equation

$$\nabla^2 h = \frac{h}{\ell^2}, \quad (3.12)$$

which can be solved in polar coordinates for the height $h(r, \phi)$, either through a real-space route as in Refs. [116, 144] or via a Fourier transform as in Ref. [147]. Following the former, we use separation of variables

$$h(r, \phi) = \psi(r)\Phi(\phi) \quad (3.13)$$

to write Eq. 3.11 (with $\Delta p = 0$) into an angular part

$$-\frac{1}{\Phi} \frac{\partial^2 \Phi}{\partial \phi^2} = m^2, \quad (3.14)$$

with $m \in \mathbb{N}$, which is solved by the set of functions

$$\Phi_m(\phi) = c_m \cos(m\phi - b_m), \quad (3.15)$$

and a radial part

$$r^2 \frac{\partial^2 \psi}{\partial r^2} + r \frac{\partial \psi}{\partial r} - \left(\frac{r^2}{\ell^2} - m^2 \right) \psi = 0, \quad (3.16)$$

which is solved by the so-called *modified Bessel functions* of the second kind K_m^* :

$$\psi_m(r) = a_m K_m(r/\ell). \quad (3.17)$$

The general solution for the deformation height field $h(r, \phi)$ is then given by a linear combination of the various modes m :

$$h(r, \phi) = a_0 K_0(r/\ell) + \sum_{m=1}^{\infty} a_m K_m(r/\ell) \cos(m\phi - b_m). \quad (3.18)$$

*Technically the modified Bessel functions of the first kind $\psi_m(r) = D_m I_m(r/\ell)$ are also valid solutions, but they are discarded by the boundary condition $h(r \rightarrow \infty, \phi) = 0$.

Due to its similarity with electrostatics, this procedure is referred to as a *multipole expansion*, with the various $m \in \{0, 1, 2, 3, \dots\}$ referred to as the capillary monopole (or charge), dipole, quadrupole, hexapole, etc. We have split off the monopole term $m = 0$ in Eq. 3.18 for two reasons. The first is that its angular dependence is trivial (there is none). The second is that this monopolar term contains the deformation due to gravity. Simply put, a particle adsorbing onto a fluid-fluid interface will push the interface one way or another due to its weight – “down” if it is heavier or “up” if it is lighter than the two fluids. For this reason, the monopolar term is always present. However, its significance depends on the relative strength of the gravitational and interfacial forces, and it is thus only important if the adsorbed particles are heavy enough. As our particles (~ 200 nm) are small compared to the capillary length $\ell \approx 2$ mm, $K_0(r/\ell)$ varies only very little over the length scales we are interested in (i.e. $r/\ell \ll 1$). Thus, it can be neglected for individual particles, although it may become relevant for the assembly of aggregates [147]. In this limit of $r/\ell \ll 1$, we can simplify the remaining multipole terms by using the limiting behaviour of the modified Bessel functions $K_m(x)$ for $x \ll 1$ [147]:

$$K_m(x) \approx \frac{(m-1)!}{2} \left(\frac{2}{x}\right)^m \quad (x \ll 1, m = 1, 2, 3, \dots) \quad (3.19)$$

to obtain:

$$h(r, \phi) = \sum_{m=1}^{\infty} \alpha_m \left(\frac{1}{r}\right)^m \cos(m\phi - B_m), \quad (3.20)$$

where α_m denotes the combination of a_m with the additional constants from the approximation. This is the same set of solutions we would have obtained if we had approximated $h/\ell^2 = 0$ in Eq. 3.12 and solved the resulting Laplace equation $\nabla^2 h = 0$. It is instructive to consider which of these modes are actually relevant for self-assembly. The dipolar mode $m = 1$ is not very common, because any particle adsorbed onto the interface with a dipolar deformation can rotate to eliminate said deformation. They are only found as the dominant mode when the orientation of the particles is pinned by e.g. an external electric or magnetic field or by surface roughness [116]. The quadrupolar mode $m = 2$, however, cannot be eliminated by rotation and is often found as the dominant term in experimental systems [30, 33, 116, 126], though in other cases it is the hexapolar mode $m = 3$ [124, 131]. Interactions between particles adsorbed at the interface now arise because the interfacial deformation can be further minimized by arranging particles such that the positive and negative “poles” of the multipoles are brought together[†]. In general, this is a strong many-body effect. However, especially for dilute systems, one can obtain the qualitative behaviour by considering only pairwise multipole-multipole interactions. A pairwise capillary quadrupole-quadrupole potential was first calculated by Stamou, Duschel and Johannsmann [116] for small particles and negligible gravity, while later Danov et al. calculated the potential for arbitrary multipole-multipole interactions, first in the same limit of small particles and negligible gravity ($r/\ell \gg 1$) [146], and later including the effects of gravity [147]. For two capillary multipoles i, j of order $m_i, m_j \geq 1$, in the limit of negligible gravity and for distances r larger than the particle diameter L ,

[†]In contrast to electromagnetism, like capillary charges do not repel, but attract.

the pair interaction energy u is of the form [146]:

$$u_{m_i, m_j}(r, \phi_i, \phi_j) = -A_{m_i, m_j} \left(\frac{1}{r}\right)^{m_i + m_j} \cos(m_i \phi_i + m_j \phi_j), \quad (3.21)$$

where we have summarized all constants into the term A_{m_i, m_j} because we will be determining this combined constant from our capillary deformation calculations. It has dimensions of [energy]/[distance] $^{m_i + m_j}$ and depends on the multipole orders, the interfacial tension, the height of the capillary deformations around both particles individually and on their size. Note that in Eq. 3.21 the sign of ϕ_j is different than in Refs. [146, 147] — this is merely a different choice of coordinates.

3.3 Results & Discussion

This section is organized as follows. In Section 3.3.1 we use the method for computing capillary deformations described in Section 3.2.2 to calculate the ways in which individual hourglass-shaped particles adsorb onto a fluid-fluid interface. In Section 3.3.2 we investigate the self-assembly of hard hourglass-shaped particles that additionally interact via a capillary multipole-multipole interaction. As we will see, a polar multipole expansion fails to capture the experimentally observed behaviour, and so in Section 3.3.3 we simulate the adsorption of *two* particles onto an interface and discuss possible improvements to the polar multipole description.

3.3.1 Adsorption modes

Using the method described in Section 3.2.2, we calculate the adsorption energy $E(\psi, \varphi)$ as a function of the particle orientation given by the two angles ψ and φ . Because of the hexagonal symmetry around the particle's long axis, we only need to consider $\psi \in [0, \pi/6]$, while its mirror symmetry perpendicular to its long axis allows us to restrict the φ -domain to $\varphi \in [0, \pi/2]$. While the interfacial tension γ of the air-hexane interface is known, the particle-air and particle-hexane interfacial tensions γ_1 and γ_2 are unfortunately not, and hence we do not know the actual contact angle θ of our system. We therefore repeat our simulations for multiple contact angles $\cos \theta \leq 0.6$. Simulating smaller contact angles (higher $\cos \theta$) is difficult, as our current method runs into numerical issues when we approach the regime of complete wetting $\cos \theta \rightarrow 1$.

In Fig. 3.9 we show the adsorption energy $E(\psi, \varphi)$ and the (meta)stable adsorption configurations for the particle shape of Fig. 3.5 for contact angles $\cos \theta = 0, 0.2, 0.4$ and 0.6 . We express the adsorption energy in units of the thermal energy $k_B T_r$ at room temperature $T_r = 293$ K. From these figures it can be seen that there are three possible configurations for a particle to adsorb at the interface: *vertically*, largely immersed in hexane with its long axis perpendicular to the interface; *horizontally*, mostly in hexane but with its long axis in the same plane as the interface, and *tilted*, with its long axis making an angle of around 63° with the plane of the interface. Each adsorption configuration deforms the interface in its own way: the vertical mode does not deform the interface at all apart from the negligible monopolar deformation, while the horizontal and tilted

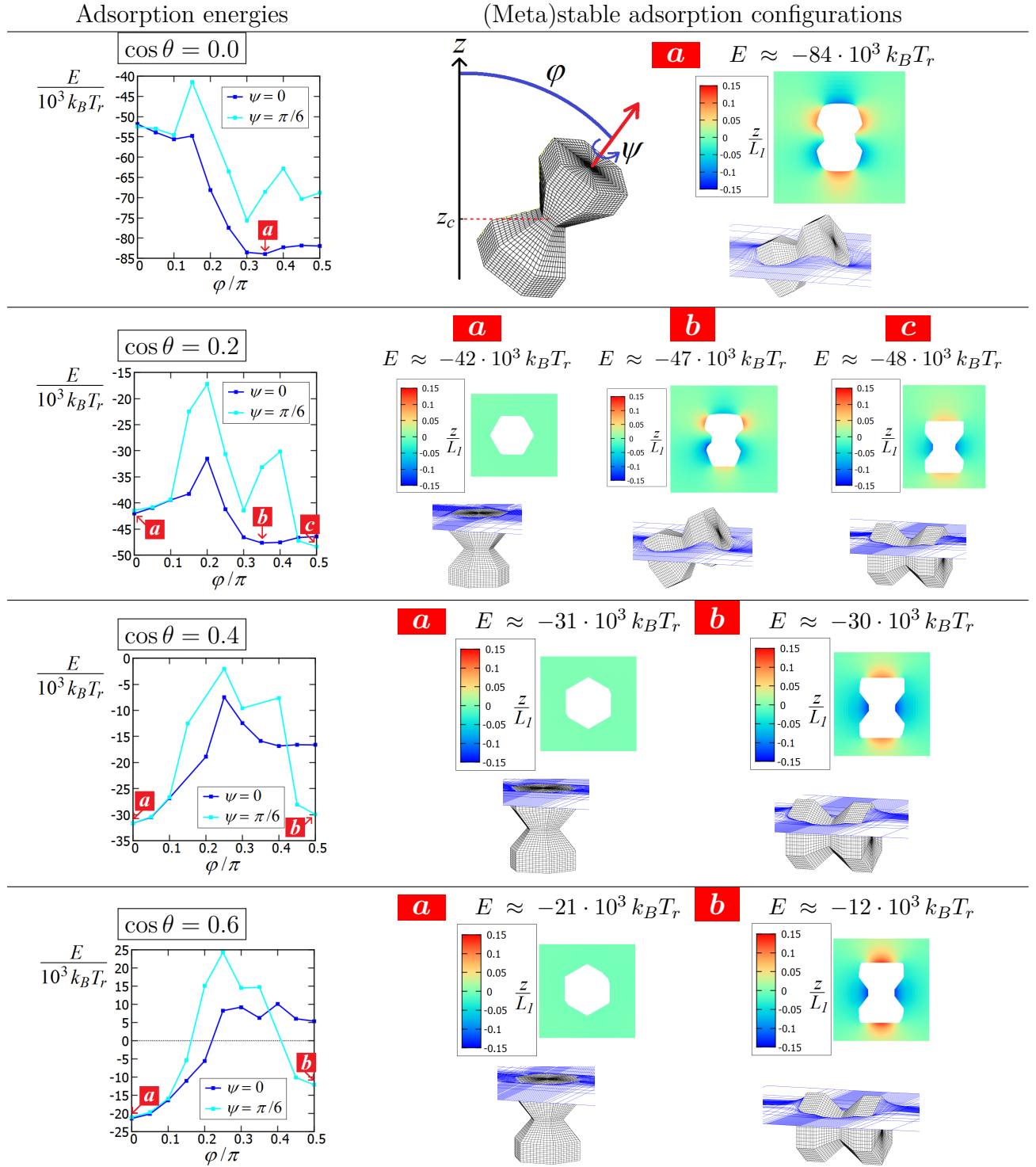


Figure 3.9: (Left:) Adsorption energies E (Eq. 3.7) in terms of the thermal energy at room temperature $k_B T_r$ as a function of the angles φ and ψ (top middle), for contact angles $\cos \theta = 0, 0.2, 0.4$ and 0.6 , corresponding to interfacial tensions $\gamma_1 = \gamma_2 + 0$ N/m, 0.0036 N/m, 0.0072 N/m and 0.0108 N/m, respectively. The energy $E = 0$ corresponds to the particle desorbed from the interface and completely immersed in hexane. (Right:) predicted (meta)stable particle orientations and the adsorption energies and capillary deformation fields. In the contour plot, the plane $z = 0$ corresponds to the air-hexane interface level far away from the particle.

modes deform the interface with an approximately quadrupolar and hexapolar profile, respectively. The relative stability of these modes depends strongly on the contact angle, and only rather weakly on the specific hourglass shape. The tilted mode is preferred when the waist is thick and the contact angle is high i.e. $\cos\theta < 0.2$, such that there is little preference for one of the two fluid phases and the problem essentially reduces to finding the maximum area of the fluid-fluid interface that can be excluded. On the other end, the vertical mode is preferred when there is a strong preference for either hexane i.e. for $\cos\theta \geq 0.6$, since there is a large energy cost when exposing the particle surface to air. In between, for $0.2 \leq \cos\theta \leq 0.6$, we find the horizontal mode, which provides a balance between the two. Importantly, the vertical and horizontal configurations are always separated by a large energy barrier on the order of $10^4 k_B T$. Due to this large barrier, thermal fluctuations will be unable to change the orientation of the particles once they settle into either of these two (meta-)stable configurations. This may explain why we see particles in both the horizontal and the vertical configuration in the TEM images of Figs. 3.2 and 3.3. We note, however, that we would not be able to see the tilted configuration in the TEM images, as they are of a fully dried system on a solid substrate, and without a fluid-fluid interface to support the particles they would simply fall into the horizontal orientation. However, we could still find evidence of the tilted configuration in the structure of self-assembled aggregates, especially since its capillary interaction is different from the horizontal adsorption configuration due to its hexapolar capillary deformation. Regardless, there are two reasons to believe we are in the low contact angle (high $\cos\theta$) regime, where the tilted mode is unstable: i) all EM images show particles in both the vertical and horizontal orientations; ii) string-like assemblies such as those seen in Fig. 3.3 cannot be formed by the tilted configuration as they would be energetically unfavorable.

We now perform simulations on the self-assembly of hourglass-shaped particles. We assume that we are in the low contact angle regime such that there is a mixture of horizontally and vertically adsorbed particles at the interface. For simplicity we assume a 50/50 mixture of both orientations. Starting with a dilute system, the system will increase in density as the hexane evaporates, thereby driving the particles together. We simulate this process by performing a Monte Carlo simulation of hard hourglass-shaped particles in both (meta-)stable orientations in an isobaric (NpT) ensemble in which the pressure is incrementally increased. Fig. 3.10 shows two representative snapshots of such a simulation for $N = 800$ hourglass particles following a compression from $\beta p W_1^2 = 2$ to $\beta p W_1^2 = 20$ over $4 \cdot 10^6$ MC cycles – a relatively rapid compression. At low density (reduced density $\rho^* = N W_1^2 / A = 0.41$) the system forms a disordered, mixed fluid phase. At higher density ($\rho^* = 0.63$) We observe the formation of locally ordered structures, but find no large-scale ordering or demixing. Most notable is the presence of dense-packed domains of horizontally oriented particles and the absence of large hexagonally ordered domains of vertically oriented particles. At no stage do we observe string-like assemblies. On the whole, the structure we find is quite different from what we observe experimentally. This should come as no surprise: we have not added any capillary interactions yet, despite knowing that they play a major role in the self-assembly. We therefore turn to including those interactions now.

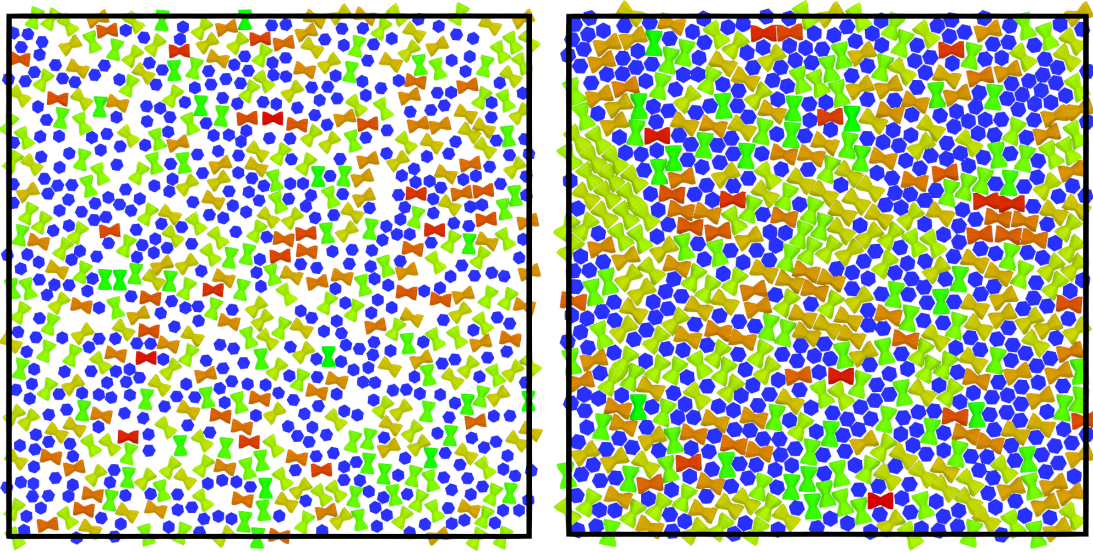


Figure 3.10: A system of $N = 800$ hourglass particles without capillary interactions as obtained from simulations in which the pressure is increased from $\beta p W_1^2 = 2$ to $\beta p W_1^2 = 20$ over $4 \cdot 10^6$ MC cycles. Left: at $\beta p W_1^2 = 2.6$ and $N W_1^2 / A = 0.41$. Right: $\beta p W_1^2 = 20$ and $N W_1^2 / A = 0.63$. The colour indicates the particle orientation. Locally ordered structures form, but there is no demixing or long-ranged order.

3.3.2 Capillary pair interactions

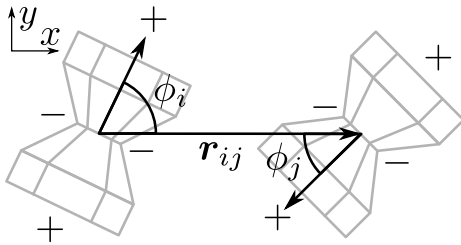


Figure 3.11: Schematic of coordinates for the capillary quadrupole-quadrupole interaction of two horizontally oriented hourglass particles.

Capturing the full capillary interaction in a many-particle simulation is not feasible due to its many-body character. However, it is possible to capture the qualitative behaviour by considering a simplified pairwise interaction between particles based on the dominant multipole mode of their interfacial deformation. As noted in Section 3.1, our hourglass particles are in the size regime where gravitational effects are negligible. In that case, the potential energy u of the quadrupole-quadrupole interaction between two particles i and j is of the form [116, 146, 147]:

$$u(D_{ij}, \phi_{ij}) = \epsilon \cos[2\phi_{ij}] / D_{ij}^4, \quad (3.22)$$

where $D_{ij} = |\mathbf{r}_{ij}| = |\mathbf{r}_j - \mathbf{r}_i|$ is the center-of-mass distance between the particles and $\phi_{ij} = \phi_i + \phi_j$ is the sum of the angles of the quadrupole moments relative to the center-of-mass vector \mathbf{r}_{ij} , shown schematically in Fig. 3.11. The constant ϵ sets the energy scale and depends on the height of the interfacial deformation induced by the particles, as well as on their size.

We now repeat the self-assembly simulations from Fig. 3.10, but additionally let horizontally aligned particles interact with the quadrupole-quadrupole potential given by Eq. 3.22. We again initialize the system at a low density in a roughly 50/50 mixture of

horizontal and vertical orientations, and compress by increasing the pressure. Figure 3.12 shows the trajectory of such a simulation where horizontally oriented particles interact with the quadrupole-quadrupole potential of Eq. 3.22 with $\epsilon = 20 k_B T W_1^4$. This leads to a fairly strong interaction when compared to the thermal energy: two particles that touch side-by-side (i.e. $D = W_1$, $\phi_{ij} = \pi$) are bonded with an energy of $20 k_B T$, and end-to-end ($D = L_1$, $\phi_{ij} = 0$) with roughly $11 k_B T$. We compressed the system from $\beta p W_1^2 = 2$ to $\beta p W_1^2 = 20$ over $4 \cdot 10^6$ MC cycles to show the behaviour at both low and high densities. Again, this constitutes a fairly rapid compression. At low densities, the strong quadrupole-quadrupole interactions cause the formation of string-like assemblies whereby horizontally oriented particles attach side-by-side. Over time, these strings assemble into 2D sheets and the hourglasses with different adsorption configurations demix. Given enough time, the system will evolve towards two phase-separated domains of horizontally and vertically aligned particles.

Although this quadrupole-quadrupole interaction captures part of the experimentally observed behaviour, such as the formation of string-like assemblies at low density, there are significant discrepancies: 2D ordered sheets of horizontal particles are not observed in the experiments, and experimentally strings of particles are arranged end-to-end rather than side-by-side. It appears that Eq. 3.22 fails to capture an anisotropy of the quadrupolar deformation field that is crucial to the self-assembly. We investigate this discrepancy in the next section, where we simulate the capillary deformation due to *two* horizontally adsorbed particles to determine the pair interaction in detail.

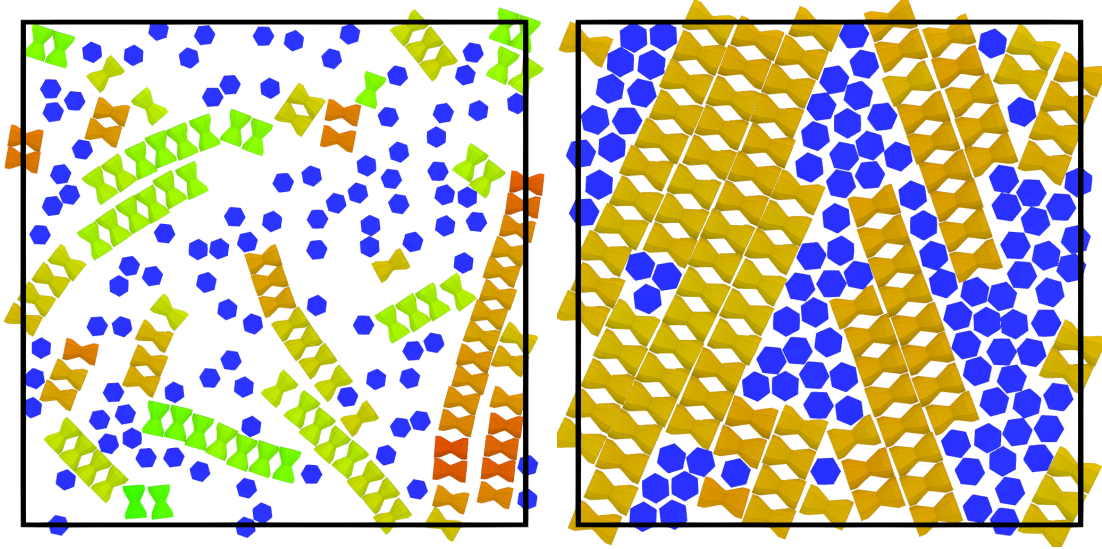


Figure 3.12: A system of $N = 200$ hourglass particles as obtained from simulations in which the pressure is increased from $\beta p W_1^2 = 2$ to $\beta p W_1^2 = 20$ over $4 \cdot 10^6$ MC cycles. The horizontally aligned particles interact with a quadrupole-quadrupole pair interaction (Eq. 3.22) with $\epsilon = 20 k_B T W_1^4$ in addition to their hard shape. The colour indicates the particle orientation. (Left:) at low density ($\rho^* = 0.28$) horizontally adsorbed particles form strings. (Right:) at high density ($N W_1^2 / A = 0.56$) the horizontal and vertical orientations have demixed.

3.3.3 Elongation of the quadrupolar mode

The method that we used in Section 3.3.1 to determine the capillary deformation field $h(r, \phi)$ and adsorption energy of the particles can also be applied to multiple particles. We determine the total adsorption energy E of two adsorbed particles as a function of the interparticle distance D , and use this to determine the effective pair potential $u(D)$ between them. We consider two cases: two particles aligned end-to-end, and two particles aligned side-by-side. We show the results in the plots shown in the bottom left of Figs. 3.13 and 3.14. The contour plots show the associated height profiles of the interface, similar to Fig. 3.9. By fitting the expected quadrupole-quadrupole form of Eq. 3.22 to the end-to-end and side-by-side energy profiles $E(D)$ separately we obtain the constants $\epsilon_{side-side} = -0.274 k_B T_r \mu m^4$ and $\epsilon_{end-end} = -2.464 k_B T_r \mu m^4$. Note that numerical quality of the side-by-side energy profile $E(D)$ is lower due to the smaller energy scale of this interaction. In contrast to the quadrupole-quadrupole interaction of Eq. 3.22, the end-to-end interaction is roughly a factor of 9 stronger than the side-by-side interaction. There are a number of ways to include this additional anisotropy. We could compute and tabulate the pair interaction energy $E(D, \phi)$ for the range of distances D and relative angles ϕ that we wish to consider in the many-particle simulations. However, while efficient for use in the many-particle simulations, this would require a significant number of capillary deformation calculations, and the resulting tabulated potential would only be applicable for one specific particle shape and contact angle θ . Another way forward might be to include higher-order multipole moments in our description of the deformation field. Including an octupolar deformation, for instance, could cause the end-to-end interaction to become stronger than the side-by-side one, as shown for spheres [145]. However, deriving the resulting pair interaction may be a challenging endeavour, especially if the quadrupole and octupole modes cannot be decoupled. Furthermore, the resulting expression may not be cheap to evaluate computationally. A third way may be to consider a different type of quadrupole that better fits the elongated particle shape. Literature on the capillary deformations of rodlike particles [30, 33, 122, 124, 126] has reported some success in describing the height profile and pair interactions by considering not a polar quadrupole, but instead an elliptical quadrupole i.e. one where the distance between the “+” charges is not the same as that between the “−” ones [31, 33, 122]. Unfortunately, no closed-form expression for the pair interaction energy was given, nor is it clear *a priori* whether an ellipsoidal quadrupole could capture the full anisotropy of the hourglass shape and correctly describe the near-field capillary interactions.

For an accurate approximation of the capillary interactions one should consider the methods above. However, a cruder approximation may already suffice to explore the effect of a stronger end-to-end interaction. Let us consider a minimum modification to the quadrupole-quadrupole interaction Eq. 3.22 that would include the asymmetry by introducing an angle dependence to the amplitude constant ϵ such that it captures correctly the ratio of end-to-end and side-by-side amplitudes:

$$u_2(D, \phi_i, \phi_j) = \epsilon_2(\phi_i, \phi_j) \cos[2(\phi_i + \phi_j)] / D^4. \quad (3.23)$$

This function $\epsilon_2(\phi_i, \phi_j)$ modifies the pair interaction in such a way that the correct ratio of energies of the end-to-end and side-by-side configurations is obtained. To obtain a proper form for this function, we must make sure to retain the proper symmetries:

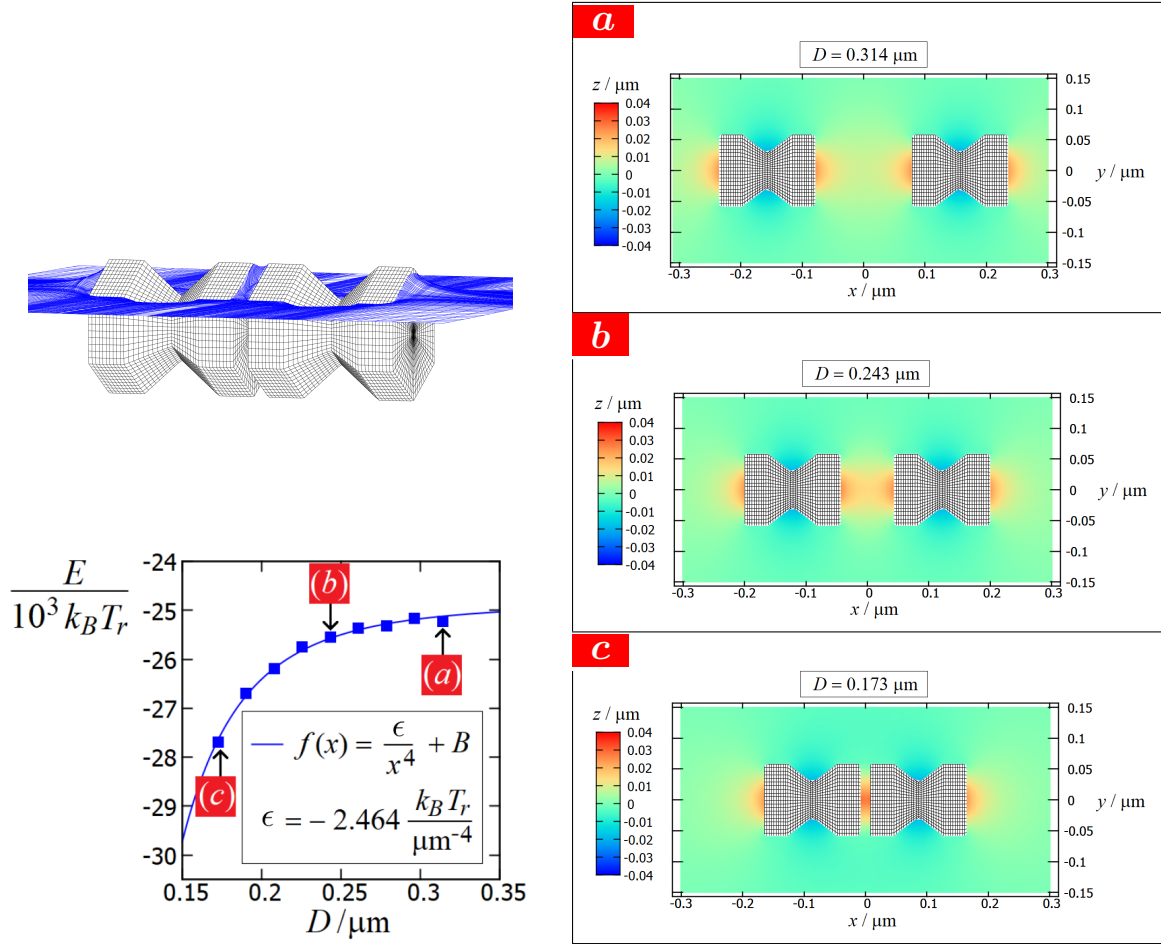


Figure 3.13: Total adsorption energy E of two horizontally adsorbed hourglass particles (shape 0, Fig. 3.6a) in the end-to-end configuration, as a function of their center-of-mass distance D and for a contact angle of $\cos \theta = 0.6$. The energy level $E = 0$ corresponds to both particles fully immersed in hexane, and $z = 0$ to the height of the interface far away from the particle. The blue points are values computed with the numerical method described in Section 3.2.2, while the blue line shows a fit to the theoretically expected quadrupole-quadrupole interaction Eq. 3.22. The contour plots on the right as well as the 3D view show the corresponding height profiles of the interface at points (a), (b) and (c).

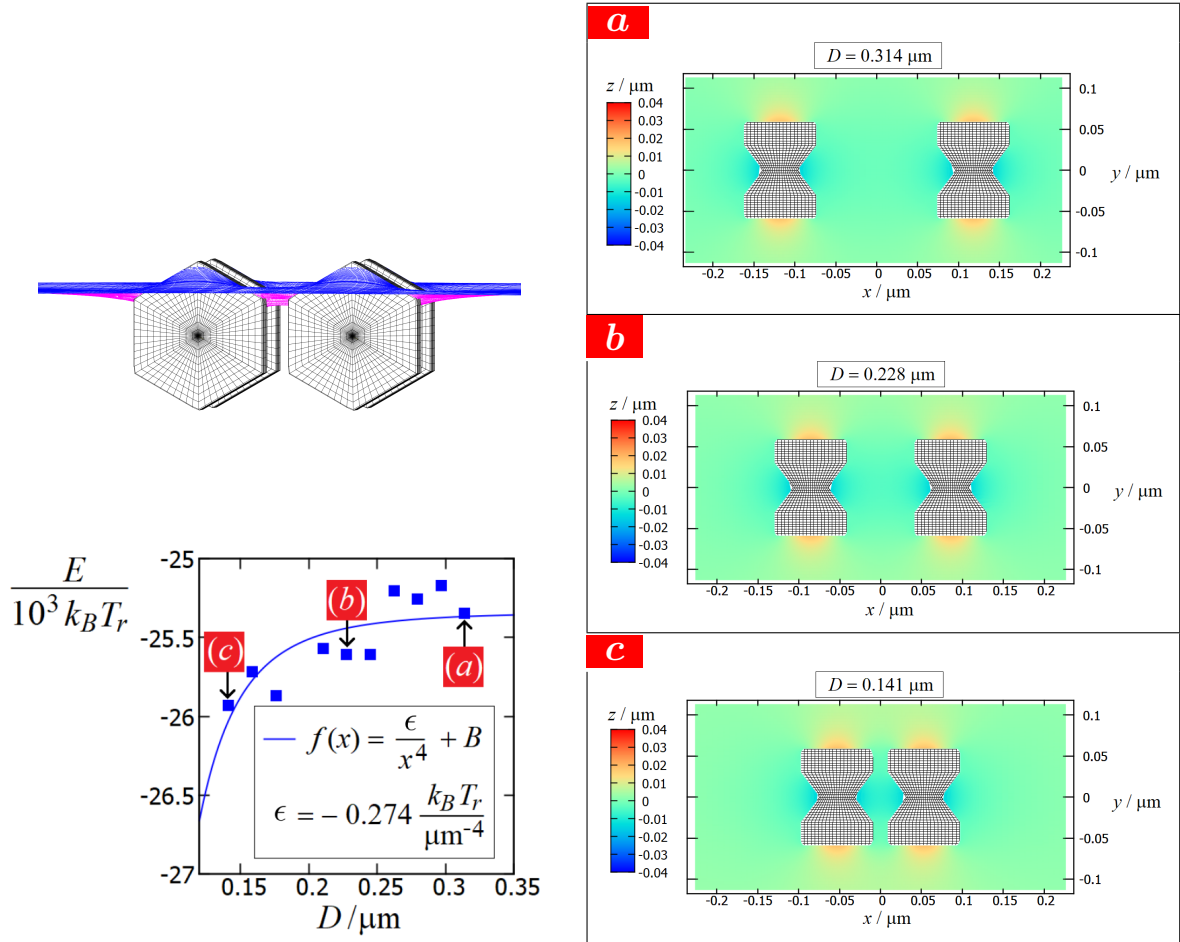


Figure 3.14: Total adsorption energy E of two horizontally adsorbed hourglass particles (shape 0, Fig. 3.6a) in the side-by-side configuration, as a function of their center-of-mass distance D and for a contact angle of $\cos \theta = 0.6$. The energy level $E = 0$ corresponds to both particles fully immersed in hexane, and $z = 0$ to the height of the interface far away from the particle. The blue points are values computed with the numerical method described in 3.2.2, while the blue line shows a fit to the theoretically expected quadrupole-quadrupole interaction Eq. 3.22. Note the smaller energy scale and the comparatively larger numerical noise when compared to the end-to-end configuration in Fig. 3.13. The contour plots on the right as well as the 3D view show the corresponding height profiles of the interface at points (a), (b) and (c).

- Rotating our particles in-plane by π results in the same configuration:

$$\begin{aligned} u_2(D, \phi_i, \phi_j) &= u_2(D, \phi_i + n\pi, \phi_j + m\pi) \quad \forall n, m \in \mathbb{Z} \\ \Rightarrow \epsilon_2(\phi_i, \phi_j) &= \epsilon_2(\phi_i + n\pi, \phi_j + m\pi) \quad \forall n, m \in \mathbb{Z}. \end{aligned} \quad (3.24)$$

- The two particles are identical, so exchanging them may not change the energy:

$$u_2(D, \phi_i, \phi_j) = u_2(D, \phi_j, \phi_i) \Rightarrow \epsilon_2(\phi_i, \phi_j) = \epsilon_2(\phi_j, \phi_i). \quad (3.25)$$

- $\epsilon_2(\phi_i, \phi_j)$ must provide the correct ratio between the side-by-side and end-to-end configurations such that:

$$\frac{\epsilon_2(0, 0)}{\epsilon_2(\pi/2, \pi/2)} = \frac{\epsilon_{end-end}}{\epsilon_{side-side}}. \quad (3.26)$$

Equation 3.25 is satisfied[‡] if we choose

$$\epsilon_2(\phi_i, \phi_j) = \epsilon_c f(\phi_i) f(\phi_j), \quad (3.27)$$

as long as $f(\phi) = f(\phi + n\pi) \quad \forall n \in \mathbb{Z}$, per Eq. 3.24. One such function is $f(\phi) = c + \cos[2\phi]$, with which Eq. 3.26 is solved for the two solutions

$$\frac{(c+1)^2}{(c-1)^2} = \frac{\epsilon_{end-end}}{\epsilon_{side-side}} = \frac{2.464 k_B T_r \mu m}{0.274 k_B T_r \mu m} \Rightarrow c \approx 2 \text{ or } c \approx 1/2. \quad (3.28)$$

Our approximated capillary pair interaction thus becomes:

$$u_2(D, \phi_i, \phi_j) = \frac{\epsilon_c}{D^4} (c + \cos[2\phi_i]) (c + \cos[2\phi_j]) \cos[2(\phi_i + \phi_j)], \quad (3.29)$$

for either $c \approx 2$ or $c \approx 1/2$. Filling in the condition for the magnitude of the energy scale yields the two energy constants ϵ_c :

$$u_2(D, 0, 0) = \frac{\epsilon_{c=2}}{D^4} (2 + \cos 0)^2 = \frac{\epsilon_{end-end}}{D^4} \Rightarrow \epsilon_{c=2} = \frac{1}{9} \epsilon_{end-end} \quad (3.30)$$

$$u_2(D, 0, 0) = \frac{\epsilon_{c=1/2}}{D^4} (1/2 + \cos 0)^2 = \frac{\epsilon_{end-end}}{D^4} \Rightarrow \epsilon_{c=1/2} = \frac{4}{9} \epsilon_{end-end} \quad (3.31)$$

We show contour plots of the angular dependence of this new pair potential with in Fig. 3.15 (b) and (c) for $c = 2$ and $c = 1/2$, respectively, as well as that of the quadrupole-quadrupole pair potential Eq. 3.22 in (a). Since the angular dependence can be decoupled from the distance dependence, we express the energy in arbitrary units. We show the corresponding particle orientations for clarity. The behaviour of the two solutions with $c = 2$ and $c = 1/2$ is qualitatively different. For $c = 2$, the side-by-side configuration is a saddle point and thus unstable, while for $c = 1/2$ it is a local minimum, which, while

[‡]The functions $\epsilon_2(\phi_i, \phi_j) = \epsilon_c (c + \cos[2(\phi_i \pm \phi_j)])$ also qualify, but they cannot fulfill the ratio requirement of Eq. 3.26.

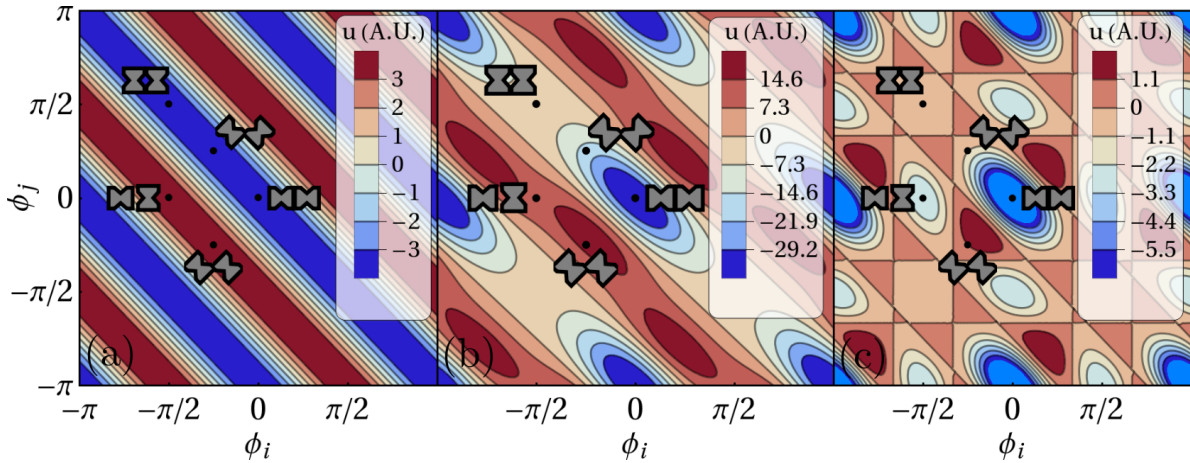


Figure 3.15: Contour plots of the pair interaction energies u as a function of the particle angles ϕ_i and ϕ_j , for (a) the quadrupole-quadrupole pair potential Eq. 3.22, (b) the modified pair potential Eq. 3.29 with $c = 2$ and (c) the modified pair potential Eq. 3.29 with $c = 1/2$. The energy is given in arbitrary units since the angular dependence is the same for all distances. Insets show the corresponding orientations of the two particles.

metastable, may be long-lived due to the large energy scale. Additionally, the end-to-side configuration also becomes a local minimum for $c = 1/2$ (which is deeper than the side-by-side configuration), while it is a saddle point for $c = 2$. It should be stressed at this point that *the modification we make here is very much ad hoc*. It is possible that neither $c = 2$ nor $c = 1/2$ case are good approximations of the angular energy landscape. However, the real landscape must still respect the symmetry requirements of Eqs. 3.24 and 3.25 as well as break the end-to-end / side-by-side symmetry by virtue of Eq. 3.26, and so we expect the real landscape to have similar properties to our ad hoc modification.

Another way to represent the modification of the pair potential is to fix the in-plane orientation of the particles and vary their relative positions. Let us fix the position of particle i at the origin and fix the long axes of particles i and j to be parallel. Note that this does *not* imply that $\phi_i = \phi_j$, as these angles are defined with respect to the center-of-mass vector \mathbf{r}_{ij} . In Fig. 3.16 we show the pair interaction energy as a function of the position (x, y) of the second particle for (a) the original quadrupole-quadrupole expression (Eq. 3.22) and (b,c) our modified one (Eq. 3.29) with $c = 2$ and (c) $c = 1/2$, respectively. In this representation it is clear that our modification constitutes an amplification of the end-to-end stacking energy while retaining the overall symmetry. Fig. 3.16 also shows a second particle in the position corresponding to the densest packing, with its center of mass indicated by the black dot. This packing is energetically unfavorable, regardless of our modification. This suggests that the densest packing cannot be formed while capillary interactions dominate the self-assembly. However, we are making the assumption here that our pair potential is representative for the interactions at very close distances. This is a dangerous assumption: it is likely that higher-order multipole terms play a role at these shorter distances.

To check whether the dense packing is indeed unfavorable, we also calculate the capillary deformation for a configuration close to dense packing. Fig. 3.17 shows the height

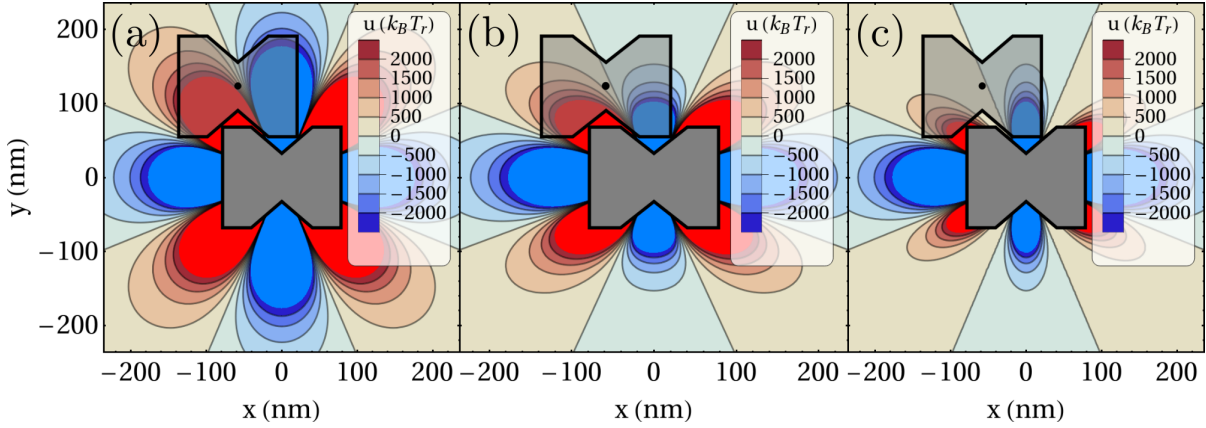


Figure 3.16: Contour plots of the pair interaction energies u as a function of the relative position for (a) the quadrupole-quadrupole pair potential Eq. 3.22 with $\epsilon = \epsilon_{\text{end-end}} = -2.464 \cdot 10^{12} k_B T_r \mu\text{m}^4$, and (b) the modified pair potential Eq. 3.29 with $c = 2$, $\epsilon_{c=2} = (1/9)\epsilon_{\text{end-end}}$ and (c) the modified pair potential Eq. 3.29 with $c = 1/2$, $\epsilon_{c=1/2} = (4/9)\epsilon_{\text{end-end}}$. Additionally, a second particle is shown in the position corresponding to the densest packing. Regardless of the exact pair potential, this dense packing is energetically unfavorable.

profile $z(x, y)$ of the interface deformed by the adsorption of two horizontally aligned hourglass particles in the dense packing configuration. The total adsorption energy $E = -24 \cdot 10^3 k_B T_r$ is roughly $10^3 k_B T_r$ higher than the energy of the two adsorbed particles at infinite separation such that $u \sim +10^3 k_B T_r$, confirming that the dense configuration is unfavorable even when taking into account the full deformation of the interface.

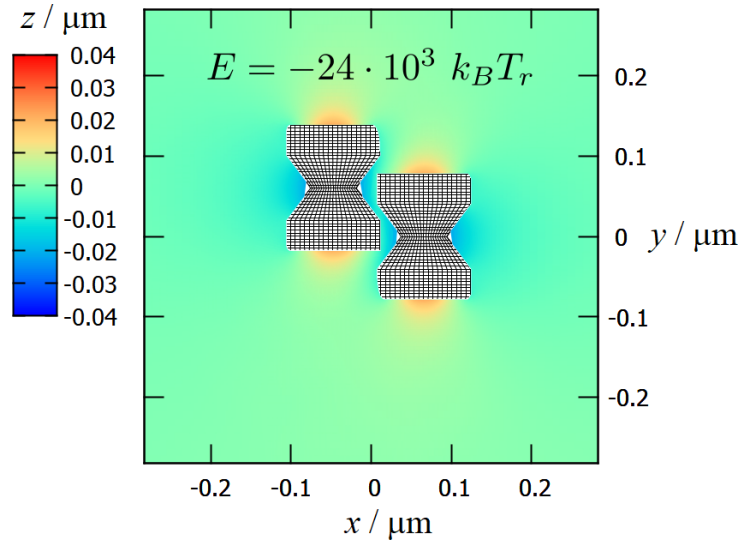


Figure 3.17: Height profile $z(x, y)$ of the interface and associated total adsorption energy E for two horizontally aligned hourglass particles in the dense packing configuration.

Let us now investigate what effect the modification of the quadrupole-quadrupole interaction has on the self-assembly. We follow again a similar procedure in which we prepare

3 a system of hourglass particles at low density in a roughly 50/50 mixture of horizontal and vertical orientations, and compress it by increasing the pressure. Figs. 3.18(a,b) and 3.19(a,b) show representative snapshots for these simulations where we increase the pressure from a low value of $\beta p W_1^2 = 0.01$ to a high value of $\beta p W_1^2 = 40$. In Fig. 3.18 horizontally adsorbed particles interact with the modified quadrupole-quadrupole interaction of Eq. 3.29 with $c = 1/2$ and $\epsilon_{c=1/2} = -20k_B T_r W_1^4 = -0.00685 k_B T_r \mu m^4$ and in Fig. 3.19 with $c = 2$ and $\epsilon_{c=2} = -5k_B T_r W_1^4 = -0.0017125 k_B T_r \mu m^4$. Note that we do not use the full value of $\epsilon_{end-end}/9 = -2.464 k_B T_r \mu m^4$, as this leads to extremely strong capillary interactions on the order of $10^3 k_B T_r$, and local Monte Carlo sampling becomes prohibitively inefficient for potentials with wells deeper than several tens of $k_B T$. Instead, we choose values of ϵ_c as high as possible while still retaining adequate sampling. For $c = 1/2$ in Fig. 3.18(b) we can see that the strings combine into sheets of horizontally adsorbed particles, causing them to demix from the vertically adsorbed ones. For $c = 2$ in Fig. 3.19(b) we do not see any sheet formation. This is probably because the side-by-side configuration is unstable for $c = 2$, while it is metastable for $c = 1/2$. Finally, at $\beta p W_1^2 = 40$ we disable the capillary interactions and further increase the pressure to $\beta p W_1^2 = 60$ to mimic what happens when there is no longer sufficient hexane to maintain the air/hexane interface. These results are shown in Figs. 3.18(c) and 3.19(c). In reality two things will take place: capillary bridging of hexane will occur between nearby particles, pulling them together, and particles will adsorb onto the interface between air and the support fluid (diethylene glycol) instead. It should be noted that the final configurations shown in Figs. 3.18(c) and 3.19(c) are quite different: the formation of a string network appears to trap vertically adsorbed particles, limiting the demixing and thereby the domain size of aggregates of horizontally and vertically adsorbed particles. This suggests that the self-assembly depends quite sensitively on the exact shape of the angular energy landscapes such as those shown in Fig. 3.15. Again: because capillary interactions are many times the thermal energy, seemingly shallow local minima can be long-lived and of significant influence. To achieve better control over the self-assembly, these pair interactions must be established in greater detail. It may be possible to tune this landscape via a judicious choice of particle shape and contact angle. It may also be necessary to consider the three-body interactions similar to what was done for spheres in Ref. [145], especially when one considers the formation of sheets from strings.

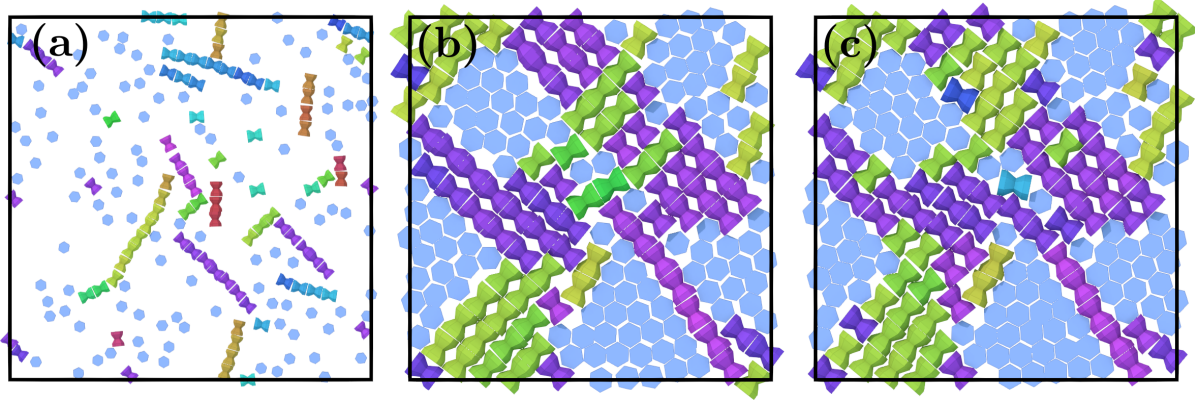


Figure 3.18: Typical simulation configuration of a system of $N = 200$ hourglass particles following an isotropic pressure annealing. Horizontally aligned particles interact with a modified quadrupole-quadrupole pair interaction (Eq. 3.29, with $c = 1/2$ and $\epsilon_{c=1/2} = -20k_B T_r W_1^4 = -0.00685 k_B T_r \mu m^4$) in addition to their hard shape. Colors represent the particle orientation. (a) At low density, particles form end-to-end aligned strings. (b) upon sufficient compression the strings combine into sheets, but the dense packing is inhibited by the capillary interactions. (c) upon turning off capillary interactions, the system further compresses and particles enter their densest packings.

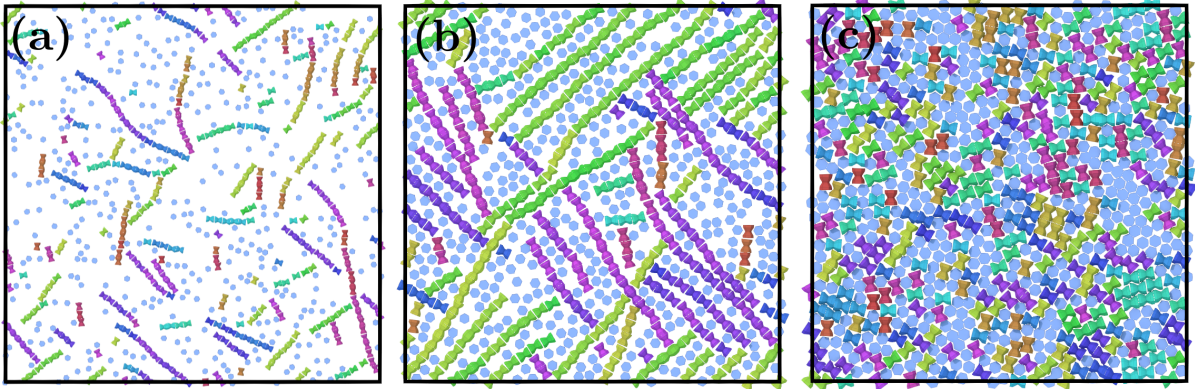


Figure 3.19: Typical simulation configuration of a system of $N = 800$ hourglass particles following an isotropic pressure annealing. Horizontally aligned particles interact with a modified quadrupole-quadrupole pair interaction (Eq. 3.29, with $c = 2$ and $\epsilon_{c=2} = -5k_B T_r W_1^4 = -0.0017125 k_B T_r \mu m^4$) in addition to their hard shape. Colors represent the particle orientation. (a) At low density, particles form end-to-end aligned strings. (b) at higher densities, a network of strings forms. (c) upon turning off capillary interactions, the system further compresses and particles enter their densest packings.

3.4 Conclusions

In this chapter we investigated the self-assembly of hourglass-shaped nanoparticles at an air-hexane interface. For parameters similar to those of the experimental system described in Section 3.1 i.e. particles of roughly 200 nm in size, we found that the self-assembly is dominated by capillary interactions many thousands of times larger than the thermal energy. There are three (meta)stable orientations for particles to adsorb onto the interface: horizontal, with their long axis in the interfacial plane; vertical, with their long axis perpendicular to the plane, and tilted, with the long axis at an angle of around 63° with respect to the plane. Which of these adsorption configurations are preferred depends on the (unknown) contact angle θ of the air/hexane/particle system, with our best estimates suggesting this contact angle is small i.e. $\cos \theta \geq 0.6$. In this regime, the two (meta)stable orientations are the vertical and horizontal ones. For vertically adsorbed particles, there are no capillary pair interactions and the self-assembly leads to close-packed 2D hexagonal domains. For horizontally adsorbed particles, there is a quadrupole-quadrupole capillary pair interaction that causes particles to form end-to-end attached strings. A polar quadrupole (i.e. where the charges are distributed at equal distances) is not sufficient to describe this behaviour and leads to side-by-side attached strings. We recover the preference for end-to-end attachment by modifying the quadrupole-quadrupole pair potential, taking care to retain the underlying (a)symmetries. We argue that the size of structurally ordered domains resulting from the self-assembly is limited by two effects. First, the dense packing of horizontally adsorbed particles is energetically unfavorable due to the capillary interactions. Second, depending on the exact form of the capillary pair interaction, 1D strings may be favored over 2D sheets, as is the case for Eq. 3.29 with $c = 2$. The relative preference of 1D strings versus 2D sheets also affects the demixing of horizontally and vertically aligned particles. If strings are favored over sheets, a network of strings is formed which arrests the demixing, limiting the domain size via a caging effect.

Our results extend the knowledge of self-assembly at fluid-fluid interfaces that has been established for spheres [116, 145, 146], rods [30, 31, 33, 122, 124, 126, 149] and to some extent, cubes [32, 128, 129, 131] by considering a more anisotropic, non-convex particle shape. We establish many similarities to the self-assembly of spheres and rods and cubes, but also a number of differences. As is the case for spheres, rods and cubes, the decomposition of capillary deformations into multipole modes is highly effective. Similar to rods, however, the use of “simple” polar multipoles is insufficient to describe the capillary deformations and interactions, as it fails to capture the stretching of the deformation field caused by the elongated particle shape. In contrast to spheres and rods, but similar to cubes [129], (meta)stable configurations play a crucial role in the self-assembly. Both in the experiments and in our simulations we find particles adsorbed in both the vertical and horizontal adsorption modes, with substantially different capillary interactions.

How do we proceed from here? Can we, given the tools available, predict the self-assembly of any arbitrary particle adsorbing onto a fluid-fluid interface? Almost. On the computational side, current methods can predict the adsorption of non-convex and patterned particles (present work and Ref. [129]) and can be used to compute the associated two-, three- and many-body interactions. The theoretical frameworks developed over the

last two decades [146, 147] provide a means to accurately capture the two-body interactions by (possibly elliptical) multipole-multipole interactions. There are still some open questions, however. A systematic investigation into the three- and four-body effect has to our knowledge only been done for spheres [145], where it was revealed to be significant. Whether the same holds for other systems is unknown. Describing the three- and four-body interactions analytically is likely to be challenging: to our knowledge, no analytical expression for three-body capillary multipole interactions has been derived. The present work and recent studies on colloidal rods [30, 31, 33, 122, 124, 126, 149] suggests that an elliptical multipole expansion may be superior in describing the capillary deformations of elongated particles. However, analytical expressions for the elliptical multipole-multipole pair interactions have not yet been derived. This may be a fruitful avenue to pursue.

The sheer strength of capillary interactions for nano- and colloidal-scale particles makes it a powerful tool for directed self-assembly, but it also makes the self-assembly susceptible to local minima in adsorption and pair interaction energies. Meanwhile, the strong many-body nature of capillary interactions complicates a simple description. However, it does not prohibit it. The tools discussed in this chapter offer a very promising means of characterizing the capillary interactions and self-assembly of anisotropic particles at fluid-fluid interfaces, while accurate theoretical descriptions are just a few improvements away. Tailored capillary interactions are a significantly underused tool to guide the self-assembly of nano- and microscale particles given the large number of synthesis procedures in which capillary interactions are used. We suspect that in the next few years, a far greater control over the self-assembly of particles at fluid-fluid interfaces can be established than what was previously possible.

3.5 Acknowledgements

I would like to thank Stan Najm for initiating this fascinating study, and Giuseppe Soligno for performing the capillary deformation calculations that we show in this chapter. Both are also gratefully acknowledged for the numerous interesting discussions we had while figuring out the physics of this system.

Densest packings and bulk phase behaviour of rounded tetrahedra

Using simulations we study the phase behavior of a family of hard spherotetrahedra, a shape that interpolates between tetrahedra and spheres. We identify thirteen close-packed structures, some with packings that are significantly denser than previously reported. Twelve of these are crystals with unit cells of $N = 2$ or $N = 4$ particles, but in the shape-regime of slightly rounded tetrahedra we find that the densest structure is a quasicrystal approximant with a unit cell of $N = 82$ particles. All thirteen structures are also stable below close packing, together with an additional fourteenth plastic crystal phase at the sphere-side of the phase diagram, and upon sufficient dilution to packing fractions below 50-to-60% all structures melt. Interestingly, however, upon compressing the fluid phase self-assembly only takes place spontaneously at the tetrahedron- and the sphere-side of the family but *not* in an intermediate regime of tetrahedra with rounded edges.

4.1 Introduction

Recent advances in colloid synthesis allow for a plethora of shapes for particles in the nanometer-to-micrometer scale [15, 114, 150–154]. These particles have a Brownian character when suspended in a liquid such as water or toluene, which causes self-assembly into a huge variety of ordered structures at sufficiently high concentrations. These self-assembled structures can then form materials with useful optical [155], photonic [156], electronic [157], or catalytic [158] properties. Simulations and experiments on monodisperse systems of sterically stabilised anisotropic particles exhibit a wealth of densest-packed structures far beyond the well-known face-centered-cubic (FCC) crystal phase for spheres and the simple cubic (SC) crystal for cubes [18, 159–163]. The study of such close-packed structures of rigid hard bodies has a long history with relevance far beyond nanoparticle self-assembly; from Kepler’s stacking of cannonballs in 1611 [164] to the packing of sand piles in more recent times [165]. During the past years, various simulation methods have been employed to predict the self-assembled structures and densest packings of hard-particle systems such as tetrahedra [41, 166–169], Platonic solids [41, 159, 167, 169], rounded cubes [170–174], cuboctahedra [18, 161, 162, 175], truncated tetrahedra [176] and even families of shapes without conventional names [167, 169, 177–179].

In this chapter, we will follow a similar path to investigate the phase behaviour of hard spherotetrahedra, a shape that interpolates between tetrahedra and spheres. Our motivation for studying this particular system is twofold. The first is a peculiar finding by Jin. et al. [47], who investigated the dense packings of spherotetrahedra and found their densest packing for a specific range of shapes to be an 82-particle quasicrystal approximant, one which was considered earlier by Haji-Akbari et al. [166, 168] as a candidate for the densest packing of (non-rounded) tetrahedra. This was a remarkable result: the studies of densest packings mentioned earlier all yielded dense packings that were crystals with relatively small unit cells of four particles or fewer. An 82-particle unit cell would be unprecedentedly large. Second is a curious observation made by experimentalists in our group on the self-assembly of such shaped particles: when nanoscale CdSe particles with a spherotetrahedral shape (Fig. 4.1a) are allowed to self-assemble via a droplet evaporation procedure, the result of which can be seen in Fig. 4.1b, the resulting supraparticles (particles of many smaller particles) are crystalline, but their morphology is consistently nonspherical, often elongated and egg-shaped. This is unexpected: we generally expect droplet evaporation self-assembly to yield spherical supraparticles, due to the constituent particles taking on the spherical shape that is preferred by the surface tension of the droplet solvent. The self-assembly of these supraparticles is a complicated process with many components: particle anisotropy, ligand interactions, early-stage evaporation inducing spherical confinement for the self-assembly, and late-stage evaporation causing capillary bridging interactions. To study such a complex process, it makes sense to start as simple as possible. These two results motivate us to investigate the dense packings and general phase behaviour of hard spherotetrahedra in greater detail. As it turns out, the bulk phase behaviour of these particles is already remarkably complex, so much so that we dedicate this entire chapter to describing it in detail, Chapter 5 to find ways to automate and simplify characterizing their phase behaviour, and only come back to the supraparticle self-assembly in Chapter 6. The outline of this chapter is as follows: in

Section 4.2 we describe the necessary theoretical concepts and computational methods required and employed to investigate the phase behaviour of these anisotropic particles. In Section 4.3 we use these methods to predict, identify and characterize the dense packings, first in general and then focusing specifically on the quasicrystal approximant. Section 4.4 then uses the knowledge of these dense packings to investigate the phase behaviour at intermediate densities and to find the bulk solid phases as a function of particle shape and density.

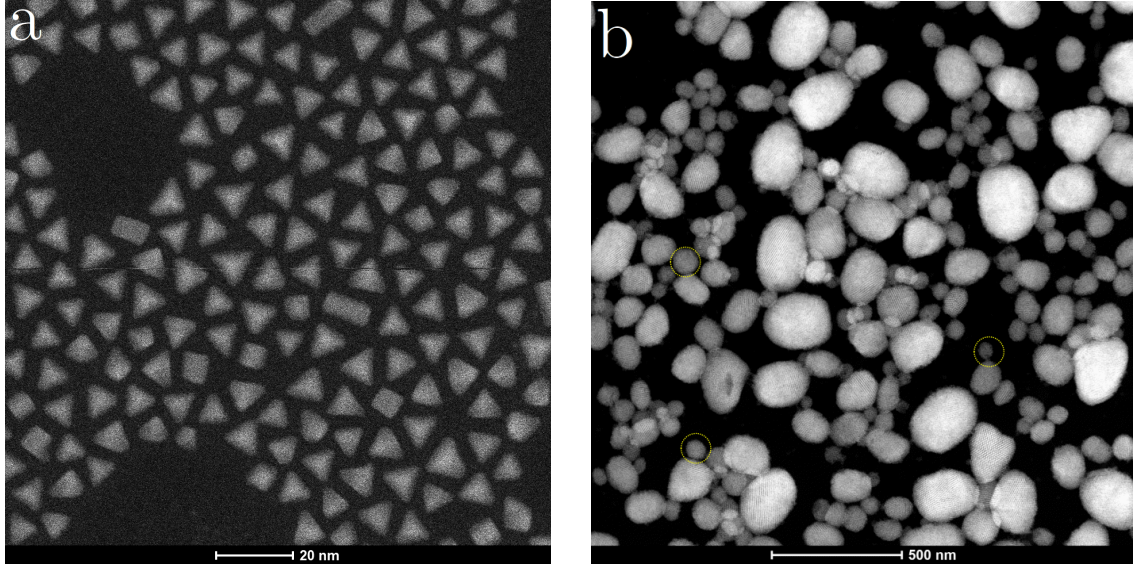


Figure 4.1: a) Scanning Transmission Electron Microscopy (STEM) image of spherotetrahedral CdSe nanoparticles. b) EM image of supraparticles of spherotetrahedral nanoparticles. Most supraparticles show clear crystal planes, but their morphology is egg-shaped, often elongated or at least nonspherical.

4.2 Model & Methods

4.2.1 The spherotetrahedron shape

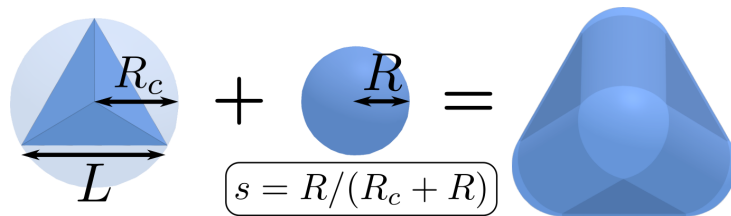


Figure 4.2: A spherotetrahedron is the Minkowski sum of a tetrahedron (edge length L and circumscribed radius $R_c = \sqrt{6}L/4$) and a sphere (radius R). The shape is fully described by the dimensionless shape parameter s .

We define the spherotetrahedron shape in terms of Minkowski sums: a spherotetrahedron is the Minkowski sum of a tetrahedron of edge length L with a sphere of radius

R , both centered around the origin. This is equivalent to the volume within a distance R from a tetrahedron of edge length L . It is fully characterized by a shape parameter $s = R/(R_c + R) \in [0, 1]$, with $R_c = \sqrt{6}L/4$ the radius of the circumscribed sphere around the tetrahedron. The limiting cases describe a tetrahedron ($s = 0$) and a sphere ($s = 1$), so s can also be interpreted as the roundness. For all simulations in this chapter we consider these particles as hard particles, which is to say that the pair interaction energy U between two particles i and j is given by:

$$U(\mathbf{r}_i, \mathbf{\Omega}_i, \mathbf{r}_j, \mathbf{\Omega}_j) = \begin{cases} 0 & \text{if not overlapping} \\ \infty & \text{if overlapping} \end{cases} \quad (4.1)$$

where $\mathbf{r}_{i,j}$ and $\mathbf{\Omega}_{i,j}$ are the particle positions and orientations, respectively. To perform Metropolis Monte Carlo simulations (MC) on these particles, we thus need a method to evaluate whether the shapes associated with the two particles i and j are overlapping. Fortunately, the Minkowski sum definition lends itself well to various collision/overlap detection algorithms currently in use. In our own implementation, we use the Gilbert-Johnson-Keerthi (GJK) algorithm [43]. We will not describe this algorithm in detail in this thesis, as there are many excellent resources freely available due to GJK's popularity as a collision detection algorithm in computer games. We *do* mention two alternative collision detection algorithms for the interested reader: the simpler Separating Axis Theorem (SAT) [42] or the more modern Minkowski Portal Refinement (MPR) [46].

Aside from the overlap condition, there is one more important property of this shape that we will need if we are to investigate the dense packings and their packing efficiency: the volume occupied by the shape. For a tetrahedron, this is quite simple: given its four arbitrary vertices $\mathbf{r}_0, \mathbf{r}_1, \mathbf{r}_2$ and \mathbf{r}_3 , the volume is given by

$$V = \frac{1}{6} \det |\mathbf{r}_1 - \mathbf{r}_0, \mathbf{r}_2 - \mathbf{r}_0, \mathbf{r}_3 - \mathbf{r}_0|, \quad (4.2)$$

i.e. it follows from the determinant of the square matrix with the three edges $\mathbf{r}_{1,2,3} - \mathbf{r}_0$ as its rows. One can also use this expression to calculate the volume of *any* convex polyhedron, by simply building up said polyhedron from smaller tetrahedra, as we describe in Appendix A. To get the volume of the corresponding convex *spheropolyhedron* is a fair bit more involved: one needs to calculate the volume contributions of i) triangular slabs formed by the outwardly moved faces, ii) cylinder segments around all edges and iii) sphere segments around all vertices. We describe an algorithm to calculate these contributions for arbitrary convex spheropolyhedra in Appendix A.

4.2.2 Predicting the densest packings

To determine the densest packings of spherotetrahedra as a function of the shape parameter s , we use the floppy-box Monte Carlo (FBMC) algorithm described in Ref. [169]. In short, this algorithm finds densest packings of hard particles by numerically compressing unit cells of variable shapes with periodic boundary conditions and a small number of particles to increasingly high pressures. The reported densest packings for each particle shape (roundness s) are the result of at least 20 independent compression runs, each of which compressed either an $N = 1, 2, 3$ or 4-particle unit cell from a dimensionless

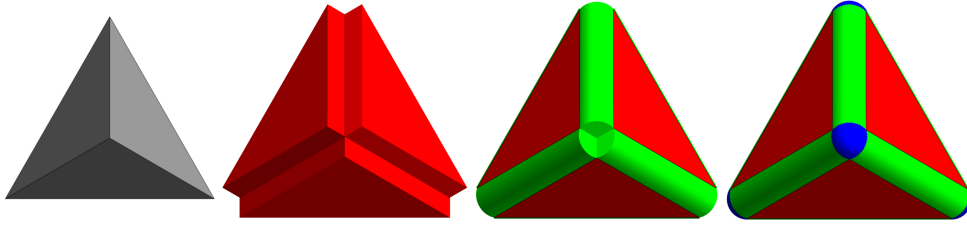


Figure 4.3: Schematic representation of contributions to the volume of a spheropolyhedron with a rounding radius R : (gray) the polyhedron itself, (red) triangular slabs formed by moving all faces in their outward normal directions by a distance R , (green) segments of cylinders with radius R around all edges and (blue) segments of spheres with radius R around all vertices.

pressure $p_{start}^* = \beta p v_p = 1$ to $p_{end}^* = \beta p v_p = 10^7$, with p the pressure, v_p the particle volume and $\beta = 1/k_B T$ with k_B Boltzmann's constant and T the temperature. To sample different compression routes, we increased the pressure of each MC cycle m as $p_m^* = p_{start}^* + (p_{end}^* - p_{start}^*)(m/M)^\gamma$ over a total of $M = 10^7$ MC cycles. The exponent γ was set randomly within the interval $5.2 \leq \gamma \leq 9$. These values seemed to provide the best sampling to reliably reproduce the known dimer crystal packing of tetrahedra, and we made the assumption that this provides good sampling for other shapes as well. The space group of the crystal was identified using FindSym [180, 181] on the obtained primitive unit cell.

4.2.3 Crystallography and bond-orientational order parameters

There are many ways to characterize the structural order of a collection of particles. For periodic structures i.e. crystals, this is essentially the entire field of crystallography. Without going into too much detail, the key description of a crystal structure is the *unit cell*, which is the repeating unit that can be stacked infinitely to fill all of space and which gives the crystal structure. Unit cells are composed of two essential elements: the description of the cell itself (of the *lattice*) and the description of what it contains (the *basis*). The cell description is simple and universal: for three-dimensional space, one defines three *lattice vectors* that span a parallelepiped:

$$\begin{aligned} \mathbf{a}_1 &= (a_{1,x}, a_{1,y}, a_{1,z}) \\ \mathbf{a}_2 &= (a_{2,x}, a_{2,y}, a_{2,z}) \\ \mathbf{a}_3 &= (a_{3,x}, a_{3,y}, a_{3,z}). \end{aligned} \tag{4.3}$$

One can reduce this nine-number description to six numbers by instead considering the *lattice lengths* a, b, c and *lattice angles* α, β, γ , which are respectively the lengths of and angles between the three lattice vectors. The contents of the unit cell can vary based on what we want to describe: for some crystals we need to consider the atom types of the particles, their charges, magnetic moments, orientations and so on. In all cases, however, we must define their *positions*. For N particles in the unit cell, these are the N basis vectors $\{\mathbf{r}_i\}$ with $i \in [1, N]$. The positions \mathbf{R} of all particles in the lattice can now be

constructed as:

$$\mathbf{R}_{i,j,k,l} = \mathbf{r}_i + j\mathbf{a}_1 + k\mathbf{a}_2 + l\mathbf{a}_3 \quad j, k, l \in \mathbb{Z}, \quad i \in [1, N]. \quad (4.4)$$

One can fully describe all possible crystal structures in this way. However, this description is not without its flaws. One can define multiple unit cells that yield the same crystal structures. Often one takes the smallest possible unit cell, but occasionally crystal structures are more easily described by a larger, cubic unit cell. The translational symmetries of crystal structures allow for multiple choices for the lattice and basis vectors without changing the described structure. And of course, not all structures are crystals. One simply cannot describe the structure of aperiodic systems such as gases, liquids, glasses or quasicrystals by means of a repeating unit cell. So since we know that spherotetrahedra can form a quasicrystal, it would be advantageous to have a different way to describe structural order. And as we would at some point like to study how a crystal forms from a fluid, we would like it to be able to do so *locally*. Fortunately, such structural descriptors exist.

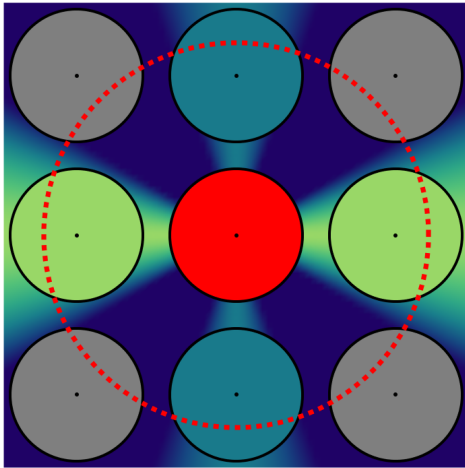


Figure 4.4: Schematic representation of $q_{4,0}$. The background plot shows the azimuthal plane of $Y_{4,0}$. The red particle will have a large $q_{4,0}$ because its neighbouring particles, whose centroids are within the red circled cutoff radius R_c , are aligned with the peaks of $Y_{4,0}$.

In a seminal paper, Steinhardt, Nelson and Ronchetti [182] described the so-called bond-orientational order parameters (BOP): a set of structural descriptors using spherical harmonics to quantify the local structural order surrounding a particle. These are defined as follows: consider a particle i with other particles j in its vicinity (say, within some cutoff radius R_c). For each *neighbour* j in its vicinity, we say that particle i has a *bond* to this neighbour, \mathbf{r}_{ij} . One can then define a number q_{lm} which captures how similar the neighbourhood of i is to the spherical harmonic Y_{lm} ,

$$q_{lm}(i) = \frac{1}{N_b(i)} \sum_{j=1}^{N_b(i)} Y_{lm}(\hat{\mathbf{r}}_{ij}), \quad (4.5)$$

with $N_b(i)$ the number of bonds and $\hat{\mathbf{r}}_{ij}$ the direction of the bond.

However, this number is not yet a particularly useful order parameter as it is both a complex number and not yet rotationally invariant. We would like to be able to describe structural order without having to define a reference orientation. For this reason we usually use

$$q_l(i) = \sqrt{\frac{4\pi}{2l+1} \sum_{m=-l}^l |q_{lm}(i)|^2} \quad (4.6)$$

instead, which provides a rotationally invariant real number that quantifies the symmetry of bonds in the neighbourhood of particle i corresponding to a certain quantum number

l . For instance, a simple cubic lattice has a high value of q_4 since the bonds between particles have a largely cubic symmetry (see Fig. 4.4). One can also define higher-order moment variants of these order parameters,

$$w_l(i) = \sum_{m_1+m_2+m_3=0} \begin{pmatrix} l & l & l \\ m_1 & m_2 & m_3 \end{pmatrix} q_{lm_1}(i) q_{lm_2}(i) q_{lm_3}(i), \quad (4.7)$$

where

$$\begin{pmatrix} l & l & l \\ m_1 & m_2 & m_3 \end{pmatrix} \quad (4.8)$$

are the Wigner $3j$ symbols. By looking at a collection of q_l and w_l of different l one can define a “fingerprint” for different structures. In particular q_4 , q_6 , w_4 and w_6 can be used to distinguish between the FCC, HCP, BCC and fluid phases of spheres [183]. Since its introduction several improvements to this order parameter have been proposed for the purposes of crystal structure detection. The first improvement pertains to the definition of the local neighbourhood and is provided by Mickel et al. [184]: while defining the neighbourhood by means of a distance cutoff is a simple solution, it introduces both a parameter dependence through the cutoff radius R_c and a sensitivity to local fluctuations, as particles that are just within or just outside of R_c contribute either fully or not at all to the value of the order parameter.

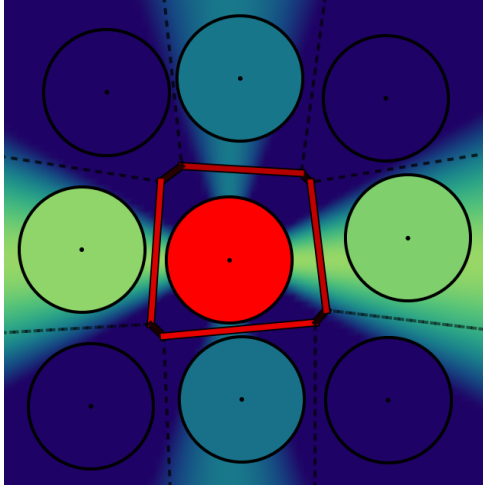


Figure 4.5: Schematic representation of $q_{4,0}$ with the Voronoi neighbour definition. The background plot shows the azimuthal plane of the real part of $Y_{4,0}$. The contribution from each neighbouring particle to $q_{4,0}$ is now weighted by the shared facets shown in red.

Both of these problems can be eliminated by a different definition of the local neighbourhood. There are two notable ways to eliminate the parameter dependence: one can either define the neighbours of i through a Voronoi diagram [184], or by means of the solid-angle nearest neighbour (SANN) algorithm [185]. In the remainder of this thesis we will use the Voronoi method. Following Ref. [184], the sensitivity to fluctuations can be reduced by weighting the Y_{lm} contributions of neighbours by the area of the Voronoi their facets

$$q_{lm}(i) = \sum_{j=1}^{N_b^V(i)} \frac{a_{ij}}{A_i} Y_{lm}(\mathbf{r}_{ij}), \quad (4.9)$$

where a_{ij} is the area of the Voronoi facet shared by particle i and j , A_i is the total area of the Voronoi cell of i and the sum is over all Voronoi neighbours N_b^V of particle i . In this way, nearby particles contribute more to q_{lm} and their contribution is reduced smoothly as they get further away (Fig. 4.5). The q_l use these reweighted q_{lm} , but are otherwise the same as in Eq. 4.6:

$$q_l(i) = \sqrt{\frac{4\pi}{2l+1} \sum_{m=-l}^l |q_{lm}(i)|^2}. \quad (4.10)$$

We use the suggested term “Minkowski structure metric” from Ref. [184] to indicate the weighted order parameters when we need to differentiate between weighted and unweighted q_{lm} , q_l and w_l , and “order parameter” to refer to either. Defining bonds through the Voronoi construction makes the method parameter-free, and weighting by the shared facet area makes the structure metrics less susceptible to fluctuations in the number of bonds. A second improvement is given by Lechner and Dellago [186], who show that one can reduce the influence of thermal noise on the order parameters by averaging the q_{lm} over the first neighbour shell. Analogous to the averaged Steinhardt bond order parameters defined in Ref. [186], we define averaged Minkowski structure metrics by simply averaging the weighted q_{lm} (Eq. 4.9) over the (Voronoi) neighbours:

$$\bar{q}_{lm}(i) = \frac{1}{\tilde{N}_b^V(i)} \sum_{j=1}^{\tilde{N}_b(i)} q_{lm}(j), \quad (4.11)$$

where $\tilde{N}_b^V(i)$ denotes the set of Voronoi neighbours of i plus i itself, and q_{lm} denotes the non-averaged structure metrics. The averaged rotationally invariant \bar{q}_l are then obtained by simply replacing q_{lm} with \bar{q}_{lm} :

$$\bar{q}_l(i) = \sqrt{\frac{4\pi}{2l+1} \sum_{m=-l}^l |\bar{q}_{lm}(i)|^2}, \quad (4.12)$$

In the bulk of our analysis we consider structure metrics \bar{q}_l with $l \in [2, 12]$. The structure metrics \bar{q}_0 and \bar{q}_1 are excluded since they are always one and zero, respectively [184]. The q_l of odd l are not invariant under inversion and require defining a direction for each bond [182]; we choose this direction to be “outward” i.e. they point *from* each particle i *to* its neighbours j . The source code for our implementation of the calculation of these structure metrics is available on Github [187].

4.2.4 Self-assembly and equation of state simulations

To probe the self-assembly behaviour and to calculate the equations of state we performed simulations using HOOMD-blue’s [188, 189] hard-particle Monte Carlo (HPMC) [190] module (versions 2.6.0 through 2.9.3). We used MC simulations in the NVT ensemble using 10^8 MC cycles to study the self-assembly. A relatively large number of MC cycles is needed as previous studies showed that the formation of a quasicrystal of hard tetrahedra is quite slow, requiring on the order of $\sim 2 \cdot 10^7$ to occur [166, 168, 191]. Particles were allowed to translate and rotate with a variable step size such that the acceptance ratio of such moves was 30%. To calculate the equations of state, we performed MC simulations of $N \sim 400$ particles in a constant-pressure ensemble, where in addition to particle moves and rotations the simulation box was allowed to change its volume and to shear. The step sizes of these latter moves were tuned to an acceptance ratio of 15%. We used 10^7 MC cycles for equilibration and 10^5 MC cycles for sampling. Initial configurations were either a low-density fluid, a high-density crystal whose unit cell we obtained from the FBMC simulations, or the quasicrystal approximant.

4.3 Dense packings

Before we discuss the densest packings we obtained, it is worthwhile to consider which densest packings for these shapes are already known. The spherotetrahedral shape reduces to a sphere for $s = 1$ and a tetrahedron for $s = 0$, and the densest packings for these structures are known. The densest packing of hard spheres is the FCC/HCP crystal with a well-established maximum packing fraction of $\phi_{\max} = \pi/(3\sqrt{2}) \approx 0.74$, with the FCC crystal being the more thermodynamically stable when not at dense packing [192]. The best-packed structure of tetrahedra was the subject of a flurry of publications some years back [41, 159, 166, 168, 193–198], when numerical simulations revealed that a dodecagonal quasicrystal forms spontaneously from the fluid via a first-order phase transition, and that a quasicrystal approximant can be compressed to a packing fraction as high as $\phi = 0.8503$ [166, 168]. This raised the conjecture that the densest packing of tetrahedra might be aperiodic, although later work showed that the periodic dimer crystal [195, 197] achieves a packing fraction of $\phi_{\max} = 4000/4671 = 0.856347$, which is the established densest packing of tetrahedra as of now. For slightly rounded spherotetrahedra, Jin *et al.* [47] surprisingly found that a quasicrystal approximant packs denser than the dimer crystal structure. This fascinating result inspired us to re-investigate in more detail the densest packings of spherotetrahedra over the full shape range of shapes $s \in [0, 1]$, as opposed to the more limited range of shapes that were seen experimentally.

To obtain the densest packings we used the FBMC algorithm method as described in section 4.2.2. In Fig. 4.6(a) we present the resulting maximum packing fraction ϕ_{\max} as a function of the shape parameter s along with those of Jin *et al.* [47] for comparison. We reproduce the well-known limiting close-packed densities for $s = 0$ and $s = 1$, but obtain substantially higher maximum packing fractions for intermediate shapes than previously reported by Jin *et al.*. A careful analysis of the bond-order parameters \bar{q}_l and the lattice lengths and angles reveals twelve structurally distinct, disconnected dense packings of spherotetrahedra, which we will henceforth refer to with roman numerals. Some of these dense packings are extremely similar and we label these with primes, with the non-primed roman numeral being the structure that is stable over the largest range of s . As an example, the densest packing for $s \geq 0.3745(5)$ is a deformed FCC lattice with three variants, so we refer to these as VII'', VII' and VII, where the last is non-primed because it is stable for $s \in [0.4135(1), 1]$, which is the largest range of the three.

We shall first discuss how exactly the division into these twelve lattices is made, then look at the individual lattices in more detail. After that we will investigate the packing efficiency of the quasicrystal approximant in more detail.

4.3.1 Classification of dense packings

Previous work has distinguished dense crystal structures based on discontinuities in (the derivatives of) the shape-dependent maximum packing fraction $\phi_{\max}(s)$ [176, 199] or in the lengths L_i of and the angles θ_i between the three vectors that span the unit cell [161], which are shown in Figs. 4.6(a), (b) and (c), respectively. Both these methods have important drawbacks. Discontinuities in the derivatives of the maximum packing fraction can indeed be the result of jumps from one crystal structure to another, but can also be the result of

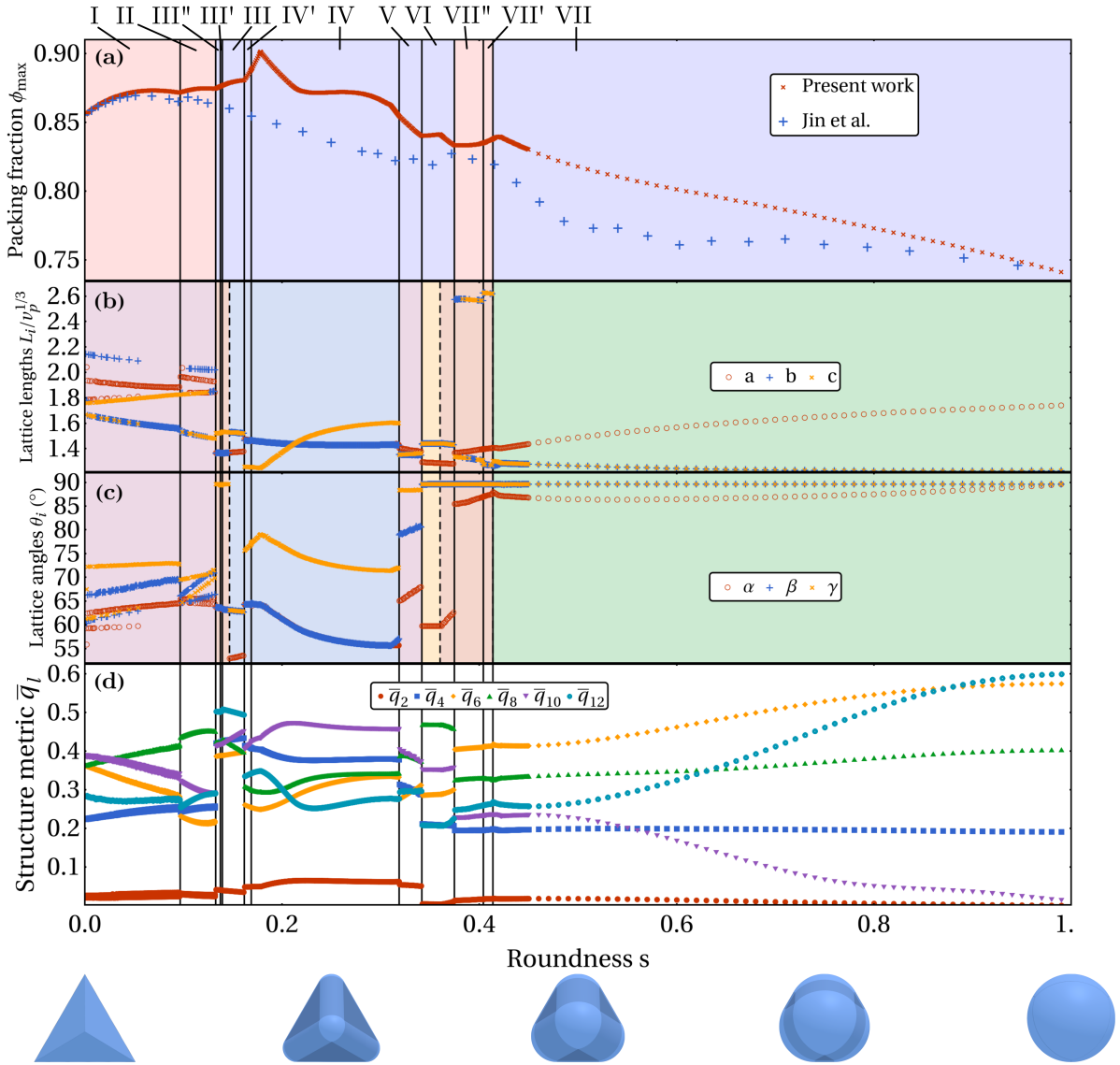


Figure 4.6: Floppy-box Monte Carlo simulation results of the shape-parameter dependence of (a) the maximum packing fractions ϕ_{\max} , (b) the lengths L_i of the lattice vectors, (c) the lattice cell angles θ_i , and (d) the (modified) bond order parameters \bar{q}_l for $l = 2, 4, \dots, 12$ (see text), all for the densest structure we have found. Roman numerals denote the different crystal structures, and vertical solid black lines indicate the transitions between these structures. In (a) the red and blue backgrounds indicate four- and two-particle unit cells, respectively, and in (b) different background colors denote the different lattice types also noted in Fig. 4.12. The dashed lines in (b) and (c) indicate transitions in lattice symmetry.

a change in continuous deformation of *the same* lattice, e.g. from a shear along one axis to shear along another. The lattice parameters also do not uniquely describe a crystal structure: some crystal structures are degenerate, i.e. multiple unit cells can form that same structure, as is the case for regions I, II, VII'' and VII' in Fig. 4.6(b) and (c). Perhaps most important, however, is that the analysis of lattice parameters of the unit cell is

inherently not extendable to aperiodic structures such as quasicrystals, fluids, mesophases, glasses, etc., because one cannot describe these structures by a single repeating unit cell. It is for these reasons that we instead define the regions I-VII through discontinuities in the Minkowski Structure Metrics (MSM) described in Section 4.2.3. In this way, the set of all \bar{q}_l forms a unique “fingerprint” for each crystal structure. One should note that since the \bar{q}_l are essentially an expansion into spherical harmonics, this fingerprint is not *guaranteed* to be mathematically unique unless an infinite number of angular quantum numbers l are taken into account. However, in practice one only needs a few \bar{q}_l ’s in order to distinguish all dense packings from each other. For the crystals commonly formed by spherical particles: face-centered cubic (FCC), hexagonal close-packed (HCP) and body-centered cubic (BCC), one can distinguish between all of them and the disordered fluid using only \bar{q}_4 and \bar{q}_6 [186]. However, since the crystals formed by spherotetrahedra may have very different symmetries than those formed by spheres, there is no guarantee that \bar{q}_4 and \bar{q}_6 are also good order parameters here. The questions of how many and which \bar{q}_l are needed are intriguing, and we consider them in detail in Chapter 5. In Fig. 4.6(d) we show the subset $\{\bar{q}_2, \bar{q}_4, \dots, \bar{q}_{12}\}$ for the dense packings of spherotetrahedra as a function of their shape parameter s . We find a first-order discontinuity in all $\bar{q}_l(s)$ whenever the densest packing switches from one structure to another, which we denote with the solid black vertical lines. Second-order discontinuities also occur. These correspond to changes in continuous deformation of the lattice e.g. when (with changing shape s) the lattice first compresses along \hat{z} but switches to extension along \hat{x} . Focusing on regions I, II, VII’ and VII”, it is clear that the \bar{q}_l do not suffer from the same degeneracy issues that the lattice parameters do. However, it is important to note that for larger unit cells such as the four-particle unit cells of the dimer crystals I and II, the structure metrics \bar{q}_l can be different for different particles in the unit cell, as the local structural environments of particles within the unit cell can be different.

Some of the discontinuities in the structure metrics are very small and are not visible on the scale of Fig. 4.6(d). In Figures 4.8 through 4.10 we show zoomed-in graphs for specific regions of interest where the lattice parameters are discontinuous or where $\phi_{\max}(s)$ changes curvature or is discontinuous in its derivative. It is on this scale that the transitions between the primed lattices become visible. Figure 4.8 shows the transitions between structures III”, III’ and III, Figure 4.9 between structures IV’ and IV and Figure 4.10 between structures VII”, VII’ and VII. Additionally, Figure 4.11 shows that a discontinuity in the first derivative or a change in the second derivative of the maximum packing fraction $\phi_{\max}(s)$ does not necessarily indicate a change in structure, as all of our structural indicators remain continuous in the shown regions.

In these zoomed-in plots we also show an additional property of the dense packings: the distribution of facet areas in the Voronoi cells around particles. The Voronoi construction method used to define the neighbourhood of particles can also be used to access topological and additional geometric information of the local bond network. For instance, one can calculate the number of neighbours for each structure or the shape of the Voronoi cell, the latter of which provides an alternative method of characterizing the various crystal phases. We found that the distribution of the areas of the facets of the Voronoi cells, shown in Figure 4.7, provides insight into the degree of symmetry that needs to be broken to achieve the densest packing. For lattices with high symmetry (e.g. IV or VII) the

facet areas are degenerate *i.e.* many facets have identical areas, while for lattices with low symmetry there are many facets with a unique area. In Figure 4.7, values of s where the degeneracy changes generally correspond to points of interest in the dense packings where the lattice symmetry changes and/or there are kinks in the packing fraction curve $\phi_{\max}(s)$.

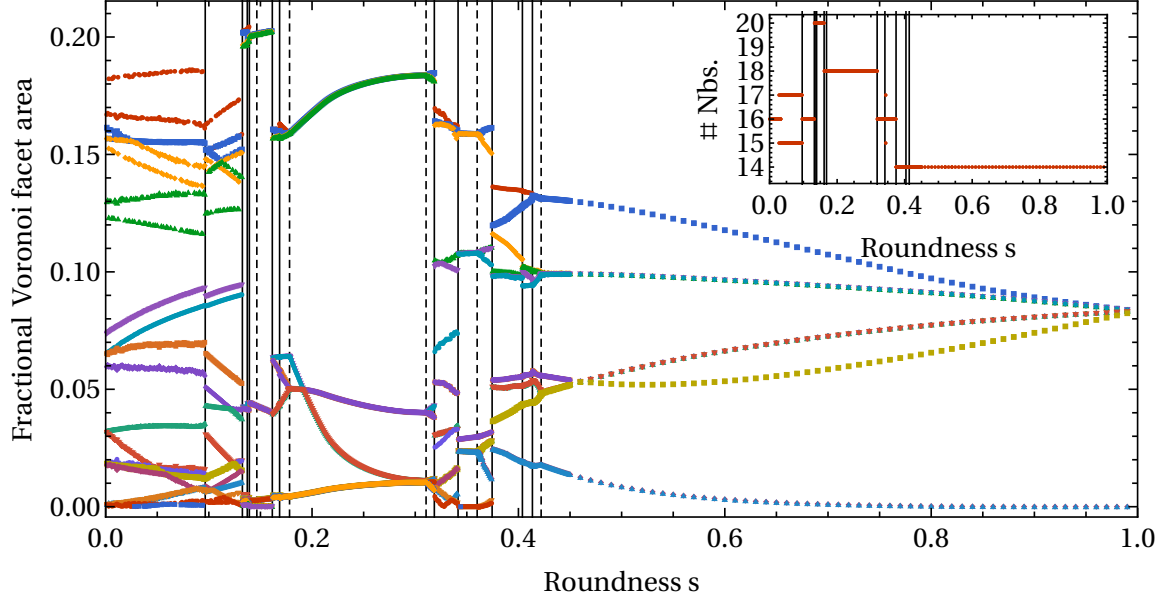


Figure 4.7: Areas spanned by individual facets of the Voronoi cells, as a fraction of the total area of the cell. Dashed lines indicate values for s for which the facet degeneracy changes. Three of these dashed lines also correspond to changes in the lattice type (*e.g.* monoclinic to orthorhombic). Inset: number of neighbours in the Voronoi tessellation.

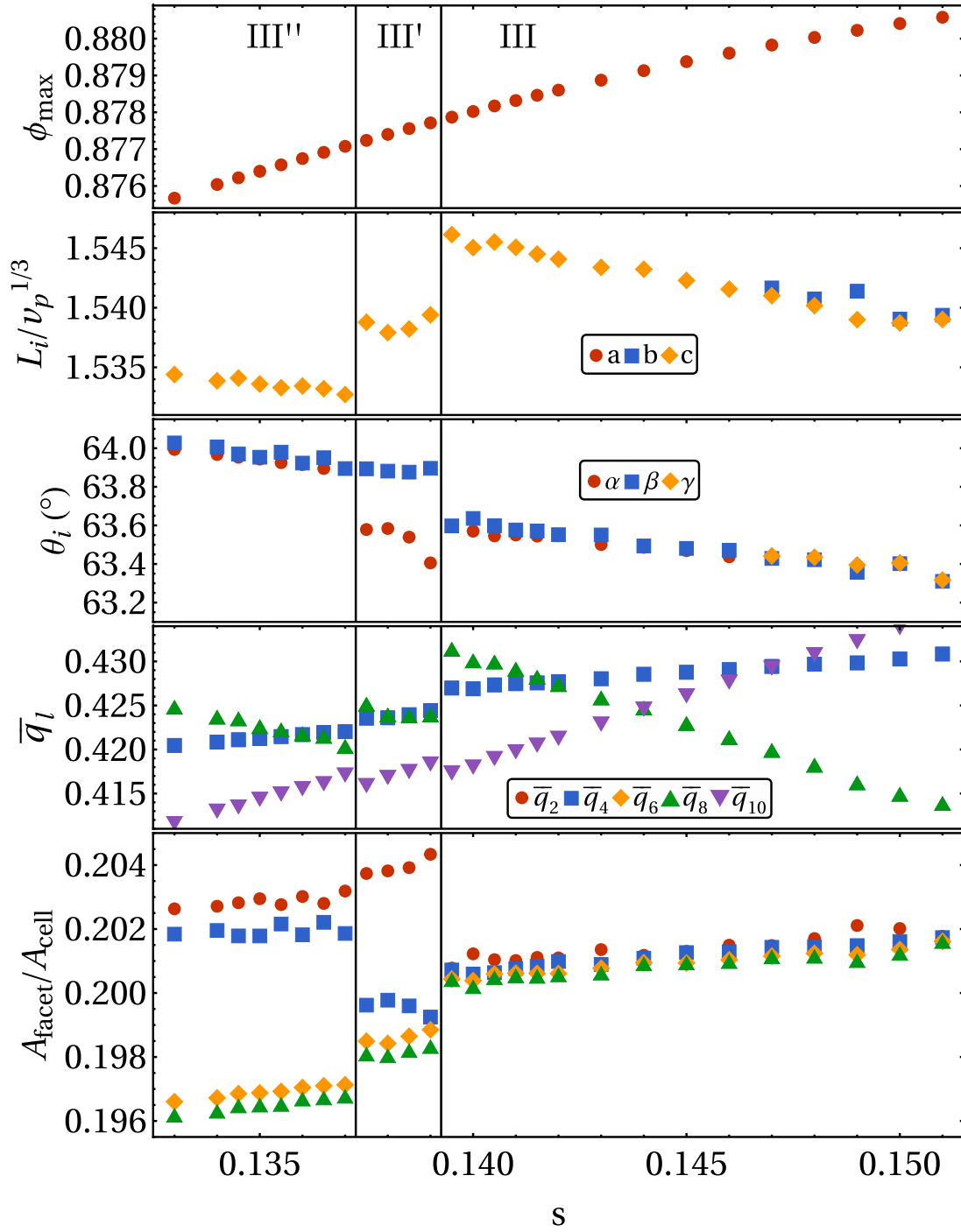


Figure 4.8: A zoomed-in view of a region of interest for the shape-parameter dependence of (top to bottom) the maximum packing fractions ϕ_{\max} , the lengths L_i of the lattice vectors, the lattice cell angles θ_i , the structure metrics \bar{q}_l for $l = 2, 4, \dots, 12$ and the fractional Voronoi cell areas $A_{\text{facet}}/A_{\text{cell}}$. Roman numerals denote the different crystal structures, and vertical solid black lines transitions between these structures. Transitions between structures manifest themselves as first-order discontinuities in all shown properties except for the maximum packing fraction ϕ_{\max} .

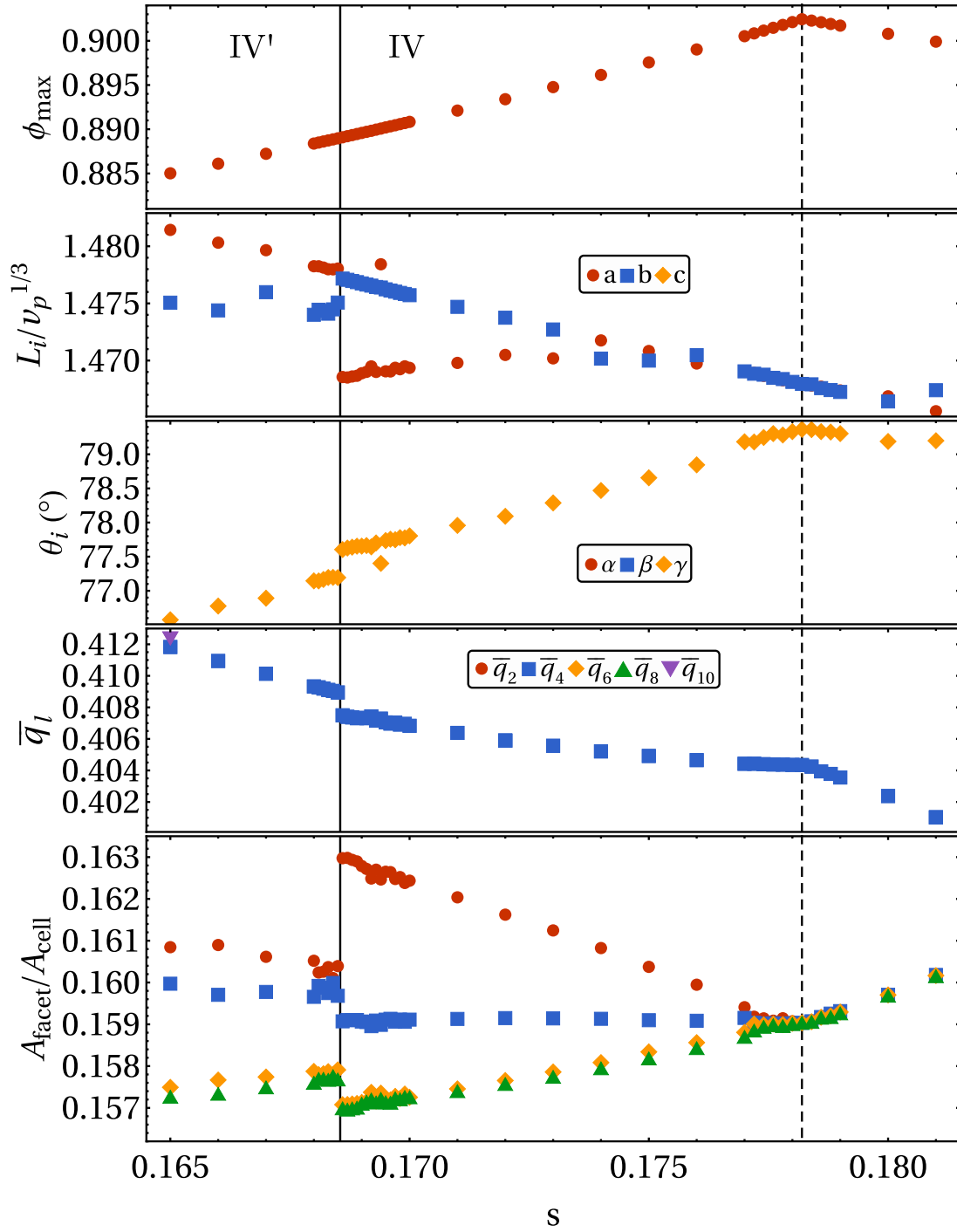


Figure 4.9: A zoomed-in view of a region of interest for the shape-parameter dependence of (top to bottom) the maximum packing fractions ϕ_{\max} , the lengths L_i of the lattice vectors, the lattice cell angles θ_i , the structure metrics \bar{q}_l for $l = 2, 4, \dots, 12$ and the fractional Voronoi cell areas $A_{\text{facet}}/A_{\text{cell}}$. Roman numerals denote the different crystal structures, vertical solid black lines transitions between these structures, and dotted lines values of s for which the Voronoi facets change degeneracy. Transitions between structures manifest as first-order discontinuities in all shown properties except for the maximum packing fraction ϕ_{\max} .

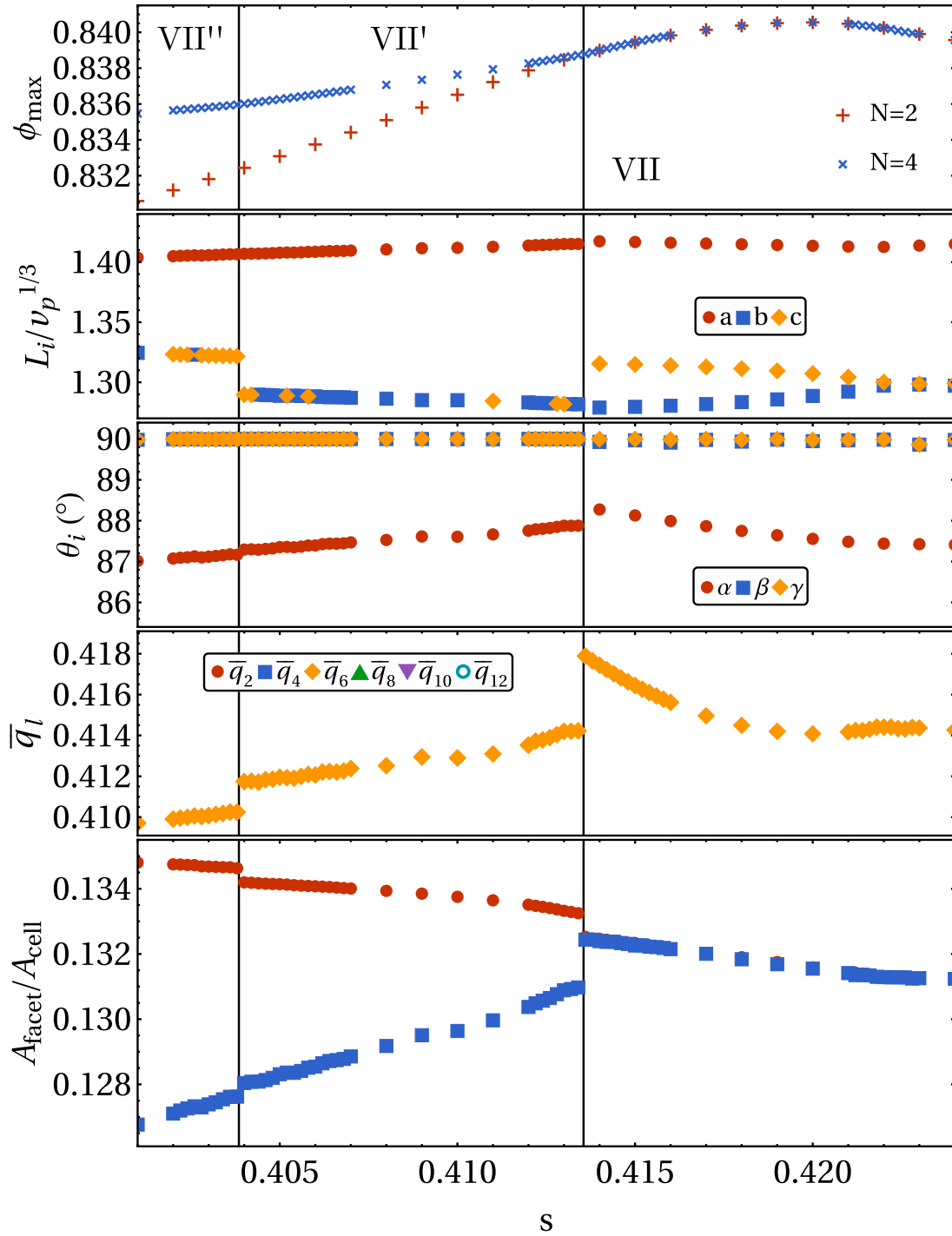


Figure 4.10: A zoomed-in view of a region of interest for the shape-parameter dependence of (top to bottom) the maximum packing fractions ϕ_{\max} , the lengths L_i of the lattice vectors, the lattice cell angles θ_i , the structure metrics \bar{q}_l for $l = 2, 4, \dots, 12$ and the fractional Voronoi cell areas $A_{\text{facet}}/A_{\text{cell}}$. Roman numerals denote the different crystal structures, and vertical solid black lines transitions between these structures. Transitions between structures manifest as first-order discontinuities in all shown properties except for the maximum packing fraction ϕ_{\max} . In the top $\phi_{\max}(s)$ graph we show both the $N = 2$ and $N = 4$ particle variants of the unit cells of structures VII'', VII' and VII to highlight the differences. In the other graphs we show only the properties of the densest variant: $N = 4$ for VII'' and VII' and $N = 2$ for VII.

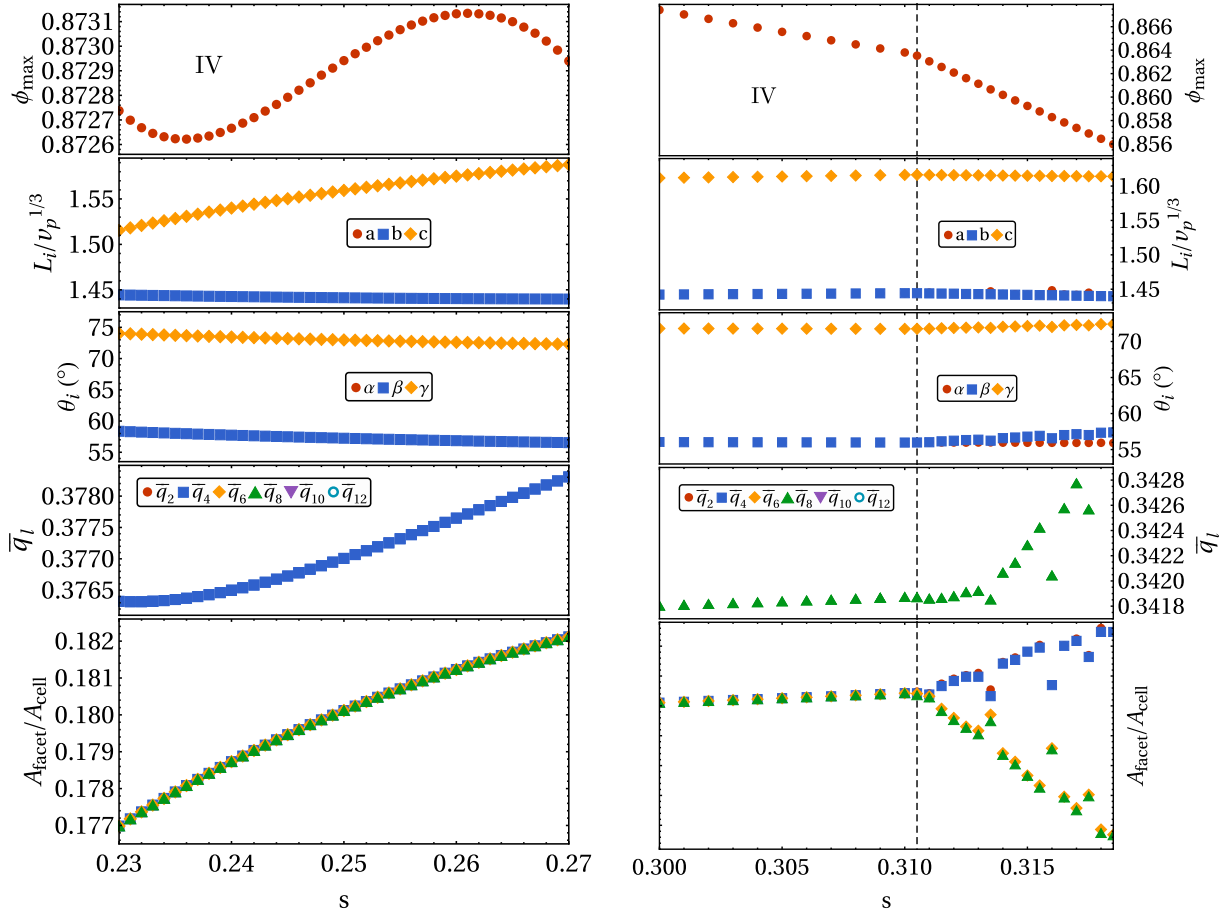


Figure 4.11: A zoomed-in view of a region of interest for the shape-parameter dependence of (top to bottom) the maximum packing fractions ϕ_{\max} , the lengths L_i of the lattice vectors, the lattice cell angles θ_i , the structure metrics \bar{q}_l for $l = 2, 4, \dots, 12$ and the fractional Voronoi cell areas $A_{\text{facet}}/A_{\text{cell}}$. Roman numerals denote the different crystal structures, and vertical solid black lines transitions between these structures. Transitions between structures manifest as first-order discontinuities in all shown properties except for the maximum packing fraction ϕ_{\max} .

4.3.2 Crystal structures

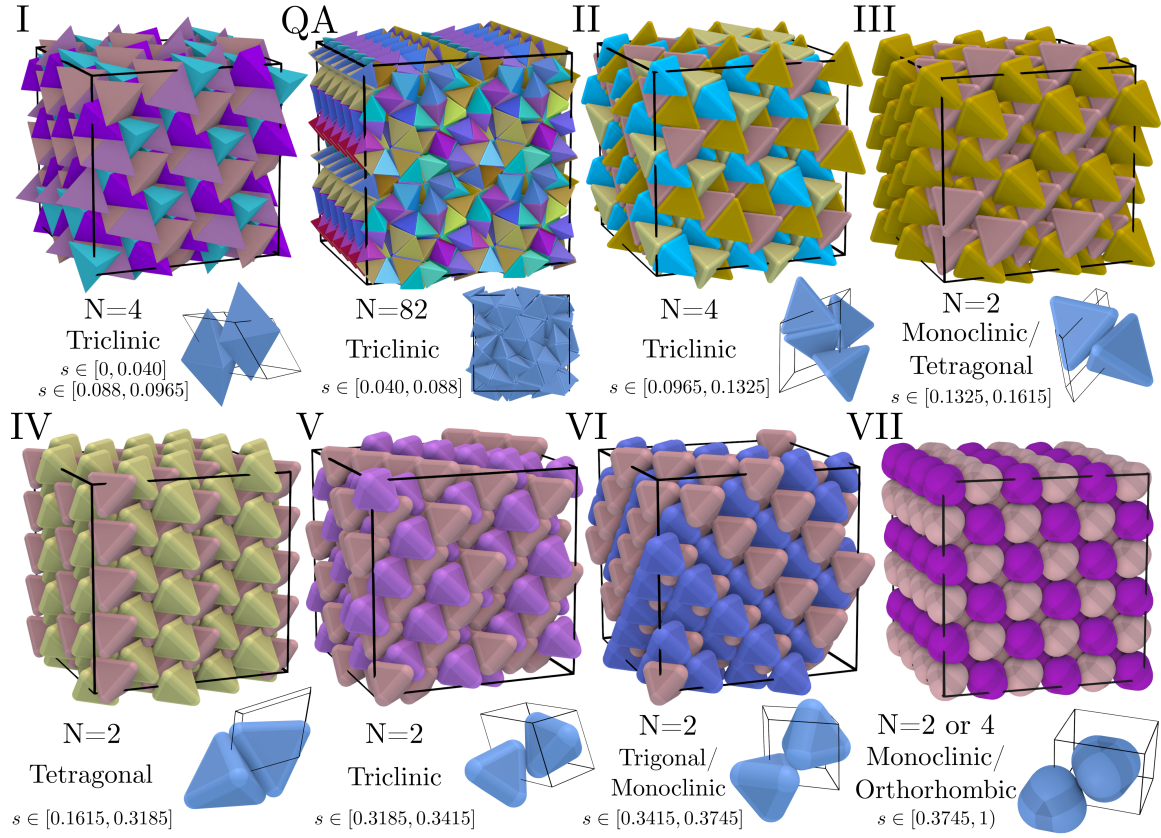


Figure 4.12: Cubic supercells (with distinct colors indicating differently oriented particles in the unit cell) and primitive unit cells of eight of the densest crystal structures, shown with their lattice type and the shape-parameter s -regime in which they are the densest packing. Roman numerals denote crystal structures obtained from the floppy-box Monte Carlo simulations, and “QA” indicates the quasicrystal approximant.

Now that we have established how we divided the obtained dense packings into twelve structures, let us take a look at the individual structures in a bit more detail. We can establish a loose grouping of the crystal structures I-VII into deformed dimer (I, II), deformed β -tin (IV', IV), and deformed FCC (VII'', VII', VII), with intermediate structures (III'', III', III, V, VI). Let us go through them in order of increasing roundness, starting from tetrahedra ($s = 0$). For $s \in [0, 0.1325(5)]$, close to tetrahedra, we find two very similar dimer crystals I and II: both are triclinic lattices with $N = 4$ particles in a unit cell in which the tetrahedra form dimers with almost perfect facet-to-facet alignment. The difference between the two lattices is a subtle shift in the relative position and orientation of the two dimers with respect to one another, which is shown in Fig. 4.14. The particles in the crystal structures III''-VII do not form perfect facet-to-facet aligned dimers, but instead align with respect to one another rotated by 60° around a common facet normal. Each of these crystal structures has its own noteworthy properties. In crystal structures III'', III' and III, stable for $s \in [0.1325(5), 0.1615(5)]$, particles have an unusually high number of Voronoi neighbours (inset Fig. 4.7). Additionally, at $s = 0.1465$ its lattice

type switches from monoclinic to tetragonal. Crystal structures IV' and IV, stable for $s \in [0.1615(5), 0.3185(5)]$, bear a close resemblance to the β -tin lattice found for truncated tetrahedra in Ref. [176]: they are tetragonal and at a rounding ratio of $s = 0.178$ crystal VI packs as efficiently as $\phi = 0.90212$, which is the densest of all spherotetrahedra. While crystal structure IV is stable over a large range of shapes, its packing efficiency decreases with increasing roundness s , until it is superseded by crystal structure V, a triclinic transition structure that is only stable over a small range of shapes: $s \in [0.3185(5), 0.3415(5)]$. This is followed by crystal structure VI in the region $s \in [0.3415(5), 0.3745(5)]$, which is trigonal for $s < 0.36$ and monoclinic for $s \geq 0.36$. The trigonal region $s \in [0.3415, 0.36]$ is the only region for all spherotetrahedra for which a change in the particle shape does not change the crystal structure significantly. Finally, crystals VII'', VII' and VII are deformations of an FCC lattice and fill the range $s \in [0.3745(5), 1)$. To achieve the densest packing for non-spheres, the lattice must deform from the cubic FCC and become orthorhombic rather than cubic for $s \in [0.4135(1), 1)$, and requires two particles in the aforementioned opposing orientations. For $s \in [0.3745(5), 0.4135(1)]$ there are additional changes: here the even denser packings VII'' and VII' can be achieved by four-particle unit cells if the two additional particles are slightly rotated (Fig. 4.13) and the lattice symmetry is reduced from orthorhombic to monoclinic.

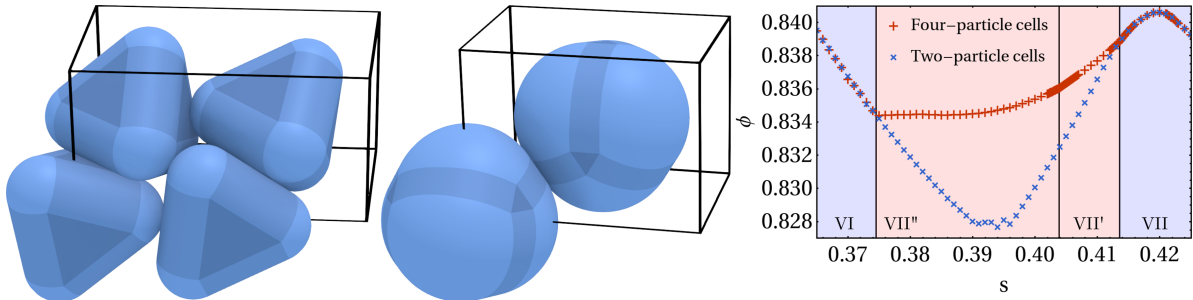


Figure 4.13: Unit cells for the four-particle crystal VII'' ($s = 0.402$) and two-particle crystal VII ($s = 0.8$) and a graph of their maximum packing fractions. Note that in the four-particle unit cell, each particle has a unique orientation.

As previous studies report that more centrally symmetric particles tend to pack into simpler lattices [159, 176], we might expect the densest packings of spherotetrahedra to become simpler and with fewer particles in the unit cell with increasing shape parameter s . Interestingly, this trend does not hold here. While the number of particles per unit cell initially decreases from $N = 4$ to $N = 2$ when the shape parameter increases up to $s = 0.3745$, this trend is broken in the region $s \in [0.3745, 0.4135]$, where the crystal structures VII'' and VII' require $N = 4$ particles to obtain their densest packing. The densest packing can also become less symmetric as the shape becomes more spherical: while the crystal structures up to IV indeed become more symmetric, crystal V is again triclinic. In general, while we could expect that making particles more spherical will yield more symmetric lattices at intermediate densities due to entropy considerations, it appears that these symmetries may need to be broken in order to achieve the densest packing.

Label	Shape parameter s	N	Voronoi neighbours	Space group	
I	[0, 0.040(5)]	4	4×16	$P\bar{1}$	Deformed dimer
QA	[0.040(5), 0.088(5)]	82	-	P1	Quasicrystal approximant
I	[0.088(5), 0.0965(5)]	4	$2 \times 15 + 2 \times 17$	$P\bar{1}$	Deformed dimer
II	[0.0965(5), 0.1325(5)]	4	4×16	$P\bar{1}$	Deformed dimer
III''	[0.1325(5), 0.1372(1)]	2	2×20	C2/c	Intermediate
III'	[0.1372(1), 0.1392(1)]	2	2×20	C2/c	Intermediate
III	[0.1392(1), 0.1465(5)]	2	2×20	C2/c	Intermediate
III	[0.1465(5), 0.1615(5)]	2	2×20	I4 ₁ /amd	Intermediate
IV'	[0.1615(5), 0.1685(1)]	2	2×18	I4 ₁ /amd	deformed β -tin
IV	[0.1685(1), 0.3185(5)]	2	2×18	I4 ₁ /amd	deformed β -tin
V	[0.3185(5), 0.3415(5)]	2	2×16	$P\bar{1}$	Intermediate
VI	[0.3415(5), 0.362(1)]	2	2×16	P3m1	Intermediate
VI	[0.362(1), 0.3745(5)]	2	2×16	C2/m	Intermediate
VII''	[0.3745(5), 0.4038(1)]	4	4×14	P2 ₁ /c	deformed FCC
VII'	[0.4038(1), 0.4135(1)]	4	4×14	P2 ₁ /c	deformed FCC
VII	[0.4135(1), 1)	2	2×14	Cmcm	deformed FCC

Table 4.1: Summary of the properties of the close-packed crystal structures of hard spherotetrahedra: the label I-VII, the shape parameter s range for which they are the densest packing, the number of particles per unit cell N , Voronoi neighbours, lattice symmetry space group and a qualitative descriptor.

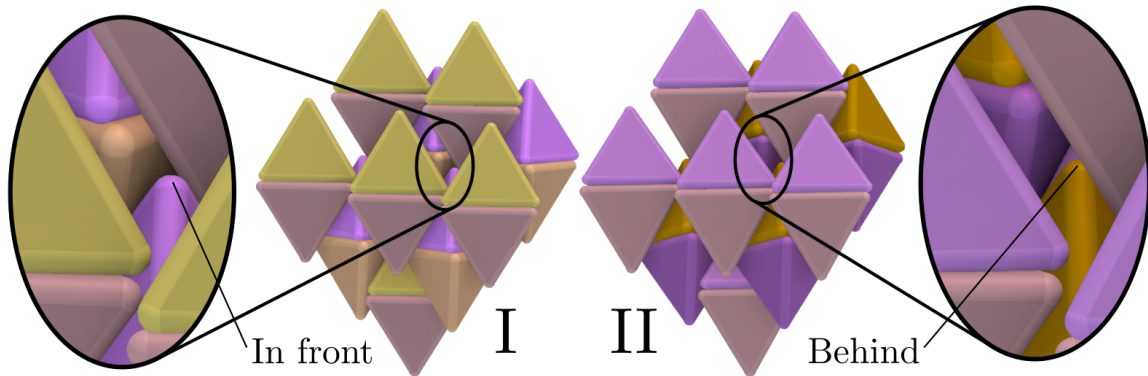


Figure 4.14: Visualization of the difference between dimer crystals I and II. While both crystals feature virtually identical pairs of dimers, the orientation of the two dimers with respect to one another is subtly different, here indicated as “In front” and “Behind”.

4.3.3 The maximum packing fraction of the quasicrystal approximant

Using the floppy-box Monte Carlo method, we found a variety of crystal structures of hard spherotetrahedra with a significantly higher maximum packing fraction than previously found in former literature [47]. We now investigate whether these densest-packed crystal structures have a better packing than the quasicrystal approximant found in Ref. [47]. To this end, we first refine our search in the region $s \in [0.02, 0.12]$ to 200 compression runs per shape parameter value s . In addition, we increase the total number of MC cy-

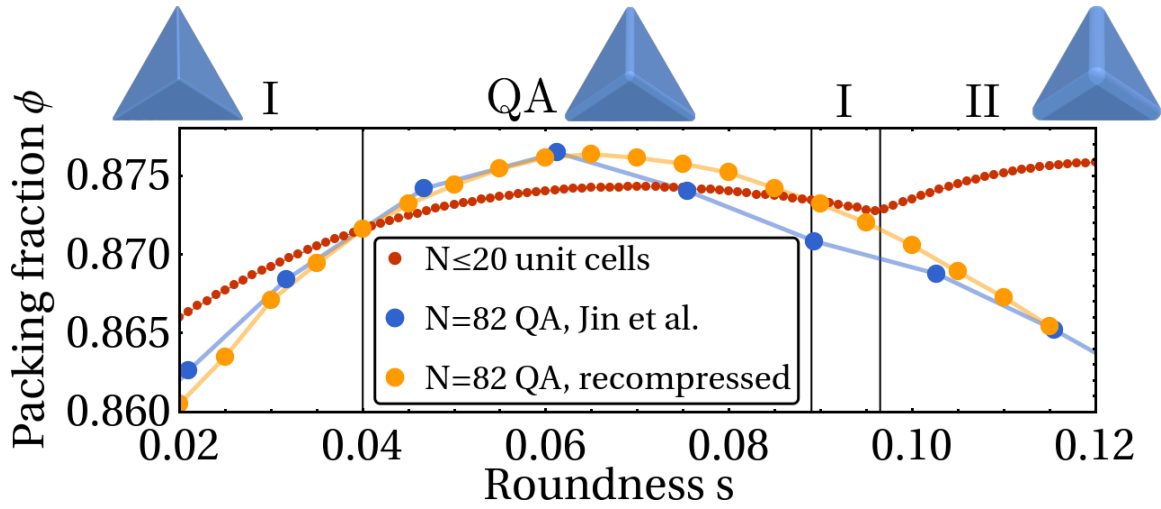


Figure 4.15: Maximum packing fraction of hard spherotetrahedra as a function of the roundness s for the densest-packed crystal structures obtained from floppy-box Monte Carlo simulations using unit cells with $N \leq 20$ particles (red dots), and for the quasicrystal approximant reported by Jin *et al.* [47], where previous and our results are denoted by blue and orange dots, respectively. In the region $s \in [0.040, 0.088]$, the quasicrystal approximant is denser than the dimer crystal.

cles to $M = 10^8$ in our floppy-box Monte Carlo method, and investigate unit cells with $4 \leq N \leq 20$ particles. Despite these refinements, we find no new crystal structures that pack denser than the $N = 4$ dimer crystals I and II for $s \in [0.02, 0.12]$. Subsequently, we determine the maximum packing fraction of the quasicrystal approximant reported in Ref. [47] by further compressing the unit cell of the quasicrystal approximant of $N = 82$ particles. In Fig. 4.15, we plot the maximum packing fraction for the quasicrystal approximant obtained in this work and the earlier results from Ref. [47] (large orange and blue dots, respectively) along with the maximum packing fractions of the crystal structures with a unit cell of $N \leq 20$ particles (small red dots). We make the following observations. In comparison to Jin *et al.* [47] we find higher packing fractions for the quasicrystal approximant for $s \in [0.065, 0.115]$, but slightly lower for $s \in [0.02, 0.06]$. The most interesting part, however, is that the maximum density of the approximant surpasses that of the smaller unit cells for $s \in [0.04, 0.088]$. This is quite unique: all the densest packings of single-component systems reported in literature up until now (that we are aware of) have had unit cells with $N \leq 4$ [40, 41, 159, 161, 167, 171, 177, 200], making the $N = 82$ approximant the largest unit cell for a densest packing of a single-component hard-particle system to date. It also raises the fascinating question whether the densest packing of spherotetrahedra in this shape regime may even be a truly aperiodic quasicrystal. Determining whether this is the case is not trivial. One possible means would be to construct quasicrystal approximants with increasingly larger unit cells and to determine their density to see whether it increases with the system size. A similar approach was taken for hard tetrahedra in Ref. [168]. However, it was found that a quasicrystal approximant of $N = 1142$ particles does not necessarily correspond to a higher density than an approximant with $N = 82$. Thus, it is not clear whether this approach will

even be able to answer the question definitively. Furthermore, the construction of such cells necessitates resolving the orientations of the particles such that the approximant is a non-overlapping configuration of spherotetrahedra, and it is at present not clear to us how to do so analytically. A brute force generation is also out of the question due to the rapidly increasing number of particles required to form an approximant prohibiting the efficient exploration of the available phase space required to find valid dense packings. Due to the aforementioned difficulties, we will not pursue this question further in this thesis. However, we consider it a promising and intriguing question to try to answer. Its possible implication — that the densest packing for some (even convex!) shapes cannot always be achieved with a periodic structure — seems profound in some ways, and we would be interested to see it revisited in the future.

4.4 Phase behaviour at intermediate density

In this section we will investigate the full phase behaviour of hard spherotetrahedra as a function of density. To study the self-assembly, we perform Monte Carlo simulations in the canonical (NVT) ensemble using the disordered fluid phase as the initial configuration. We use a relatively large number of Monte Carlo cycles, $M \sim 10^7 - 10^8$, to study the self-assembly from the fluid phase as previous simulations showed that the formation of a quasicrystal of hard tetrahedra is a slow process [166, 168, 191]. Additionally, we measure the equations of state i.e. the pressure as a function of density, of the fluid and solid phases by performing Monte Carlo simulations in a constant-pressure (NpT) ensemble in which the shape of the simulation volume is allowed to deform in order to allow stresses in the crystal to relax. We determine the phase boundaries by combining information from the equations of state and the structure metrics \bar{q}_l . The former is sufficient when phase transitions are accompanied by a large jump in density, while the latter allows us to perceive structural transformations even if the density of the two phases is very similar. We show the equations of state starting from either the fluid, a dense packing lattice or the quasicrystal approximant for a selection of shape state points s in Figure 4.16. Additionally, we show in Fig. 4.17 the structure metrics \bar{q}_4 versus \bar{q}_6 for the crystal phases I-VII, the quasicrystal QA and the fluid phase. At a glance, most structures are fairly well separated in this representation, but there is significant overlap between the distributions of I and VII, I and V, and the fluid and the quasicrystal approximant. Of course, these structures may only overlap in this particular representation, but perhaps not in another e.g. \bar{q}_2 versus \bar{q}_{10} . In Chapter 5 we perform a detailed analysis of the high-dimensional structure metric space for this system, where we use Principal Component Analysis to reduce its dimensionality and determine which order parameters are important for distinguishing the various spherotetrahedron phases.

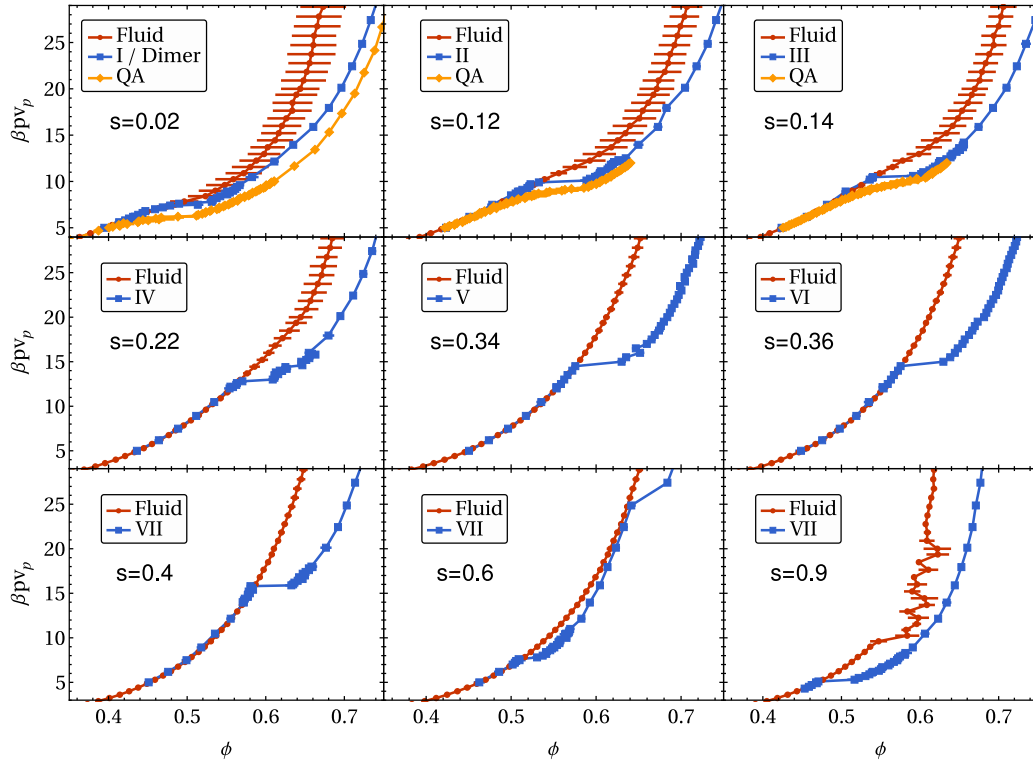


Figure 4.16: Packing fraction ϕ versus dimensionless pressure βpv_p equations of state for a selection of shape state points s . The legend marks the different initial configurations, which were either a disordered fluid, a dense packing lattice, or the quasicrystal approximant. All dense packing lattice equations of state display a jump at their melting pressure.

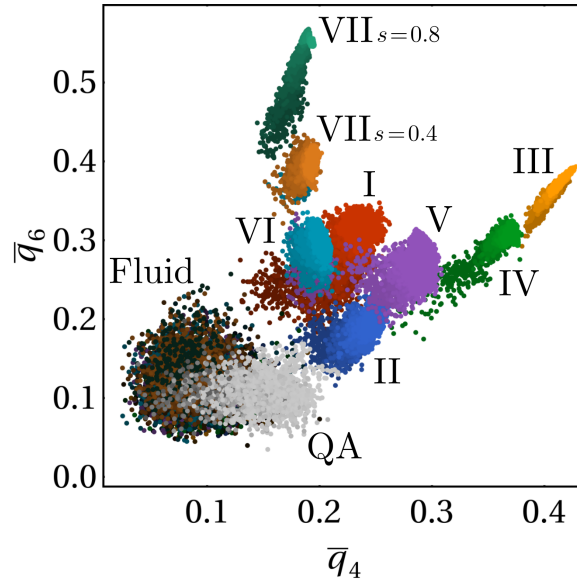


Figure 4.17: Distributions of structure metrics \bar{q}_4 versus \bar{q}_6 for crystals I ($s = 0.04$), II ($s = 0.12$), III ($s = 0.14$), IV ($s = 0.22$), V ($s = 0.34$), VI ($s = 0.36$), VII ($s = 0.4$ and $s = 0.8$), the quasicrystal QA ($s \in [0.02, 0.1]$) and the fluid phases for all these rounding ratios. The color distinguishes the different solid phases, while the brightness of the color indicates the packing fraction: the darker the color, the lower the packing fraction.

4.4.1 Quasicrystal self-assembly near $s = 0$

For shapes close to tetrahedra ($s \in [0, 0.16]$), a quasicrystal self-assembles from the fluid phase, as apparent from the twelve-fold symmetry present in the diffraction pattern in Fig. 4.18. We only found clear quasicrystal self-assembly during long NVT ensemble simulations and not in our NpT ensemble simulations, probably because the latter were ran for a shorter duration and for smaller system sizes and quasicrystalline order is more difficult to detect for such small systems. For both the dense packing and the approximant the density and pressure at which they melt increases as the particle shape becomes rounder. For $s = 0$ [168] and $s = 0.02$ (Fig. 4.16) both the dimer crystal and the approximant melt at a packing fraction of $\phi \approx 0.51$. For $s = 0.14$ this increases to $\phi \approx 0.61$. Since the densest packing for $s \in [0.040, 0.088]$ is the quasicrystal approximant, it is likely that quasicrystalline order is stable all the way from the fluid up to the maximum packing. However, the approximant and the quasicrystal are not strictly identical, and there may be a transition from one to the other at a certain density. Current evidence suggests that the approximant is the stable phase for tetrahedra ($s = 0$), but the difficulty of calculating the free energy of a quasicrystal prevents the confirmation of that hypothesis [168]. Our equations of state do not display a transition from the approximant into the quasicrystal, and so we will assume that the equilibrium phase is the approximant when a) the self-assembled phase shows quasicrystalline order for that s and b) the approximant can reach that packing fraction ϕ .

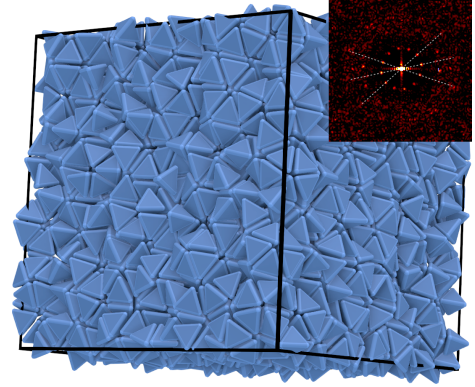


Figure 4.18: A quasicrystal self-assembled from a disordered fluid phase of hard spherotetrahedra with a shape parameter $s = 0.16$ at a packing fraction $\phi = 0.64$. The diffraction pattern is averaged over 100 configurations and displays the 12-fold symmetry indicative of a dodecagonal quasicrystal.

4.4.2 Plastic crystal pFCC for $s > 0.5$

For $s = 0.6$ an additional jump from a packing fraction of $\phi \approx 0.69$ to $\phi = 0.64$ can be seen in the equation of state starting from crystal VII. We show in Fig. 4.19 that this higher density jump corresponds to crystal VII melting into a plastic undeformed face-centered cubic crystal, which we label pFCC. The inset shows bond order diagrams (BOD) for each of the three branches of the equation of state. The BODs are histograms of the angular distribution of bonds between particles: sharp peaks denote bond-orientational order, and thus translational order. In the diagrams labeled OBCD (Orientation Bond Correlation Diagram), the bonds are additionally rotated by the orientation of the neighbouring particle, which makes the diagram represent not only positional but also (particle) orientational order. For $\phi > 0.69$, both the BOD and the OBCD show sharp peaks, indicating both positional and orientational order. For $0.53 \leq \phi \leq 0.64$ the BOD shows sharp peaks at the same positions as for $\phi > 0.69$, but the OBCD is disordered, indicating positional

order but no orientational order, *i.e.* a plastic crystal. For $\phi < 0.53$ both diagrams are disordered, corresponding to a fluid phase. The same loss of orientational order but preservation of positional order can also be seen from the snapshots shown in Fig. 4.19b-e. A similar inspection for the shape parameter range $s \in [0.5, 1.0]$ reveals that this VII-pFCC transition occurs at increasingly higher densities as the shape becomes rounder. This is to be expected: at $s = 1$ the particle shape reduces to a sphere, for which the orientation no longer matters and any crystal must be a plastic crystal. Furthermore, the deformation of crystal VII reduces with increasing s , and it reduces to the undeformed FCC at $s = 1$. Thus, when approaching $s = 1$ the VII-pFCC transition must approach the hard sphere close packing density. We find this is exactly what happens.

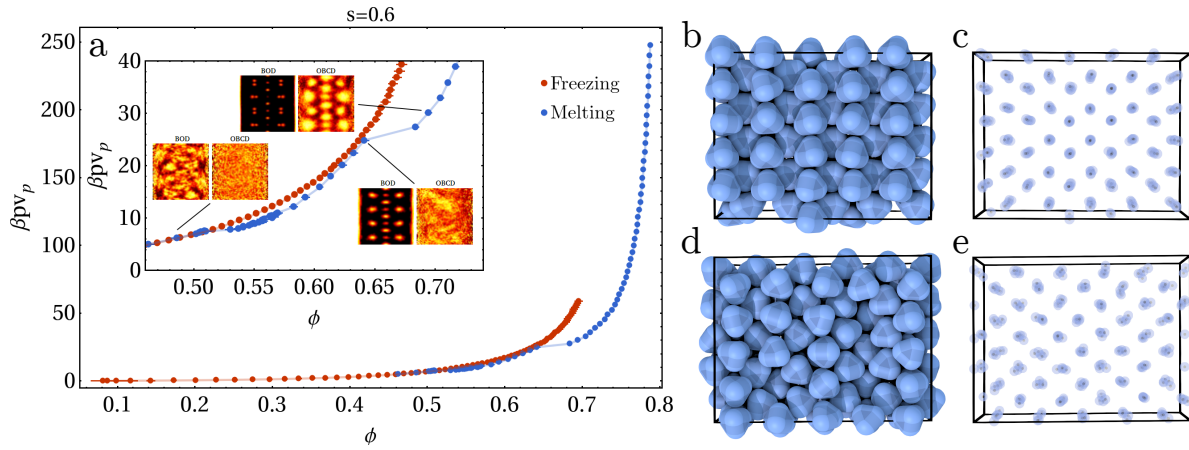


Figure 4.19: (a) Pressure $\beta p v_p$ versus packing fraction ϕ equation of state for hard spherotetrahedra with a shape parameter $s = 0.6$, starting from either (blue) the dense packing crystal VII or (red) a disordered fluid. The inset zooms in on the region for which a plastic crystal is found. For the plastic crystal pFCC, the BOD shows sharp peaks while the OBCD is disordered, indicating the simultaneous presence of positional order and absence of orientational order characteristic of a plastic crystal. (b,c) Snapshots of the particles (b) and their centroids (c) at a pressure of $\beta p v_p = 27.42$. (d,e) similar snapshots at $\beta p v_p = 24.84$. There is a clear loss of orientational order, but the centroids reveal that positional order is preserved.

4.4.3 Absence of crystallization for $s \in (0.16, 0.5)$

Despite the aforementioned high number of Monte Carlo cycles, we do not observe any crystallization whatsoever in the region $s \in (0.16, 0.5)$. Figure 4.20 shows the structure metrics $\langle \bar{q}_2 \rangle$, $\langle \bar{q}_4 \rangle$, ..., $\langle \bar{q}_{12} \rangle$ averaged over the final configurations of a series of self-assembly simulations at packing fractions $\phi \in [0.45, 0.68]$. For these simulations we rapidly compressed a disordered fluid to the shown packing fraction, then ran a MC simulation in the NVT ensemble for $10^7 - 10^8$ MC cycles - enough to observe the early stages of the slow formation of the tetrahedron ($s = 0$) quasicrystal, though admittedly not enough for it to fully relax to a single quasicrystalline equilibrium state. The $\langle \bar{q}_l \rangle$ for the fluid state are all consistently in the range $\langle \bar{q}_l \rangle \in [0.04, 0.12]$, except for $\langle \bar{q}_2 \rangle$, which is usually smaller, about $\langle \bar{q}_2 \rangle \in [0.01, 0.04]$. For small rounding ratios $s \in [0, 0.16]$ we observe a small bump in the values of $\langle \bar{q}_2 \rangle$ and $\langle \bar{q}_4 \rangle$, which upon inspection of the diffraction pattern coincides

with the early stages of the formation of a dodecagonal quasicrystal (see Fig. 4.18). We see no notable change in the other order parameters. The rather small increase in the $\langle \bar{q}_l \rangle$ for the quasicrystal in comparison to the fluid suggests that the \bar{q}_l are not particularly good order parameters for capturing quasicrystalline order. In fact, as suggested by Fig. 4.17, the \bar{q}_l of the quasicrystal are quite low and very similar to the fluid. We discuss the quality of the \bar{q}_l as order parameters for the quasicrystal in further detail in Chapter 5. For large rounding ratios $s \in [0.54, 1]$ we find a significant increase in $\langle \bar{q}_4 \rangle$, $\langle \bar{q}_6 \rangle$, $\langle \bar{q}_8 \rangle$ and $\langle \bar{q}_{12} \rangle$ accompanying the formation of a plastic FCC crystal. In the intermediate range $s \in (0.16, 0.5)$ we observe no significant changes in any of the $\langle \bar{q}_l \rangle$, and neither the real-space visualizations of the final configurations nor their corresponding diffraction patterns show the self-assembly of any ordered structures. Furthermore, the melting density of the crystals in this region is relatively high, about $\phi \approx 0.6$. This absence of self-assembly was also found for similarly shaped truncated tetrahedra [176, 178], which was attributed to the competition of multiple local structural motifs [179]. We investigated the similarity of the structural composition of the fluid and of the dense packings by comparing their radial distribution functions $g(r)$ near the melting density. These are shown in Fig. 4.21. Also shown are the coordination numbers CN of the fluid, crystal and quasicrystal phases, defined as the integral of $g(r)$ up to their first minimum. For the two structures whose self-assembly we *do* observe, the quasicrystal QC and plastic crystal pFCC, the corresponding radial distribution functions are quite similar to those of the high density fluid. Structures III-VII, however, are relatively dissimilar to the high density fluid. Possibly, the structural dissimilarity between the fluid and solid phases inhibits crystallization in this region $s \in (0.16, 0.5)$. There may be both a statistical and a dynamic effect at play here: the structural dissimilarity may provide a high nucleation barrier, while the high density slows down the dynamics such that the exploration of phase space required to surmount the barrier is further inhibited.

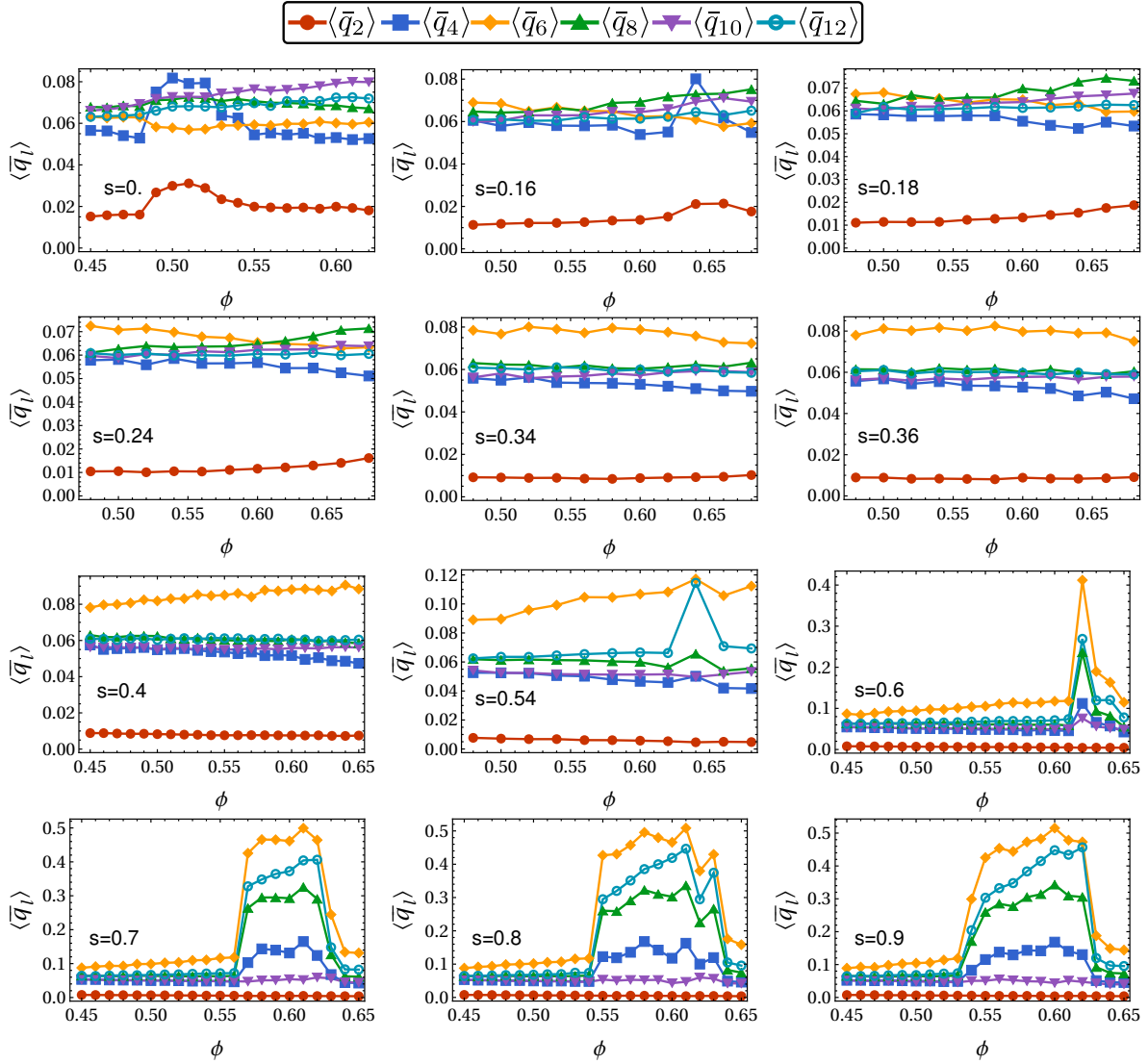


Figure 4.20: Snapshot averages of averaged Minkowski structure factors $\langle \bar{q}_l \rangle$ as a function of packing fraction ϕ for a series of self-assembly simulations with a fluid as initial configuration. For $s = 0$ and $s = 0.16$ a bump can be seen in $\langle \bar{q}_2 \rangle$ and $\langle \bar{q}_4 \rangle$ which coincides with the nucleation of a dodecagonal quasicrystal. For $s > 0.54$, a similar peak occurs in $\langle \bar{q}_4 \rangle$, $\langle \bar{q}_6 \rangle$, $\langle \bar{q}_8 \rangle$ and $\langle \bar{q}_{12} \rangle$ which indicates the nucleation of a face-centered cubic lattice. No peaks are observed for $0.16 < s < 0.54$, indicating that no ordered structures have formed in these simulations. The lack of order when starting from a high packing fraction fluid also suggests a strong slowdown of dynamics.

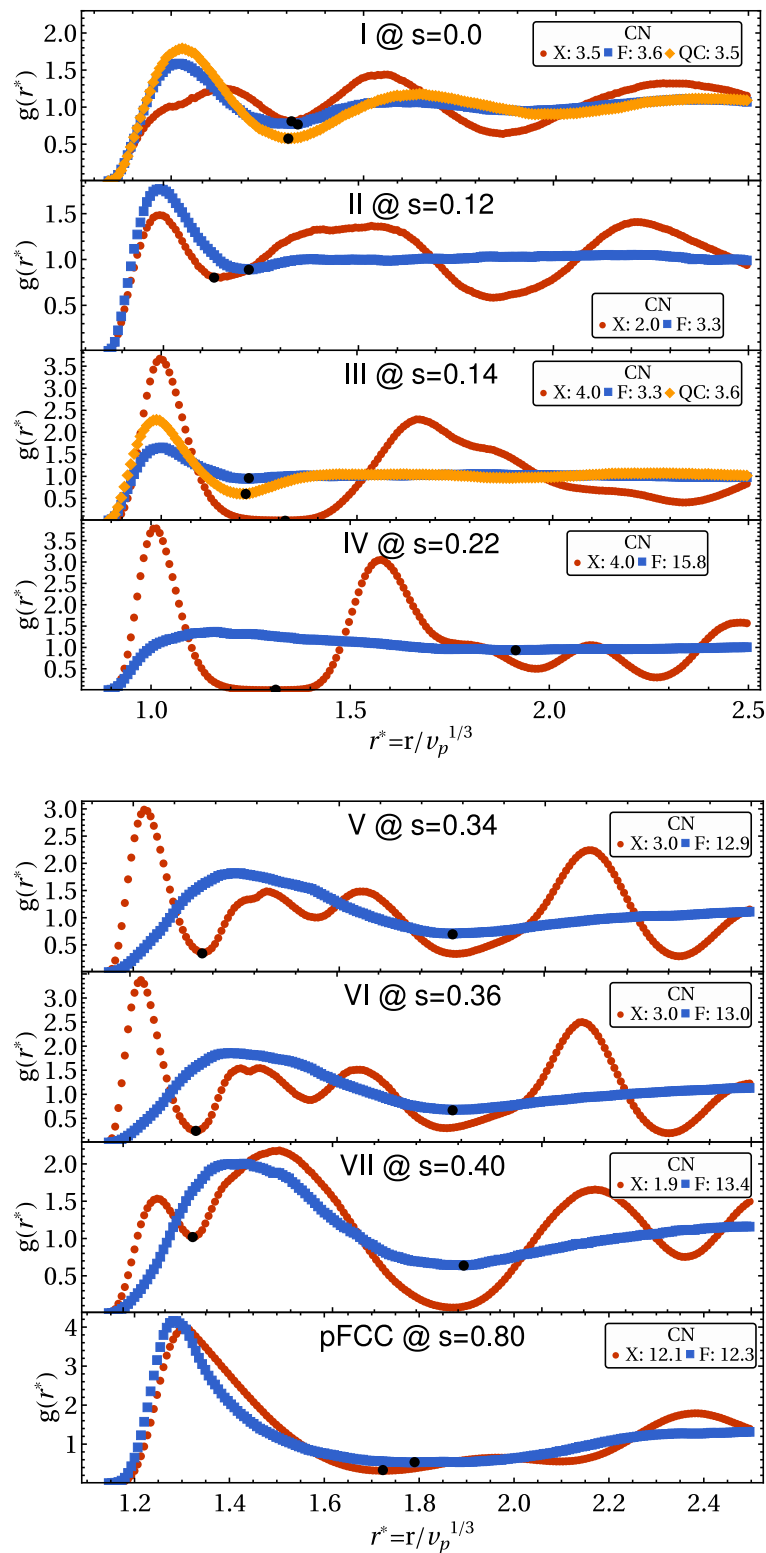


Figure 4.21: Radial distribution functions $g(r)$ taken near the melting transition for various crystal structures, along with their corresponding coordination numbers, defined as the integral of $g(r)$ up to its first minimum, which is indicated by the black dots. “F” indicates the fluid, “X” the crystal and “QC” the quasicrystal, if present. As a general trend, whenever the difference in $g(r)$ between the crystal and the dense fluid is large, the crystal does not self-assemble (easily).

4.4.4 Transitions between crystals V, VI and VII

For $s \in [0.32, 0.36]$ and $\phi \approx 0.62$, we find that the structures V and VI do not melt directly into a fluid, but instead follow the sequence $V \rightarrow VI \rightarrow VII \rightarrow \text{Fluid}$ *i.e.* the less symmetric crystal structures first transform via solid-solid transitions into more symmetric structures before fully melting. This is somewhat visible from the equations of state in Fig. 4.16, but it is most clearly seen in by evaluating the order parameters \bar{q}_l , either their distributions as shown in shown in Fig. 4.22 or their snapshot averages as in Fig. 4.23. Fig. 4.22 shows the structure metrics \bar{q}_4 versus \bar{q}_6 with the distributions for $s = 0.34$ and $s = 0.36$ highlighted in purple and teal. For both Figs. 4.22 and 4.23 the order parameters were obtained from the final configurations of long (10^8 MC cycles) MC simulations in the isothermal-isotension ensemble for rounding ratios $0.31 \leq s \leq 0.38$ and pressures $12 \leq \beta p v_p \leq 45$. The densest packings at these rounding ratios served as the initial configurations for these simulations, these were structures V and VI for $s = 0.34$ and $s = 0.36$ in Fig. 4.22, respectively. For $s = 0.34$ there are three clearly separated distributions (plus that of fluid), corresponding to structures V, VI and VII. For $s = 0.36$ the two distributions belonging to structures VI and VII are also clearly separated. By mapping the snapshot averages \bar{q}_l against the density as we do in Fig. 4.23 we can additionally estimate the coexistence densities from the density gap between the two phases. One should however note that this estimate requires the phase transition to actually take place in simulation, which for the solids may require very long simulation times, especially if it should occur at higher densities. Furthermore, the small system size we employed for these simulations ($N \sim 250\text{-}500$ particles) introduces finite-size effects that may shift the boundaries. A more accurate estimate can be obtained by resolving the relative free energies e.g. using the Frenkel-Ladd method [201, 202] for the solids, but we shall not do so in this chapter.

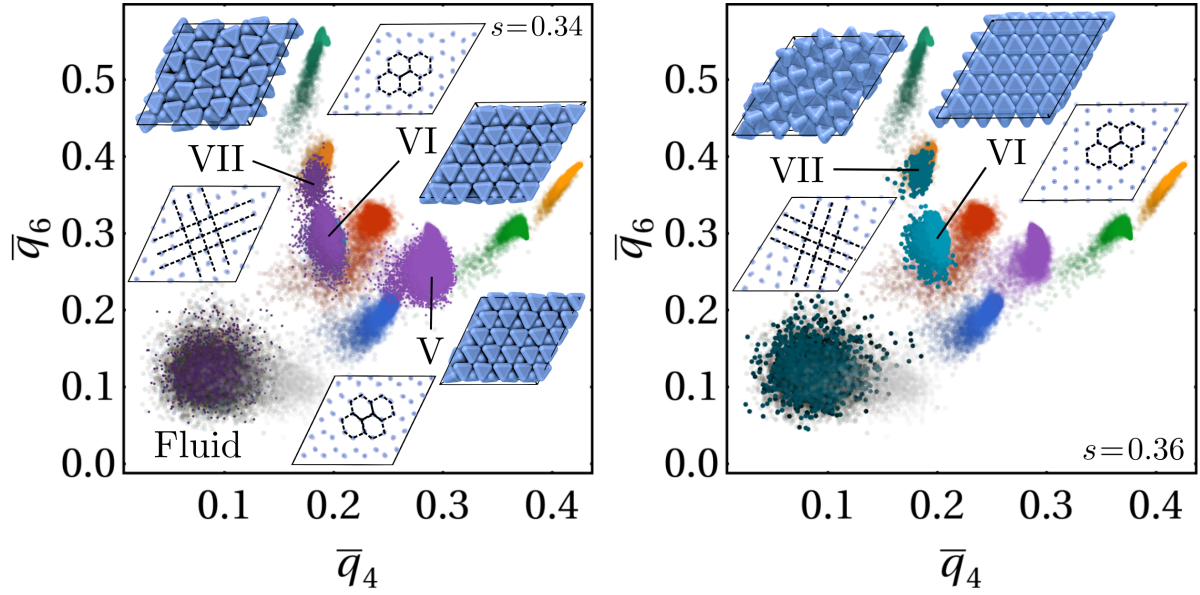


Figure 4.22: Structure metric distributions \bar{q}_4 versus \bar{q}_6 , highlighting the transitions between structures V, VI and VII for $s = 0.34$ (purple) and $s = 0.36$ (teal). Also shown are snapshots of a crystal plane where $V \rightarrow VI$ is represented by the symmetrization of a hexagon, and $VI \rightarrow VII$ by going from a hexagonal projection to a roughly square one.

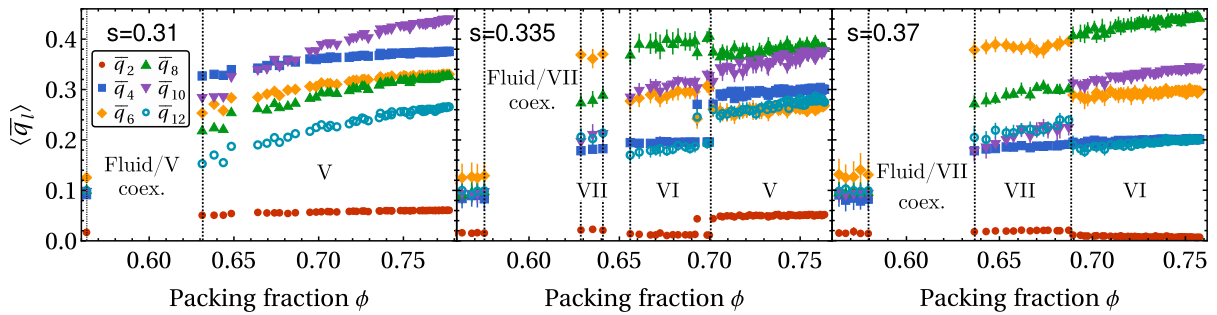


Figure 4.23: Snapshot averaged structure metrics $\langle \bar{q}_i \rangle$ as a function of the packing fraction ϕ for a set of NpT simulations with the densest packing as initial configuration. The boundaries between phases can be seen as discontinuities in $\langle \bar{q}_i \rangle(\phi)$, while the gaps between phases denote the coexistence regions.

To conclude this section we summarize the observed phase behaviour as a function of the shape s and packing fraction ϕ in the phase diagram shown in Fig. 4.24. We indicate the estimated phase boundaries between solid phases that were not determined with reasonable accuracy with dotted lines. These remaining boundaries are all hindered by the slow dynamics associated with the high density at which they are likely to be found (I, II, III, primed lattices), small structural differences inhibiting a clear distinction between the two relevant phases (primed lattices), or the inherently slow dynamics of the quasicrystal (the QA/IV boundary). All these could be much better determined using free-energy calculations, but we leave this refinement to future work.

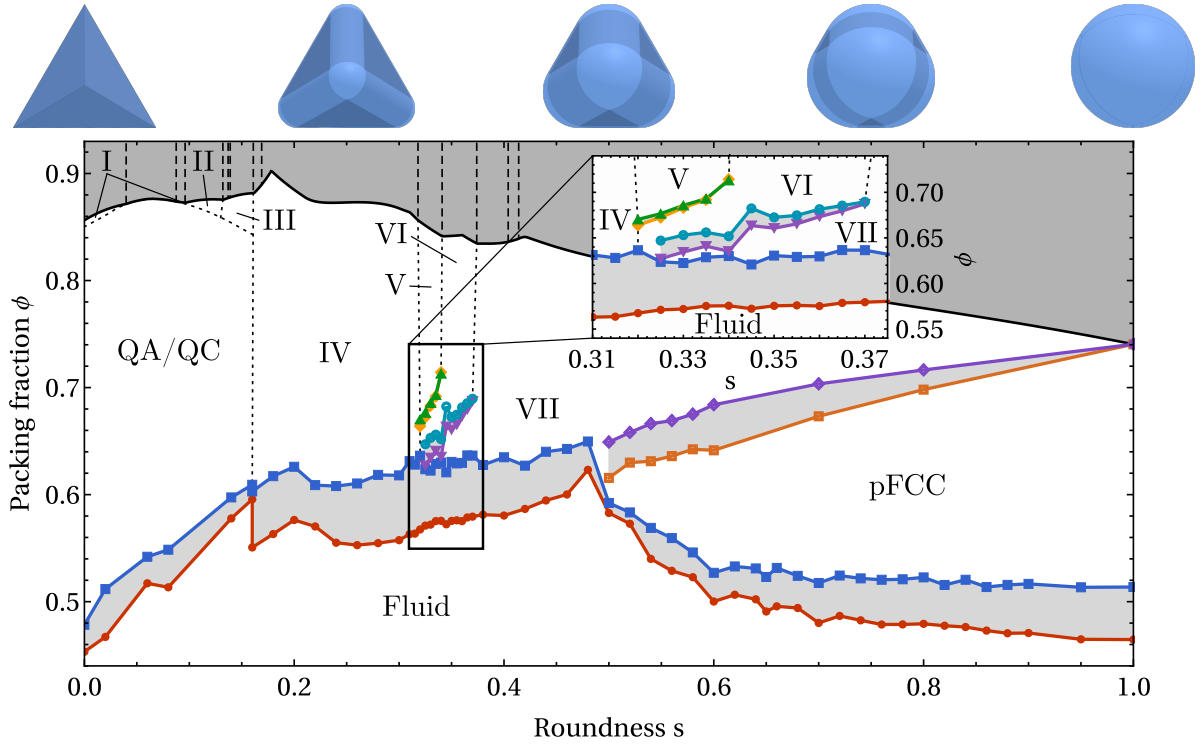


Figure 4.24: Phase diagram of hard spherotetrahedra in the shape parameter s and packing fraction ϕ representation, with the forbidden region beyond close-packing in dark gray. Solid lines in the forbidden region denote transitions between densest packings. Symbols (connected by a solid line to guide the eye) denote the boundaries of the gray shaded coexistence regions. Dotted lines indicate estimates for phase boundaries of solid phases for which transitions were not observed.

4.5 Conclusions & Outlook

In this chapter we have investigated the dense packings and phase behaviour of hard spherotetrahedra, a family of shapes that interpolates between hard tetrahedra and hard spheres. Our results demonstrate the structural complexity that arises in the solid phases of these particles due to a competition between directional entropic forces from flat facets, geometric constraints to achieve the densest packing, and rotational entropy. In the dense-packing limit, rounding tetrahedra enforces the formation of complex distorted lattices

where symmetries are broken in order to achieve optimal packing. We have found thirteen separate close-packed structures, most of which are significantly denser than previously reported [47]. Most strikingly, we find the $N = 82$ quasicrystal approximant to be the densest packing for a shape parameter $s \in [0.04, 0.088]$, in partial agreement with Jin et al. [47]. To the best of our knowledge, this is the largest unit cell for the densest packing of any single-component hard-particle system found thus far [40, 41, 159, 161, 167, 171, 177, 200]. That the densest packing for this system is a quasicrystal approximant again raises the fascinating possibility of an aperiodic densest packing. We could not determine whether it is the periodic approximant that is densest or the aperiodic quasicrystal in this work. A more rigorous study is needed to resolve this question.

At intermediate densities, rounding the edges and vertices of tetrahedra seems to have a dramatic effect on the crystallization rate and melting density of crystal phases, to the point where we did not observe any crystallization from the fluid phase for $s \in (0.16, 0.5)$ even after 10^8 Monte Carlo cycles. The lack of self-assembly for similarly shaped truncated tetrahedra [178] was attributed to a competition between several local structural motifs [179]. Given the many dense packings we observe in this region, a similar mechanism may be at play here as well. It would be interesting to see in which way truncation and rounding of polyhedra differ in the suppression and enhancement of self-assembling (quasi)crystal structures. Perhaps even greater control could be achieved by combining them.

Acknowledgements

This chapter came about as part of two separate collaborations, one together with Da Wang to investigate the behaviour of rounded tetrahedral nanoparticles, and another with Gabriele Coli to study the viability of dimensionality reduction for automating the classification of crystal phases. I would like to thank Da for motivating this study and for discussions on the experimental properties and findings on this system, and Gabriele for many discussions on machine learning and dimensionality reduction. We continue both collaborations in the next two chapters.

5

Determining order parameters for crystals of rounded tetrahedra using dimensionality reduction

In this chapter we investigate how to automate the process of finding good order parameters to identify and distinguish between various crystals of hard rounded tetrahedra. We do this by performing a Principal Component Analysis (PCA) on a data set containing trajectories from all rounded tetrahedron phases that we observed in Chapter 4. The simplicity of PCA provides us immediate insight into which bond order parameters \bar{q}_l are most important for the classifying the various phases. We perform this PCA on two sets of candidate order parameters, one containing the local bond order parameters \bar{q}_l with $2 \leq l \leq 12$ and one containing both \bar{q}_l and w_l with $2 \leq l \leq 24$. In both cases we find that the first principal component yields a general measure for crystallization, while the second and third principal components serve to distinguish the various crystal phases from one another.

Based on:

R. van Damme, G.M. Coli, R. van Roij and M. Dijkstra, “*Classifying Crystals of Rounded Tetrahedra and Determining Their Order Parameters Using Dimensionality Reduction*”, ACS Nano, 14, 11, 15144–15153 (2020)

5.1 Introduction

Categorizing the behaviour of molecular systems into distinct thermodynamic phases is an essential part of modern material design. However, for anything beyond trivial model systems, this cataloguing can be a serious challenge. Take water, for instance. While most people are only familiar with its liquid and solid ice phases, its phase diagram as we currently understand it features no fewer than 17 different possible phases of ice [203], and this number is still growing. Water has been studied in detail for many years, and there is a large amount of previous literature to use as a starting point when trying to identify new phases. What if this were not the case? How would we determine a phase diagram for a molecular or colloidal system for which we lack this luxury of prior knowledge? Roughly speaking, the process of constructing a phase diagram in such a case can be divided into three steps: i) the generation of particle trajectories, ii) finding a set of variables that can distinguish between the various phases and iii) using these variables to classify phases and construct the phase diagram. The first step can be performed with a large variety of molecular dynamics (MD) or Monte Carlo (MC) based techniques, and these can be automated quite effectively already. The latter two steps, however, often involve a fair amount of trial and error. In the previous chapter we have performed these three steps manually, and in this chapter we will investigate how to automate the second step. Let us first frame the problem in the language of equilibrium statistical thermodynamics. Within this framework, the different phases manifest as distinct probability distributions $P(\Gamma)$ in the phase space Γ . This phase space is typically extremely high-dimensional, as it is spanned by all possible coordinates of all the particles in the system.

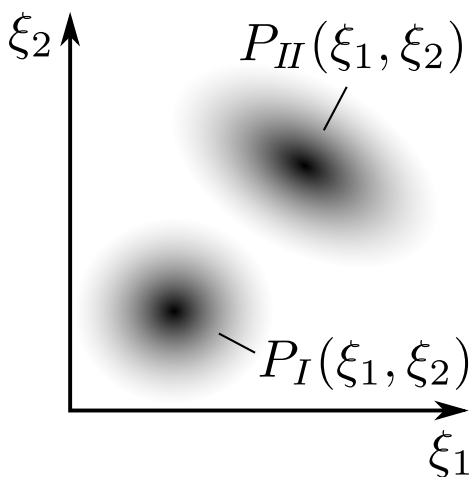


Figure 5.1: Schematic representation of the probability distributions $P_I(\xi_1, \xi_2)$ and $P_{II}(\xi_1, \xi_2)$ of two phases that are separable by the order parameters ξ_1 and ξ_2 .

In general, these probability distributions are not separable by looking at the raw values of the particle coordinates Γ that make up the trajectories we obtain from MC/MD. However, they can be separated by considering specific functions $\xi(\Gamma)$ of these coordinates, such as the distance between two specific atoms in DNA [204] or the tetrahedrality of bonds between water molecules forming ice Ih [205]. We call these functions *collective variables* or *order parameters*. Good order parameters are rarely known *a priori*, but one can often guess decent candidates. Figure 5.1 shows an example of a close to ideal choice of order parameters ξ_1 and ξ_2 . In the space spanned by these two variables, the probability distributions of two phases $P_I(\xi_1, \xi_2)$ and $P_{II}(\xi_1, \xi_2)$ are completely separable. It is finding these functions $\xi(\Gamma)$ what constitutes the trial-and-error process that we alluded to earlier.

For the problem of identifying and distinguishing between different crystal structures specifically, there exist classes of functions that are known to often yield good candidates. One such class, and the one we will consider in this chapter, are the *bond-orientational order pa-*

rameters (BOPs), which describe the symmetry of the bonds* that individual particles make with other nearby particles. Their origin traces back to the hexatic order parameter proposed by Nelson, Rubinstein and Spaepen [206], which they used to investigate structural order in 2D systems of hard disks. Shortly after Steinhardt, Nelson and Rochetti [182] proposed a three-dimensional variant that describes local structure by expanding the bond directions between particles into spherical harmonics. These bond-orientational order parameters (BOPs) have found great success in describing local structure, and have been used to study nucleation in systems including hard spheres [183, 207–210], Lennard-Jones systems [211–213], ice [214] and sodium chloride [215], defects in crystals [216], and links between structure and dynamics in glasses [217–219]. Many improvements and variations have been proposed since Steinhardt’s seminal work. Auer and Frenkel used the Steinhardt q_{lm} to construct a local order parameter for nucleation and used this to measure the nucleation barrier of hard spheres [208]. Lechner and Dellago improved the resolving power between FCC, HCP, BCC and fluid phases by averaging the q_{lm} over the second neighbour shell [186]. Parameter-free versions of the bond-orientational order parameters have been proposed by both Meel et al. [185] and Mickel et al. [184], the latter of which also proposed a weighting to make these parameters less susceptible to thermal fluctuations. One key parameter in all variants of the bond order parameters is the quantum number l that prescribes the symmetry of bonds to capture. By far the most popular choice is to look at $l = 4$ and $l = 6$, for which FCC, HCP, BCC and fluid phases are usually well-resolved. Most literature on crystal phase identification has been restricted to a small set of order parameters. Historically, good order parameters are discovered and subsequently re-used often.

With recent advances in computing power and the growing popularity of machine learning (ML) methods, however, a different methodology is developing. These new methods are rapidly being applied to take over the task of human trial and error in finding good order parameters. Instead, one typically considers a large set of candidate order parameters, and applies statistical or ML techniques to filter out the good ones. This process, however, is often opaque. Neural networks are often used as “black box” methods, in which questions such as “which features are the most important?” can be difficult to answer.

In this chapter we explore this new methodology by using the hard spherotetrahedron system as a testbed. In the previous chapter we found that a system of hard spherotetrahedra has a diverse set of possible phases, featuring seven crystal phases and additionally both a quasicrystal and a plastic crystal phase. We found that in the dense packing limit one can identify crystal-crystal transitions by simultaneous discontinuities in the shape dependence of the Minkowski structure metrics \bar{q}_l . For most of the crystal structures we found, these structure metrics are non-zero. One thing we did not investigate, however, is which structure metrics are the most important. Can we capture the nucleation of all crystal structures with $l = 4$ and $l = 6$? Which order parameters do we need to distinguish between the different phases at finite density? How many q_l do we really need to do this?

Finding the essential features (\bar{q}_l ’s) that distinguish different phases is an example of

*A “bond” in this case does not denote a *chemical* bond, but rather simply the vector between two nearby particles, regardless of their chemical or physical interaction.

a dimensionality reduction problem. The generic problem is to project high-dimensional data onto a space of much smaller dimension while preserving a notion of similarity: “close” structures in the high-dimensional space should remain close even in the subspace, and likewise for those “far away”. Instead of using an opaque neural-network-based method to tackle this problem, we use the simple and transparent method of Principal Component Analysis (PCA), which defines a linear basis transformation in such a way that the projection of the data onto a hopefully small subset of these so-called “principal components” carry most of the variance or information of the data. Specifically, PCA provides two directly interpretable objects: a set of eigenvalues from which the effective dimensionality of the data set can be inferred, and a set of eigenvectors (particular linear combinations of \bar{q}_l ’s) that provides information which features (\bar{q}_l ’s) are most relevant.

This chapter is laid out as follows: in section 5.2 we describe how we construct the data set of trajectories to which we apply PCA. In section 5.3 we apply the PCA to a data set of all \bar{q}_l with $l = 2, 3, 4, \dots, 12$, while in 5.4 we consider a larger data set of all \bar{q}_l with $l = 2, 3, 4, \dots, 24$ as well as w_l with $l = 2, 4, 6, \dots, 24$.

5.2 Data set construction

We construct our bond order data set from the NpT Monte Carlo simulations of hard rounded tetrahedra performed in Chapter 4, with typically 250-256 particles in the simulation box for crystalline structures and 1968 particles for the quasicrystal approximant (QA) structure. For 25 equidistantly distributed particles shape parameters $s \in \{0.02, 0.04, \dots, 0.5\}$ and for 5 additional ones $s \in \{0.6, 0.7, 0.8, 0.9\}$, we calculate for every particle in the system the set of eleven bond order parameters $|q\rangle \equiv (\bar{q}_2, \bar{q}_3, \dots, \bar{q}_{12})$, for many configurations at pressures p in the interval $5 \leq pv_p/k_B T \leq 250$ with v_p the particle volume and T the temperature. Here the \bar{q}_l are the Minkowski Structure Metrics (MSM) proposed by Mickel et al. [184], where the complex q_{lm} have been averaged over the first neighbour shell according to the method of Lechner and Dellago [186]. For a more detailed description of these order parameters, see Section 4.2.3. The use of the “ket-vector” notation for the one-particle state $|q\rangle$ will become clear below. In the crystalline states for $s \geq 0.1$ we consider 55 pressures p yielding packing fractions $\phi \in [0.38, 0.88]$, and in the QA states for $0.02 \leq s \leq 0.1$ we consider 58 pressures yielding $\phi \in [0.28, 0.86]$. We thus consider configurations of all phases in the phase diagram of spherotetrahedra, *i.e.* the fluid phase, the quasicrystal approximant phases, and all crystal phases at close-packing and intermediate densities. This provides us with an $11 \times \mathcal{N}$ matrix of input data, where $\mathcal{N} = \sum_{\{s\}} N_s N_{c,s} = 987180$ with s the label of the considered shapes and N_s and $N_{c,s}$ the number of particles and the total number of configurations considered for particle shape s , respectively. This large matrix thus contains all the information on the local structure of all particles in the various thermodynamic phases and of the various shapes considered. In fact we also considered an even higher-dimensional set of bond order parameters in which we included the \bar{q}_l structure metrics with as well as their higher-order invariants w_l , both with $2 \leq l \leq 24$, for which the corresponding one-particle states were $|Q\rangle = (\bar{q}_2, \bar{q}_3, \dots, \bar{q}_{24}, w_4, w_6, \dots, w_{24})$ and the input data matrix thus has $35 \times \mathcal{N}$ elements.

5.3 Principal component analysis with \bar{q}_l for $2 \leq l \leq 12$

We perform a PCA on the $11 \times \mathcal{N}$ data matrix, which gives rise to a symmetric 11×11 covariance matrix, scaled such that its trace (and hence the sum of its 11 eigenvalues) equals unity. We denote the eigenvalues of the covariant matrix by λ_i and its 11-dimensional eigenvectors in “bra-ket” notation by $|v_i\rangle$ for $i = 1, \dots, 11$. Note that all eigenvalues are real since the covariant matrix is hermitian by construction. Figure 5.2 shows the eigenvectors and eigenvalues obtained from this analysis. The three largest eigenvalues are $\lambda_1 = 0.66$, $\lambda_2 = 0.25$, and $\lambda_3 = 0.04$, such that (loosely speaking) the three-dimensional linear subspace $|v_1\rangle \oplus |v_2\rangle \oplus |v_3\rangle$ accounts for a fraction as large as $\lambda_1 + \lambda_2 + \lambda_3 = 0.95$ of the variance of the data, *i.e.* 95%, which signifies a substantial dimensionality reduction. Recalling that we denoted the one-particle state by the 11-dimensional ket-vector $|q\rangle = (\bar{q}_2, \bar{q}_3, \dots, \bar{q}_{12})$, we can define the inner product $y_i \equiv \langle v_i | q \rangle$ as the projection of $|q\rangle$ on the principal components $|v_i\rangle$ for $i = 1, 2, 3$. In addition to the projections y_i of one-particle states, it also turns out to be convenient to consider its average $\langle y_i \rangle$ over all particles in the system (for a given shape s at a given state point).

In Fig. 5.3 we show the resulting average projections $\langle y_1 \rangle$ (a), $\langle y_2 \rangle$ (b), and $\langle y_3 \rangle$ (c) as a function of the packing fraction ϕ , in all three cases for eight judiciously chosen particle shapes $s \in \{0.04, 0.12, 0.14, 0.22, 0.34, 0.36, 0.4, 0.8\}$ that exhibit at sufficiently high ϕ seven of the thirteen close-packed crystal structures or the plastic crystal pFCC. For the quasicrystal approximant (QA), we show data for $s = 0.06$. The pie charts in Fig. 5.3 represent the three dominant eigenvectors $|v_1\rangle$ (a), $|v_2\rangle$ (b), and $|v_3\rangle$ (c) also shown in Fig. 5.2(b,c,d), where the parts of the pie denote the weights of the eleven components \bar{q}_l (including the relative sign).

The first eigenvector $|v_1\rangle$ with eigenvalue $\lambda_1 = 0.66$ is seen to be comprised of all \bar{q}_l with l even in roughly equal measure, except for \bar{q}_2 which is virtually absent in $|V_1\rangle$. In other words, up to an overall scaling factor we have $y_1 \simeq \bar{q}_4 + \bar{q}_6 + \bar{q}_8 + \bar{q}_{10} + \bar{q}_{12}$, where we set the five $\mathcal{O}(1)$ coefficients exactly equal to unity for illustration purposes. The projection y_1 of the state of a particle (or its average $\langle y_1 \rangle$ over all particles) can thus be interpreted as an overall but non-specific measure for the degree of crystallinity of the particular state. This is confirmed by the ϕ -dependence of $\langle y_1 \rangle$ in Fig. 5.3(a), which for all particle shapes is a universal (non-zero) constant in the low- ϕ fluid state while any departure from this constant indicates a crystal structure. In the crystal regime, y_1 captures the increase in structural order with increasing density.

The second eigenvector $|v_2\rangle$ is dominated by large positive \bar{q}_{10} and \bar{q}_4 components and negative \bar{q}_6 and \bar{q}_{12} components. The corresponding projection is then, again up to an overall scaling factor and with rough estimates for the coefficients, given by $y_2 \simeq \bar{q}_4 - \bar{q}_6 + 2\bar{q}_{10} - \bar{q}_{12}$. The eigenvector $|v_2\rangle$, with eigenvalue $\lambda_2 = 0.25$ and hence capturing 25% of the variance of the data, therefore mainly distinguishes four-fold tetrahedron-like crystals (with large \bar{q}_4 and \bar{q}_{10}) from the hexagonal sphere-like ones (with large \bar{q}_6 and \bar{q}_{12}). Also this interpretation is confirmed by the density dependence of the average projection $\langle y_2 \rangle$ on $|v_2\rangle$ in Fig. 5.3(b) for all nine shapes, which clearly shows a positive result for crystal IV and many of the other tetrahedron-like crystals and (deeply) negative results for the structures pFCC and VII. Clearly, however, $\langle y_2 \rangle$ cannot disentangle many of the four-fold structures.

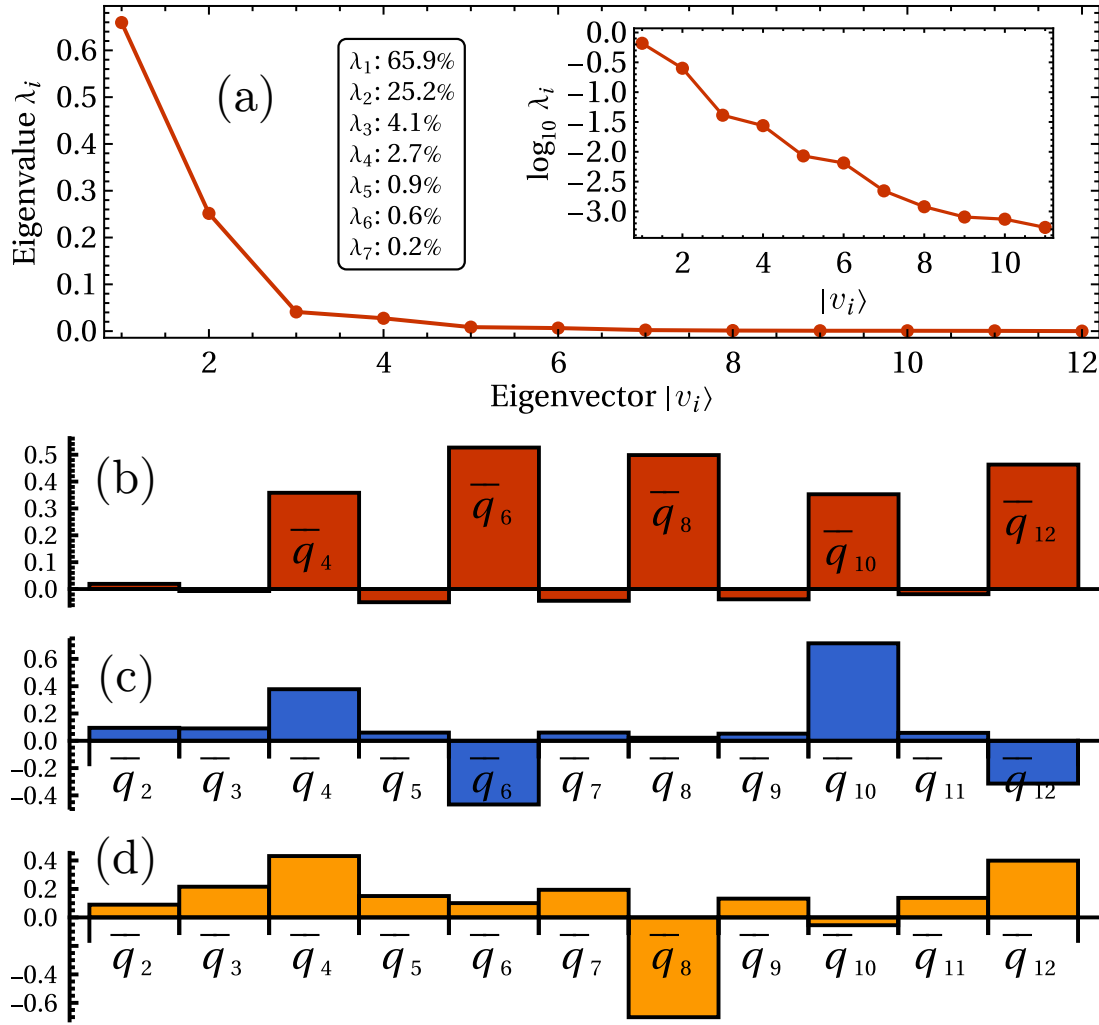


Figure 5.2: (a) Eigenvalues and first three eigenvectors of the PCA using $|q\rangle = (\bar{q}_2, \bar{q}_3, \dots, \bar{q}_{12})$ as input. The inset shows the eigenvalues on a logarithmic scale and the legend shows the percentage of the variance captured by each eigenvalue. A mild drop in eigenvalue can be seen after the second and fourth eigenvector. (b,c,d) The weights associated with each component \bar{q}_i for the three largest eigenvectors (b) $|v_1\rangle$, (c) $|v_2\rangle$ and (d) $|v_3\rangle$.

The disentanglement of many of the tetrahedron-like crystals is accomplished by the projection $\langle y_3 \rangle$ of the data on the third eigenvector $|v_3\rangle$ as shown in Fig. 5.3(c). The pie chart shows that $|v_3\rangle$ is dominated by a positive \bar{q}_8 component combined with negative \bar{q}_4 and \bar{q}_{12} components, such that with rough estimates of the prefactors we have up to an overall constant that $y_3 \simeq \bar{q}_4 - 2\bar{q}_8 + \bar{q}_{12}$. In other words, 8-fold symmetries play a role that are *not* simply higher harmonics of a 4-fold symmetry as their weights in y_3 have opposite signs compared to the weights in y_1 . Even though the corresponding eigenvalue is as small as $\lambda_3 = 0.04$ such that the projection y_3 only captures 4% of the variance, the density dependence of $\langle y_3 \rangle$ shown in Fig. 5.3(c) separates essentially all different crystals relatively well. We can thus conclude that the largest variance in structure is found between any of the crystals and the fluid, followed by the dissimilarity of the sphere-like and tetrahedron-like crystals, followed by the dissimilarity between the tetrahedron-like crys-

tals. The resolving power of the projections $\langle y_2 \rangle$ and $\langle y_3 \rangle$ is best exemplified by following the lines of structures V and VI in Fig. 5.3, both of which display jumps that respectively correspond to the solid-solid transitions $V \rightarrow VI$ and $VI \rightarrow VII$ that these structures undergo before melting into the fluid, as described in chapter 4.

To summarize, we find that $y_1 \simeq \bar{q}_4 + \bar{q}_6 + \bar{q}_8 + \bar{q}_{10} + \bar{q}_{12}$, which strongly correlates with density, separates well the fluid phase and QA from the crystal structures, whereas specific differences in \bar{q}_l 's effectively distinguishes the different crystal structures, *e.g.* $y_2 \simeq \bar{q}_4 - \bar{q}_6 + 2\bar{q}_{10} - \bar{q}_{12}$ separates well the tetrahedron-like crystals from the sphere-like crystals, and $y_3 \simeq \bar{q}_4 - 2\bar{q}_8 + \bar{q}_{12}$ distinguishes the various tetrahedron-like crystals.

To illustrate this further, we study the distributions of the local bond order parameters, rather than the all-particle-averaged global bond order parameters. Fig. 5.4 shows three two-dimensional projections of the 11-dimensional $|q\rangle$ space of all our data, where the different crystals are color-coded with a brightness that increases with density. In Fig. 5.4(a,b,c) we show the projections onto the principal components. The projection of the one-particle states onto the two dominant principal axes $|v_1\rangle$ and $|v_2\rangle$ is shown in Fig. 5.4a, where the fluid and QA are well separated from all crystal structures by the line $y_1 \simeq 0.4$. Moreover, the sphere-like crystals (VII and pFCC) at $y_2 < 0$ are well separated from the tetrahedron-like crystals (I-VI) at $y_2 > 0$ with III and IV resolved from the other four crystal structures. Fig. 5.4 also shows that the QA is in between the fluid and the crystal phases with a unique \bar{q}_l fingerprint, which could for instance be used as an order parameter in umbrella sampling techniques to aid nucleation of a quasicrystal [220, 221]. We note, however, that the \bar{q}_l alone are likely not optimal for detecting quasicrystalline order due to their limited spatial range. Combining them with a longer-ranged order parameter *e.g.* based on the radial distribution function $g(r)$ may yield better results. Fig. 5.4c illustrates that y_2 and y_3 serve to distinguish between the various crystals, as most structure occupy different corners of this subspace. The exception to this are the distributions of crystals I, II, V and VI, which overlap significantly in all of these projections. However, these four can be resolved by looking at specific combinations of \bar{q}_l inspired by the principal components. We show these combinations in Fig. 5.5. The “standard” combination (\bar{q}_4, \bar{q}_6) shown in Fig. 5.5a, resolves nearly all relevant crystal structures, except for the significantly overlapping distributions of crystals I and VI, and those of the fluid and the approximant. Taking the combination $(\bar{q}_4 - \bar{q}_8, \bar{q}_{12})$ in Fig. 5.5b as suggested by $|v_3\rangle$ resolves the overlap of the former, while the combination $(\bar{q}_4, \bar{q}_{10})$ in Fig. 5.5c as suggested by $|v_2\rangle$ partially resolves the latter.

Evidently all crystal structures can be distinguished from one another in this structure metric space, but for specific combinations such as for crystals I and VI this separation requires combinations of structure metrics rather than individual ones.

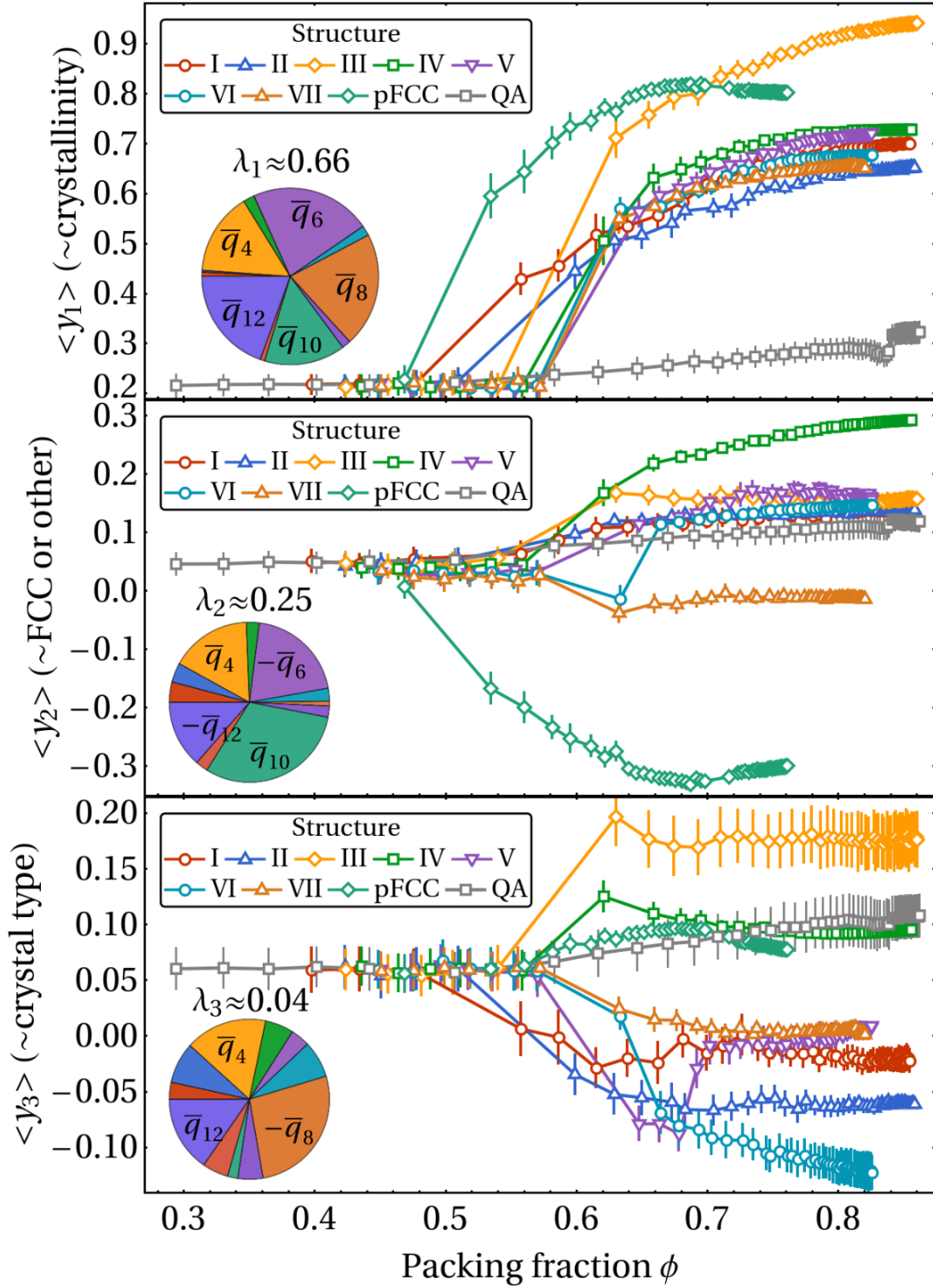


Figure 5.3: Global order parameters $\langle y_i \rangle$ with their corresponding eigenvectors (pie charts) and eigenvalues λ_i obtained from PCA as a function of the packing fraction ϕ , for various particle shapes s . Here $\langle y_1 \rangle$ describes the increase of non-specific crystalline order with increasing density, $\langle y_2 \rangle$ distinguishes sphere-like from tetrahedron-like crystals, and $\langle y_3 \rangle$ further distinguishes the various tetragonal crystals.

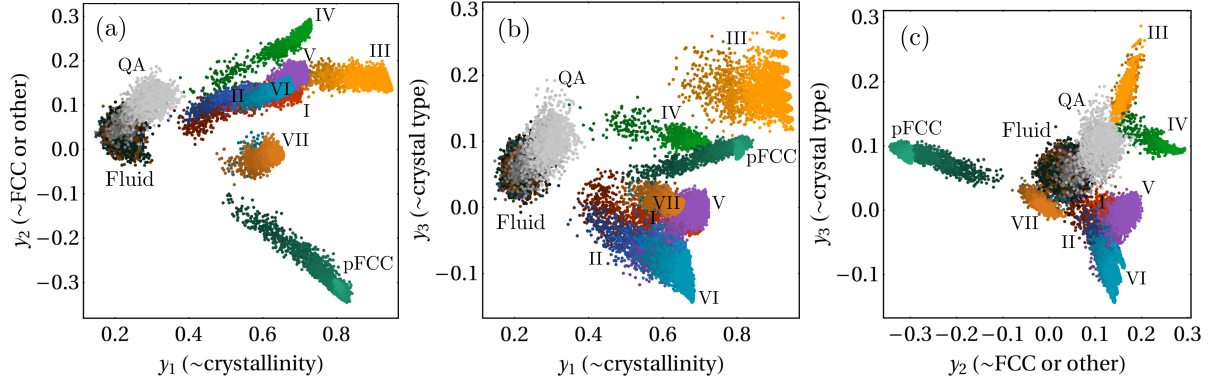


Figure 5.4: 2D distributions of the projections y_i of the one-particle vectors $|q\rangle$ onto the three principal components. (a) Onto $|v_1\rangle$ and $|v_2\rangle$, (b) onto $|v_1\rangle$ and $|v_3\rangle$ and (c) onto $|v_2\rangle$ and $|v_3\rangle$. The different phases are color-coded, and the color brightness indicates the density, with darker shades being lower packing fractions and brighter ones higher.

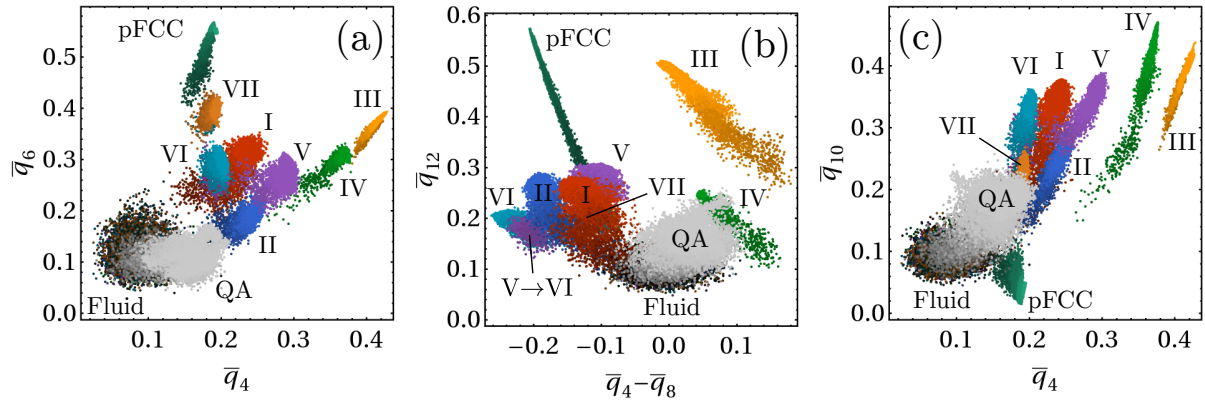


Figure 5.5: 2D subspaces for distinguishing between spherotetrahedron phases. (a) (\bar{q}_4, \bar{q}_6) , distinguishing most phases except the QA from the fluid and I from VI, (b) $(\bar{q}_4 - \bar{q}_8, \bar{q}_{12})$, in which I can be distinguished from VI, and (c) $(\bar{q}_4, \bar{q}_{10})$, in which we find the greatest separation between the fluid and the QA. The different phases are color-coded, and the color brightness indicates the density, with darker shades being lower packing fractions and brighter ones higher.

5.4 A larger set of possible bond order parameters with \bar{q}_l and w_l for $2 \leq l \leq 24$

Using the Voronoi tessellation method, we found that spherotetrahedra can have up to 20 neighbours. One could argue that this makes our choice for $l_{max} = 12$ too restrictive, as symmetries higher than 12-fold may become important. In this section we describe the effect of including bond order parameters with higher rotational symmetries in our principal component analysis. Using the same data set as described in Section 5.2, we now consider the set of bond order parameters $|Q\rangle = (\bar{q}_2, \bar{q}_3, \dots, \bar{q}_{24}, w_2, w_4, \dots, w_{24})$, which includes the structure metrics \bar{q}_l with $2 \leq l \leq 24$ as well as their higher-order moments w_l . These higher-order moments read:

$$w_l(i) = \frac{\sum_{m_1+m_2+m_3=0} \begin{pmatrix} l & l & l \\ m_1 & m_2 & m_3 \end{pmatrix} q_{lm_1}(i) q_{lm_2}(i) q_{lm_3}(i)}{\left(\sum_{m=-l}^l |q_{lm}(i)|^2 \right)^{3/2}}. \quad (5.1)$$

using the facet-weighted (but not averaged) q_{lm} as described in Section 4.2.3. The w_l of odd l are all zero. We denote the corresponding PCA eigenvectors of this expanded set as $|V_i\rangle$ and the projections of the one-particle state its projections onto the principal components as $Y_i \equiv \langle V_i | Q \rangle$. Fig. 5.6 shows the eigenvalues and eigenvectors obtained from the PCA of this data set. The effective dimensionality of this data set is somewhat higher, with the first three eigenvalues being $\lambda_1 = 0.533$, $\lambda_2 = 0.194$ and $\lambda_3 = 0.097$ for a total of 82.4% of the variance being contained in the first three principal components. To reach the same 95% threshold as before we now require six principal components. Interestingly, when plotted on a logarithmic scale there is a sharp drop after the sixth eigenvalue.

Looking at the first few eigenvectors, we find that $|V_1\rangle$ and $|V_2\rangle$ are similar to $|v_1\rangle$ and $|v_2\rangle$ of the smaller set, with the first eigenvector being a roughly equal contribution of all even \bar{q}_l describing crystallinity, and the second eigenvector consisting primarily of \bar{q}_4 , \bar{q}_6 , \bar{q}_{10} and \bar{q}_{12} . However, $|V_1\rangle$ also contains contributions from \bar{q}_l of higher l , and $|V_2\rangle$ gaining a large contribution of w_2 and w_4 . The third eigenvector $|V_3\rangle$, however, is quite different from its counterpart: where $y_3 \simeq \bar{q}_4 - 2\bar{q}_8 + \bar{q}_{12}$, $Y_3 \simeq -2\bar{q}_6 + \bar{q}_{10} - \bar{q}_{12} - 4w_2 + w_4$. It would thus seem that w_2 is an important order parameter for this system. However, when we investigate the distributions of w_2 for the various phases in the system, we find that while its variance is large, it is not a particularly good order parameter. As can be seen in Fig. 5.7(a): its mean and variance are largely the same for all phases, and so it cannot be used to distinguish them. Additionally, Fig. 5.7(b) shows that the large contribution of w_2 smears out the distributions of the projections along the first two principal axes, leading to a worse distinguishability than in the case of $l_{max} = 12$.

This decrease in distinguishability highlights one of the weaknesses of the PCA method: a large variance along a specific direction does not necessarily imply distinguishability. Other dimensionality reduction techniques such as diffusion maps [222] or autoencoders [219] would most likely fare better as these methods are not inherently built around maximizing the variance.

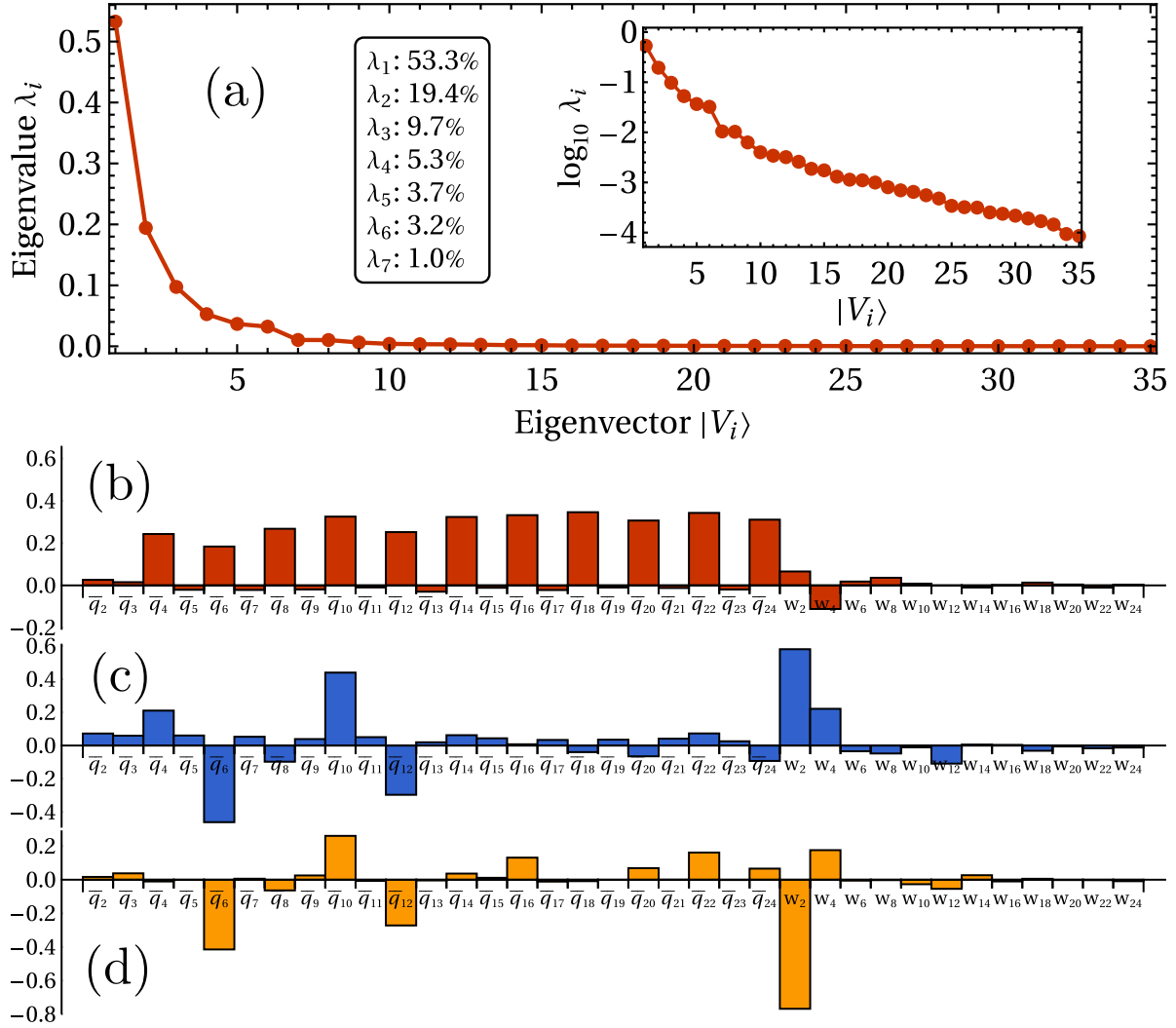


Figure 5.6: (a) Eigenvalues and first three eigenvectors of the PCA using $|Q\rangle = (\bar{q}_2, \bar{q}_3, \dots, \bar{q}_{24}, w_2, w_4, \dots, w_{24})$ as input. The inset shows the eigenvalues on a logarithmic scale and the legend shows the percentage of the variance captured by each eigenvalue. A sudden drop in eigenvalue can be seen after the sixth eigenvector. (b,c,d) The weights associated with each component \bar{q}_l for the three largest eigenvectors (b) $|V_1\rangle$, (c) $|V_2\rangle$ and (d) $|V_3\rangle$.

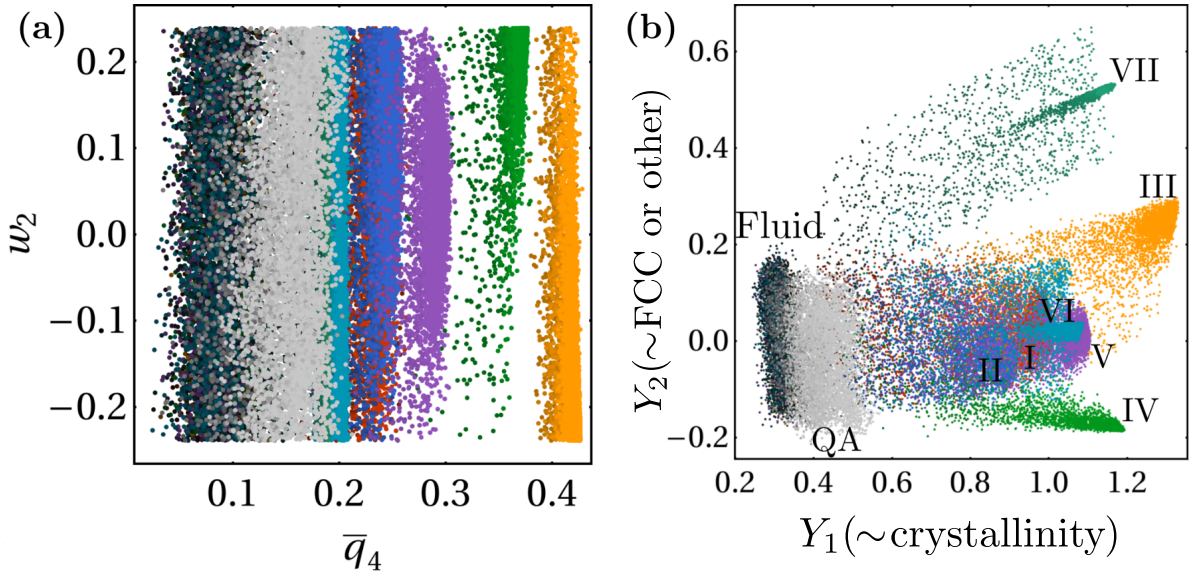


Figure 5.7: (a) View along the (\bar{q}_4, w_2) -plane. While w_2 has a large variance, the distributions of all phases strongly overlap, and thus it cannot be used to distinguish between crystal phases. (b) 2D distributions of projections Y_1 versus Y_2 when using $|Q\rangle = (\bar{q}_2, \bar{q}_3, \dots, \bar{q}_{24}, w_2, w_4, \dots, w_{24})$ as input. The different phases are labeled and color-coded, while the color brightness indicates the density.

5.4.1 Excluding w_2

To better compare the effect of expanding our set of considered order parameters we now exclude w_2 from our input features and apply the PCA again. We show the resulting eigenvalues and eigenvectors in Fig. 5.6. Without w_2 the effective dimensionality of the system is slightly lower, with the first three eigenvalues being $\lambda_1 = 0.609$, $\lambda_2 = 0.184$ and $\lambda_3 = 0.064$ for a total of 85.7% of the variance being contained in the first three principal components. We still require six principal components to capture 95% of the variance, but the sudden drop in eigenvalue now occurs after the fifth eigenvalue instead of after the sixth. The first two eigenvectors $|V_1\rangle$ and $|V_2\rangle$ are almost entirely unaffected by the removal of w_2 . However, $|V_3\rangle$ is again quite different, both from the smaller set as well as from the set including w_2 . Most strikingly, $|V_3\rangle$ has barely any component along \bar{q}_8 , while for $|v_3\rangle$ this was the largest component. We also investigated the other eigenvectors (up to $|V_6\rangle$), but found them to provide fairly little additional information. Furthermore, none of the other $|V_i\rangle$ resembled the $|v_i\rangle$ of the smaller data set. In all eigenvectors $|V_i\rangle$ we found the contribution of the w_l to be quite small except for w_4 .

To further compare the effect of including more candidate order parameters we plot in Fig. 5.9 the 2D subspaces formed by pairs of the projections y_i, Y_i onto the first three principal components $|v_i\rangle, |V_i\rangle$ of the two principal component analyses. Comparing the subspace (y_1, y_2) and (Y_1, Y_2) in Fig. 5.9(a,b), we see that the effect of including w_4 as well as the \bar{q}_l of higher l in $|V_1\rangle$ is to stretch out the distributions of the various phases along Y_1 in a way that exacerbates the effect of density. The reason for this is that the higher \bar{q}_l are more sensitive to noise. As the density decreases and particles move more freely, higher-order bond order is lost before the lower-order one. This makes Y_1 less effective at

distinguishing between phases, but more effective at representing the local density. The addition of w_4 to $|V_2\rangle$ does not seem to have a significant effect, as the various phases are still arranged in the same order along Y_2 as along y_2 . Interestingly, despite $|v_3\rangle$ and $|V_3\rangle$ being quite different, the projections along y_3 and Y_3 actually appear to be surprisingly similar.

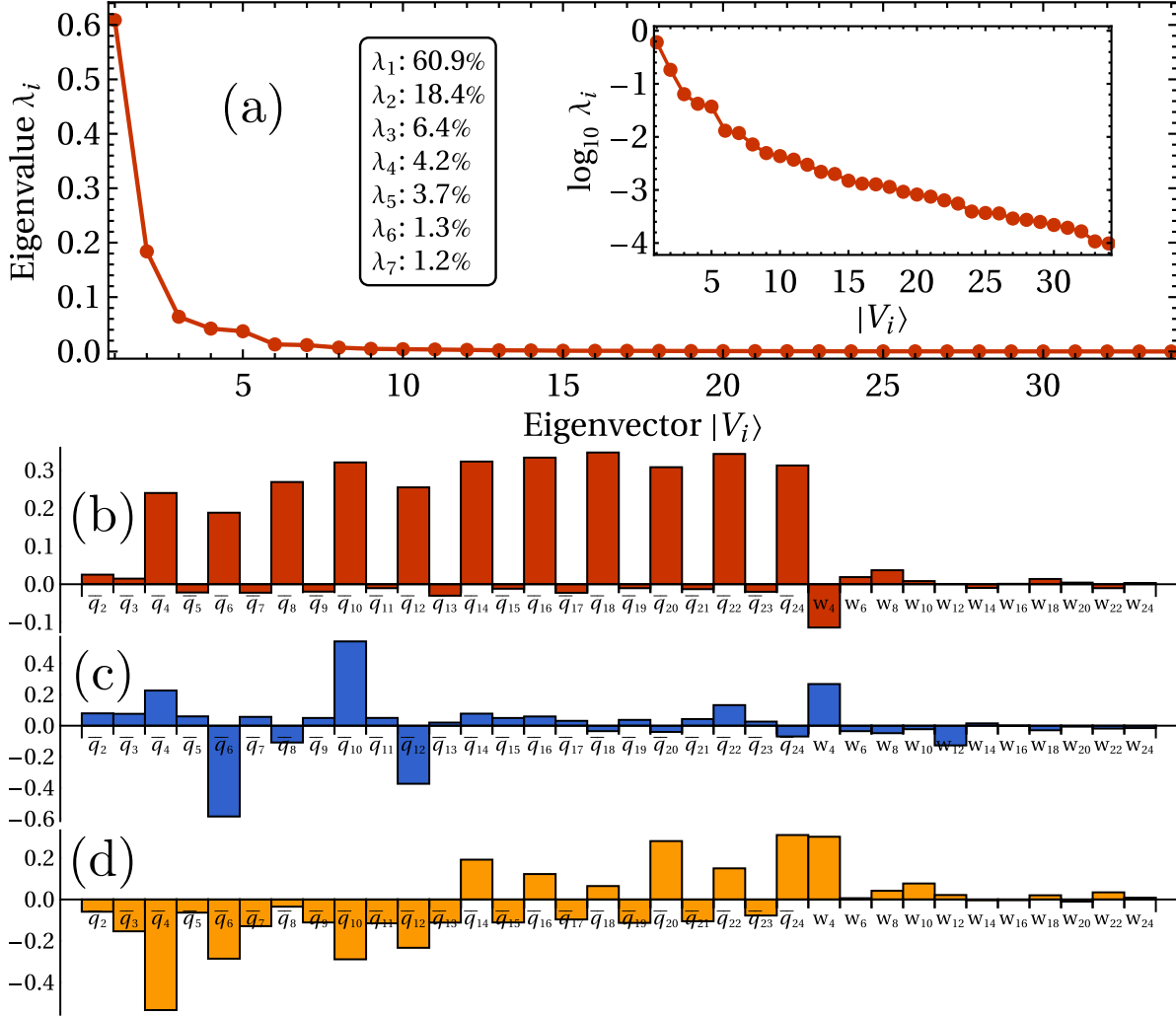


Figure 5.8: (a) Eigenvalues and first three eigenvectors of the PCA using $|Q\rangle = (\bar{q}_2, \bar{q}_3, \dots, \bar{q}_{24}, w_4, w_6, \dots, w_{24})$ as input. The inset shows the eigenvalues on a logarithmic scale and the legend shows the percentage of the variance captured by each eigenvalue. A sudden drop in eigenvalue can be seen after the fifth eigenvector. (b,c,d) The weights associated with each component \bar{q}_l for the three largest eigenvectors (b) $|V_1\rangle$, (c) $|V_2\rangle$ and (d) $|V_3\rangle$.

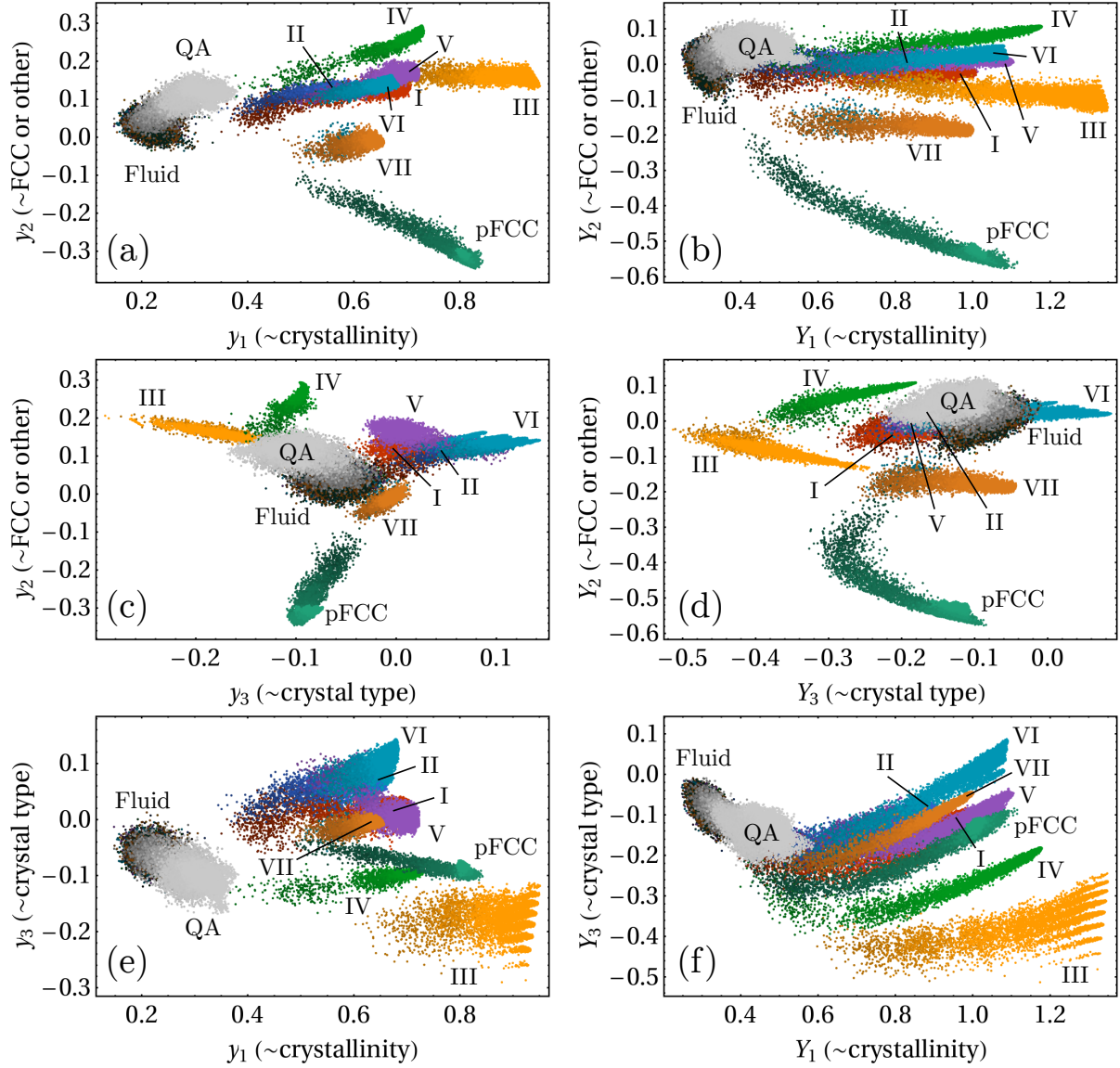


Figure 5.9: (a,c,e) 2D distributions of the projections y_i of the one-particle vectors $|q\rangle = (\bar{q}_2, \bar{q}_3, \dots, \bar{q}_{12})$ onto its three principal components. (b,d,f) 2D distributions of the projections Y_i of the one-particle vectors $|Q\rangle = (\bar{q}_2, \bar{q}_3, \dots, \bar{q}_{24}, w_4, w_6, \dots, w_{24})$ onto its three principal components. The different phases are color-coded, and the color brightness indicates the density, with darker shades being lower packing fractions and brighter ones higher.

5.5 Conclusions

We conclude that the (reweighted) bond order parameters \bar{q}_l provide an excellent means of distinguishing local structures, even for the rather complex hard-particle systems studied here. Our PCA on the basis of \bar{q}_l for $2 \leq l \leq 12$ shows that not only the expected \bar{q}_4 and \bar{q}_6 play a key role in the characterisation of the self-assembled structures, but that a surprisingly large role is also played by \bar{q}_{10} , mainly to distinguish hexagonal from tetragonal structures, and the QA from the fluid and the crystal phases. Moreover, we find \bar{q}_8 to be crucial for disentangling several of the tetragonal phases, even though the corresponding eigenvalue in the PCA (λ_3 in this case) is an order of magnitude smaller than the largest two eigenvalues. Most, but not all crystal structures can be distinguished based on individual \bar{q}_l . The “standard” combination (\bar{q}_4, \bar{q}_6) works well for this system as well, resolving most crystals except for crystal structures I and VI, which overlap in this subspace. Taking the difference $\bar{q}_4 - \bar{q}_8$, as suggested by the third eigenvector obtained from PCA, allows one to distinguish between these two structures as well.

When applying PCA to a larger set of bond order parameters which uses \bar{q}_l as well as w_l for $2 \leq l \leq 24$, we found a surprisingly large component of the variance to be contained in w_2 . However, upon closer inspection this variance is similar across all phases of interest and thus cannot be used to distinguish between them. Excluding w_2 from the analysis produces principal components very similar to that of smaller set using only \bar{q}_l for $2 \leq l \leq 12$. In both cases, the first principal component is a sum of all even \bar{q}_l in roughly equal measure, which provides a general measure of overall crystallinity that may prove useful in nucleation studies, enhanced sampling techniques or inverse-design methods. The second component in both cases is roughly $y_1 \simeq Y_1 \simeq \bar{q}_4 - \bar{q}_6 + 2\bar{q}_{10} - \bar{q}_{12}$ and distinguishes tetrahedron-like crystals (I-VI, QA) from sphere-like crystals (VII, pFCC). The third component is quantitatively different for the two cases, but in both cases serves to further distinguish the tetrahedron-like crystals from one another.

In general, we find that to optimally distinguish between many crystal phases, it is worthwhile to consider \bar{q}_l beyond just $l = 4$ and $l = 6$. Considering all \bar{q}_l with $l = 4, 6, \dots, 12$ seems to be a reasonable choice if one only wishes to include a small number of them. Of the higher-order moments w_l we find w_4 to be the most important to consider — w_2 appears to be extremely noisy for most phases of interest, while w_l with $l > 4$ yield little variance across the phases considered here.

Acknowledgements

This chapter is part of a fruitful collaboration between the author and Gabriele Coli. The author provided the data set, while Gabriele performed the PCA, and the interpretation of its results was an interesting back-and-forth with both Gabriele as well as René van Roij and Marjolein Dijkstra, for which they are all gratefully acknowledged. I would also like to thank Sander Kuipers, Peter Cats, Sacha de Wind and Cyril Delaporte for interesting discussions on machine learning and dimensionality reduction that provided further insights and context for the present work.

6

Egg-shaped supraparticles of rounded tetrahedra

In this chapter we investigate why CdSe nanoparticles with a rounded tetrahedral shape form elongated, egg-shaped supraparticles, as observed in experiments carried out by Wang et al. in Ref. [223]. We first determine the range of particle shapes encountered in the experiments, and map this onto the hard spherotetrahedron model we investigated in Chapter 4. We find that the experimentally synthesized nanoparticles correspond to a shape parameter $s \approx 0.5 \pm 0.1$, and that the crystalline supraparticles have a structure that corresponds to a slightly deformed face-centered cubic (FCC) lattice that is similar, but not quite identical to what we would expect on the basis of the hard spherotetrahedron model. Using free-energy calculations, we determine the phase coexistence between the fluid, plastic crystal pFCC and crystal VII phases in the vicinity of their triple point, which is near the experimental shape parameter $s \approx 0.5$. We find that the coexistence densities as well as the supersaturation display a significant sensitivity to the exact particle shape in this region, which warrants caution for studies into the nucleation properties. Finally, we perform self-assembly simulations under spherical confinement to mimic the experimental droplet evaporation self-assembly. We find that supraparticles of hard spherotetrahedra with a roundness down to $s = 0.7$ display Mackay/anti-Mackay order that is similar to what was found for hard spheres. For less rounded tetrahedra ($s < 0.7$) we find no bulk ordered structure, but significant order at the boundary, with a complex pattern reminiscent of dodecagonal quasicrystalline layers arising for $s \in [0, 0.2]$, a simpler triangular lattice for $s = 0.3$, and orientational alignment with the boundary but no structural order for $s \in [0.4, 0.5]$. Ultimately, we are not yet able to explain the egg shape of the experimental supraparticles, but our results should provide a useful basis for further studies, which we discuss in the closing remarks of this chapter.

This chapter is based on a collaboration between the author (under the supervision of Prof. M. Dijkstra and Prof. R. van Roij), Dr. Da Wang (under the supervision of Prof. A. van Blaaderen) and Dr. Yaoting Wu (under the supervision of Prof. C.B. Murray).

6.1 Introduction

In Chapter 3 we introduced the spherotetrahedron system by remarking the peculiar behaviour of supraparticles composed of rounded tetrahedron CdSe nanoparticles found in Ref. [223]. Specifically, when such supraparticles are formed in experiments from a droplet evaporation self-assembly, they attain an elongated, egg-like shape, as shown in Fig. 6.1. The nanoparticles used in the experiments are composed of a CdSe core of roughly 9 nm in size, capped by oleic acid ligands whose maximum length is roughly 2 nm [224]. They are initially dispersed in cyclohexane (a good solvent), until for the self-assembly they are emulsified with water (a bad solvent) with a surfactant added to stabilize the droplets. Self-assembly then occurs in the slowly evaporating cyclohexane droplets. In Chapter 4 we investigated the bulk phase behaviour of these particles via a hard-particle model and characterized the many resulting crystal phases. In Chapter 5 we discovered an order parameter that could reliably distinguish all hard spherotetrahedron crystals from the fluid. In this chapter we connect back to the experimental system (described in detail in Ref. [223]) and further investigate the self-assembly of these rounded tetrahedral nanoparticles.

The observed anisotropy of the supraparticles is too large to be the result of locked-in thermal fluctuations of the droplet shape. Assuming supraparticles with a diameter D of roughly $D = 100$ nm and taking the cyclohexane-water surface tension γ to be approximately 0.05 N/m [225, 226], a back-of-the-envelope estimate for the energy cost of forming an ellipsoidal droplet of cyclohexane in water with the observed aspect ratio of ~ 1.4 instead of a spherical one yields a cost of $\sim 10^4 k_B T$. This suggests that there is instead some process that actively drives the supraparticles to become egg-shaped. We have two hypotheses for such a process. First, the elongation of the crystalline supraparticles may be the result of a strong preference for crystal growth along certain axes. To test this, we will need to characterize the nucleation process, for which we need to know the exact particle shape, which crystal is formed and at what densities. We determine the particle shape in Section 6.2, the supraparticle crystal structure in Section 6.3, and phase coexistence properties using free-energy calculations in Section 6.4. Our second hypothesis is that the egg shape is the result of an interplay between crystal growth and the geometric confinement. Hence, in Section 6.5 we perform self-assembly simulations under spherical confinement to investigate the geometric effects induced by the droplet geometry.

6.2 Mapping the experimental particle shape to the model

As cyclohexane is a good solvent for the stabilized particles, the ligands on the CdSe cores will be in a swelled state during most of the self-assembly. We approximate the particle interactions as a pairwise hard-particle interaction, with the ligands adding an extra effective roundness to the particle shape. The quality of this approximation depends on currently unknown factors such as the ligand density: the denser the ligand layer on the nanoparticles, the steeper the repulsions between them. We estimate the effective

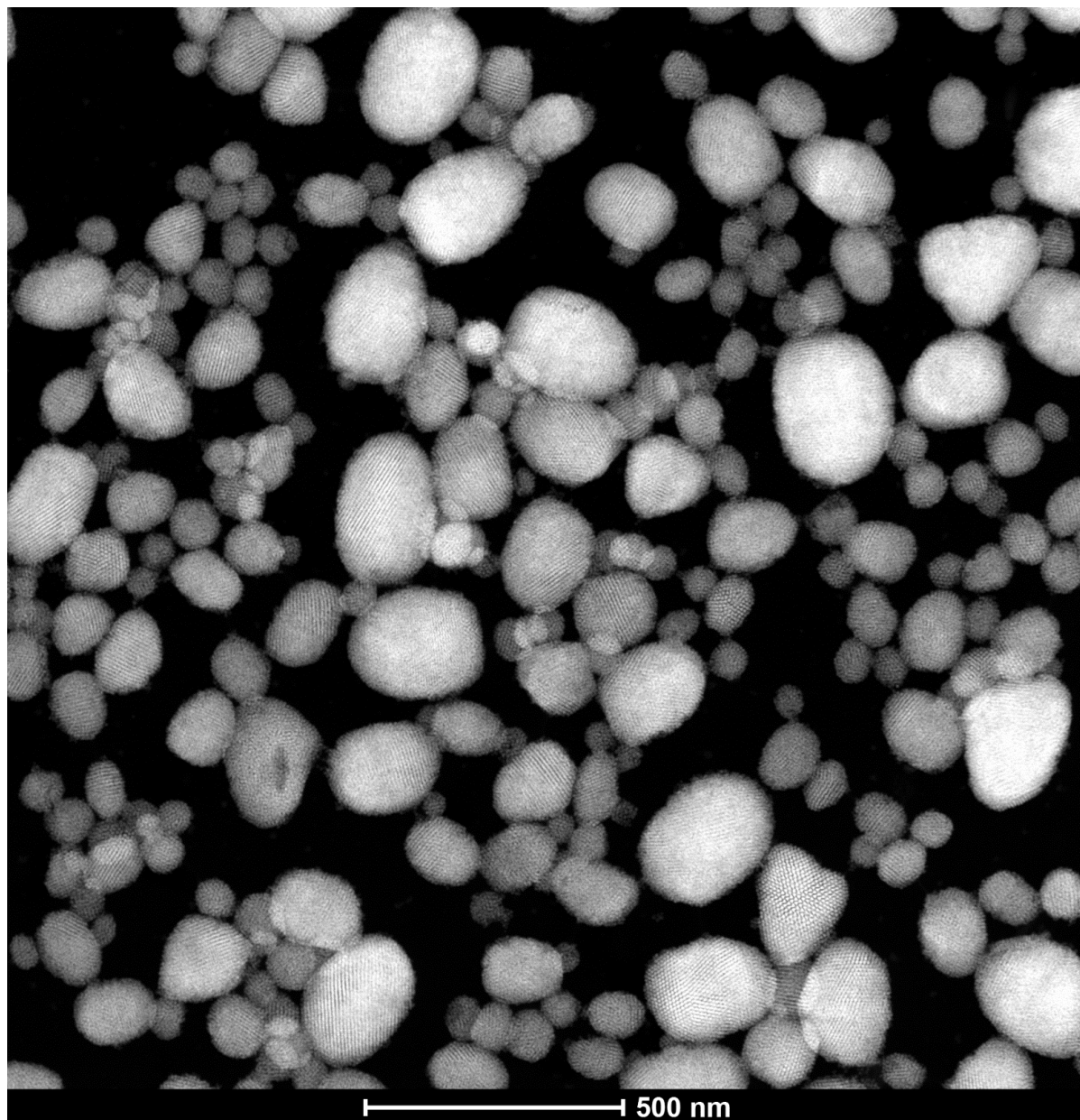


Figure 6.1: EM image of supraparticles obtained from droplet evaporation with spherotetrahedral particles, as synthesized and imaged by Wang et al. [223]. Most of the supraparticles show clearly defined crystalline domains, yet many are elongated/egg-shaped rather than spherical or faceted.

rounding ratio s by analyzing electron microscopy (EM) images. Obtaining the rounding ratio s for experimental particles is challenging if one tries to do so by measuring the edge length L and rounding radius R . The rounding radius R could in principle be measured from spherical caps at the vertices, but experimentally obtained particles rarely display perfect spherical caps. Furthermore, the contrast of these caps is quite poor in EM images. The edge length L is likewise hard to measure as it is difficult to draw a distinction where the flat edge stops and the spherical cap begins. A less error-prone measure is to instead measure the center-to-vertex and center-to-edge distances, henceforth denoted by l_1 and l_2 . These two distances are easily and reliably measured from EM images. Because particles tend to align their flat facets with the EM substrate, one can simply measure all particles with triangular projections to ensure the appropriate 2D projection to measure l_1 and l_2 . We can then calculate the edge length L and rounding radius R from l_1 and l_2 and obtain the corresponding rounding ratio s . This mapping is given by:

$$L = 2\sqrt{3}(l_1 - l_2); \quad R = 2l_1 - l_2; \quad s = R/(\sqrt{6}L/4 + R). \quad (6.1)$$

Using measured values of l_1 and l_2 from a series of EM images we compute the average rounding ratio of the CdSe cores to be $s = 0.31 \pm 0.11$. Note that the oleic acid ligands are not visible in the EM images due to their atomic nuclei being lighter than the atoms in the CdSe cores. However, we can estimate their effective length by measuring the distance between two nanoparticles that are aligned edge-to-edge. Using this measure we obtain an effective ligand length of approximately 1.4 nm, slightly smaller than the maximum length of the oleic acid ligands of ~ 2 nm when fully stretched. Fig. 6.2a shows the resulting shape model for the experimental particles, with $R_{l,measured}$ and $R_{l,max}$ the effective rounding radii when we include the measured and maximum ligand lengths leading to the effective rounding ratios $s = 0.48 \pm 0.10$ and $s = 0.52 \pm 0.09$, respectively. The hard spherotetrahedron crystals that lie within this region are the crystals IV, V, VI, VII, and pFCC that we described in Chapter 4. We thus have five candidate crystal structures.

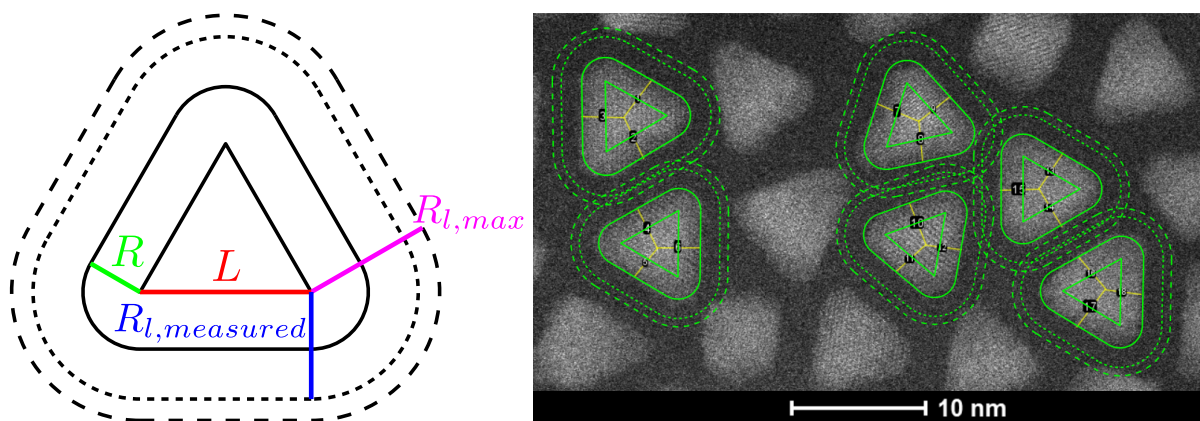


Figure 6.2: Left: Model of the shape of the ligand-capped spherotetrahedral particles, with core edge length L , core rounding radius R , and effective rounding radii $R_{l,measured}$ and $R_{l,max}$ that include the core radius R plus the measured and maximally stretched ligand lengths, respectively. Right: Model with measured values manually overlaid onto an EM image.

6.3 Determining the supraparticle crystal structure from its structure metric fingerprint

We determine which of our candidate crystal structures (if any) is the one formed in the experiments by calculating the structure metric fingerprints of the experimental supraparticles and comparing them to those of the candidate structures from Chapter 4. To compute the structure metric fingerprints of the experimental supraparticles, however, we must know the experimental particle positions. Since we are interested specifically in identifying a crystal structure, we can take advantage of the periodicity of the structure by reconstructing the nanoparticle positions within a supraparticle from the diffraction pattern that is created by this supraparticle. In brief, we take the 3D diffraction pattern based on an electron tomography reconstruction and calculate an Inverse (Fast) Fourier Transform (IFFT) to obtain the particle positions that created it. We perform such an analysis for two supraparticles, for which we show 3D volume renderings along three orthogonal directions and the corresponding IFFT reconstruction in Figs. 6.3 and 6.4. The reconstructed supraparticles are somewhat smaller, as the IFFT reconstruction procedure only uses the brightest diffraction peaks, which effectively discards information about the (typically less ordered) particles at the surface. The IFFT procedure also does not provide us with the particle orientations, and so we show particles as spheres in the reconstruction.

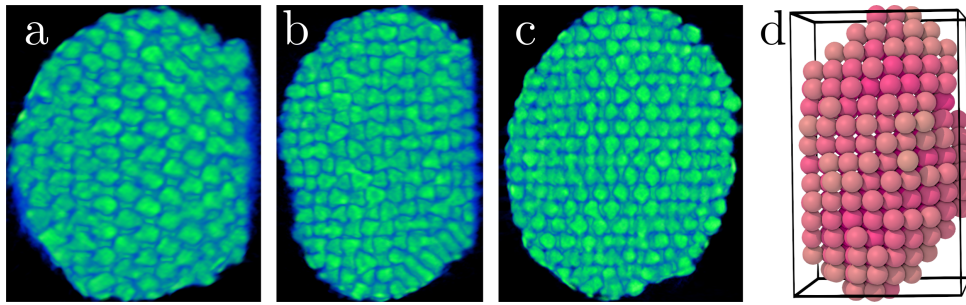


Figure 6.3: Cross-section views along a,b,c,) xy , xz and yz -planes through the supraparticle designated “Exp. 1”. Especially the cross-section view of the xz -plane reveals that particles in the core take on two opposing orientations. d) Spheres placed at the positions reconstructed from the IFFT, with brighter magenta colors indicating higher values of \bar{q}_6 . Particles at the boundary are lost due to their intensity being too low to be included in the IFFT reconstruction.

We now calculate the structure metrics that correspond to these reconstructed coordinates. Specifically, we calculate \bar{q}_2 , \bar{q}_4 , \bar{q}_6 , \bar{q}_8 , \bar{q}_{10} and \bar{q}_{12} , which we defined in Section 4.2.3. We compare the fingerprints of the measured supraparticles to the hard spherotetrahedron crystals IV, V, VI and VII in Fig. 6.5 by looking at their structure metrics in the spaces (\bar{q}_4, \bar{q}_6) , $(\bar{q}_8, \bar{q}_{12})$ and $(\bar{q}_2, \bar{q}_{10})$. The space (\bar{q}_4, \bar{q}_6) is the “conventional” choice for distinguishing between crystal phases and also resolves the various hard spherotetrahedron crystals quite well (see Chapters 4 and 5). We found in Chapter 5 that including information from \bar{q}_8 and \bar{q}_{12} can aid in further resolving the hard spherotetrahedron crystals. The space $(\bar{q}_2, \bar{q}_{10})$ provides information about geometric frustration due to 10-fold order via \bar{q}_{10} and general disorder through \bar{q}_2 [184]. What we observe is that both supraparticles, denoted by Exp. 1 and Exp 2, closely match the structure metric signature of

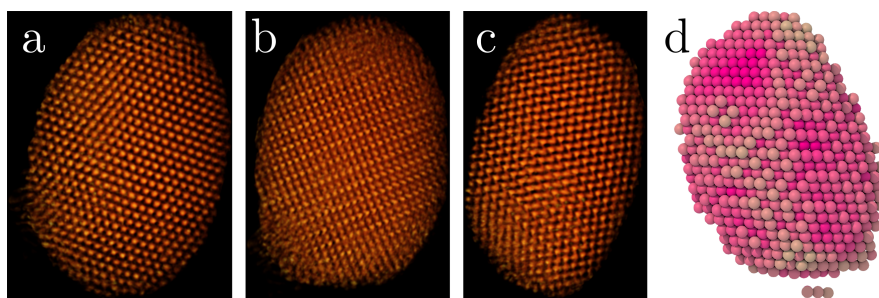


Figure 6.4: a,b,c) Three views along crystal planes through the supraparticle designated “Exp. 2”. d) Spheres placed at the positions reconstructed from the IFFT, with brighter magenta colors indicating higher values of \bar{q}_6 . Particles at the boundary are lost due to their intensity being too low to be included in the IFFT reconstruction.

crystal structure VII in both (\bar{q}_4, \bar{q}_6) and $(\bar{q}_8, \bar{q}_{12})$. Specifically, since crystal VII undergoes a continuous deformation with the rounding ratio, the supraparticles best match $\text{VII}_{s=0.9}$, which is a nearly undeformed FCC crystal. While supraparticle Exp. 1 matches the (\bar{q}_4, \bar{q}_6) - and $(\bar{q}_8, \bar{q}_{12})$ -fingerprints of crystal $\text{VII}_{s=0.9}$ and matches relatively well in \bar{q}_2 , it does not match in \bar{q}_{10} . We speculate that this is due to a higher amount of geometric frustration present in this supraparticle, possibly due to its attachment to the flat substrate (which can be seen as the flat facet in Fig. 6.3a and 6.3b). Exp. 2 also largely matches the $(\bar{q}_2, \bar{q}_{10})$ signature of crystal VII, but it has a long tail of larger \bar{q}_2 values. As higher values of \bar{q}_2 were found to correspond to jammed packings for hard spheres [184] (as compared to a crystal), we hypothesize that this long tail is due to locally jammed regions, possibly formed during the late stages of droplet evaporation.

As stated before, we cannot extract the orientation of the particles by using the IFFT method. However, real-space images of the supraparticles such as Figs. 6.3a-c and 6.4a-c suggest that the spherotetrahedral nanoparticles can have either of two opposing orientations. We conclude that the supraparticle crystal structure best matches crystal VII, and is thus a mildly deformed FCC lattice with a unit cell of two spherotetrahedra in opposing orientations. However, the deformation in the experimental system is less than what we find for a hard-particle model of the estimated effective roundness. This mismatch in deformation can be explained in two ways. It could be a result of polydispersity in the experimental system, which is not taken into account in the perfectly monodisperse hard-particle model. Alternatively, it could be the result of approximating the ligand interactions as hard-particle interactions, instead of a softer steric repulsion.

For hard spherotetrahedra, the shape $s = 0.5$ is very close to the triple point of the fluid, plastic crystal pFCC and crystal VII phases. Though the experimental supraparticles best match crystal VII, there may be two self-assembly pathways available to reach this structure: either from the fluid directly to crystal VII for $s < 0.5$, or from the fluid to a plastic crystal pFCC, and then from pFCC to crystal VII for $s > 0.5$. This offers a third possible hypothesis for the egg shape of the supraparticles: it may be the result of a (martensitic) transformation from pFCC to VII, possibly with an influence of the spherical boundary. The same condition holds as for our first two hypotheses: to test it we must first determine the coexistence densities between these phases in detail, and we do so in the next section.

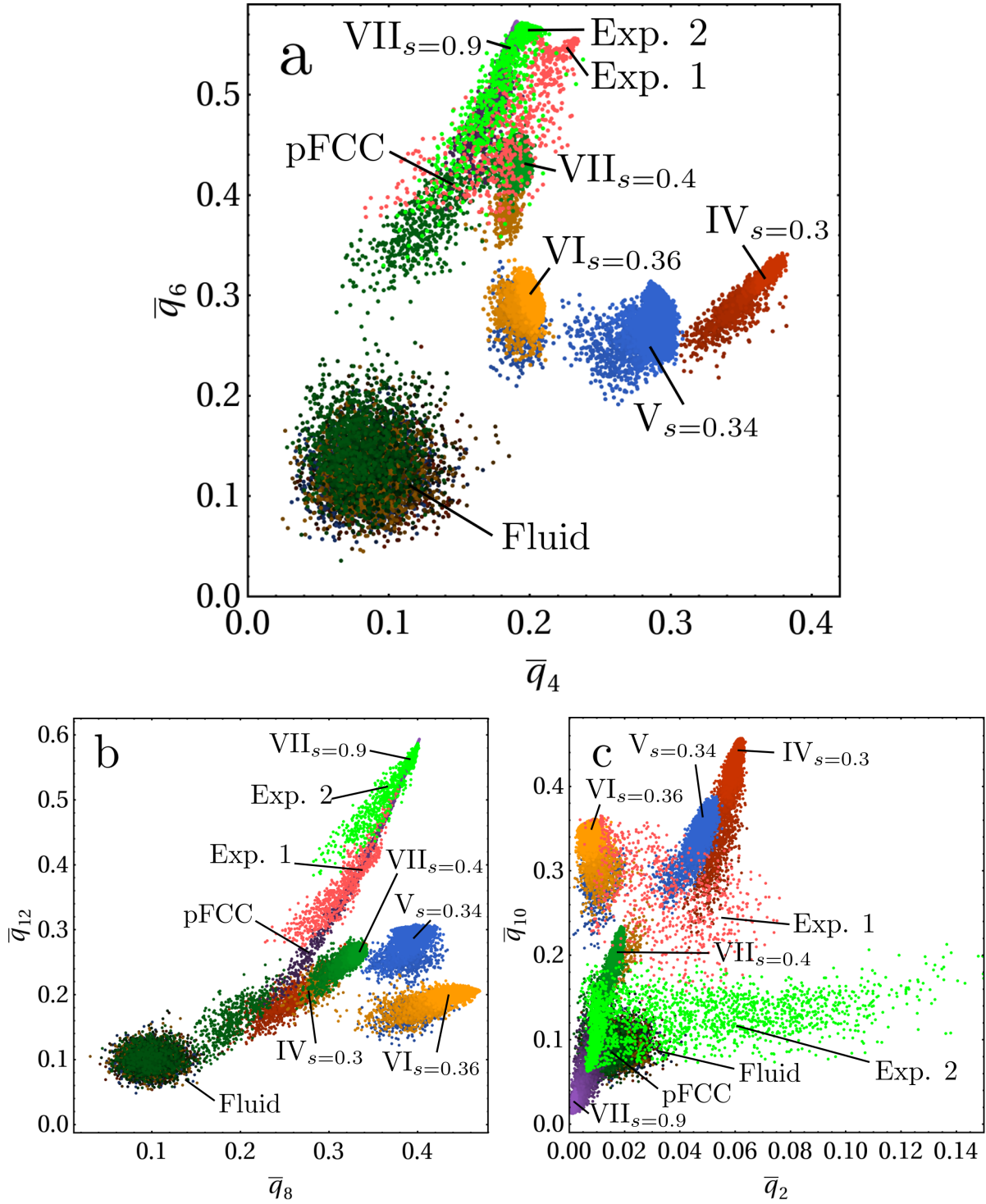


Figure 6.5: Minkowski structure metric distributions for five rounding ratios s displaying the five candidate hard tetrahedron phases IV, V, VI, VII, and pFCC, as well as for the fluid and the two reconstructed supraparticles Exp. 1 and Exp. 2. a) (\bar{q}_4, \bar{q}_6) , in which the supraparticle distributions overlap with those of crystal VII_{s=0.9}, which is a nearly undeformed FCC crystal. b) $(\bar{q}_8, \bar{q}_{12})$, in which the supraparticle and VII_{s=0.9} distributions also overlap. c) $(\bar{q}_2, \bar{q}_{10})$, in which Exp. 2 overlaps with the fluid and both VII crystals and Exp. 1 with a wide range of phases. \bar{q}_2 generally increases with disorder [184]. Structure metrics from different rounding ratios s are color-coded, with brighter colors indicating higher densities.

6.4 Free-energy calculations

Before we can investigate the nucleation processes of spherotetrahedra in detail, we have to accurately establish the region of phase space in which nucleation takes place. As explained in Section 1.8, we can extract the coexistence properties from the free energies of the fluid and the crystal(s). The structure metric analysis of the experimental supraparticles suggests that their final structure is crystal VII. However, there are two pathways to reach crystal VII, either by direct crystallization from the fluid, or with pFCC as an intermediate phase. Thus, we should consider both the fluid-VII and fluid-pFCC as well as the pFCC-VII transitions. For each of these three phases we require a different method to calculate its free energy, and we outline these methods below.

6.4.1 Free energy of the fluid

We calculate the free energy of the spherotetrahedron fluid by determining the excess chemical potential using the Widom test-particle insertion method [9]. This method determines the excess chemical potential μ_{ex} by sampling the Boltzmann probabilities of inserting an $(N + 1)$ -th particle at a random position \mathbf{r}_{N+1} and orientation \mathbf{q}_{N+1} into a configuration of N particles:

$$\beta\mu_{ex} = -\ln \int d\mathbf{r}_{N+1} d\mathbf{q}_{N+1} \left\langle \exp \left[-\beta \left(U(\mathbf{r}^{N+1}, \mathbf{q}^{N+1}) - U(\mathbf{r}^N, \mathbf{q}^N) \right) \right] \right\rangle_N, \quad (6.2)$$

where the average $\langle \dots \rangle_N$ indicates the ensemble average over an N -particle system. For a hard-particle system, this expression reduces to the particularly simple form:

$$\beta\mu_{ex} = -\ln \langle P_{insert} \rangle, \quad (6.3)$$

where $\langle P_{insert} \rangle$ is the probability that one could insert a particle into a system without creating any overlap with one of the other N particles, averaged over all possible positions \mathbf{r}_{N+1} and orientations \mathbf{q}_{N+1} . We can then calculate the Helmholtz free energy per particle by adding the ideal gas chemical potential $\beta\mu_{id}$ and subsequently using the definitions of the Gibbs free energy $G/N = \mu$ and $G = F + pV$, such that:

$$\frac{\beta F}{N} = \beta\mu_{id} + \beta\mu_{ex} - \frac{\beta v_p p}{\phi}, \quad (6.4)$$

where ϕ is the packing fraction, p the pressure and v_p is the particle volume which enters as an additional factor from working in packing fractions instead of densities. We list the determined excess chemical potentials in Table 6.1. The free energy at different packing fractions ϕ can then be obtained by integrating the equation of state $p(\phi)$:

$$\frac{\beta F(\phi)}{N} = \frac{\beta F(\phi_{ref})}{N} + \int_{\phi_{ref}}^{\phi} \frac{\beta v_p p(\phi')}{\phi'^2} d\phi', \quad (6.5)$$

where ϕ_{ref} is the reference packing fraction at which the free energy is determined using Eq. 6.4.

Table 6.1: Excess chemical potentials $\beta\mu_{ex}$ and ideal gas chemical potentials $\beta\mu_{id} = \ln \phi$ of a spherotetrahedron fluid of $N = 1000$ particles at various rounding ratios s , along with the packing fractions ϕ and pressures $\beta v_p p$ at which they were determined.

s	ϕ	$\beta v_p p$	$\beta\mu_{id}$	$\beta\mu_{ex}$
0.40	0.244(3)	0.822	-1.412(11)	3.975(15)
0.41	0.205(4)	0.5625	-1.583(19)	3.075(16)
0.42	0.206(4)	0.5625	-1.581(19)	2.915(16)
0.43	0.206(4)	0.5625	-1.579(19)	2.861(14)
0.44	0.207(4)	0.5625	-1.577(19)	2.931(15)
0.45	0.207(4)	0.5625	-1.575(19)	2.974(11)
0.46	0.207(4)	0.5625	-1.573(19)	3.079(11)
0.47	0.208(4)	0.5625	-1.572(19)	3.069(11)
0.48	0.208(4)	0.5625	-1.570(19)	2.902(10)
0.49	0.208(4)	0.5625	-1.668(19)	3.008(15)
0.50	0.201(3)	0.5171	-1.606(14)	2.611(3)
0.51	0.209(4)	0.5625	-1.565(19)	2.965(5)
0.55	0.202(3)	0.5171	-1.600(14)	2.618(4)
0.60	0.204(3)	0.5171	-1.591(14)	2.643(4)
0.65	0.205(3)	0.5171	-1.587(13)	2.594(4)
0.70	0.205(3)	0.5171	-1.583(14)	2.596(4)
0.75	0.206(3)	0.5171	-1.581(14)	2.558(4)
0.80	0.207(3)	0.5171	-1.576(14)	2.601(4)
0.85	0.207(3)	0.5171	-1.574(14)	2.539(4)
0.90	0.207(3)	0.5171	-1.574(14)	2.522(4)
0.95	0.208(3)	0.5171	-1.572(14)	2.466(3)
1.00	0.207(3)	0.5171	-1.573(13)	2.530(6)

6.4.2 Free energy of the plastic crystal pFCC

To compute the free energy of the plastic crystal pFCC, we employ the Frenkel-Ladd method [201, 202]. In brief, we compute the free energy of the hard spherotetrahedron crystal by calculating the change in free energy along a reversible path from a reference state with a known free energy to the crystal of interest. This reference state is a noninteracting Einstein crystal, in which particles are bound to their lattice sites by a harmonic potential:

$$\beta U_{Ein}(\mathbf{r}^N) = \lambda \sum_{i=1}^N \left(\frac{\mathbf{r}_i}{\sigma} - \frac{\mathbf{r}_{i,0}}{\sigma} \right)^2, \quad (6.6)$$

where \mathbf{r}_i are the particle positions, $\mathbf{r}_{i,0}$ their lattice positions, λ a dimensionless coupling constant, and σ the length scale, in our simulations set equal to $\sigma = v_p^{1/3} = 1$ as we normalize the particle volume. The total energy of the system is then given by the sum of this lattice energy and the hard particle interactions $U = U_{hard} + U_{Ein}$. The reversible path is constructed by varying the coupling constant λ : at $\lambda = 0$ we recover the hard spherotetrahedron crystal, while for $\lambda \rightarrow \infty$ particles are bound so strongly to their lattice sites that they never interact, and we recover the noninteracting Einstein crystal. The

free energy of the hard spherotetrahedron crystal is then computed by integrating the free energy over this path according to:

$$F = F_{Ein}(\lambda_{max}) - \int_{\lambda_{min}}^{\lambda_{max}} \left\langle \frac{\partial U}{\partial \lambda} \right\rangle_{\lambda} d\lambda, \quad (6.7)$$

with λ_{min} and λ_{max} given respectively appropriately small and large values to reach the aforementioned limits. The reference free energy F_{Ein} is given by the analytical expression

$$\frac{\beta F_{Ein}(\lambda)}{N} = -\frac{3}{2} \frac{N-1}{N} \ln \left(\frac{\pi}{\lambda} \right), \quad (6.8)$$

where the factor $(N-1)/N$ follows from a constraint placed upon the center of mass of the system[168, 201]. Note that this Einstein crystal potential couples only to the particle positions and not to their orientations. This is intentional: since pFCC is a *plastic* crystal, the particle orientations must remain disordered along the entire reversible path. However, this freedom of rotation also poses a challenge. When we impose no potential on the particle orientations, rotations of particles can make them come into contact even when their positions are tightly bound to their lattice sites (i.e. at $\lambda \rightarrow \infty$). For an undeformed FCC lattice, this occurs for all packing fractions $\phi > \phi_{free}$, where ϕ_{free} is the maximum packing fraction for which spherotetrahedra can freely rotate when fixed upon an FCC lattice. This packing fraction is given by:

$$\phi_{free} = \frac{4v_p}{(\frac{4}{\sqrt{2}}r_c)^3}, \quad (6.9)$$

with v_p the volume of one particle and $r_c = \sqrt{6}L/4 + R$ the circumscribed radius of a spherotetrahedron of edge length L and rounding radius R . To reach the noninteracting Einstein crystal limit, we add an additional step to our calculation in which we integrate over the equation of state $\beta p v_p(\phi)$ of a system of spherotetrahedra that are bound to their lattice sites with λ_{max} from a high density to a density low enough that particles can rotate freely and never come into contact. This density is typically lower than that for which pFCC is stable without the applied Einstein crystal potential, but adding this extra potential stabilizes it such that a reversible path can be constructed:

$$\frac{\beta F(\phi_{ref})}{N} = \frac{\beta F_{Ein}(\lambda_{max})}{N} - \int_{\lambda_{min}}^{\lambda_{max}} \left\langle \frac{\partial(\beta U/N)}{\partial \lambda} \right\rangle_{\lambda, \phi_{ref}} d\lambda + \int_{\phi_{free}}^{\phi_{ref}} \frac{\beta v_p p(\phi)}{\phi^2} \Big|_{\lambda_{max}} d\phi, \quad (6.10)$$

This method is similar to the lattice-coupling-expansion method [227]. Finally, to obtain the free energy of pFCC at various densities we can simply integrate over the equation of state $\beta v_p p(\phi)$ of a hard spherotetrahedron system. The final path to obtain the free energy of a system of N spherotetrahedra of rounding ratio s at a packing fraction ϕ is thus:

$$\begin{aligned} \frac{\beta F(\phi)}{N} = & \frac{\beta F_{Ein}(\lambda_{max})}{N} - \int_{\lambda_{min}}^{\lambda_{max}} \left\langle \frac{\partial(\beta U/N)}{\partial \lambda} \right\rangle_{\lambda, \phi_{ref}} d\lambda \\ & + \int_{\phi_{free}}^{\phi_{ref}} \frac{\beta v_p p(\phi')}{\phi'^2} \Big|_{\lambda_{max}} d\phi' + \int_{\phi_{ref}}^{\phi} \frac{\beta v_p p(\phi')}{\phi'^2} d\phi', \end{aligned} \quad (6.11)$$

Note that the integration from ϕ_{free} to ϕ_{ref} is only performed when required, which is when $\phi_{\text{free}} < \phi_{\text{ref}}$. We show the free energies of pFCC obtained in this way in Table 6.2, along with the values of ϕ_{free} . As an example, we show the equation of state of $s = 0.55$ at $\lambda = \lambda_{\text{max}}$ in Fig. 6.6. Note that the phase transition visible in Fig. 6.6 at $\phi \approx 0.63$ is simply the pFCC-VII transition.

Once we have calculated the free energies of the fluid and of the plastic crystal, we can find the properties of the fluid-pFCC phase coexistence by means of a common tangent construction, as described in Section 1.8. In Table 6.3 we show the obtained coexistence densities, pressure and chemical potentials for the fluid-pFCC coexistence of spherotetrahedra with various rounding ratios $s \in [0.5, 1.0]$. One can observe that the coexistence densities, pressure and chemical potential increase significantly when approaching the triple point at $s \approx 0.5$. We did not find a common tangent at $s = 0.5$, which could be either due to it being the triple point or due to the limited accuracy of the computed free energies. Since we are interested in the nucleation properties of the pFCC crystal, it is also instructive to consider the supersaturation $\beta\Delta\mu = \beta\mu_{\text{fluid}} - \beta\mu_{\text{pFCC}}$ at pressures and fluid packing fractions above coexistence. This supersaturation describes the free-energy difference between the bulk fluid and crystal phases that forms the driving force for the nucleation of the crystal phase. Fig. 6.7 shows the supersaturation $\beta\Delta\mu$ as a function of the fluid packing fraction (a) and the pressure (b). We can see that the supersaturation decreases significantly towards $s = 0.5$, indicating that it becomes more and more difficult to nucleate the pFCC crystal for these smaller rounding ratios.

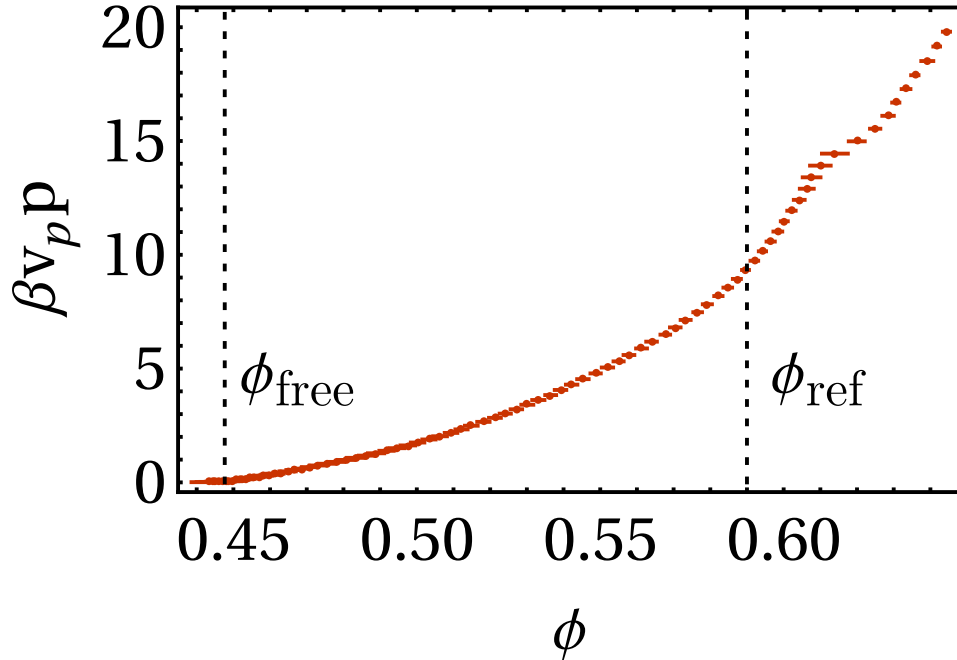


Figure 6.6: Equation of state of $N = 864$ spherotetrahedra with $s = 0.55$ in the pFCC phase, bound to their lattice sites by Eq. 6.6 with $\lambda = \lambda_{\text{max}} = 59874.1$. To reach the noninteracting Einstein crystal limit, we integrate over this equation of state from ϕ_{ref} to ϕ_{free} .

Table 6.2: Free energies of the ideal Einstein crystal F_{Ein} (Eq. 6.8), free-energy differences along the Einstein integration path ΔF_{Ein} , packing fraction required for free rotation ϕ_{free} , free-energy differences along the expansion path to free rotation $F_{\lambda_{\text{max}}}$ and the resulting free energies of the pFCC crystal F . All integrations were performed using an FCC lattice with $N = 864$ particles at a packing fraction of $\phi = 0.59$ and with coupling parameters $\ln \lambda_{\text{min}} = -5$ and $\ln \lambda_{\text{max}} = 11$, except for $s = 0.51$ for which we used $N = 500$, $\phi = 0.59$, $\ln \lambda_{\text{min}} = -3$ and $\ln \lambda_{\text{max}} = 12$.

s	$\beta F_{Ein}/N$	$\beta \Delta F_{Ein}/N$	ϕ_{free}	$\beta \Delta F_{\lambda_{\text{max}}}/N$	$\beta F/N$
0.50	14.7658	9.752(91)	0.412794	2.174(2)	7.188(91)
0.51	16.2503	11.171(106)	0.419764	2.047(2)	7.126(106)
0.55	14.7658	9.493(89)	0.447642	1.585(2)	6.857(89)
0.60	14.7658	9.303(88)	0.482404	1.074(2)	6.537(88)
0.65	14.7658	9.111(87)	0.516940	0.584(2)	6.239(87)
0.70	14.7658	8.992(86)	0.551108	0.203(2)	5.976(86)
0.75	14.7658	9.017(86)	0.584767	0.008(2)	5.757(86)
0.80	14.7658	9.180(86)	0.617776	-	5.586(86)
0.85	14.7658	9.306(87)	0.649993	-	5.460(87)
0.90	14.7658	9.391(88)	0.681277	-	5.375(88)
0.95	14.7658	9.438(88)	0.711486	-	5.328(88)
1.00	14.7658	9.455(88)	$\pi/(3\sqrt{2})$	-	5.310(88)

Table 6.3: Fluid-pFCC coexistence data: the rounding ratio s , coexistence densities $\phi_{\text{fluid},c}$ and $\phi_{\text{pFCC},c}$, and the coexistence pressure $\beta v_p p_c$ and chemical potential $\beta \mu_c$.

s	$\phi_{\text{fluid},c}$	$\phi_{\text{pFCC},c}$	$\beta v_p p_c$	$\beta \mu_c$
0.51	0.576	0.584	14.0	30.9
0.55	0.592	0.600	15.9	33.8
0.60	0.549	0.568	10.5	24.3
0.65	0.535	0.562	9.17	21.7
0.70	0.520	0.554	7.96	19.3
0.75	0.514	0.556	7.52	18.4
0.80	0.503	0.548	6.75	16.9
0.85	0.504	0.554	6.80	16.9
0.90	0.504	0.555	6.73	16.7
0.95	0.507	0.561	6.91	17.0
1.00	0.501	0.555	6.54	16.3

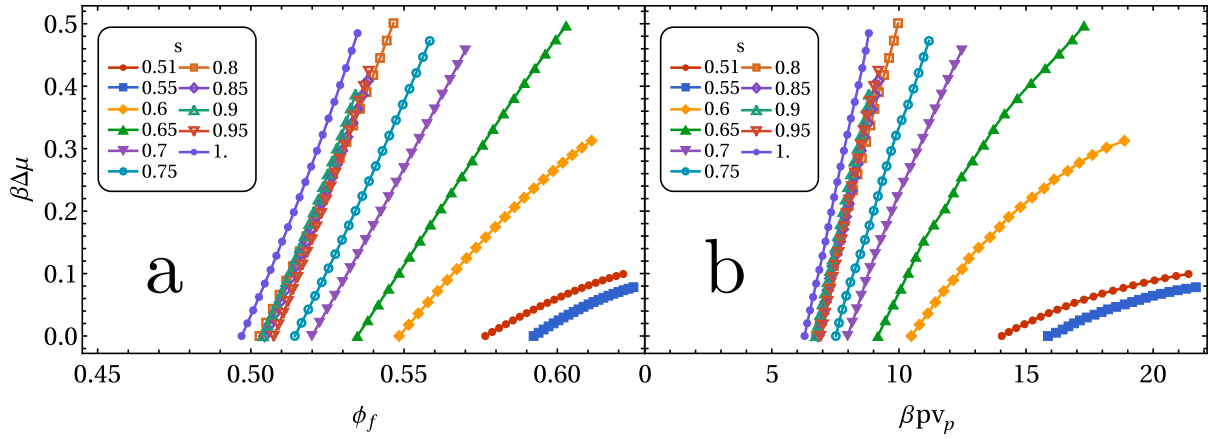


Figure 6.7: Supersaturation $\beta\Delta\mu$ for spherotetrahedra of different rounding ratios s as a function of a) the fluid packing fraction ϕ_f and b) the dimensionless pressure $\beta p v_p$. For increasingly less rounded tetrahedra, the coexistence density and pressure increase, and the supersaturation increases less rapidly with density and pressure.

6.4.3 Free energy of crystal VII

We calculate the free energy of crystal VII with a similar approach as taken for the plastic crystal pFCC. However, for crystal VII we must also consider that the particles are orientationally ordered. We again construct a reversible path using the Einstein crystal as a reference state, but this time we add a potential energy term that couples to the orientations, which are represented using unit quaternions $\hat{\mathbf{q}}$:

$$\beta U(\mathbf{r}^N, \hat{\mathbf{q}}^N) = \lambda \sum_{i=1}^N \left(\frac{\mathbf{r}_i}{\sigma} - \frac{\mathbf{r}_{i,0}}{\sigma} \right)^2 + c\lambda \sum_{i=1}^N \min_{\{\hat{\mathbf{Q}}\}} (\hat{\mathbf{q}}_i - \hat{\mathbf{q}}_{i,0})^2, \quad (6.12)$$

where \mathbf{r}_i are the particle positions and their lattice positions $\mathbf{r}_{i,0}$ as before, $\hat{\mathbf{q}}_i$ and $\hat{\mathbf{q}}_{i,0}$ are the unit quaternions describing the particle and ideal lattice orientations, and c is a constant that sets the ratio between the translational and orientation coupling, which we henceforth set to $c = 1$ for simplicity, such that λ is the coupling parameter of both the positions and the orientations. To account for the orientational symmetries that our particles possess we consider also rotations of $\hat{\mathbf{q}}_i$ by the quaternions $\{\hat{\mathbf{Q}}\}$ that produce equivalent orientations for a particular symmetry, and take the combination of $\hat{\mathbf{q}}_i$ and $\hat{\mathbf{q}}_{i,0}$ for which $(\hat{\mathbf{q}}_i - \hat{\mathbf{q}}_{i,0})^2$ is minimal. For tetrahedra, there are $N_{sym} = |\{\mathbf{Q}\}| = 24$ of such quaternions, formed by the 12 tetrahedral symmetry group elements, times two for the $\hat{\mathbf{q}} \leftrightarrow -\hat{\mathbf{q}}$ symmetry inherent to quaternions. The free energy of the corresponding noninteracting Einstein crystal reference state is given by:

$$\frac{\beta F_{Ein}(\lambda)}{N} = -\frac{3}{2} \frac{N-1}{N} \ln \left(\frac{\pi}{\lambda} \right) - \frac{3}{2} \ln \left(\frac{\pi}{c\lambda} \right) - \ln N_{sym}, \quad (6.13)$$

where the last term $\ln N_{sym} = \ln 24 \approx 3.17805$ describes the entropy granted by the orientational symmetry. We derive this expression in Appendix B.4. Including the orientational symmetry at the level of the potential has the additional benefit of preventing the integrand $\langle \partial U / \partial \lambda \rangle$ from diverging at intermediate densities and low coupling due

to particles hopping between symmetry-equivalent orientations. Without this symmetry, one can only perform the free-energy calculation at densities high enough for particles to never switch between symmetry-equivalent orientations. Because the applied Einstein crystal field also couples to orientations, we can reach the noninteracting limit at high values of λ without any additional steps. The total integration path is thus given by:

$$\frac{\beta F(\phi)}{N} = \frac{\beta F_{Ein}(\lambda_{max})}{N} - \int_{\lambda_{min}}^{\lambda_{max}} \left\langle \frac{\partial(\beta U/N)}{\partial \lambda} \right\rangle_{\lambda, \phi_{ref}} d\lambda + \int_{\phi_{ref}}^{\phi} \frac{\beta v_p p(\phi')}{\phi'^2} d\phi'. \quad (6.14)$$

We report the free energies of crystal VII calculated in this way in Table 6.4. To correctly calculate the fluid-VII coexistence, we also have to consider the rotational free energy of spherotetrahedra in the fluid phase. Specifically, when we compute the chemical potential of the ideal gas reference state in Eq. 6.4, we should remember to add the rotational free energy of an ideal gas of nonsymmetric rotators. As we derive in Appendix B.3, this free-energy contribution is equal to $\beta F_{id,rot}/N = -\ln 2\pi^2 \approx -2.98261$. To calculate the pFCC-VII coexistence, we should also add this contribution to the free energy of the plastic crystal. We show the fluid-VII and pFCC-VII coexistence data in Tables 6.5 and 6.6, and the resulting part of the (s, ϕ) -phase diagram in Fig. 6.8. The coexistence densities of the fluid-pFCC transition are somewhat higher than its melting and freezing densities, but for the fluid-VII and pFCC-VII transitions this difference is significantly smaller.

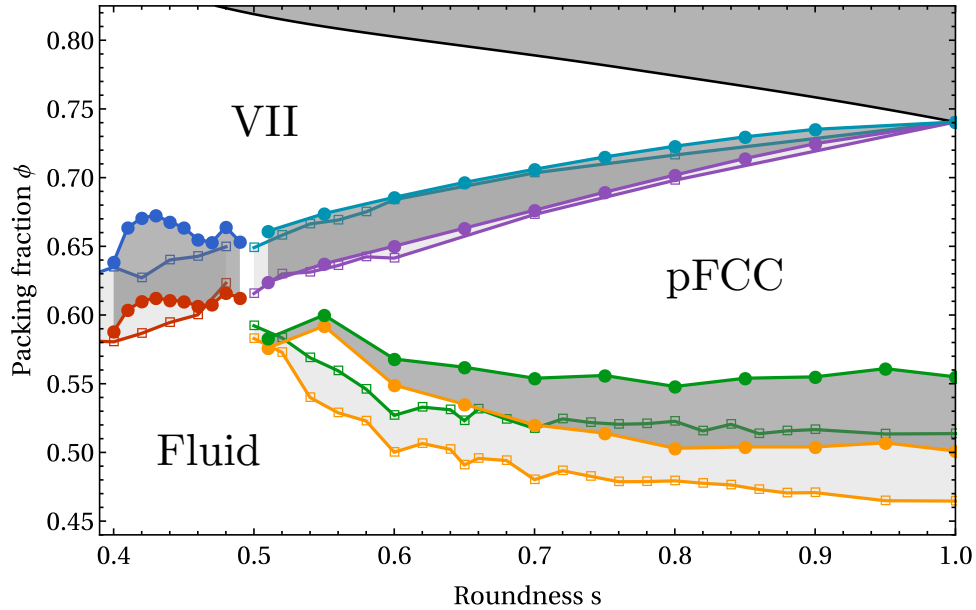


Figure 6.8: Phase diagram in the roundness s versus packing fraction ϕ representation for the high rounding ratios $s > 0.375$. The empty squares indicate the melting and freezing densities calculated in Chapter 4, and the lightly shaded region between them the resulting estimate for the coexistence region. The dark shaded regions between the filled circles indicate the coexistence densities from Tables 6.5 and 6.6 determined using free-energy calculations, while the dark shaded region in the top right indicates “forbidden” packing fractions higher than the established dense packings indicated by the solid black line.

Having obtained the free energies of all three phases, we can now compare the supersaturation of the fluid-pFCC transition to those of the fluid-VII and pFCC-VII ones. We do so in Fig. 6.9, where we can see that the supersaturation of the latter two increases quite rapidly with packing fraction, more so than the supersaturation of the fluid-pFCC transition. This is somewhat surprising, given crystal VII does not readily form from either the fluid or crystal VII in our simulations. However, classical nucleation theory states that the nucleation barrier is composed of two opposing parts: while the difference in bulk free energies as described by the supersaturation $\Delta\mu$ drives the system towards nucleation, it is counteracted by the free-energy cost associated with creating an interface between the two phases. This interface has an associated interfacial tension, which describes the energy cost of creating one unit area of interface. It is quite plausible that the fluid-VII interface has a higher interfacial tension than the fluid-pFCC interface. To self-assemble the crystal VII from the fluid, particles must pay an additional entropy cost in order to attain the orientational order of the crystal VII phase, while no such orientational cost is required when going from the fluid to the plastic crystal pFCC. It is possible to determine the interfacial tension or the full nucleation barrier by using e.g. nucleus size pinning simulations [228] or umbrella sampling [209, 220, 221]. We will not perform such calculations in this work, but we view it as an interesting possible follow-up.

Our free-energy calculations reveal that the nucleation process for a bulk system of spherotetrahedra can be quite different depending on the exact rounding ratio of the particles, especially in the proximity of the triple point at $s \approx 0.5$. The data we provide here should serve as a useful basis for performing more involved studies that investigate the nucleation of spherotetrahedra in this region.

Table 6.4: Number of particles N , reference packing fraction ϕ_{ref} , and the coupling constants $\ln \lambda_{\min}$ and $\ln \lambda_{\max}$ used in the Einstein integration, alongside the resulting ideal Einstein crystal free energy F_{Ein} (Eq. 6.13), free energy difference along the Einstein integration path ΔF_{Ein} and the free energies F of crystal VII, for varying rounding ratios s .

s	N	ϕ_{ref}	$\ln \lambda_{\min}$	$\ln \lambda_{\max}$	$\beta F_{\text{Ein}}/N$	$\beta \Delta F_{\text{Ein}}/N$	$\beta F/N$
0.40	500	0.67	-2	10	23.3612	14.91(12)	8.45(12)
0.41	500	0.70	-2	10	23.3612	13.59(9)	9.77(9)
0.42	432	0.70	-2	10	23.3570	13.60(10)	9.75(10)
0.43	432	0.70	-2	10	23.3570	13.62(10)	9.73(10)
0.44	432	0.70	-2	10	23.3570	13.63(10)	9.72(10)
0.45	432	0.70	-2	10	23.3570	13.64(10)	9.72(10)
0.46	432	0.70	-2	10	23.3570	13.63(10)	9.73(10)
0.47	432	0.70	-2	10	23.3570	13.62(10)	9.73(10)
0.48	432	0.70	-2	10	23.3570	13.61(10)	9.74(10)
0.49	432	0.70	-2	10	23.3570	13.61(10)	9.75(10)
0.50	1458	0.70	-2	10	23.3786	13.61(5)	9.77(5)
0.51	500	0.70	-2	10	23.3612	13.60(9)	9.77(9)
0.55	432	0.74	-2	14	35.3431	22.66(17)	12.68(17)
0.60	432	0.74	-2	14	35.3431	22.48(17)	12.86(17)
0.65	432	0.74	-2	14	35.3431	22.30(16)	13.04(16)
0.70	432	0.74	-2	14	35.3431	22.05(16)	13.29(16)
0.75	432	0.74	-2	14	35.3431	21.72(16)	13.62(16)
0.80	432	0.74	-2	14	35.3431	21.24(16)	14.10(16)
0.85	432	0.74	-2	14	35.3431	20.56(16)	14.78(16)
0.90	432	0.74	-2	14	35.3431	19.52(15)	15.82(15)

Table 6.5: Fluid-VII coexistence data: the rounding ratio s , coexistence densities $\phi_{\text{fluid},c}$ and $\phi_{\text{VII},c}$, and the coexistence pressure $\beta v_p p_c$ and chemical potential $\beta \mu_c$.

s	$\phi_{\text{pFCC},c}$	$\phi_{\text{VII},c}$	$\beta v_p p_c$	$\beta \mu_c$
0.51	0.624	0.661	21.4	40.0
0.55	0.637	0.674	24.2	44.2
0.60	0.650	0.686	27.9	49.6
0.65	0.663	0.697	32.8	56.4
0.70	0.676	0.706	39.2	65.5
0.75	0.689	0.715	48.6	78.7
0.80	0.702	0.723	63.0	98.8
0.85	0.714	0.730	88.0	133.5
0.90	0.725	0.735	140.5	205.5

Table 6.6: pFCC-VII coexistence data: the rounding ratio s , coexistence densities $\phi_{\text{pFCC},c}$ and $\phi_{\text{VII},c}$, and the coexistence pressure $\beta v_p p_c$ and chemical potential $\beta \mu_c$.

s	$\phi_{\text{fluid},c}$	$\phi_{\text{VII},c}$	$\beta v_p p_c$	$\beta \mu_c$
0.40	0.588	0.639	16.1	34.9
0.41	0.604	0.664	18.7	36.3
0.42	0.610	0.671	19.8	37.9
0.43	0.612	0.673	20.2	38.5
0.44	0.611	0.668	19.8	37.9
0.45	0.610	0.664	19.6	37.5
0.46	0.607	0.655	18.9	36.5
0.47	0.608	0.653	19.1	36.6
0.48	0.616	0.664	20.6	38.9
0.49	0.612	0.653	19.8	37.7

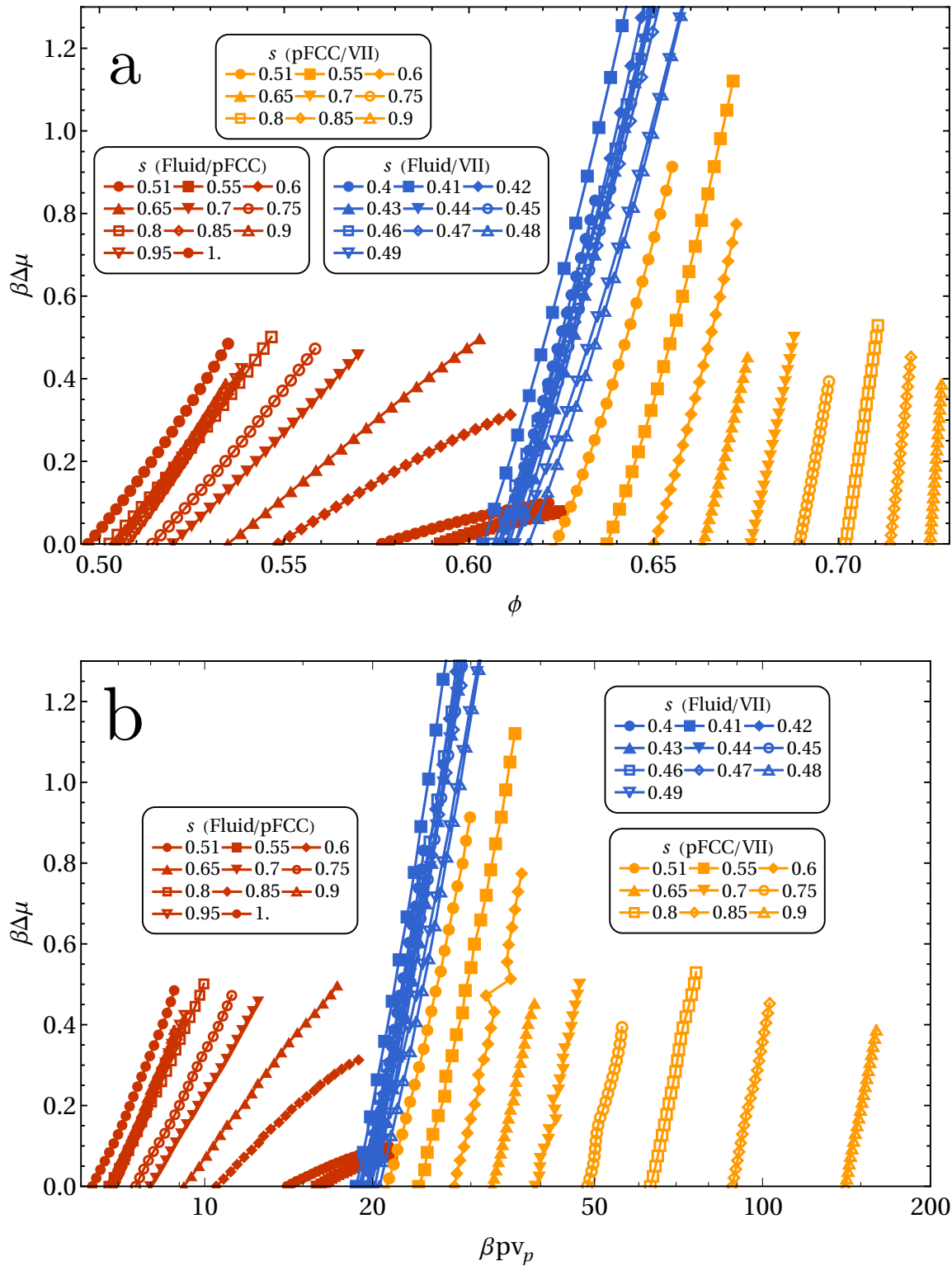


Figure 6.9: Supersaturation $\beta\Delta\mu$ for spherotetrahedra of different rounding ratios s as a function of a) the packing fraction of the lower phase ϕ (either fluid or pFCC) and b) the dimensionless pressure $\beta p v_p$. The fluid-pFCC coexistence is shown in red, with fluid-VII and pFCC-VII in blue and yellow, respectively.

6.5 Hard spherotetrahedra in spherical confinement

In the experimental system of Ref. [223], the self-assembly takes place within the confinement of a slowly evaporating droplet of cyclohexane. The surface tension of the droplets will drive them towards a spherical geometry. To mimic this self-assembly process, we perform MC- NVT simulations of hard spherotetrahedra within a hard spherical confinement that is compressed at a fixed rate. Specifically, we do so by increasing the packing fraction ϕ by 0.0001 every 10^4 MC sweeps, compressing the system accordingly, and removing any overlaps that are created by the compression step. It is also possible to mimic the shrinking spherical confinement in the NpT ensemble by constantly increasing the pressure p and performing MC moves on the volume of the spherical confinement. However, it is difficult to define the rate at which the confinement shrinks in such an ensemble, as this requires knowledge of the pressure-density equation of state $p(\phi)$, which is generally not known in advance. Since this rate is an important parameter for the self-assembly process, we prefer the MC- NVT approach. While we have performed these simulations for the entire range of shapes $s \in [0, 1]$, we will focus primarily on the range that is most relevant for the experimental self-assembly, which is roughly $s \in [0.4, 1]$. In this range, the equilibrium bulk phase at high density is the crystal VII phase, although depending on the system parameters we may also expect to find the self-assembly process to pass through the plastic crystal pFCC first.

6.5.1 Mackay/anti-Mackay structural order

Given that in the range $s \in [0.4, 1]$ the particle shape is quite close to that of hard spheres, it is instructive to first review their behaviour under spherical confinement. The self-assembly of hard spheres ($s = 1$) in spherical confinement has been studied in detail in a number of recent works. De Nijs et al. [26] showed that depending on the number of particles within the confinement, hard spheres do not self-assemble into the bulk FCC structure, but rather into structures with icosahedral order corresponding to a Mackay/anti-Mackay [229, 230] packing. These results were later refined by Wang et al. [27], who demonstrated that hard spheres in spherical confinement display a “magic number” effect, in which supraparticles with specific numbers of constituent particles are more stable than others due to these numbers corresponding to the optimal Mackay/anti-Mackay clusters.

We note that as demonstrated for spheres, there is a strong system size effect on the self-assembly of supraparticles. In fact, there are three main factors that govern the self-assembly of particles under spherical confinement: the shape and interactions of the particles, the size of the system, and the rate of compression. The former two determine the equilibrium structure, while the latter determines whether this structure can be reached. A possible fourth component are the interactions between the particles and the boundary. For hard spheres, these were shown to be largely insignificant [26], but they become more important for anisotropic particles such as rounded cubes [174] or the spherotetrahedra we consider here. To limit the number of variables, we restrict ourselves to compression rates that are likely to be slow enough to reach the equilibrium structure. Furthermore, we focus primarily on a single system size of $N = 4096$ particles,

which is roughly on the order of the number of nanoparticles in the supraparticles in the experimental system. The particle/wall interaction is assumed to be a hard interaction for simplicity.

To investigate whether spherotetrahedra exhibit a similar effect to hard spheres, we characterize the obtained compressed structures using the bond-order parameter approach outlined in Ref. [26]. To this end, we define the dot product

$$d_6(i, j) = \frac{\sum_{m=-6}^6 q_{6m}(i) q_{6m}^*(j)}{\left(\sum_{m=-6}^6 |q_{6m}(i)|^2\right)^{1/2} \left(\sum_{m=-6}^6 |q_{6m}(j)|^2\right)^{1/2}}, \quad (6.15)$$

and define solid-like bonds between neighbouring particles as those bonds for which $d_6 > 0.6$ and solid-like particles as those with at least $n_{bond} = 7$ solid-like bonds. We differentiate between crystal domains by composing clusters of solid-like particles connected by bonds with $d_6 > 0.9$.

Fig. 6.11 shows the fraction of crystalline particles as a function of the packing fraction ϕ within the supraparticles. While very rounded spherotetrahedra for $s \in [0.7, 1.0]$ crystallize nearly as well as spheres, the total fraction of crystalline particles drops sharply for less rounded shapes, dropping to nearly zero for $s \leq 0.5$. In Fig. 6.10 we show the self-assembled clusters, where we have colored solid-like particles according to the crystal domain they belong to. This labeling reveals that the core of the supraparticles is nearly completely crystalline and ordered in the icosahedral Mackay structure beneath a surface layer of roughly 3 particles in width. For spheres, this surface layer would eventually order into a truncated anti-Mackay structure according to Ref. [27]. We can see some hints of anti-Mackay surface ordering in Fig. 6.10 for $s = 0.8$, which suggests that the same process holds for spherotetrahedra. However, for spherotetrahedra the Mackay/anti-Mackay structure should eventually be overtaken in packing efficiency by one with orientational order, likely one resembling crystal VII. For $s < 0.6$ there is no longer any crystalline order in the core, and most crystalline particles are located at the surface, instead.

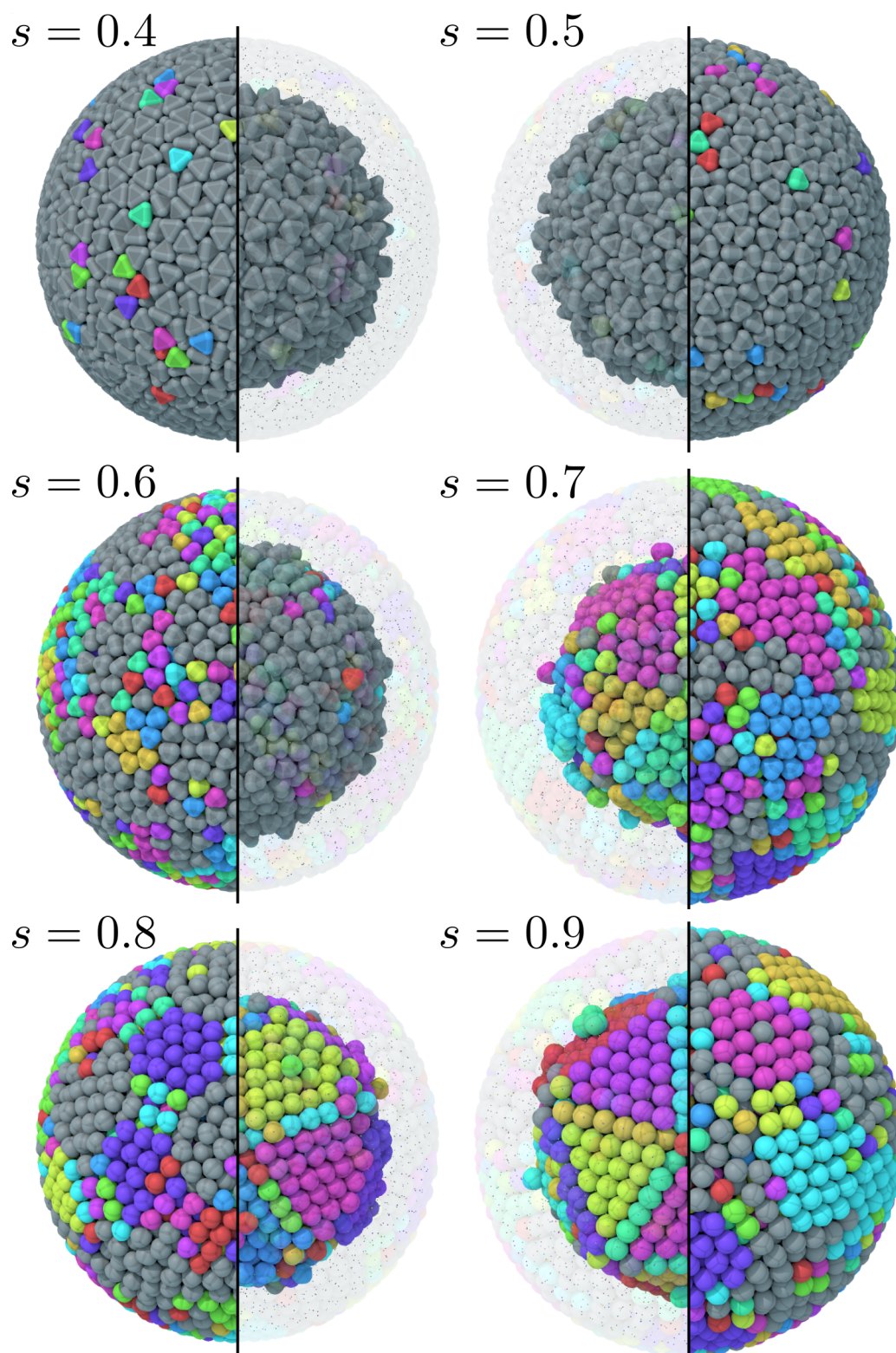


Figure 6.10: Self-assembled clusters of spherotetrahedra in spherical confinement for $s \in [0.4, 0.9]$, with solid-like particles colored according to which cluster they belong to and disordered particles colored in gray. For each supraparticle we also show the cores, for which we have hidden the roughly three particle wide surface. For $s \in [0.7, 0.9]$ the cores exhibit Mackay ordering, while for $s \in [0.4, 0.6]$ the cores are disordered, with most order being present on the surface.

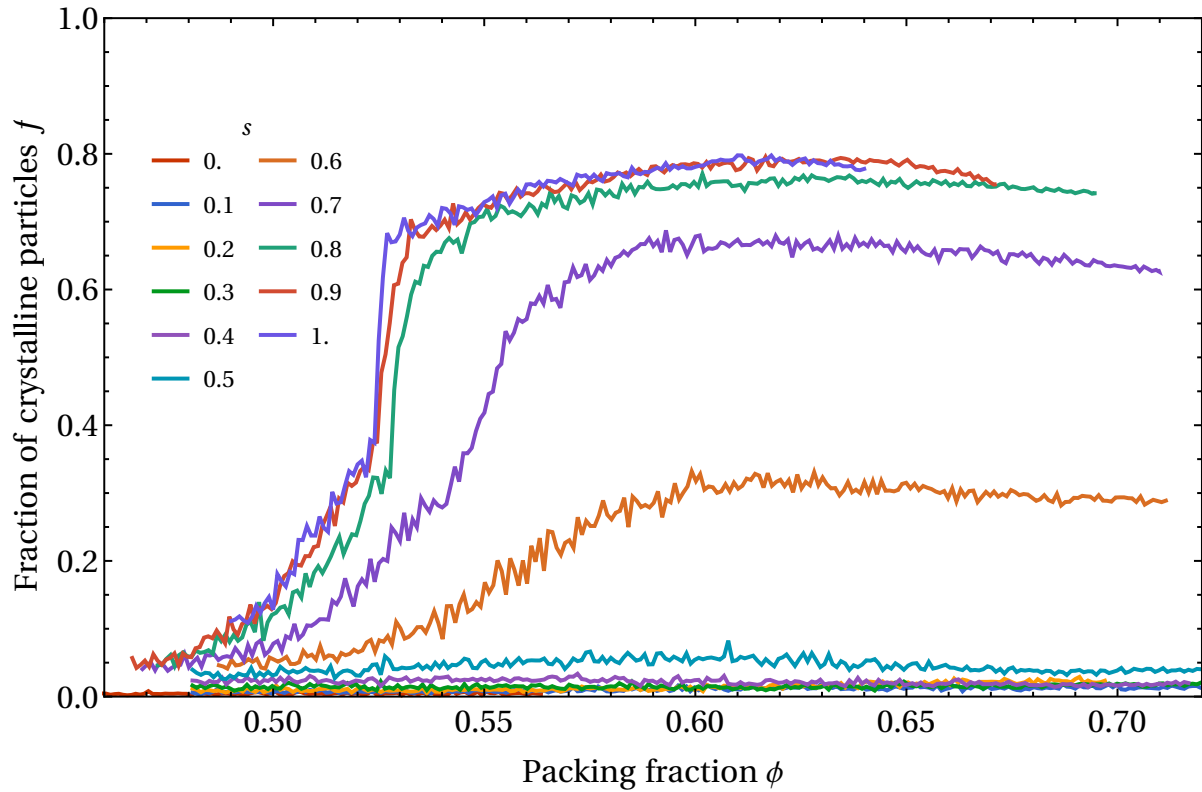


Figure 6.11: Fraction of crystalline particles f as a function of the packing fraction ϕ . Crystalline particles (according to the criterion also used for hard spheres) are only found in appreciable fractions for $s > 0.5$.

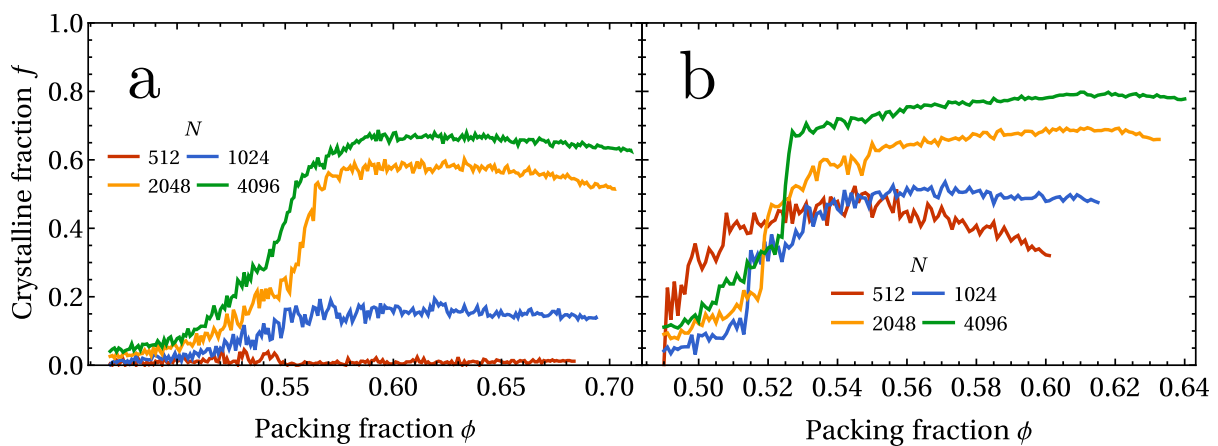


Figure 6.12: Fraction of crystalline particles f as a function of the packing fraction ϕ , for varying numbers of particles N , for a) hard spherotetrahedra at $s = 0.7$ and b) hard spheres at $s = 1.0$.

6.5.2 Orientational order at the spherical boundary

We speculate that for the rounding ratios $s \in [0.4, 0.6]$ the sphere packing competes with the preference for orientational order, which manifests in two ways. The first is that bulk undeformed FCC ordering becomes less stable and harder to form, as we have shown with the free-energy calculations in Section 6.4. Second is that this competition is even stronger at the spherical boundary. Because the spherical boundary in our model is hard, there is a preference for spherotetrahedra to orient themselves to pack favorably at the boundary, an effect that becomes stronger for smaller roundness s . To quantify this effect, we define an order parameter that measures how aligned the spherotetrahedron's facets are with the radial direction $\hat{\mathbf{r}}$ of the confining sphere. This order parameter ψ is given by:

$$\psi = \frac{3}{2} \max_i (\hat{\mathbf{n}}_i \cdot \hat{\mathbf{r}}) - \frac{1}{3}. \quad (6.16)$$

Here $\hat{\mathbf{n}}_i$ is the normal of facet i of the spherotetrahedron, and symmetry is accounted for by taking the maximum value of this dot product over all facets. For tetrahedral symmetry, this dot product has a range $[1/3, 1]$, which we transform such that $\psi \in [0, 1]$. The value $\psi = 0$ corresponds to a vertex pointing in the radial direction, $\psi = 1/\sqrt{3}$ to the normal of an edge and $\psi = 1$ to the normal of a facet. Fig. 6.13 shows the degree of surface alignment for the supraparticles that were also shown in Fig. 6.11. For $s \in [0.7, 0.9]$, there is almost no orientational ordering at the surface, but there is a small increase for $s = 0.6$ and a sharp one for $s = 0.5$ and $s = 0.4$. Outside the relevant range for the experimental supraparticle assembly, simulations for $s \in [0, 0.3]$ (shown in Fig. 6.14) reveal that surface orientational order becomes extremely pronounced at lower rounding ratios, though the exact surface packing pattern is different between $s \in [0, 0.2]$ and $s \in [0.3, 0.4]$. As shown in Fig. 6.15, we find for $s \in [0, 0.2]$ a quite complicated lattice with an $N = 20$ -particle unit cell reminiscent of dodecagonal quasicrystal layers [166, 168] or virus capsids [231]. For $s = 0.3$ we find a much simpler two-particle triangular lattice.

For spheres in spherical confinement, the crystallization process starts at the surface, and from there grows into the bulk [26]. We hypothesize that orientational ordering inhibits the onset of crystallization into an FCC-like structure for $s \in [0.4, 0.6]$. It should be noted that this inhibition is likely a dynamic effect rather than an equilibrium one: given a slow enough compression, even slow homogeneous nucleation could start crystallization, even when heterogeneous nucleation at the surface is inhibited.

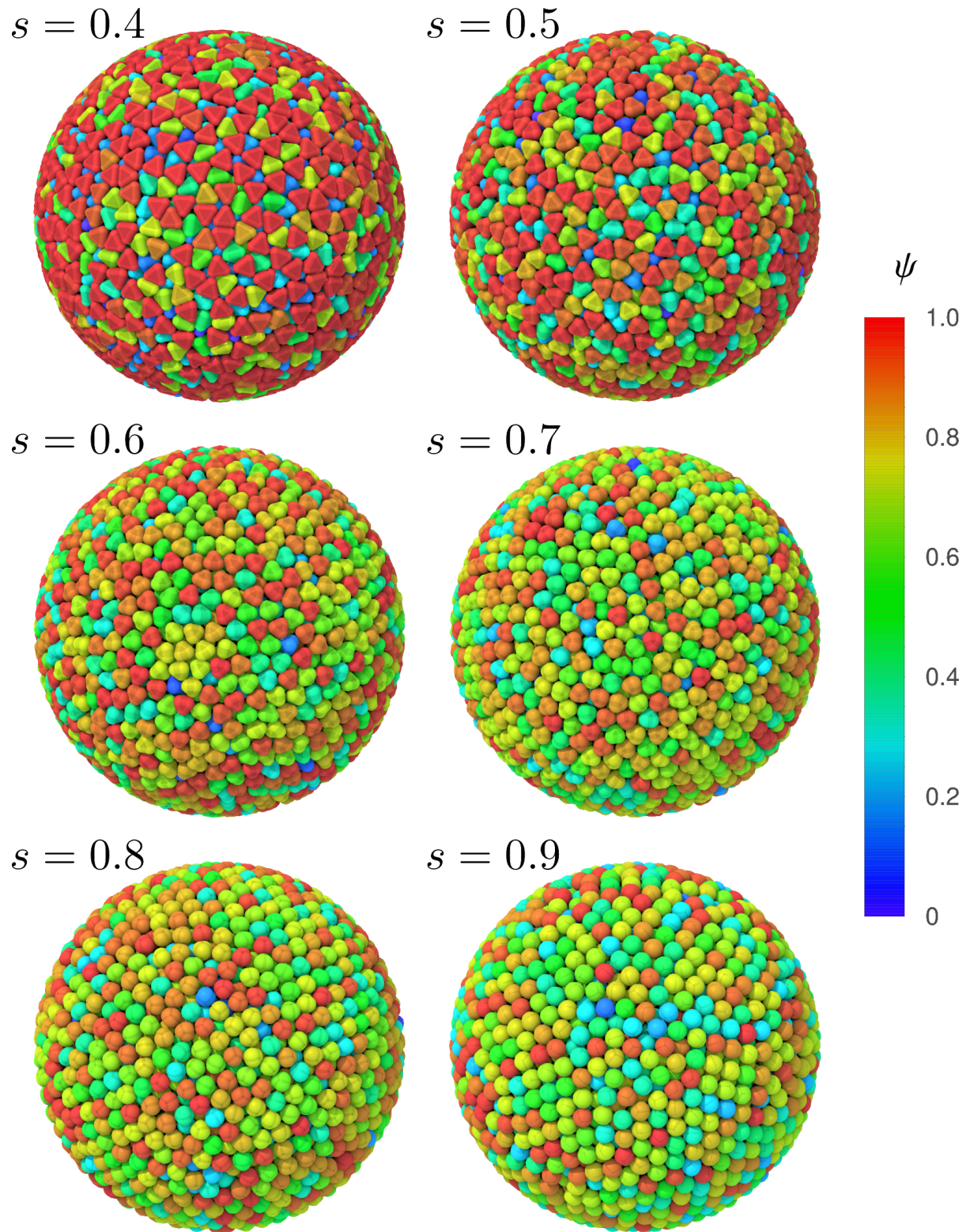


Figure 6.13: Self-assembled clusters of spherotetrahedra in spherical confinement for $s \in [0.4, 0.9]$, with particles colored according to the radial orientation order parameter ψ (Eq. 6.16). Orientational order at the surface is largely absent for $s \in [0.7, 1.0]$, but becomes very pronounced for $s = 0.4$ and $s = 0.5$.

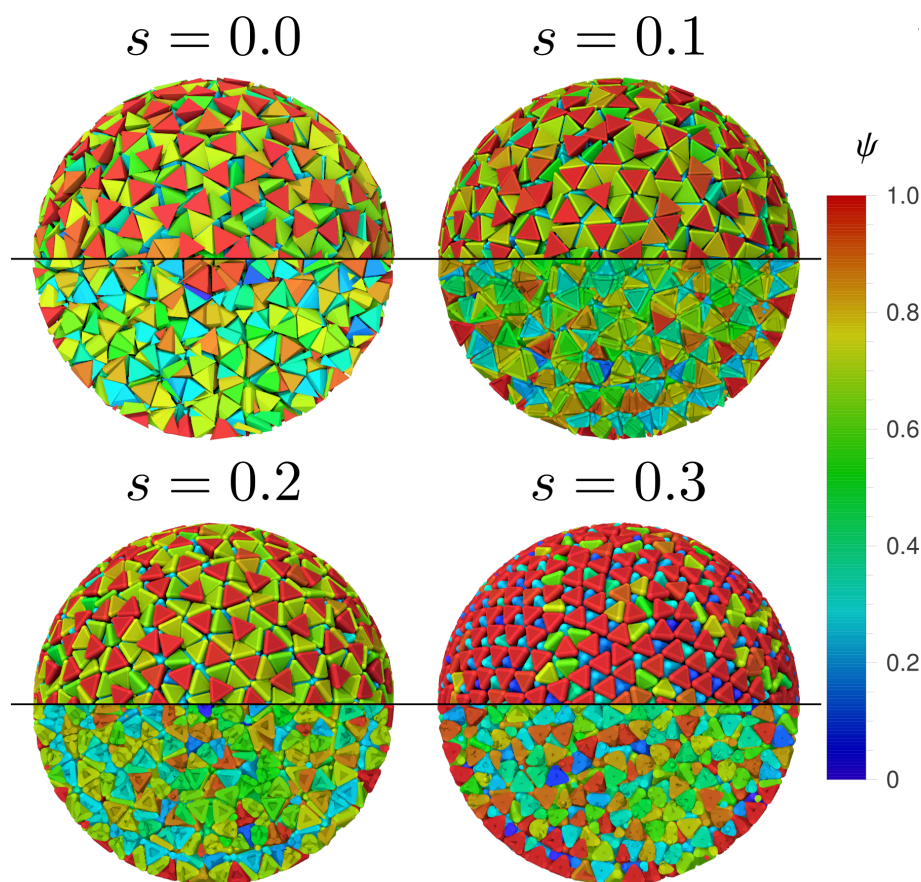


Figure 6.14: Self-assembled clusters of spherotetrahedra in spherical confinement for $s \in [0.0, 0.3]$, with particles colored according to the radial orientation order parameter ψ (Eq. 6.16).

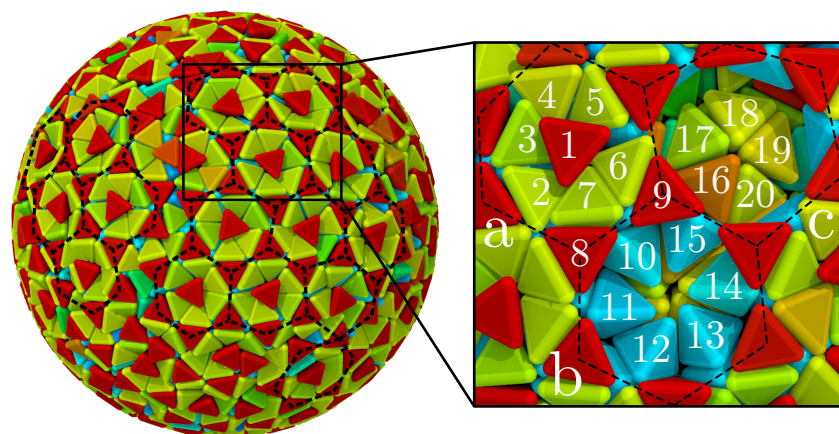


Figure 6.15: Surface structure for $s = 0.2$. The surface structure is formed by roughly hexagonal cells. Moving progressively inward, we can see are each cell is composed of a) a facet-aligned central particle surrounded by six edge-aligned particles, plus two connecting facet-aligned particles, b) six more particles in a hexagon with orientations between edge and vertex-aligned and c) a wagon-wheel of five spherotetrahedra.

6.6 Conclusions

Our goal in this study was to explain why rounded tetrahedral nanoparticles form egg-shaped supraparticles. Our initial hypotheses were that i) the crystal formed by the nanoparticles has a strong preference towards growth in certain directions and ii) there is some kind of interplay between the spherical confinement and crystal growth which causes elongation along one axis. There were several steps to undertake before we could test these hypotheses. For either hypothesis, we had to identify the crystal formed in the experimental system, verify the applicability of the hard spherotetrahedron model, and establish accurately the density regime in which crystallization takes place.

Approximating the ligands to add effective roundness to a hard-particle model, we established the shape of the experimental nanoparticles to have an approximate rounding ratio of $s \approx 0.5 \pm 0.1$, with the CdSe core corresponding to $s \approx 0.31 \pm 0.11$. By comparing their structure metric fingerprints with those of the hard spherotetrahedron crystals we identified in Chapter 4, we established the supraparticle crystal structure to be a two-particle deformed FCC lattice, where the two particles take opposing orientations and the deformation is a compression along one of the cubic axes of the FCC lattice. This lattice matches the hard spherotetrahedron crystal VII, but the deformation in the experimental system is less than in the model system. We suspect that the limited but still present polydispersity in the experimental system favors a less deformed lattice over the more specifically deformed lattice found for a perfectly monodisperse model system. A similar preference may also arise from the softness of the ligand interactions.

Having established that the experimental crystal structure matches the model reasonably well, we performed free-energy calculations to establish the coexistence properties of the three hard spherotetrahedron phases relevant to the experimental self-assembly: the fluid, the plastic crystal pFCC, and the orientationally ordered crystal VII. The measured shape of $s \approx 0.5$ corresponds nearly exactly to the triple point of these three phases, and so there are two possible paths to crystallization: fluid \rightarrow VII for $s < 0.5$, and fluid \rightarrow pFCC \rightarrow VII for $s > 0.5$. We find that the supersaturation $\Delta\mu$ of the fluid-pFCC transition drops sharply when approaching the triple point at $s = 0.5$, suggesting that this transition is highly sensitive to the exact particle shape in this regime.

Finally, we performed self-assembly simulations under a shrinking spherical confinement to investigate the effects of the evaporating droplet geometry in which the supraparticles are formed. We find that the Mackay/anti-Mackay structure recently found for confined hard spheres [26, 174] persists down to $s = 0.7$, but that it is absent for less rounded tetrahedra. In fact, we find no bulk ordered structures to form for $s < 0.7$ for the range of system sizes and shrinking rates we investigated. There is, however, significant order to be found at the boundaries. For $s < 0.6$, particles at the boundary have a strong preference to order with their facets towards the boundary, which in turn induces two different structures at the boundary: a quite complicated lattice reminiscent of dodecagonal quasicrystal layers [166, 168] for $s \in [0, 0.2]$ and a two-particle triangular lattice for $s = 0.3$, respectively. It is debatable whether this surface ordering would also occur in the experimental self-assembly. The particle-wall interaction in the experiments involves interactions between the cores and ligands of the particles with the surfactant-covered cyclohexane-water interface. At this stage, it is largely unknown how well this interac-

tion can be modeled as a hard wall. Given that we did not observe any bulk ordered supraparticles for $s \in [0, 0.6]$ in our simulations, it is possible that a hard-wall model is insufficient to adequately describe the self-assembly.

6.7 Outlook

The results shown in this chapter are not yet sufficient to truly test the validity of any of our hypotheses. Further work is still needed to determine why these supraparticles attain an egg-like shape in the self-assembly experiments of Ref. [223].

It should be possible to investigate the confined crystallization within a soft confinement. In the ideal case, a two-way coupling should be established between the particles and the wall, enabling the confining wall to deform if the crystallization process yields significant anisotropy. Such a model would require a more educated guess for the experimental particle-wall interaction. If these are such that particles do not adsorb to the interface at all, a relatively simple form of the confining potential could be used. If particles do adsorb, a boundary layer with particles in fixed orientations could be used as a confinement. Using such a model, one could investigate whether the fluid→VII or pFCC→VII transitions are sufficiently anisotropic to deform the confining boundary.

Another avenue one could pursue is to perform umbrella sampling [220, 221] or nucleus-size pinning simulations [228] to investigate whether the fluid→VII or pFCC→VII transitions yield any significant anisotropy in bulk. Identifying the size of the crystal nucleus requires a good order parameter, which may be constructed from the general crystallization order parameter $\Sigma = \frac{1}{5}(\bar{q}_4 + \bar{q}_6 + \bar{q}_8 + \bar{q}_{10} + \bar{q}_{12})$ that we identified in Chapter 5. As nucleation events for these transitions seem to be quite rare and the high density may lead to slow dynamics, it may be useful to employ a seeding approach [232].

We expect the results and methods discussed in this chapter to provide a useful basis for follow-up studies along these lines.

Acknowledgements

The CdSe rounded tetrahedral nanoparticles were synthesized by Dr. Yaoting Wu under the supervision of Prof. Christopher Murray at the University of Pennsylvania. All other experimental work shown in this chapter, which includes the nanoparticle self-assembly into supraparticles, measurements of the experimental particle shape (the center-to-edge and center-to-vertex lengths), and the inverse Fourier transform reconstruction of the supraparticles were performed by Dr. Da Wang under the supervision of Prof. Alfons van Blaaderen at Utrecht University.

A

An algorithm for calculating the volume of arbitrary convex spheropolyhedra

The volume of *any* convex polyhedron characterized by a set of vertices $v = \{\mathbf{r}_i\}$ can be calculated exactly by a simple algorithm. Take any point \mathbf{r}_0 inside the polyhedron, and form a tetrahedron whose vertices are this point \mathbf{r}_0 and three unique vertices $\mathbf{r}_{1,2,3}$ from the polyhedron's vertices v . The volume V of this tetrahedron is:

$$V = \frac{1}{6} \det |\mathbf{r}_1 - \mathbf{r}_0, \mathbf{r}_2 - \mathbf{r}_0, \mathbf{r}_3 - \mathbf{r}_0|. \quad (\text{A.1})$$

Choosing \mathbf{r}_0 as the origin simplifies matters. Now simply repeat this procedure for every three vertices that form a face of the polyhedron, sum up the volumes of the tetrahedra, and one obtains the volume of the polyhedron. To get the volume of the corresponding convex *spheropolyhedron* with rounding radius R one does the following: first calculate the polyhedron volume, and then add to this the volume of a) triangular slabs that extend (the triangulation of) the polyhedron's faces outward by R , b) cylinder segments of radius R around each of the polyhedron's edges and c) sphere segments of radius R around each of the polyhedron's vertices. For each triangular face composed of three vertices $\mathbf{r}_{0,1,2}$ the volume of the triangular slab is:

$$V_{\text{slab}} = \frac{1}{2} R |\mathbf{e}_1 \times \mathbf{e}_2|, \quad (\text{A.2})$$

where $\mathbf{e}_{1,2} = \mathbf{r}_{1,2} - \mathbf{r}_0$ are two of the edges of this face.

For the cylinder and sphere contributions we must calculate how much of the cylinder and sphere contributes to the volume, which depends on the angles between faces connected by edges and faces meeting at a vertex, respectively. Consider now an edge $\mathbf{e} = \mathbf{r}_1 - \mathbf{r}_0$ that connects two triangular faces $\mathbf{f}_{0,1}$. The two additional vertices that are part of the faces $\mathbf{f}_{0,1}$ but not part of the edge are $\mathbf{r}_{3,4}$, respectively. We first find the dihedral angle between the two faces from their surface normals:

$$\hat{\mathbf{n}}_0 = \frac{\mathbf{e} \times (\mathbf{r}_3 - \mathbf{r}_0)}{|\mathbf{e}| |(\mathbf{r}_3 - \mathbf{r}_0)|} \quad (\text{A.3})$$

$$\hat{\mathbf{n}}_1 = \frac{(\mathbf{r}_4 - \mathbf{r}_0) \times \mathbf{e}}{|\mathbf{e}| |(\mathbf{r}_4 - \mathbf{r}_0)|} \quad (\text{A.4})$$

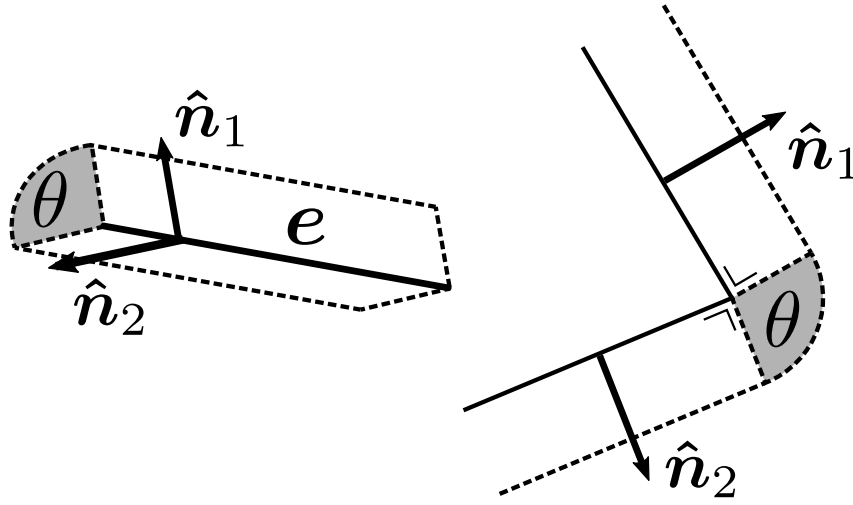


Figure A.1: Two views of a cylinder segment around a spheropolyhedron's edge. The edge e is adjacent to two faces with normals \hat{n}_1 and \hat{n}_2 .

Note that depending on the vertex order, these normals are either both facing inward or both facing outward. As long as the shapes are convex, the angle that provides the fraction of the cylinder which contributes to the volume is then given by the angle between the faces:

$$\theta = \arccos(\hat{n}_0 \cdot \hat{n}_1) \quad (\text{A.5})$$

and the contributing volume of the cylinder segment becomes

$$V_{\text{cyl}} = \pi R^2 |e| \frac{\theta}{2\pi} \quad (\text{A.6})$$

The vertex segments require some extra attention, because even for convex spheropolyhedra there may be any number of faces meeting at a particular vertex. For each vertex \mathbf{r} we generate a set of new vertices that are moved outward by the rounding radius R into the normal directions \hat{n}_i of vertex \mathbf{r} 's adjacent faces:

$$\mathbf{r} \rightarrow \{\mathbf{r} + R\hat{n}_i\} \quad (\text{A.7})$$

These new vertices are the points where the cylinder segments around edges containing the vertex \mathbf{r} , the outwardly moved facets adjacent to \mathbf{r} and the spherical caps around \mathbf{r} all intersect each other simultaneously. To then calculate how much of the volume of the spherical cap around the vertex contributes to the volume, we construct a set of non-overlapping tetrahedra from the old vertex \mathbf{r} to the new vertices $\{\mathbf{r} + R\hat{n}_i\}$ and sum the solid angles made from \mathbf{r} to triplets of these new vertices. For each such tetrahedron, the solid angle Ω subtended from \mathbf{r} to three new vertices can be calculated with the following expression [233]:

$$\Omega = 2 \arctan \left(\frac{\mathbf{a} \cdot (\mathbf{b} \times \mathbf{c})}{abc + |\mathbf{a} \cdot \mathbf{b}|c + |\mathbf{b} \cdot \mathbf{c}|a + |\mathbf{c} \cdot \mathbf{a}|b} \right) \quad (\text{A.8})$$

where \mathbf{a} , \mathbf{b} and \mathbf{c} are vectors from \mathbf{r} to three of the new vertices and a , b and c are their lengths. The sum of these solid angles divided by 4π is the fraction of the sphere around the vertex \mathbf{r} that contributes to the volume of the spheropolyhedron.

B

Free energies of three-dimensional ideal rotator systems

B.1 Rotational free energy of an ideal gas of classical uniaxial rotators

The orientations of particles with a uniaxial symmetry can be fully represented by a unit vector $\hat{\mathbf{n}}$ on the unit sphere \mathbb{S}^2 . The rotational configuration integral of a system of uniaxial rotators is then given by:

$$Z_{or,id} = \int_{\mathbb{S}^2} \exp[-\beta U(\hat{\mathbf{n}})] d\hat{\mathbf{n}} = \int_{\mathbb{S}^2} d\hat{\mathbf{n}}. \quad (\text{B.1})$$

This integral is simply the surface area of the unit sphere \mathbb{S}^2 , which can be computed in spherical coordinates:

$$Z_{or,id} = \int_0^{2\pi} \int_0^\pi \sin \theta d\theta d\phi = 4\pi. \quad (\text{B.2})$$

The corresponding dimensionless free energy per particle then becomes:

$$\beta F_{or,id}/N = -\ln 4\pi \quad (\text{B.3})$$

B.2 Rotational free energy of an ideal Einstein crystal of classical uniaxial rotators

Consider the orientational energy of an Einstein crystal of N particles with nematic symmetry (uniaxial rotators):

$$\beta U(\theta^N) = \lambda \sum_{i=1}^N \sin^2 \theta_i, \quad (\text{B.4})$$

where θ_i is the angle between the particle orientation and the nematic director. The configuration integral is then:

$$Z_{or,Ein} = \left(\int_0^{2\pi} d\phi \int_0^\pi \exp[-\lambda \sin^2 \theta] \sin \theta d\theta \right)^N. \quad (\text{B.5})$$

For $\lambda \gg 1$, the integrand $\exp[-\lambda \sin^2 \theta] \sin \theta$ becomes sharply peaked around $\theta = 0$ and $\theta = \pi$. In this limit, we can approximate the integral in Eq. B.5 as the sum of two approximations of the integrand around these peaks: respectively using the (Taylor) expansions of $\sin \theta$ around $\theta = 0$ and $\theta = \pi$ (see Fig. B.1).

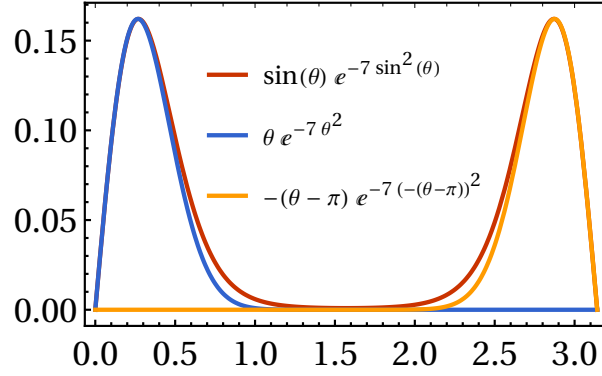


Figure B.1: Approximation of the integrand of Eq. B.5 by the sum of two functions obtained by Taylor expanding the $\sin \theta$ around $\theta = 0$ and $\theta = \pi$, using $\lambda = 7$.

These two functions are each other's symmetric counterpart around $\pi/2$, and so their integrals over $[0, \pi]$ are identical, and we can replace Eq. B.5 by:

$$Z_{or,Ein} = \left(2 \int_0^{2\pi} d\phi \int_0^\pi \exp[-\lambda \theta^2] \theta d\theta \right)^N. \quad (\text{B.6})$$

Now evaluate the integral over ϕ and substitute $x = \lambda \theta^2$, $dx = 2\lambda \theta d\theta$:

$$Z_{or,Ein} = \left(4\pi \int_0^{\pi^2 \lambda} \exp[-x] \frac{1}{2\lambda} dx \right)^N = \left(\frac{2\pi}{\lambda} (1 - \exp[-\pi^2 \lambda]) \right)^N \approx \left(\frac{2\pi}{\lambda} \right)^N \quad (\text{B.7})$$

Where in the final step we again applied $\lambda \gg 1$. Then the corresponding free energy is:

$$F_{or,Ein} = -k_B T \ln \left[\left(\frac{2\pi}{\lambda} \right)^N \right] \Rightarrow \beta F_{or,Ein} / N = -\ln \left[\frac{2\pi}{\lambda} \right], \quad (\text{B.8})$$

which is the expression reported in literature [11].

B.3 Rotational free energy of an ideal gas of classical rigid body rotators using quaternion orientations

The rotational free energy of a rotator in \mathbb{R}^3 is given by the volume of the space of the orientation representation. The rods considered in the previous section possessed a uniaxial symmetry, which allows us to represent their orientations by points on the unit sphere \mathbb{S}^2 . Without this symmetry, we need a different representation to fully capture all possible

orientations. There are multiple ways to represent rotations in three-dimensional space, with the most common being Euler angles, rotation matrices and unit quaternions. In our own calculations, we use the unit quaternion representation. A unique mapping between orientations of 3D objects and unit quaternions is given by the set of unit quaternions $\hat{\mathbf{q}}$ on one half of a four-dimensional unit hypersphere \mathbb{S}^3 . If uniqueness is not required, a twofold degenerate representation is given by all unit quaternions on \mathbb{S}^3 , with $+\hat{\mathbf{q}}$ and $-\hat{\mathbf{q}}$ representing the same rotation. The volume of this representation is thus the three-dimensional surface volume S of \mathbb{S}^3 , which is given by (e.g. Ref. [234]):

$$S = \int_0^{2\pi} \int_0^\pi \int_0^\pi \sin(\theta)^2 \sin(\alpha) d\theta d\alpha d\beta = 2\pi^2. \quad (\text{B.9})$$

The corresponding partition function of an ideal gas of 3D rotators is then:

$$Z_{or,id} = \int_{\mathbb{S}^3} e^{-0} d\hat{\mathbf{q}} = S = 2\pi^2, \quad (\text{B.10})$$

and the dimensionless free energy per particle:

$$\beta F/N = -\ln [2\pi^2] \approx -2.98261 \quad (\text{B.11})$$

B.4 Rotational free energy of an ideal Einstein crystal of arbitrarily symmetric objects

One can use unit quaternions to describe the orientations of arbitrarily symmetric objects in \mathbb{R}^3 . Consider the rotational energy of an Einstein crystal of such objects, which is given by:

$$\beta U_{or} = \lambda \sum_{i=1}^N \min_{\hat{\mathbf{Q}}} (\hat{\mathbf{q}}_i - \hat{\mathbf{q}}_{i,0})^2, \quad (\text{B.12})$$

where $\hat{\mathbf{q}}_i$ and $\hat{\mathbf{q}}_{i,0}$ are the unit quaternions representing the particle and lattice orientations and λ a coupling constant. To account for the orientational symmetries that our particles possess we consider also rotations of $\hat{\mathbf{q}}_i$ by the quaternions $\{\hat{\mathbf{Q}}\}$ that produce equivalent orientations for a particular symmetry, and take the combination of $\hat{\mathbf{q}}_i$ and $\hat{\mathbf{q}}_{i,0}$ for which $(\hat{\mathbf{q}}_i - \hat{\mathbf{q}}_{i,0})^2$ is minimal. Equivalently, one can consider the minimum to work over the reference orientations $\hat{\mathbf{q}}_0$ instead. For such a system, the one-particle configurational integral Z is given by:

$$Z_1 = \int_{\mathbb{S}^3} \exp \left[-\lambda \min_{\hat{\mathbf{Q}}} (\hat{\mathbf{q}} - \hat{\mathbf{q}}_0)^2 \right] d\hat{\mathbf{q}} \quad (\text{B.13})$$

When the dimensionless coupling constant λ is very large, i.e. $\lambda \gg 1$, the orientations $\hat{\mathbf{q}}$ will remain very close to one of the $N_{sym} = |\{\hat{\mathbf{Q}}\}|$ symmetry-equivalent reference orientations $\hat{\mathbf{q}}_0$. Furthermore, the vast majority of the Boltzmann weight will be concentrated around N_{sym} well-separated peaks. This allows the integral to be split up into N_{sym} identical integrals:

$$Z_1 \approx N_{sym} \int_{\mathbb{S}^3} \exp \left[-\lambda (\hat{\mathbf{q}} - \hat{\mathbf{q}}_0)^2 \right] d\hat{\mathbf{q}} \quad (\text{B.14})$$

The integration domain of the remaining integral is over the space of unit quaternions, which live on the surface of a four-dimensional hypersphere \mathbb{S}^3 . Given that $\lambda \gg 1$, the domain over which the Boltzmann weight is significantly non-zero will be very small compared to the size of the space. As shown schematically in Fig. B.2, the curvature of \mathbb{S}^3 as well as its periodicity will then be negligible over this domain, and we can approximate the integral over the surface volume \mathbb{S}^3 by one over an entire Cartesian three-dimensional volume \mathbb{R}^3 :

$$Z_1 \approx N_{sym} \int_{\mathbb{R}^3} \exp \left[-\lambda (\boldsymbol{\Omega} - \boldsymbol{\Omega}_0)^2 \right] d\boldsymbol{\Omega}. \quad (\text{B.15})$$

From here, we can use the same approach as for the positional part of the Einstein crystal. We substitute $\boldsymbol{\omega} = \boldsymbol{\Omega} - \boldsymbol{\Omega}_0 = (x, y, z)$, expand the 3D integral into its separate coordinates, and use the Gaussian integral identity:

$$\begin{aligned} Z_1 &= N_{sym} \int_{\mathbb{R}^3} \exp \left[-\lambda \boldsymbol{\omega}^2 \right] d\boldsymbol{\omega} \\ &= N_{sym} \int_{-\infty}^{\infty} e^{-\lambda x^2} dx \int_{-\infty}^{\infty} e^{-\lambda y^2} dy \int_{-\infty}^{\infty} e^{-\lambda z^2} dz \\ &= N_{sym} \left(\frac{\pi}{\lambda} \right)^{3/2} \end{aligned} \quad (\text{B.16})$$

With which the free energy becomes:

$$F = -k_B T \ln \left[Z_1^N \right] \Rightarrow \beta F / N = -\ln N_{sym} - \frac{3}{2} \ln \left[\frac{\pi}{\lambda} \right], \quad (\text{B.17})$$

which is the expression reported in literature [168].

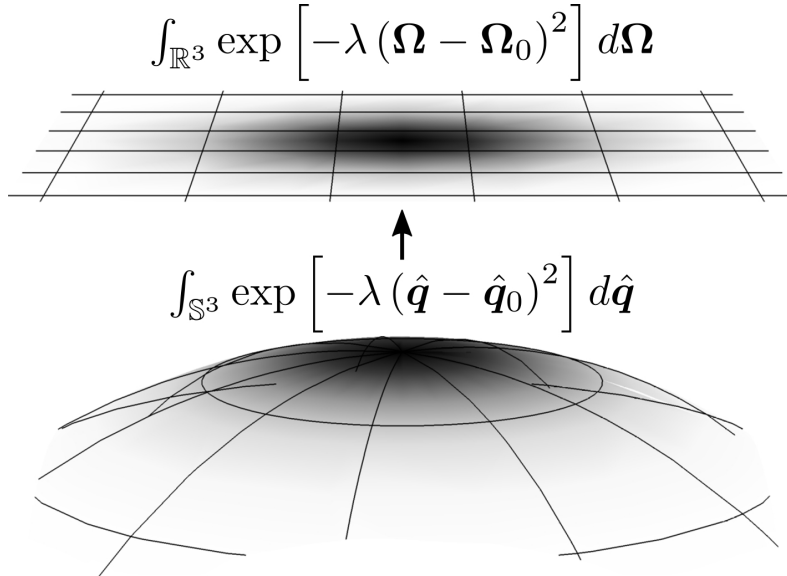


Figure B.2: Three-dimensional visualization for the approximation going from Eq B.14 to Eq. B.15: when the domain where the integrand takes on large values is small compared to the full space \mathbb{S}^3 , its curvature can be ignored and the integral can be approximated as one over a flat space of one fewer dimensions.

References

- [1] R. Brown, “XXVII. A brief account of microscopical observations made in the months of June, July and August 1827, on the particles contained in the pollen of plants; and on the general existence of active molecules in organic and inorganic bodies,” *The Philosophical Magazine* **4**, 161–173 (1828).
- [2] W. Sutherland, “LXXV. A dynamical theory of diffusion for non-electrolytes and the molecular mass of albumin,” *The London, Edinburgh, and Dublin Philosophical Magazine and Journal of Science* **9**, 781–785 (1905).
- [3] A. Einstein, “Über die von der molekularkinetischen Theorie der Wärme geforderte Bewegung von in ruhenden Flüssigkeiten suspendierten Teilchen,” *Annalen der Physik* **322**, 549–560 (1905).
- [4] J. Perrin, “Mouvement brownien et réalité moléculaire,” *Annales de Chimie et de Physique* **18**, 5–104 (1909).
- [5] T. Graham, “X. Liquid diffusion applied to analysis,” *Philosophical Transactions of the Royal Society of London* **151**, 183–224 (1861).
- [6] W. W. Wood and J. D. Jacobson, “Preliminary Results from a Recalculation of the Monte Carlo Equation of State of Hard Spheres,” *The Journal of Chemical Physics* **27**, 1207–1208 (1957).
- [7] B. J. Alder and T. E. Wainwright, “Phase Transition for a Hard Sphere System,” *The Journal of Chemical Physics* **27**, 1208–1209 (1957).
- [8] B. J. Alder and T. Wainwright, “Investigation of the Many-Body Problem by Electronic Computers,” in *The many-body problem* (1963), p. 511.
- [9] D. Frenkel and B. Smit, *Understanding molecular simulation: from algorithms to applications* (Academic press, 2001).
- [10] M. Mareschal, “Early years of Computational Statistical Mechanics,” *The European Physical Journal H* **43**, 293–302 (2018).
- [11] P. Bolhuis and D. Frenkel, “Tracing the phase boundaries of hard spherocylinders,” *The Journal of Chemical Physics* **106**, 666–687 (1997).
- [12] S. Shen, T. Gu, D. Mao, X. Xiao, P. Yuan, M. Yu, L. Xia, Q. Ji, L. Meng, W. Song, C. Yu, and G. Lu, “Synthesis of Nonspherical Mesoporous Silica Ellipsoids with Tunable Aspect Ratios for Magnetic Assisted Assembly and Gene Delivery,” *Chemistry of Materials* **24**, 230–235 (2012).
- [13] E. C. Greyson, J. E. Barton, and T. W. Odom, “Tetrahedral Zinc Blende Tin Sulfide Nano- and Microcrystals,” *Small* **2**, 368–371 (2006).
- [14] L. Rossi, S. Sacanna, W. T. Irvine, P. M. Chaikin, D. J. Pine, and A. P. Philipse, “Cubic Crystals From Cubic Colloids,” *Soft Matter* **7**, 4139–4142 (2011).

- [15] J. Henzie, M. Grünwald, A. Widmer-Cooper, P. L. Geissler, and P. Yang, “Self-Assembly of Uniform Polyhedral Silver Nanocrystals Into Densest Packings and Exotic Superlattices,” *Nat. Mater.* **11**, 131–137 (2012).
- [16] Y. Wu, S. Cai, D. Wang, W. He, and Y. Li, “Syntheses of Water-Soluble Octahedral, Truncated Octahedral, and Cubic Pt–Ni Nanocrystals and Their Structure–Activity Study in Model Hydrogenation Reactions,” *Journal of the American Chemical Society* **134**, 8975–8981 (2012).
- [17] J. Hao, Y. Yang, F. Zhang, Z. Yang, and J. Wei, “Faceted Colloidal Au/Fe₃O₄ Binary Supracrystals Dictated by Intrinsic Lattice Structures and Their Collective Optical Properties,” *The Journal of Physical Chemistry C* **124**, 14775–14786 (2020).
- [18] U. Agarwal and F. A. Escobedo, “Mesophase Behaviour of Polyhedral Particles,” *Nat. Mater.* **10**, 230–235 (2011).
- [19] P. F. Damasceno, M. Engel, and S. C. Glotzer, “Predictive Self-Assembly of Polyhedra into Complex Structures,” *Science* **337**, 453–457 (2012).
- [20] C. Markos, J. C. Travers, A. Abdolvand, B. J. Eggleton, and O. Bang, “Hybrid photonic-crystal fiber,” *Reviews of Modern Physics* **89**, 045003 (2017).
- [21] C. Chen, H. Ding, Y. Yue, and C. Han, “The Self-Assembly Composite Photonic Crystal: Toward Easy Humidity Detection by a Smartphone,” *IEEE Photonics Technology Letters* **32**, 1469–1472 (2020).
- [22] V. Saranathan, C. O. Osuji, S. G. J. Mochrie, H. Noh, S. Narayanan, A. Sandy, E. R. Dufresne, and R. O. Prum, “Structure, function, and self-assembly of single network gyroid (I4132) photonic crystals in butterfly wing scales,” *Proceedings of the National Academy of Sciences* **107**, 11676–11681 (2010).
- [23] S. Zobl, W. Salvenmoser, T. Schwerte, I. C. Gebeshuber, and M. Schreiner, “Morpho peleides butterfly wing imprints as structural colour stamp,” *Bioinspiration & Biomimetics* **11**, 016006 (2016).
- [24] F. Schenk, B. D. Wilts, and D. G. Stavenga, “The Japanese jewel beetle: a painter’s challenge,” *Bioinspiration & Biomimetics* **8**, 045002 (2013).
- [25] S. Jungblut and C. Dellago, “Pathways to self-organization: Crystallization via nucleation and growth,” *The European Physical Journal E* **39**, 77 (2016).
- [26] B. de Nijs, S. Dussi, F. Smalenburg, J. D. Meeldijk, D. J. Groenendijk, L. Filion, A. Imhof, A. van Blaaderen, and M. Dijkstra, “Entropy-driven formation of large icosahedral colloidal clusters by spherical confinement,” *Nature Materials* **14**, 56–60 (2015).
- [27] J. Wang, C. F. Mbah, T. Przybilla, B. Apele Zubiri, E. Spiecker, M. Engel, and N. Vogel, “Magic number colloidal clusters as minimum free energy structures,” *Nature Communications* **9** (2018) 10.1038/s41467-018-07600-4.
- [28] K. Muangnapoh, C. Avendaño, F. A. Escobedo, and C. M. Liddell Watson, “Degenerate crystals from colloidal dimers under confinement,” *Soft Matter* **10**, 9729–9738 (2014).
- [29] J. M. McBride and C. Avendaño, “Phase behaviour and gravity-directed self assembly of hard convex spherical caps,” *Soft Matter* **13**, 2085–2098 (2017).
- [30] J. C. Loudet, A. M. Alsayed, J. Zhang, and A. G. Yodh, “Capillary Interactions Between Anisotropic Colloidal Particles,” *Physical Review Letters* **94**, 018301 (2005).

- [31] H. Lehle, E. Noruzifar, and M. Oettel, “Ellipsoidal particles at fluid interfaces,” *The European Physical Journal E* **26**, 151–160 (2008).
- [32] G. Soligno, M. Dijkstra, and R. van Roij, “Self-assembly of cubic colloidal particles at fluid-fluid interfaces by hexapolar capillary interactions,” *Soft Matter* **14**, 42–60 (2017).
- [33] M. Cavallaro, L. Botto, E. P. Lewandowski, M. Wang, and K. J. Stebe, “Curvature-driven capillary migration and assembly of rod-like particles,” *Proceedings of the National Academy of Sciences of the United States of America* **108**, 20923–20928 (2011).
- [34] D. D. Nolte, “The tangled tale of phase space,” *Physics Today* **63**, 33–38 (2010).
- [35] N. Metropolis, A. W. Rosenbluth, M. N. Rosenbluth, A. H. Teller, and E. Teller, “Equation of State Calculations by Fast Computing Machines,” *The Journal of Chemical Physics* **21**, 1087 (1953).
- [36] W. K. Hastings, “Monte Carlo sampling methods using Markov chains and their applications,” *Biometrika* **57**, 97–109 (1970).
- [37] V. I. Manousiouthakis and M. W. Deem, “Strict detailed balance is unnecessary in Monte Carlo simulation,” *The Journal of Chemical Physics* **110**, 2753–2756 (1999).
- [38] C. Vega and S. Lago, “A fast algorithm to evaluate the shortest distance between rods,” *Comput. Chem.* **18**, 55–59 (1994).
- [39] “Neighbor list collision-driven molecular dynamics simulation for nonspherical hard particles. II. Applications to ellipses and ellipsoids,” *Journal of Computational Physics* **202**, 765–793 (2005).
- [40] Y. Jiao, F. H. Stillinger, and S. Torquato, “Optimal Packings of Superballs,” *Phys. Rev. E* **79**, 041309 (2009).
- [41] S. Torquato and Y. Jiao, “Dense Packings of Polyhedra: Platonic and Archimedean Solids,” *Phys. Rev. E* **80**, 041104 (2009).
- [42] S. Gottschalk, M. C. Lin, and D. Manocha, “OBBTree: A hierarchical structure for rapid interference detection,” in *Proceedings of the 23rd annual conference on computer graphics and interactive techniques* (1996), pp. 171–180.
- [43] E. Gilbert, D. Johnson, and S. Keerthi, “A Fast Procedure for Computing the Distance Between Complex Objects in Three-Dimensional Space,” *IEEE Robot. Autom. Lett.* **4**, 193–203 (1988).
- [44] G. van den Bergen, “A Fast and Robust GJK Implementation for Collision Detection of Convex Objects,” *Journal of Graphics Tools* **4**, 7–25 (1999).
- [45] Reducible, *A Strange But Elegant Approach to a Surprisingly Hard Problem (GJK Algorithm)*, Accessed: July 6th, 2021, (Mar. 2021) <https://youtu.be/ajv46BSqcK4>.
- [46] G. Snethen, “Complex Collision Made Simple,” *Game Programming Gems* **7**, 165–178 (2008).
- [47] W. Jin, P. Lu, and S. Li, “Evolution of the Dense Packings of Spherotetrahedral Particles: From Ideal Tetrahedra to Spheres,” *Sci. Rep.* **5**, 15640 (2015).
- [48] I. Theurkauff, C. Cottin-Bizonne, J. Palacci, C. Ybert, and L. Bocquet, “Dynamic Clustering in Active Colloidal Suspensions with Chemical Signaling,” *Phys. Rev. Lett.* **108**, 268303 (2012).

- [49] J. Palacci, S. Sacanna, A. P. Steinberg, D. J. Pine, and P. M. Chaikin, “Living Crystals of Light-Activated Colloidal Surfers,” *Science* **339**, 936–940 (2013).
- [50] I. Buttinoni, J. Bialké, F. Kümmel, H. Löwen, C. Bechinger, and T. Speck, “Dynamical Clustering and Phase Separation in Suspensions of Self-Propelled Colloidal Particles,” *Phys. Rev. Lett.* **110**, 238301 (2013).
- [51] F. Ginot, I. Theurkauff, F. Detcheverry, C. Ybert, and C. Cottin-Bizonne, “Aggregation-fragmentation and individual dynamics of active clusters,” *Nat. Commun.* **9**, 696 (2018).
- [52] T. Vicsek, A. Czirók, E. Ben-Jacob, I. Cohen, and O. Shochet, “Novel Type of Phase Transition in a System of Self-Driven Particles,” *Physical Review Letters* **75**, 1226–1229 (1995).
- [53] A. P. Solon, J. Stenhammar, R. Wittkowski, M. Kardar, Y. Kafri, M. E. Cates, and J. Tailleur, “Pressure and Phase Equilibria in Interacting Active Brownian Spheres,” *Phys. Rev. Lett.* **114**, 198301 (2015).
- [54] A. Patch, D. Yllanes, and M. C. Marchetti, “Kinetics of motility-induced phase separation and swim pressure,” *Phys. Rev. E* **95**, 012601 (2017).
- [55] Y. Fily, S. Henkes, and M. C. Marchetti, “Freezing and phase separation of self-propelled disks,” *Soft Matter* **10**, 2132–2140 (2014).
- [56] L. M. C. Janssen, “Active glasses,” *Journal of Physics: Condensed Matter* **31**, 503002 (2019).
- [57] P. Digregorio, D. Levis, A. Suma, L. F. Cugliandolo, G. Gonnella, and I. Pagonabarraga, “Full Phase Diagram of Active Brownian Disks: From Melting to Motility-Induced Phase Separation,” *Phys. Rev. Lett.* **121**, 098003 (2018).
- [58] J. U. Klamser, S. C. Kapfer, and W. Krauth, “Thermodynamic phases in two-dimensional active matter,” 1–18 (2018).
- [59] S. Paliwal and M. Dijkstra, “Role of topological defects in the two-stage melting and elastic behavior of active Brownian particles,” *Physical Review Research* **2**, 012013 (2020).
- [60] D. Levis, J. Codina, and I. Pagonabarraga, “Active Brownian Equation of State: Metastability and Phase Coexistence,” *Soft Matter* **13**, 1–5 (2017).
- [61] M. E. Cates and J. Tailleur, “Motility-Induced Phase Separation,” *Annu. Rev. Condens. Matter Phys.* **6**, 219–244 (2015).
- [62] Y. Fily and M. C. Marchetti, “Athermal Phase Separation of Self-Propelled Particles with No Alignment,” *Phys. Rev. Lett.* **108**, 235702 (2012).
- [63] G. S. Redner, M. F. Hagan, and A. Baskaran, “Structure and Dynamics of a Phase-Separating Active Colloidal Fluid,” *Phys. Rev. Lett.* **110**, 055701 (2013).
- [64] Y. Fily, A. Baskaran, and M. F. Hagan, “Dynamics of self-propelled particles under strong confinement,” *Soft Matter* **10**, 5609–5617 (2014).
- [65] M. C. Marchetti, Y. Fily, S. Henkes, A. Patch, and D. Yllanes, “Minimal model of active colloids highlights the role of mechanical interactions in controlling the emergent behavior of active matter,” *Curr. Opin. Colloid Interface Sci.* **21**, 34–43 (2016).
- [66] J. Tailleur and M. E. Cates, “Statistical Mechanics of Interacting Run-and-Tumble Bacteria,” *Phys. Rev. Lett.* **100**, 218103 (2008).

- [67] G. S. Redner, C. G. Wagner, A. Baskaran, and M. F. Hagan, “Classical Nucleation Theory Description of Active Colloid Assembly,” *Phys. Rev. Lett.* **117**, 148002 (2016).
- [68] J. Bialké, J. T. Siebert, H. Löwen, and T. Speck, “Negative Interfacial Tension in Phase-Separated Active Brownian Particles,” *Phys. Rev. Lett.* **115**, 098301 (2015).
- [69] J. Barré, R. Chétrite, M. Muratori, and F. Peruani, “Motility-Induced Phase Separation of Active Particles in the Presence of Velocity Alignment,” *J. Stat. Phys.* **158**, 589–600 (2015).
- [70] E. Sese-Sansa, I. Pagonabarraga, and D. Levis, “Velocity alignment promotes motility-induced phase separation,” *EPL* **124**, 1–7 (2018).
- [71] F. Peruani, A. Deutsch, and M. Bär, “Nonequilibrium clustering of self-propelled rods,” *Phys. Rev. E* **74**, 030904 (2006).
- [72] F. Ginelli, F. Peruani, M. Bär, and H. Chaté, “Large-Scale Collective Properties of Self-Propelled Rods,” *Phys. Rev. Lett.* **104**, 184502 (2010).
- [73] F. Peruani, “Active Brownian rods,” *Eur. Phys. J. Spec. Top.* **225**, 2301–2317 (2016).
- [74] S. Weitz, A. Deutsch, and F. Peruani, “Self-propelled rods exhibit a phase-separated state characterized by the presence of active stresses and the ejection of polar clusters,” *Phys. Rev. E* **92**, 012322 (2015).
- [75] C. Abaurrea Velasco, M. Abkenar, G. Gompper, and T. Auth, “Collective behavior of self-propelled rods with quorum sensing,” *Phys. Rev. E* **98**, 022605 (2018).
- [76] J. D. Weeks, D. Chandler, and H. C. Andersen, “Role of Repulsive Forces in Determining the Equilibrium Structure of Simple Liquids,” *The Journal of Chemical Physics* **54**, 5237–5247 (1971).
- [77] M. M. Tirado, C. L. Martínez, and J. G. de la Torre, “Comparison of theories for the translational and rotational diffusion coefficients of rod-like macromolecules. Application to short DNA fragments,” *The Journal of Chemical Physics* **81**, 2047–2052 (1984).
- [78] B. Bet, G. Boosten, M. Dijkstra, and R. van Roij, “Efficient shapes for microswimming: From three-body swimmers to helical flagella,” *J. Chem. Phys.* **146**, 084904 (2017).
- [79] F. Perrin, “Mouvement brownien d’un ellipsoïde - I. Dispersion diélectrique pour des molécules ellipsoïdales,” *J. Phys. Radium* **5**, 497–511 (1934).
- [80] S. H. Koenig, “Brownian motion of an ellipsoid. A correction to Perrin’s results,” *Biopolymers* **14**, 2421–2423 (1975).
- [81] J. Stenhammar, D. Marenduzzo, R. J. Allen, and M. E. Cates, “Phase behaviour of active Brownian particles: the role of dimensionality,” *Soft Matter* **10**, 1489–1499 (2014).
- [82] J. Bialké, H. Löwen, and T. Speck, “Microscopic theory for the phase separation of self-propelled repulsive disks,” *EPL* **103**, 30008 (2013).
- [83] A. Suma, G. Gonnella, D. Marenduzzo, and E. Orlandini, “Motility-induced phase separation in an active dumbbell fluid,” *EPL* **108**, 56004 (2014).
- [84] T. Speck, “Collective behavior of active Brownian particles: From microscopic clustering to macroscopic phase separation,” *Eur. Phys. J. Spec. Top.* **225**, 2287–2299 (2016).
- [85] I. R. Bruss and S. C. Glotzer, “Phase separation of self-propelled ballistic particles,” *Phys. Rev. E* **97**, 042609 (2018).

- [86] V. Prymidis, S. Samin, and L. Filion, “State behaviour and dynamics of self-propelled Brownian squares: a simulation study,” *Soft Matter* **12**, 4309–4317 (2016).
- [87] M. E. Cates and J. Tailleur, “When are active Brownian particles and run-and-tumble particles equivalent? Consequences for motility-induced phase separation,” *EPL* **101**, 20010 (2013).
- [88] G. S. Redner, A. Baskaran, and M. F. Hagan, “Reentrant phase behavior in active colloids with attraction,” *Phys. Rev. E* **88**, 012305 (2013).
- [89] T. Speck, A. M. Menzel, J. Bialké, and H. Löwen, “Dynamical mean-field theory and weakly non-linear analysis for the phase separation of active Brownian particles,” *J. Chem. Phys.* **142**, 224109 (2015).
- [90] T. Speck, J. Bialké, A. M. Menzel, and H. Löwen, “Effective Cahn-Hilliard Equation for the Phase Separation of Active Brownian Particles,” *Phys. Rev. Lett.* **112**, 218304 (2014).
- [91] E. P. Bernard and W. Krauth, “Two-Step Melting in Two Dimensions: First-Order Liquid-Hexatic Transition,” *Physical Review Letters* **107**, 155704 (2011).
- [92] M. Engel, J. A. Anderson, S. C. Glotzer, M. Isobe, E. P. Bernard, and W. Krauth, “Hard-disk equation of state: First-order liquid-hexatic transition in two dimensions with three simulation methods,” *Physical Review E* **87**, 042134 (2013).
- [93] W. Qi, A. P. Gantapara, and M. Dijkstra, “Two-stage melting induced by dislocations and grain boundaries in monolayers of hard spheres,” *Soft Matter* **10**, 5449 (2014).
- [94] S. C. Kapfer and W. Krauth, “Two-Dimensional Melting: From Liquid-Hexatic Coexistence to Continuous Transitions,” *Phys. Rev. Lett.* **114**, 035702 (2015).
- [95] A. L. Thorneywork, J. L. Abbott, D. G. Aarts, and R. P. Dullens, “Two-Dimensional Melting of Colloidal Hard Spheres,” *Physical Review Letters* **118**, 158001 (2017).
- [96] M. A. Bates and D. Frenkel, “Phase behavior of two-dimensional hard rod fluids,” *J. Chem. Phys.* **112**, 10034–10041 (2000).
- [97] X.-q. Shi and H. Chaté, “Self-Propelled Rods: Linking Alignment-Dominated and Repulsion-Dominated Active Matter,” (2018).
- [98] J. Stenhammar, A. Tiribocchi, R. J. Allen, D. Marenduzzo, and M. E. Cates, “Continuum Theory of Phase Separation Kinetics for Active Brownian Particles,” *Phys. Rev. Lett.* **111**, 145702 (2013).
- [99] A. Baskaran and M. Cristina Marchetti, “Nonequilibrium statistical mechanics of self-propelled hard rods,” *J. Stat. Mech. Theory Exp.* **2010**, P04019 (2010).
- [100] E. Bertin, A. Baskaran, H. Chaté, and M. C. Marchetti, “Comparison between Smoluchowski and Boltzmann approaches for self-propelled rods,” *Phys. Rev. E* **92**, 042141 (2015).
- [101] S. E. Ilse, C. Holm, and J. de Graaf, “Surface roughness stabilizes the clustering of self-propelled triangles,” *J. Chem. Phys.* **145**, 134904 (2016).
- [102] L. F. Cugliandolo, P. Digregorio, G. Gonnella, and A. Suma, “Phase Coexistence in Two-Dimensional Passive and Active Dumbbell Systems,” *Phys. Rev. Lett.* **119**, 268002 (2017).

- [103] A. Zöttl and H. Stark, “Hydrodynamics Determines Collective Motion and Phase Behavior of Active Colloids in Quasi-Two-Dimensional Confinement,” *Phys. Rev. Lett.* **112**, 118101 (2014).
- [104] R. Matas-Navarro, R. Golestanian, T. B. Liverpool, and S. M. Fielding, “Hydrodynamic suppression of phase separation in active suspensions,” *Phys. Rev. E* **90**, 032304 (2014).
- [105] J. Blaschke, M. Maurer, K. Menon, A. Zöttl, and H. Stark, “Phase separation and coexistence of hydrodynamically interacting microswimmers,” *Soft Matter* **12**, 9821–9831 (2016).
- [106] N. Oyama, J. J. Molina, and R. Yamamoto, “Purely hydrodynamic origin for swarming of swimming particles,” *Phys. Rev. E* **93**, 043114 (2016).
- [107] N. Oyama, J. J. Molina, and R. Yamamoto, “Do hydrodynamically assisted binary collisions lead to orientational ordering of microswimmers?” *Eur. Phys. J. E* **40**, 95 (2017).
- [108] A. P. Solon, Y. Fily, A. Baskaran, M. E. Cates, Y. Kafri, M. Kardar, and J. Tailleur, “Pressure is not a state function for generic active fluids,” *Nat. Phys.* **11**, 673–678 (2015).
- [109] R. Großmann, I. S. Aranson, and F. Peruani, “A particle-field approach bridges phase separation and collective motion in active matter,” *Nature Communications* **11**, 5365 (2020).
- [110] E. W. Burkholder and J. F. Brady, “Fluctuation-dissipation in active matter,” *Journal of Chemical Physics* **150** (2019) 10.1063/1.5081725.
- [111] T. P. Bigioni, X.-M. Lin, T. T. Nguyen, E. I. Corwin, T. A. Witten, and H. M. Jaeger, “Kinetically driven self assembly of highly ordered nanoparticle monolayers,” *Nature Materials* **5**, 265–270 (2006).
- [112] M. I. Bodnarchuk, M. V. Kovalenko, S. Pichler, G. Fritz-Popovski, G. Hesser, and W. Heiss, “Large-Area Ordered Superlattices from Magnetic Wüstite/Cobalt Ferrite Core/Shell Nanocrystals by Doctor Blade Casting,” *ACS Nano* **4**, 423–431 (2010).
- [113] A. Dong, J. Chen, P. M. Vora, J. M. Kikkawa, and C. B. Murray, “Binary nanocrystal superlattice membranes self-assembled at the liquid–air interface,” *Nature* **466**, 474–477 (2010).
- [114] M. A. Boles, M. Engel, and D. V. Talapin, “Self-Assembly of Colloidal Nanocrystals: From Intricate Structures to Functional Materials,” *Chemical Reviews* **116**, 11220–11289 (2016).
- [115] D. Y. Chan, J. D. Henry, and L. R. White, “The interaction of colloidal particles collected at fluid interfaces,” *Journal of Colloid And Interface Science* **79**, 410–418 (1981).
- [116] D. Stamou, C. Duschl, and D. Johannsmann, “Long-range attraction between colloidal spheres at the air-water interface: The consequence of an irregular meniscus,” *Physical Review E* **62**, 5263–5272 (2000).
- [117] P. A. Kralchevsky and K. Nagayama, “Capillary interactions between particles bound to interfaces, liquid films and biomembranes,” *Advances in Colloid and Interface Science* **85**, 145–192 (2000).
- [118] J. de Graaf, M. Dijkstra, and R. van Roij, “Triangular tessellation scheme for the adsorption free energy at the liquid-liquid interface: Towards nonconvex patterned colloids,” *Physical Review E* **80**, 051405 (2009).

- [119] J. de Graaf, M. Dijkstra, and R. van Roij, “Adsorption trajectories and free-energy separatrixes for colloidal particles in contact with a liquid-liquid interface,” *The Journal of Chemical Physics* **132**, 164902 (2010).
- [120] B. J. Newton, R. Mohammed, G. B. Davies, L. Botto, and D. M. A. Buzza, “Capillary Interaction and Self-Assembly of Tilted Magnetic Ellipsoidal Particles at Liquid Interfaces,” *ACS Omega* **3**, 14962–14972 (2018).
- [121] A. M. Luo, J. Vermant, P. Ilg, Z. Zhang, and L. M. Sagis, “Self-assembly of ellipsoidal particles at fluid-fluid interfaces with an empirical pair potential,” *Journal of Colloid and Interface Science* **534**, 205–214 (2019).
- [122] E. P. Lewandowski, M. Cavallaro, L. Botto, J. C. Bernate, V. Garbin, and K. J. Stebe, “Orientation and Self-Assembly of Cylindrical Particles by Anisotropic Capillary Interactions,” *Langmuir* **26**, 15142–15154 (2010).
- [123] L. Isa, N. Samudrala, and E. R. Dufresne, “Adsorption of sub-micron amphiphilic dumbbells to fluid interfaces,” *Langmuir* **30**, 5057–5063 (2014).
- [124] C. Anzivino, F. Chang, G. Soligno, R. van Roij, W. K. Kegel, and M. Dijkstra, “Equilibrium configurations and capillary interactions of Janus dumbbells and spherocylinders at fluid–fluid interfaces,” *Soft Matter* **15**, 2638–2647 (2019).
- [125] S. Dasgupta, M. Katava, M. Faraj, T. Auth, and G. Gompper, “Capillary Assembly of Microscale Ellipsoidal, Cuboidal, and Spherical Particles at Interfaces,” *Langmuir* **30**, 11873–11882 (2014).
- [126] J. C. Loudet and B. Pouligny, “How do mosquito eggs self-assemble on the water surface?” *The European Physical Journal E* **34**, 76 (2011).
- [127] Y. Yang, Y. H. Lee, I. Y. Phang, R. Jiang, H. Y. F. Sim, J. Wang, and X. Y. Ling, “A Chemical Approach To Break the Planar Configuration of Ag Nanocubes into Tunable Two-Dimensional Metasurfaces,” *Nano Letters* **16**, 3872–3878 (2016).
- [128] “Self-Assembly of Cubes into 2D Hexagonal and Honeycomb Lattices by Hexapolar Capillary Interactions,” *Physical Review Letters* **116**, 1–6 (2016).
- [129] C. Anzivino, G. Soligno, R. van Roij, and M. Dijkstra, “Chains of cubic colloids at fluid–fluid interfaces,” *Soft Matter* (2021) 10.1039/D0SM01815E.
- [130] Y. H. Lee, W. Shi, H. K. Lee, R. Jiang, I. Y. Phang, Y. Cui, L. Isa, Y. Yang, J. Wang, S. Li, and X. Y. Ling, “Nanoscale surface chemistry directs the tunable assembly of silver octahedra into three two-dimensional plasmonic superlattices,” *Nature Communications* **6**, 6990 (2015).
- [131] G. Soligno and D. Vanmaekelbergh, “Understanding the Formation of PbSe Honeycomb Superstructures by Dynamics Simulations,” *Physical Review X* **9**, 021015 (2019).
- [132] F. Wang, R. Deng, and X. Liu, “Preparation of core-shell NaGdF₄ nanoparticles doped with luminescent lanthanide ions to be used as upconversion-based probes,” *Nature Protocols* **9**, 1634–1644 (2014).
- [133] D. Liu, X. Xu, Y. Du, X. Qin, Y. Zhang, C. Ma, S. Wen, W. Ren, E. M. Goldys, J. A. Piper, S. Dou, X. Liu, and D. Jin, “Three-dimensional controlled growth of monodisperse sub-50 nm heterogeneous nanocrystals,” *Nature Communications* **7**, 10254 (2016).

- [134] Y. Yang, M. Kong, P. Feng, R. Meng, X. Wei, P. Su, J. Cao, W. Feng, W. Liu, and Y. Tang, "Self-Assembly of Heterogeneous Structured Rare-Earth Nanocrystals Controlled by Selective Crystal Etching and Growth for Optical Encoding," *ACS Applied Nano Materials* **2**, 3518–3525 (2019).
- [135] H.-X. Mai, Y.-W. Zhang, L.-D. Sun, and C.-H. Yan, "Size- and Phase-Controlled Synthesis of Monodisperse $\text{NaYF}_4:\text{Yb,Er}$ Nanocrystals from a Unique Delayed Nucleation Pathway Monitored with Upconversion Spectroscopy," *The Journal of Physical Chemistry C* **111**, 13730–13739 (2007).
- [136] X. Ye, J. E. Collins, Y. Kang, J. Chen, D. T. N. Chen, A. G. Yodh, and C. B. Murray, "Morphologically controlled synthesis of colloidal upconversion nanophosphors and their shape-directed self-assembly," *Proceedings of the National Academy of Sciences* **107**, 22430–22435 (2010).
- [137] J. Aguila-Hernández, I. Hernández, and A. Trejo, "Temperature dependence of the surface tension for binary mixtures of n-butanenitrile + n-alkanes," *International Journal of Thermophysics* **16**, 45–52 (1995).
- [138] B. J. Park and D. Lee, "Configuration of nonspherical amphiphilic particles at a fluid–fluid interface," *Soft Matter* **8**, 7690 (2012).
- [139] B. J. Park and D. Lee, "Equilibrium orientation of nonspherical Janus particles at fluid–fluid interfaces," *ACS Nano* **6**, 782–790 (2012).
- [140] A. R. Morgan, N. Ballard, L. A. Rochford, G. Nurumbetov, T. S. Skelhon, and S. A. Bon, "Understanding the multiple orientations of isolated superellipsoidal hematite particles at the oil–water interface," *Soft Matter* **9**, 487–491 (2013).
- [141] B. Peng, G. Soligno, M. Kamp, B. De Nijs, J. De Graaf, M. Dijkstra, R. van Roij, A. van Blaaderen, and A. Imhof, "Site-specific growth of polymers on silica rods," *Soft Matter* **10**, 9644–9650 (2014).
- [142] N. Ballard and S. A. Bon, "Equilibrium orientations of non-spherical and chemically anisotropic particles at liquid–liquid interfaces and the effect on emulsion stability," *Journal of Colloid and Interface Science* **448**, 533–544 (2015).
- [143] G. Soligno, M. Dijkstra, and R. van Roij, "The equilibrium shape of fluid–fluid interfaces: Derivation and a new numerical method for young's and young–laplace equations," *Journal of Chemical Physics* **141** (2014) 10.1063/1.4904391.
- [144] G. Soligno, "Droplets, capillary interactions, and self-assembly from the equilibrium shape of fluid–fluid interfaces," PhD thesis (Utrecht University, 2017).
- [145] J.-B. Fournier and P. Galatola, "Anisotropic capillary interactions and jamming of colloidal particles trapped at a liquid–fluid interface," *Physical Review E* **65**, 031601 (2002).
- [146] K. D. Danov, P. A. Kralchevsky, B. N. Naydenov, and G. Brenn, "Interactions between particles with an undulated contact line at a fluid interface: Capillary multipoles of arbitrary order," *Journal of Colloid and Interface Science* **287**, 121–134 (2005).
- [147] K. D. Danov and P. A. Kralchevsky, "Capillary forces between particles at a liquid interface: General theoretical approach and interactions between capillary multipoles," *Advances in Colloid and Interface Science* **154**, 91–103 (2010).
- [148] R. Goldman, "Curvature formulas for implicit curves and surfaces," *Computer Aided Geometric Design* **22**, 632–658 (2005).

- [149] L. Botto, E. P. Lewandowski, M. Cavallaro, and K. J. Stebe, “Capillary interactions between anisotropic particles,” *Soft Matter* **8**, 9957 (2012).
- [150] S. C. Glotzer and M. J. Solomon, “Anisotropy of building blocks and their assembly into complex structures,” *Nat. Mater.* **6**, 557–562 (2007).
- [151] Z. Zhuang, Q. Peng, X. Wang, and Y. Li, “Tetrahedral Colloidal Crystals of Ag₂S Nanocrystals,” *Angew. Chem., Int. Ed.* **46**, 8174–8177 (2007).
- [152] S. Sacanna and D. J. Pine, “Shape-anisotropic colloids: building blocks for complex assemblies,” *Curr. Opin. Colloid Interface Sci.* **16**, 96–105 (2011).
- [153] K. Miszta, J. de Graaf, G. Bertoni, D. Dorfs, R. Brescia, S. Marras, L. Ceseracciu, R. Cingolani, R. van Roij, M. Dijkstra, and L. Manna, “Hierarchical self-assembly of suspended branched colloidal nanocrystals into superlattice structures,” *Nat. Mater.* **10**, 872–876 (2011).
- [154] M. H. Huang and P.-H. Lin, “Shape-Controlled Synthesis of Polyhedral Nanocrystals and Their Facet-Dependent Properties,” *Adv. Funct. Mater.* **22**, 14–24 (2012).
- [155] “Two-Dimensionally Patterned Nanostructures Based on Monolayer Colloidal Crystals: Controllable Fabrication, Assembly, and Applications,” *Nano Today* **6**, 608–631 (2011).
- [156] S.-H. Kim, S. Y. Lee, S.-M. Yang, and G.-R. Yi, “Self-Assembled Colloidal Structures for Photonics,” *NPG Asia Mater.* **3**, 25–33 (2011).
- [157] J.-H. Choi, H. Wang, S. J. Oh, T. Paik, P. Sung, J. Sung, X. Ye, T. Zhao, B. T. Diroll, C. B. Murray, and C. R. Kagan, “Exploiting the Colloidal Nanocrystal Library to Construct Electronic Devices,” *Science* **352**, 205–208 (2016).
- [158] A. Stein, B. E. Wilson, and S. G. Rudisill, “Design and Functionality of Colloidal-Crystal-Templated Materials — Chemical Applications of Inverse Opals,” *Chem. Soc. Rev.* **42**, 2763–2803 (2013).
- [159] S. Torquato and Y. Jiao, “Dense Packings of the Platonic and Archimedean Solids,” *Nature* **460**, 876–879 (2009).
- [160] F. Smalenburg, L. Filion, M. Marechal, and M. Dijkstra, “Vacancy-Stabilized Crystalline Order in Hard Cubes,” *Proc. Natl. Acad. Sci. U. S. A.* **109**, 17886–17890 (2012).
- [161] A. P. Gantapara, J. de Graaf, R. van Roij, and M. Dijkstra, “Phase Diagram and Structural Diversity of a Family of Truncated Cubes: Degenerate Close-Packed Structures and Vacancy-Rich States,” *Phys. Rev. Lett.* **111**, 015501 (2013).
- [162] A. P. Gantapara, J. de Graaf, R. van Roij, and M. Dijkstra, “Phase behavior of a family of truncated hard cubes,” *J. Chem. Phys.* **142**, 054904 (2015).
- [163] B. van der Meer, R. van Damme, M. Dijkstra, F. Smalenburg, and L. Filion, “Revealing a Vacancy Analog of the Crowdion Interstitial in Simple Cubic Crystals,” *Phys. Rev. Lett.* **121**, 258001 (2018).
- [164] J. Kepler, *Strena Seu de Nive Sexangula* (Gottfried Tampach, 1966).
- [165] H. M. Jaeger, S. R. Nagel, and R. P. Behringer, “Granular Solids, Liquids, and Gases,” *Rev. Mod. Phys.* **68**, 1259–1273 (1996).
- [166] A. Haji-Akbari, M. Engel, A. S. Keys, X. Zheng, R. G. Petschek, P. Palffy-Muhoray, and S. C. Glotzer, “Disordered, Quasicrystalline and Crystalline Phases of Densely Packed Tetrahedra,” *Nature* **462**, 773–777 (2009).

- [167] J. de Graaf, R. van Roij, and M. Dijkstra, “Dense Regular Packings of Irregular Nonconvex Particles,” *Phys. Rev. Lett.* **107**, 155501 (2011).
- [168] A. Haji-Akbari, M. Engel, and S. C. Glotzer, “Phase Diagram of Hard Tetrahedra,” *J. Chem. Phys.* **135**, 194101 (2011).
- [169] J. de Graaf, L. Filion, M. Marechal, R. van Roij, and M. Dijkstra, “Crystal-Structure Prediction via the Floppy-Box Monte Carlo Algorithm: Method and Application to Hard (Non)convex Particles,” *J. Chem. Phys.* **137**, 214101 (2012).
- [170] R. D. Batten, F. H. Stillinger, and S. Torquato, “Phase Behavior of Colloidal Superballs: Shape Interpolation from Spheres to Cubes,” *Phys. Rev. E* **81**, 061105 (2010).
- [171] R. Ni, A. P. Gantapara, J. de Graaf, R. van Roij, and M. Dijkstra, “Phase Diagram of Colloidal Hard Superballs: From Cubes via Spheres to Octahedra,” *Soft Matter* **8**, 8826 (2012).
- [172] M. Marechal, U. Zimmermann, and H. Löwen, “Freezing of Parallel Hard Cubes With Rounded Edges,” *J. Chem. Phys.* **136** (2012) 10.1063/1.3699086.
- [173] L. Rossi, V. Soni, D. J. Ashton, D. J. Pine, A. P. Philipse, P. M. Chaikin, M. Dijkstra, S. Sacanna, and W. T. M. Irvine, “Shape-Sensitive Crystallization in Colloidal Superball Fluids,” *Proc. Natl. Acad. Sci. U. S. A.* **112**, 5286–5290 (2015).
- [174] D. Wang, M. Hermes, R. Kotni, Y. Wu, N. Tasios, Y. Liu, B. de Nijs, E. B. van der Wee, C. B. Murray, M. Dijkstra, and A. van Blaaderen, “Interplay between spherical confinement and particle shape on the self-assembly of rounded cubes,” *Nature Communications* **9**, 2228 (2018).
- [175] M. R. Khadilkar, U. Agarwal, and F. A. Escobedo, “Phase Behavior of Binary Mixtures of Hard Convex Polyhedra,” *Soft Matter* **9**, 11557 (2013).
- [176] P. F. Damasceno, M. Engel, and S. C. Glotzer, “Crystalline Assemblies and Densest Packings of a Family of Truncated Tetrahedra and the Role of Directional Entropic Forces,” *ACS Nano* **6**, 609–614 (2012).
- [177] E. R. Chen, D. Klotsa, M. Engel, P. F. Damasceno, and S. C. Glotzer, “Complexity in Surfaces of Densest Packings for Families of Polyhedra,” *Phys. Rev. X* **4**, 011024 (2014).
- [178] D. Klotsa, E. R. Chen, M. Engel, and S. C. Glotzer, “Intermediate Crystalline Structures of Colloids in Shape Space,” *Soft Matter* **14**, 8692–8697 (2018).
- [179] E. G. Teich, G. van Anders, and S. C. Glotzer, “Identity Crisis in Alchemical Space Drives the Entropic Colloidal Glass Transition,” *Nat. Commun.* **10**, 64 (2019).
- [180] H. T. Stokes, D. M. Hatch, and B. J. Campbell, *FINDSYM, ISOTROPY Software Suite*, iso.byu.edu.
- [181] H. T. Stokes and D. M. Hatch, “FINDSYM : Program for Identifying the Space-Group Symmetry of a Crystal,” *J. Appl. Crystallogr.* **38**, 237–238 (2005).
- [182] P. J. Steinhardt, D. R. Nelson, and M. Ronchetti, “Bond-Orientational Order in Liquids and Glasses,” *Phys. Rev. B* **28**, 784–805 (1983).
- [183] J. S. van Duijneveldt and D. Frenkel, “Computer simulation study of free energy barriers in crystal nucleation,” *The Journal of Chemical Physics* **96**, 4655–4668 (1992).

- [184] W. Mickel, S. C. Kapfer, G. E. Schröder-Turk, and K. Mecke, “Shortcomings of the Bond Orientational Order Parameters for the Analysis of Disordered Particulate Matter,” *J. Chem. Phys.* **138** (2013) 10.1063/1.4774084.
- [185] J. A. van Meel, L. Filion, C. Valeriani, and D. Frenkel, “A parameter-free, solid-angle based, nearest-neighbor algorithm,” *The Journal of Chemical Physics* **136**, 234107 (2012).
- [186] W. Lechner and C. Dellago, “Accurate Determination of Crystal Structures Based on Averaged Local Bond Order Parameters,” *J. Chem. Phys.* **129**, 114707 (2008).
- [187] R. van Damme, *Structure Metric Calculator*, <https://github.com/ArvDee/Minkowski-structure-metrics-calculator>, 2019.
- [188] J. A. Anderson, C. D. Lorenz, and A. Travesset, “General Purpose Molecular Dynamics Simulations Fully Implemented on Graphics Processing Units,” *J. Comput. Phys.* **227**, 5342–5359 (2008).
- [189] J. Glaser, T. D. Nguyen, J. A. Anderson, P. Lui, F. Spiga, J. A. Millan, D. C. Morse, and S. C. Glotzer, “Strong Scaling of General-Purpose Molecular Dynamics Simulations on GPUs,” *Comput. Phys. Commun.* **192**, 97–107 (2015).
- [190] J. A. Anderson, M. Eric Irrgang, and S. C. Glotzer, “Scalable Metropolis Monte Carlo for Simulation of Hard Shapes,” *Comput. Phys. Commun.* **204**, 21–30 (2016).
- [191] A. Haji-Akbari, “Thermodynamics of the Hard Tetrahedron System,” PhD thesis (University of Michigan, 2012).
- [192] T. Hales, M. Adams, G. Bauer, T. D. Dang, J. Harrison, H. Le Truong, C. Kaliszyk, V. Magron, S. McLaughlin, T. T. Nguyen, Q. T. Nguyen, T. Nipkow, S. Obua, J. Pleso, J. Rute, A. Solovyev, T. H. A. Ta, N. T. Tran, T. D. Trieau, J. Urban, K. Vu, and R. Zumkeller, “A formal proof of the kepler conjecture,” *Forum Math. Pi* **5**, e2 (2017).
- [193] J. H. Conway and S. Torquato, “Packing, Tiling, and Covering With Tetrahedra,” *Proc. Natl. Acad. Sci. U. S. A.* **103**, 10612–10617 (2006).
- [194] E. R. Chen, “A Dense Packing of Regular Tetrahedra,” *Discrete Comput. Geom.* **40**, 214–240 (2008).
- [195] Y. Kallus, V. Elser, and S. Gravel, “Dense Periodic Packings of Tetrahedra with Small Repeating Units,” *Discrete Comput. Geom.* **44**, 245–252 (2010).
- [196] S. Torquato and Y. Jiao, “Analytical Constructions of a Family of Dense Tetrahedron Packings and the Role of Symmetry,” *arXiv.org, e-Print Arch., Condens. Matter* (2010).
- [197] E. R. Chen, M. Engel, and S. C. Glotzer, “Dense Crystalline Dimer Packings of Regular Tetrahedra,” *Discrete Comput. Geom.* **44**, 253–280 (2010).
- [198] S. Gravel, V. Elser, and Y. Kallus, “Upper Bound on the Packing Density of Regular Tetrahedra and Octahedra,” *Discrete Comput. Geom.* **46**, 799–818 (2011).
- [199] A. Haji-Akbari, E. R. Chen, M. Engel, and S. C. Glotzer, “Packing and Self-Assembly of Truncated Triangular Bipyramids,” *Phys. Rev. E* **88**, 012127 (2013).
- [200] Y. Kallus and V. Elser, “Dense-Packing Crystal Structures of Physical Tetrahedra,” *Phys. Rev. E: Stat., Nonlinear, Soft Matter Phys.* **83** (2011) 10.1103/PhysRevE.83.036703.
- [201] D. Frenkel and A. J. C. Ladd, “New Monte Carlo method to compute the free energy of arbitrary solids. Application to the fcc and hcp phases of hard spheres,” *The Journal of Chemical Physics* **81**, 3188 (1984).

- [202] C. Vega and E. G. Noya, “Revisiting the Frenkel-Ladd method to compute the free energy of solids: The Einstein molecule approach,” *The Journal of Chemical Physics* **127**, 154113 (2007).
- [203] C. G. Salzmann, “Advances in the experimental exploration of water’s phase diagram,” *Journal of Chemical Physics* **150** (2019) 10.1063/1.5085163.
- [204] F. Hooft, A. Pérez de Alba Ortíz, and B. Ensing, “Discovering Collective Variables of Molecular Transitions via Genetic Algorithms and Neural Networks,” *Journal of Chemical Theory and Computation* **17**, 2294–2306 (2021).
- [205] A. Reinhardt, J. P. K. Doye, E. G. Noya, and C. Vega, “Local order parameters for use in driving homogeneous ice nucleation with all-atom models of water,” *The Journal of Chemical Physics* **137**, 194504 (2012).
- [206] “Order in two-dimensional binary random arrays,” *Philosophical Magazine A* **46**, 105–126 (1982).
- [207] S. Auer and D. Frenkel, “Prediction of absolute crystal-nucleation rate in hard-sphere colloids,” *Nature* **409**, 1020–1023 (2001).
- [208] S. Auer and D. Frenkel, “Numerical prediction of absolute crystallization rates in hard-sphere colloids,” *The Journal of Chemical Physics* **120**, 3015–3029 (2004).
- [209] L. Filion, M. Hermes, R. Ni, and M. Dijkstra, “Crystal nucleation of hard spheres using molecular dynamics, umbrella sampling, and forward flux sampling: A comparison of simulation techniques,” *The Journal of Chemical Physics* **133**, 244115 (2010).
- [210] J. Russo and H. Tanaka, “The microscopic pathway to crystallization in supercooled liquids,” *Scientific Reports* **2**, 505 (2012).
- [211] P. R. ten Wolde, M. J. Ruiz-Montero, and D. Frenkel, “Numerical evidence for bcc ordering at the surface of a critical fcc nucleus,” *Physical Review Letters* **75**, 2714–2717 (1995).
- [212] P. R. ten Wolde, M. J. Ruiz-Montero, and D. Frenkel, “Numerical Calculation of the Rate of Crystal Nucleation in a Lennard-Jones System at Moderate Undercooling,” *J. Chem. Phys.* **104**, 9932–9947 (1996).
- [213] P. R. ten Wolde, M. J. Ruiz-Montero, and D. Frenkel, “Numerical calculation of the rate of homogeneous gas-liquid nucleation in a Lennard-Jones system,” *The Journal of Chemical Physics* **110**, 1591–1599 (1999).
- [214] J. Russo, F. Romano, and H. Tanaka, “New metastable form of ice and its role in the homogeneous crystallization of water,” *Nature Materials* **13**, 733–739 (2014).
- [215] J. R. Espinosa, C. Vega, C. Valeriani, and E. Sanz, “The crystal-fluid interfacial free energy and nucleation rate of NaCl from different simulation methods,” *Journal of Chemical Physics* **142** (2015) 10.1063/1.4921185.
- [216] B. van der Meer, M. Dijkstra, and L. Filion, “Removing grain boundaries from three-dimensional colloidal crystals using active dopants,” *Soft Matter* **12**, 5630–5635 (2016).
- [217] N. Tasios, A. P. Gantapara, and M. Dijkstra, “Glassy dynamics of convex polyhedra,” *The Journal of Chemical Physics* **141**, 224502 (2014).
- [218] E. D. Cubuk, S. S. Schoenholz, J. M. Rieser, B. D. Malone, J. Rottler, D. J. Durian, E. Kaxiras, and A. J. Liu, “Identifying structural flow defects in disordered solids using machine-learning methods,” *Physical Review Letters* **114**, 1–5 (2015).

- [219] E. Boattini, S. Marín-Aguilar, S. Mitra, G. Foffi, F. Smallenburg, and L. Filion, “Autonomously revealing hidden local structures in supercooled liquids,” *Nature Communications* **11**, 5479 (2020).
- [220] G. Torrie and J. Valleau, “Nonphysical Sampling Distributions in Monte Carlo Free-Energy Estimation: Umbrella Sampling,” *J. Comput. Phys.* **23**, 187–199 (1977).
- [221] J. Kästner, “Umbrella Sampling,” *Wiley Interdiscip. Rev.: Comput. Mol. Sci.* **1**, 932–942 (2011).
- [222] A. W. Long and A. L. Ferguson, “Nonlinear Machine Learning of Patchy Colloid Self-Assembly Pathways and Mechanisms,” *The Journal of Physical Chemistry B* **118**, 4228–4244 (2014).
- [223] D. Wang, “Quantitative real-space analysis of colloidal supraparticles self-assembled from monodisperse nanoparticles,” PhD thesis (Utrecht University, 2018).
- [224] M. A. Boles and D. V. Talapin, “Self-Assembly of Tetrahedral CdSe Nanocrystals: Effective “Patchiness” via Anisotropic Steric Interaction,” *J. Am. Chem. Soc.* **136**, 5868–5871 (2014).
- [225] M. Alpbaz, A. Bilgesu, and O. Tutkun, “Measurement of interfacial tension by drop method,” *Commun. Fac. Sci. Univ. Ank. Serie B* **103**, 103–112 (1988).
- [226] L. Abu-Farah, F. Al-Qaessi, and A. Schönbucher, “Cyclohexane/water dispersion behaviour in a stirred batch vessel experimentally and with CFD simulation,” *Procedia Computer Science* **1**, 655–664 (2010).
- [227] E. J. Meijer, D. Frenkel, R. A. LeSar, and A. J. C. Ladd, “Location of melting point at 300 K of nitrogen by Monte Carlo simulation,” *The Journal of Chemical Physics* **92**, 7570–7575 (1990).
- [228] A. K. Sharma and F. A. Escobedo, “Nucleus-size pinning for determination of nucleation free-energy barriers and nucleus geometry,” *The Journal of Chemical Physics* **148**, 184104 (2018).
- [229] A. L. Mackay, “A dense non-crystallographic packing of equal spheres,” *Acta Crystallographica* **15**, 916–918 (1962).
- [230] S. C. Hendy and J. P. K. Doye, “Surface-reconstructed icosahedral structures for lead clusters,” *Physical Review B* **66**, 235402 (2002).
- [231] R. Twarock and A. Luque, “Structural puzzles in virology solved with an overarching icosahedral design principle,” *Nature Communications* **10**, 4414 (2019).
- [232] J. R. Espinosa, C. Vega, C. Valeriani, and E. Sanz, “Seeding approach to crystal nucleation,” *The Journal of Chemical Physics* **144**, 034501 (2016).
- [233] A. van Oosterom and J. Strackee, “The Solid Angle of a Plane Triangle,” *IEEE Transactions on Biomedical Engineering* **BME-30**, 125–126 (1983).
- [234] E. W. Weisstein, *Hypersphere*, From MathWorld—A Wolfram Web Resource. mathworld.wolfram.com/Hypersphere.html, Accessed 2021-07-09.

Summary

In this thesis we study the effects of particle shape and environment geometry on the self-assembly of colloidal particles. Colloids are particles with a size between roughly 1 nm and 1 μm . At this size, they are large enough to have a meaningful *shape*, but small enough to undergo a constant Brownian motion. This Brownian motion causes them to *self-assemble* into various thermodynamic phases such as fluids or solids. For colloids, which phases form and under what conditions is determined by the properties of the particles and their interactions. At high densities, this is determined in a large part by their shape. However, it is not only the geometric properties of the particles that are important, but also those of their environment. The process of self-assembly and the phases that arise from it can be drastically different depending on whether particles self-assemble in bulk, near walls, or confined to a smaller region such as within a small droplet or at the interface between two fluids. In this thesis we use computer simulations to study these geometric effects in four different settings.

In **Chapter 2** we investigate the effect of particle shape on a system of particles that *self-propel*, converting some form of ambient energy (“fuel”) into their own movement. Such self-propulsion is common to biological systems and can describe the movement of bacteria, schools of fish, flocks of birds, herds of sheep and even that of crowds of people. For self-propelled systems where a) each particle self-propels along its own slowly changing “forward” direction, and b) particles are not able to move through one another, one finds that beyond a certain critical density and self-propulsion strength, the system spontaneously separates into a dense and a dilute region in a phenomenon known as *Motility-Induced Phase Separation* (MIPS). However, this phenomenon is notably absent from systems of particles with a rod-like shape, such as that of certain kinds of bacteria. We use computer simulations to show that MIPS is dramatically suppressed when the shape of particles goes from disk-like/spherical to one that is rod-like. We demonstrate that this suppression is strong, preventing MIPS almost completely for two-dimensional systems of particles thrice as long as they are wide. For three-dimensional systems this suppression is even stronger, and MIPS disappears for any particles only twice as long as they are wide. We show that this suppression is the result of torques between particles: when torques between particles act in such a way that the duration of collisions between two particles in the fluid is decreased, the crucial collision-induced slowdown required for MIPS is inhibited, and the fluid phase is prevented from undergoing MIPS.

In **Chapter 3** we model the self-assembly of a system of hourglass-shaped NaYF_4 nanoparticles at an air-hexane interface. These particles, synthesized by Stan Najmr and Mingyue Zhang in the group of Christopher Murray at the University of Pennsylvania, demonstrate a number of interesting self-assembly phenomena that we show can all be traced back to the influence of shape on a particle’s adsorption to the air-hexane interface. We combine self-assembly simulations with interfacial adsorption simulations performed by Giuseppe Soligno to demonstrate that the hourglass shape causes particles

to adsorb onto the air-hexane interface in two (meta-)stable orientations: one where their long axis lies along the interface (“horizontal”) and one where it is perpendicular (“vertical”). Particles adsorbed in the horizontal orientation deform the interface in a way that can be described as a capillary quadrupole: upward at the ends of the hourglass, and downward around the middle. As a result, horizontal particles attract each other with a strong capillary quadrupole-quadrupole interaction, but this same interaction prevents them from attaining their close-packed configurations. The vertically adsorbed particles do not significantly deform the interface, and as a result do not have significant capillary interactions either with each other or with the horizontal particles. We find that this shape-dependent adsorption and the resulting capillary interactions effectively reproduce experimental observations, namely that i) particles are found in either the vertical or horizontal adsorption configurations, ii) these two configurations partially demix, iii) vertical particles form close-packed domains, but horizontal particles do not and iv) horizontal particles form end-to-end attached strings at low density.

In **Chapter 4** we study a system of hard rounded tetrahedra, motivated by two interesting recent observations. The first is that CdSe nanoparticles of this shape (as synthesized by Yaoting Wu in the group of Christopher Murray at the University of Pennsylvania) were observed to form egg-shaped supraparticles in experiments performed by Da Wang (in the group of Alfons van Blaaderen at Utrecht University). The second is a recent report in which these particles of this shape were suggested to have a quasicrystal as their densest packing [47]. We characterize the rounded tetrahedral shape by defining a roundness shape parameter s , where $s = 0$ is a tetrahedron and $s = 1$ a sphere. Using computer simulations, we determine the densest packings as a function of the roundness s and the phase diagram as a function of s and the packing fraction ϕ . We find that there are thirteen close-packed structures, most of which are crystals with $N = 2$ or $N = 4$ particles in their unit cells. However, for slightly rounded tetrahedra of approximately $s \in [0.040, 0.088]$, we find the densest packing to be an $N = 82$ -particle quasicrystal approximant, corroborating the result of Ref. [47]. All close-packed structures are also stable below close packing. In addition to the close-packed phases, for very rounded tetrahedra ($s > 0.5$) we also find a plastic crystal phase. Some of these structures are very similar to one another, which can complicate classification. We demonstrate that one can use Minkowski structure metrics, a variant of the Steinhardt bond-order parameters, to effectively distinguish and identify the various solid phases both in the close-packing limit as well as at lower densities.

In **Chapter 5** we investigate how to automate the process of finding good order parameters to identify and distinguish between various phases, using as a testbed the system of hard rounded tetrahedra. Specifically, we do so by performing a Principal Component Analysis (PCA) on a data set containing trajectories from the fourteen rounded tetrahedron phases that we observed in Chapter 4. PCA is a simple and transparent dimensionality reduction technique that gives us immediate insight into which bond order parameters \bar{q}_l are most important for classifying the various phases. We perform this PCA on two sets of candidate order parameters, one containing the Minkowski structure metrics \bar{q}_l with $2 \leq l \leq 12$ and one containing both \bar{q}_l and their higher-order invariants w_l with $2 \leq l \leq 24$. In both cases we find that the first principal component yields a general measure for crystallization, while the second and third principal components serve

to distinguish the various crystal phases from one another.

Finally, in **Chapter 6** we return to our original motivation for studying the rounded tetrahedra, and connect back to the egg-shaped supraparticles self-assembled by CdSe nanoparticles. We first determine that the experimental system corresponds to hard rounded tetrahedra with a roundness of roughly $s \approx 0.5$. Following that, we compare the order parameter fingerprints of two reconstructed supraparticles to the phases we determined in Chapter 4, and conclude that the supraparticles have a crystal structure that corresponds to hard rounded tetrahedron crystal VII — a slightly deformed FCC lattice with a two-particle unit cell of rounded tetrahedra in opposing orientations. In the model system, the roundness $s = 0.5$ corresponds to a triple point of the fluid, the plastic crystal pFCC and the crystal VII. We calculate the coexistence properties of these three phases by means of free-energy calculations. We find that the supersaturation of the fluid-pFCC transition drops sharply in the vicinity of this triple point, while those of the fluid-VII and pFCC-VII transitions remain comparatively high. This shape-sensitivity could allow for a highly tunable supraparticle nucleation in this regime, but it also warrants caution regarding the limits of applicability of our hard-particle model. By performing self-assembly simulations under a shrinking spherical confinement, we find that supraparticles of hard rounded tetrahedra with $s \in [0.7, 1]$ exhibit Mackay/anti-Mackay ordering similar to hard spheres. For less rounded tetrahedra there is significant ordering at the spherical boundary, with two different structures arising depending on the roundness s : a complex structure similar to the layers of the dodecagonal quasicrystal formed by hard tetrahedra for $s \in [0, 0.2]$, and a simpler triangular lattice for $s = 0.3$. For $s \in [0.4, 0.6]$, which covers the range of shapes found in the experiments, we find no significant structural order either in bulk or at the boundary. We hypothesize that a competition between the various modes of ordering inhibits structural order in this range. While we are ultimately not yet able to answer the question of why supraparticles of rounded tetrahedra become egg-shaped, we expect the presented results to provide a solid basis usable for further research into anisotropic supraparticle self-assembly.

Samenvatting

In dit proefschrift bestuderen we de geometrische effecten van deeltjesvorm en omgeving op de zelforganisatie van colloïdale deeltjes. Colloïden zijn deeltjes met afmetingen tussen de 1 nm en 1 μm . Met deze grootte zijn ze groot genoeg om een betekenisvolle *vorm* aan ze toe te kennen, maar klein genoeg om een constante Brownse beweging te ondergaan. Deze Brownse beweging zorgt ervoor dat de deeltjes zichzelf organiseren in verschillende thermodynamische fasen, zoals vloeistoffen of vaste stoffen. Voor colloïden worden de fasen die gevormd worden en onder welke omstandigheden bepaald door de eigenschappen van de deeltjes en hun interacties. Op hoge dichtheden is het vooral de vorm van de deeltjes die belangrijk is. Echter zijn niet alleen de eigenschappen van de deeltjes belangrijk, maar ook die van hun omgeving. Het zelforganisatieproces en de resulterende fasen kunnen drastisch verschillen afhankelijk van of deeltjes zich organiseren in bulk, in de buurt van een muur, of begrensd tot een klein gebied zoals binnenin een druppel of op het grensvlak tussen twee vloeistoffen. In dit proefschrift gebruiken we computersimulaties om dit soort geometrische effecten te bestuderen in vier verschillende kaders.

In **Hoofdstuk 2** bestuderen we het effect van deeltjesvorm op een systeem van deeltjes die zichzelf voortstuwten door energie in hun omgeving (“brandstof”) om te zetten in hun eigen beweging. Zulke zelfvoortstuwning is normaal voor veel biologische systeem, en kan de beweging beschrijven van bacteriën, scholen vis, zwermen vogels, kuddes schapen en zelfs van mensenmenigtes. Voor de meeste van deze zogeheten *actieve materie* waarbij a) de deeltjes elk zichzelf voortstuwten in een langzaam veranderende “voorwaartse” richting en b) deze deeltjes niet door of over elkaar heen kunnen bewegen, vind men dat boven een kritieke dichtheid en zelfvoortstuwingskracht het systeem zichzelf spontaan ontbindt in een gebied met een hoge en een met een lage dichtheid. Dit fenomeen staat bekend als *Motility-Induced Phase Separation* (MIPS). MIPS komt opmerkelijk genoeg niet voor in systemen van staafvormige deeltjes, zoals die van bepaalde bacteriën. We gebruiken computersimulaties om te laten zien dat MIPS onderdrukt wordt wanneer deeltjes van schijf/bolvormig naar staafvormig veranderen. We tonen aan dat deze onderdrukking sterk genoeg is om MIPS volledig te voorkomen in twee dimensies voor deeltjes drie keer zo lang als dat ze wijd zijn, en in drie dimensies zelfs voor deeltjes twee keer zo lang als dat ze wijd zijn. We laten zien dat deze onderdrukking het resultaat is van torsies tussen de deeltjes, en dat de cruciale botsingsgeïnduceerde vertraging van deeltjes, die nodig is voor MIPS, voorkomen wordt wanneer torsies de duur van botsingen tussen deeltjes verkorten.

In **Hoofdstuk 3** modelleren wij de zelforganisatie van zandlopervormige NaYF_4 nanodeeltjes aan een lucht-hexaangrensvlak. Deze deeltjes, gemaakt door Stan Najmr en Mingyue Zhang in de groep van Christopher Murray aan de Universiteit van Pennsylvania, vertonen een aantal interessante zelforganisatiefenomenen waarvan wij aantonen dat zij allen het gevolg zijn van de invloed van de deeltjesvorm op de adsorptie aan het lucht-hexaangrensvlak. We combineren zelforganisatiesimulaties met grensvlakadsorptiesimulaties uitgevoerd door Giuseppe Soligno om aan te tonen dat de zandlopervorm

ervoor zorgt dat deeltjes aan het grensvlak adsorberen in twee verschillende (meta)stabiele orientaties: een waarbij de lange as in het grensvlak ligt (“horizontaal”) en een waarbij deze er loodrecht op staat (“verticaal”). Deeltjes geadsorbeerd in de horizontale orientatie vervormen het grensvlak op een manier die beschreven kan worden als een capillaire quadrupool: omhoog bij de uiteinden van de zandloper en naar beneden rond de middel. Als gevolg van deze vervorming ondervinden de horizontale deeltjes een attractieve capillaire quadrupool-quadrupool interactie met elkaar. Echter zorgt dezelfde interactie er ook voor dat ze hun meest efficiënte pakking niet kunnen bereiken. De verticaal geadsorbeerde deeltjes vervormen het grensvlak nauwelijks, en hebben als gevolg ook bijna geen interacties met elkaar of met de horizontaal geadsorbeerde deeltjes. We vinden dat deze vorm-afhankelijke adsorptie en de resulterende capillaire interacties effectief de experimentele observaties reproduceren, namelijk dat i) deeltjes op het grensvlak gevonden kunnen worden in óf de horizontale óf de verticale orientatie, ii) dat deze twee orientaties deels ontmengen, iii) dat verticale deeltjes dicht gepakte domeinen vormen, maar horizontale deeltjes niet, en iv) dat horizontale deeltjes op lage dichtheid strengen vormen waarbij de uiteinden van de zandlopervormen aan elkaar zitten.

In **Hoofdstuk 4** bestuderen we een systeem van harde ronde tetraëders, gemotiveerd door twee interessante recente observaties. De eerste is dat CdSe nanodeeltjes met deze form (zoals gemaakt door Yaoting Wu in de groep van Christopher Murray aan de universiteit van Pennsylvania) ei-vormige supradeeltjes bleken te vormen in experimenten van Da Wang (in de groep van Alfons van Blaaderen aan de Universiteit Utrecht). De tweede is een recente publicatie waarin deeltjes met deze vorm een quasikristal als dichtste pakking lijken te hebben [47]. We beschrijven de ronde tetraëdervorm door een rondheidsvormparameter s te definiëren, waarbij $s = 0$ overeenkomt met een tetraëder en $s = 1$ met een bol. Met behulp van computersimulaties bepalen we de dichtste pakkingen als een functie van de vormparameter s , en het fasediagram als functie van s en de pakingsfractie ϕ . We vinden dat er dertien dichtste pakkingen bestaan, waarvan de meeste kristallen zijn met $N = 2$ of $N = 4$ deeltjes in hun eenheidscel. Voor licht ronde tetraëders van $s \in [0.040, 0.088]$ vinden we echter dat de dichtste pakking een $N = 82$ -deeltjes quasikristal-benadering is, in overeenstemming met Ref. [47]. Alle dertien structuren zijn ook stabiel op lagere dichtheden. Naast de dicht gepakte fasen vinden wij ook een plastische kristalfase voor zeer ronde tetraëders ($s > 0.5$). Een aantal van deze structuren lijken zeer erg op elkaar, wat het lastig kan maken om ze van elkaar te onderscheiden. We tonen aan we desondanks deze fasen effectief kunnen identificeren en onderscheiden zowel in de dichtepakkinglimiet als op lagere dichtheden met behulp van de zogeheten Minkowski structuurmetrieken, een variant op de Steinhardt bondordeparameters.

In **Hoofdstuk 5** onderzoeken we hoe we het proces van goede ordeparameters vinden om fasen te onderscheiden kunnen automatiseren, waarbij we het systeem van ronde tetraëders gebruiken als een testomgeving. Hiervoor voeren wij een *Principal Component Analysis* (PCA) uit op een dataset met data van de veertien rondetetraëderfasen uit het vorige hoofdstuk. PCA is een simpele en transparante dimensionaliteitsreductietechniek die ons duidelijk inzicht geeft in welke orderparameters \bar{q}_l het meest belangrijk zijn om de verschillende fasen te classificeren. We voeren deze PCA uit op twee sets kandidaat-ordeparameters, een met de Minkowski structuurmetrieken \bar{q}_l met $2 \leq l \leq 12$ en een met zowel \bar{q}_l als hun hogere-orde invarianten w_l , beide met $2 \leq l \leq 24$. In beide gevallen

vinden we dat de eerste hoofdcomponent een algemene maat van kristallizatie beschrijft, terwijl de tweede en derde hoofdcomponenten dienen om de verscheidene kristalfasen van elkaar te onderscheiden.

Tot slot keren we in **Hoofdstuk 6** terug naar onze oorspronkelijke motivatie om de ronde tetraëders te bestuderen, en gaan we verder met het modelleren de ei-vormige supradeeltjes gevormd door CdSe nanodeeltjes in experimenten. Eerst bepalen we dat de deeltjes in de experimenten overeen komen met harde tetraëders met een rondheid van ongeveer $s \approx 0.5$. Vervolgens vergelijken we de ordeparameter “vingerafdruk” van twee gereconstrueerde supradeeltjes met die van de fasen gevonden in Hoofdstuk 4, en concluderen we hieruit dat de supradeeltjes een kristalstructuur hebben die overeen komt met het kristal VII van harde ronde tetraëders — een licht vervormd kubisch vlakgecentreerd rooster (FCC) met een eenheidscel van twee ronde tetraëders in tegenovergestelde orientaties. In het modelsysteem komt $s = 0.5$ overeen met het driefasenpunt van de vloeistof, het plastisch kristal pFCC en kristal VII. Met behulp van vrije-energieberekeningen bepalen we de coëxistentie-eigenschappen van deze drie fasen. We vinden dat de oververzadiging van de vloeistof/pFCC-overgang scherp afneemt in de buurt van het driefasenpunt, terwijl die van de vloeistof/VII- en pFCC/VII-overgangen relatief hoog blijven. Deze gevoeligheid voor de deeltjesvorm zou kunnen dienen als een afstelknop voor de supradeeltjesnucleatie in dit gebied, maar biedt ook reden tot voorzichtigheid omtrent de grenzen van toepasbaarheid van ons hardedeeltjesmodel. Door zelforganisatiesimulaties te doen onder een krimpende bolvormige begrenzing, vinden wij dat supradeeltjes van harde ronde tetraëders met $s \in [0.7, 1]$ een Mackay/anti-Mackay orde vertonen vergelijkbaar met het gedrag van harde bollen. Voor minder ronde tetraëders is er een significante mate van orde aan het begrenzende oppervlak, met twee verschillende structuren afhankelijk van de rondheid s . Voor $s \in [0, 0.2]$ vinden we een complexe structuur die lijkt op de lagen van het dodecaëdrische quasikristal dat gevormd wordt door harde tetraëders. Voor $s = 0.3$ vinden we een veel simpeler driehoekig rooster. In het bereik $s \in [0.4, 0.6]$, wat ook het bereik van de deeltjes in de experimenten beslaat, vinden we geen enkele significante mate van structuurordening noch in de bulk noch aan het oppervlak. We veronderstellen dat een competitie tussen de verschillende ordeningsvormen de structuurordening verhindert in dit bereik. Hoewel we uiteindelijk nog niet in staat zijn om te beantwoorden waarom ronde tetraëders ei-vormige supradeeltjes vormen, verwachten we dat onze resultaten een solide basis vormen voor verder onderzoek naar de zelforganisatie van anisotrope supradeeltjes.

Acknowledgements

First and foremost I would like to thank my promotors, **Marjolein Dijkstra** and **René van Roij**. Working with you two has always been a pleasure. Considering that I did both my BSc and MSc at Utrecht and followed many of your courses, you have in a rather literal sense taught me much of all that I know. **Marjolein**, I am both impressed and grateful for the way you could always find the time to help out one of your students. It has happened far too often that I sent you an email about something that could easily wait, but for which I then received a reply with a timestamp ‘Saturday 00:04’, ‘Sunday 20:08’, or even ‘Wednesday 04:03’. You have always given me a great deal of freedom in choosing what to research, and you were always ready with advice and suggestions when this freedom occasionally proved challenging. **René**, I have always been inspired by the clear joy and curiosity you exude for discussing science. Be it teaching, questions during work discussions or in meetings, you always manage to make science fun and approachable even for the most seemingly daunting subjects. I’ve always appreciated that, first as a student of yours and later during my PhD. To the both of you: a fellow student of yours once remarked that doing a PhD under you two is a little bit like being adopted, and I agree. Thank you for making me a part of this scientific family.

Next I would like to thank the supervisor of my MSc thesis, **Laura Filion**. **Laura**, without your fantastic supervision and infectious enthusiasm and curiosity my MSc thesis would never have turned out as well as it did, and without that I doubt I would have started this PhD. Thank you for setting me on this very fulfilling path.

My thanks also to the rest of the staff: **Alfons van Blaaderen** for his inexhaustible fount of knowledge, ideas, students and very useful criticism. **Marijn van Huis**, **Gerhard Blab**, **Arnout Imhof**, **Krassimir Velikov**, **Patrick Baesjou**, **Lisa Tran**, **Freddy Rabouw**, **Henk Stoof** and **Bela Mulder** for discussions and questions during SCM and T+S work discussions. **Marion**, **Dianne** and especially **Hester**, for handling everything administrative and doing so with a smile. **Peter** for computer expertise, and **Dave** for philosophy.

Science is way too big to do all of it on your own, and in these past years I have had the great pleasure of collaborating with a number of folk both within the SCM group and outside of it, for which I would like to thank them again here. **Berend**, **Frank** and **Laura**, for the (slanted) cube crystal defects project that started it all during my MSc. **Jeroen**, for doing the heavy lifting on the theoretical side of our active matter collaboration. **Giuseppe** and **Stan** for the hourglass particle project, which is still one of my favorites despite all the trouble we had finishing it. **Gabriele**, for the multiple interesting and fruitful collaborations we had, ranging from spherotetrahedra and machine learning to nucleation. **Peter**, **Sander**, **Sacha** and again **Gabriele** for the interesting discussions

on machine learning and the very nice paper that resulted from that. And lastly **Da**, for asking a deceptively simple question about eggs.

I also want to thank **Stefania**, **Reza**, and the other folk at the Active Matter workshop in Erice. I have lived more in those five days than in months in other times.

Doing this PhD would not have been nearly as enjoyable without all the great people that make up the SCM group. There are a few people which I would like to thank in particular. **Tom** and **Sina**, I've always enjoyed sharing an office with you two, even when I had to cram in my notes on the whiteboard into a small corner so as not to erase your football predictions. **Berend**, for being kind of like a scientific big brother. **Roy**, for being the best student I have ever worked with. It came as absolutely no surprise to me when you changed from my student to my officemate and coworker—you were a competent researcher from the start. The Italians: **Massi**, **Carmine**, **Emanuele** and **Gabriele**, for competition, discussions and the fun game of trying to guess whether the heated Italian discussions in the office next door were about physics or about football—both seemed to be equally likely. **Maarten**, **Marjolein (de Jager)**, **Joost**, **Kelly** and **Meike** and others for drawing games, GeoGuessr and discussions on just about anything during the online borrels when COVID had everything locked down. **Anna**, your enthusiastic personality and curiosity always brightened my day. **Willem (Boon)**, for fun times at Physics@Veldhoven, and for a great quote. **Daniel**, for wild stories and interesting discussions at conferences and Debye events. **Chris**, for dry wit and co-supervising students. **Albert**, for being a blast to be around. **Giuliana**, **Alberto**, **Gerardo**, **Susana** and **Ethan**, for advice, commiserations and levity during the final writing stages, and after. **Nik**, for writing the awesome visualization code `partViewer3D` that I could extend to make many of the images in this thesis. **Michiel**, for supplying code to kickstart a few of my projects, and for showing me that WebGL is a thing, eventually leading me to a very fun side project. With SCM being such a large group there is no shortage of people to thank for good times, but I will keep it brief for the rest. To the old guard **Vasileios**, **Siddharth**, **Simone**, **Harini**, **Giulia**, **Jessi**, **Wiebke**, **Fabian**, **Tonnishtha**, **Douglas**, **Pepijn**, **Wessel**, **Ernest**, my PhD-generational peers **Naveed**, **Rama**, **Stijn**, **Dyaneshwar**, **Xiaobin**, **Xiaodan**, and the new folk **Zahra**, **Willem (Gispén)**, **Erik**, **Mark**, **Harith**, **Sander**, plus any I might have missed: during my time at SCM I have had nothing but pleasant and interesting encounters with all of you, thank you.

A downside to not moving far abroad for a PhD is that you make fewer new friends. Of course, the upside is that instead I get to thank more old friends here, instead! **Rinse**, **Tom**, **Michel**: turns out “E” is a pretty good letter. **Rinse**, you still have the coolest PhD project out of all of us, pun intended. **Michel**, I could hand you a copy of this thesis and you'd probably know half of what's in it already, given the number of times we've talked about it. WhatsApp is really not a good medium to discuss free-energy calculation algorithms, but we did so anyway. Thanks for being a rubber duck, a paronymph, and a friend. The boulder-bros **Niels**, **Mark** and **Anne**, for finding me a new and very fun sport and for the many boulder-boardgame-dinner weekends. Also, potjestijd? The Gloomhaven gang **Yorin**, **Martijn** and **Erik**, for the precious few in-person social inter-

actions to keep me sane throughout the tough parts of the pandemic. **Yorin** and **Martijn** (again) for online games. Need new game! **Erik**, for being a bro.

Finally, I would not be where I am without my family. **Tessa**, sis, thank you for reminding me of the world outside the ivory tower, and for teaching me about resilience. Dear parents, **Wim** en **Mar**, as usual I find it difficult to put into words how much I appreciate you. Whether I needed to vent (when research went poorly) or share my enthusiasm (when it went well), you were there for me, and it is your unconditional love and support that has pulled me through some hard times. Thank you for everything.

Publications

This thesis is based on the following publications:

- R. van Damme, J. Rodenburg, R. van Roij, M. Dijkstra, *Interparticle torques suppress motility-induced phase separation for rodlike particles*, The Journal of Chemical Physics 150, 164501 (2019). (Chapter 2)
- S. Najmr, R. van Damme, M. Zhang, G. Soligno, M. Zanini, M.A. Fernandez-Rodriguez, J.D. Lee, L. Isa, M. Dijkstra, C.B. Murray, *Synthesis of Nanocrystalline β -NaYF₄ Heterostructures with Tunable Negative Curvature and their Self-Assembly Patterns at Interfaces*, manuscript in preparation. (Chapter 3)
- R. van Damme, G.M. Coli, R. van Roij, M. Dijkstra, *Classifying Crystals of Rounded Tetrahedra and Determining Their Order Parameters Using Dimensionality Reduction*, ACS Nano 14 (11), 15144-15153 (2020). (Chapters 4 and 5)

Other publications by the author:

- R. van Damme, B. van der Meer, J.J. van den Broeke, F. Smalenburg, L. Filion, *Phase and vacancy behaviour of hard slanted cubes*, The Journal of Chemical Physics 147, 124501 (2017) (Cover image for J. Chem. Phys. Volume 147, Issue 12)
- B. van der Meer, R. van Damme, M. Dijkstra, F. Smalenburg, L. Filion, *Revealing a Vacancy Analog of the Crowdion Interstitial in Simple Cubic Crystals*, Physical Review Letters 121 (25), 258001 (2018)
- P. Cats, S. Kuipers, S. de Wind, R. van Damme, G.M. Coli, M. Dijkstra, R. van Roij *Machine-learning free-energy functionals using density profiles from simulations*, APL Materials 9, 031109 (2021)
- G.M. Coli, R. van Damme, C.P. Royall, M. Dijkstra, *Hidden in the fluid: fivefold symmetry and polymorph selection in hard spheres*, manuscript in preparation.

Oral and poster presentations

The contents of this thesis were presented at the following events:

- Summer school *Fundamental Problems in Statistical Physics XIV*, 16-29 July 2017, Bruneck, Italy.
Poster: *Collective behaviour of 3D self-propelled rods*
Authors: R. van Damme, R. van Roij, M. Dijkstra
- Physics@Veldhoven 23-24 January 2018, Veldhoven, Netherlands.
Poster: *Suppression of motility-induced phase separation for rodlike particles*
Authors: R. van Damme, J. Rodenburg, R. van Roij, M. Dijkstra
- Workshop ‘Self-Organization in Active Matter’ 2-5 October 2018, Erice, Italy.
Poster: *Suppression of motility-induced phase separation for rodlike particles*
Authors: R. van Damme, J. Rodenburg, R. van Roij, M. Dijkstra
- 5th International Soft Matter Conference (ISMC2019), 3-7 June 2019, Edinburgh, UK
Poster: *Interparticle torques suppress motility-induced phase separation for rodlike particles*
Authors: R. van Damme, J. Rodenburg, R. van Roij, M. Dijkstra
- 27th Dutch Soft Matter Meeting, 5 November 2019, Utrecht, The Netherlands
Invited talk: *Interparticle torques suppress motility-induced phase separation for rod-like particles*
Authors: R. van Damme, J. Rodenburg, R. van Roij, M. Dijkstra
- WE-Heraeus-Seminar on “Wetting and Capillarity in Complex Systems”, 24-29 November 2019, Physikzentrum Bad Honnef, Germany
Poster: *Hourglasses at a fluid-fluid interface: multipoles, demixing and hindered assembly*
Authors: S. Najmr, R. van Damme, M. Zhang, G. Soligno, M. Zanini, M.A. Fernandez-Rodriguez, J.D. Lee, L. Isa, M. Dijkstra, C.B. Murray

About the author

Robin van Damme was born September 11th of 1992 in Utrecht, the Netherlands. After finishing his secondary education at the Montessori Lyceum Herman Jordan in 2011, he started the *Physics and Astronomy* bachelor degree at Utrecht University. It was there that he developed an interest in physics simulations, choosing to do his Bachelor's thesis on simulating the shape of a liquid droplet on a deformable surface under the supervision of Prof. René van Roij. After obtaining his BSc in 2014, he went on to study *Nanomaterials: Chemistry and Physics*, also at Utrecht University. During his MSc he performed computer simulations research under the supervision of Dr. Laura Filion, and the resulting MSc thesis *Phase and vacancy behaviour of hard slanted cubes* was both awarded the EMMEPH prize for best Master's thesis in 2016 and led to his first scientific publication in *The Journal of Chemical Physics* in 2017. Having found doing research to his liking, he continued his time at Utrecht University by accepting Prof. Marjolein Dijkstra's offer for a PhD position. Here he performed research into the nonequilibrium behaviour of active nematics and the geometric effects of particle shape and confinement on self-assembly, the results of which can be found in peer-reviewed journals and/or within this thesis. In addition to his scientific pursuits, he likes to bury himself in a good scifi or fantasy book, go bouldering or swimming, or play tabletop or videogames with friends.

